Localization of Laplacian Eigenfunctions in Simple and Irregular Domains

Nguyen Binh Thanh

HAL Id: pastel-00764806
https://pastel.archives-ouvertes.fr/pastel-00764806

Submitted on 13 Dec 2012

Localization of Laplacian Eigenfunctions
in Simple and Irregular Domains

by

Nguyen Thanh Binh

A dissertation accepted in the satisfication of
the requirements for the degree of
Doctor of Science

in

Theoretical Physics and Applied Mathematics

ECOLE POLYTECHNIQUE
PALAISEAU, FRANCE

Scientific jury:

Prof.	Mark ASCH	Reviewer
Prof.	Xavier BOUTILLON	Examiner
Dr.	Denis GREBENKOV	Supervisor
Prof.	Michel LAPIDUS	Examiner
Prof.	Stephane NONNENMACHER	Reviewer
Prof.	Bernard SAPOVAL	Examiner

September 2012

Abstract

The primary goal of the thesis is to study localization of Laplacian eigenfunctions in bounded domains when an eigenfunction is mainly supported by a small region of the domain and vanishing outside this region. The high-frequency and low-frequency localization in simple and irregular domains has been investigated for both Dirichlet and Neumann boundary conditions.

Three types of high-frequency localization (whispering gallery, bouncing ball, and focusing eigemodes) have been revisited in circular, spherical and elliptical domains by deriving explicit inequalities on the norm of eigenfunctions. In turn, no localization has been found in most rectangular domains that led to formulating an open problem of characterization of domains that admit high-frequency localization.

Using the Maslov-type differential inequalities, the exponential decay of low-frequency Dirichlet eigenfunctions has been extensively studied in various domains with branches of variable cross-sectional profiles. Under an explicit condition, the L^2-norm of an eigenfunction has been shown to exponentially decay along the branch with an explicitly computed decay rate. This rigorous upper bound, which is applicable in any dimension and for both finite and infinite branches, presents a new achievement in the theory of classical and quantum waveguides, with potential applications in microelectronics, optics and acoustics.

For bounded quantum waveguides with constant cross-sectional profiles, a sufficient condition on the branch lengths has been derived for getting a localized eigenfunction. The existence of trapped modes in typical finite quantum waveguides (e.g L-shape, bent strip and cross of two strips) has been proven provided that their branches are long enough, with an accurate estimate on the required minimal length. The high sensitivity of the localization character of eigenmodes to the length of branches and to the shape of the waveguide may potentially be used for switching devices in microelectronics and optics.

The properties of localized eigenmodes in a class of planar spectral graphs have been analyzed. An efficient divide-and-conquer algorithm for solving the eigenproblem of the Laplacian matrix of undirected weighted graphs has been proposed and shown to run faster than traditional algorithms.

A spectral approach has been developed to investigate the survival probability of reflected Brownian motion in reactive media. The survival probabilities have been represented in the form of a spectral decomposition over Laplacian eigenfunctions. The role of the geometrical structure of reactive regions and its influence on the overall reaction rate in the long-time regime has been studied. This approach presents a mathematical basis for designing optimal geometrical shapes of efficient catalysts or diffusive exchangers.

Acknowledgements

some problems with Linux and technical softwares.

To my friends in PMC, I am very happy to be a member of PMC football team. Let me thank Daniel, Matteo, Slava, Lily, Long, Duc, Morgane, Nayely, Xiaoxin, Charllote, Lucie, Jong, Jie, Nan Di,... for their very interesting and funny stories about daily news all over the world. They made my life easier in France.

I owe a great debt of thanks to my friends in France and to my family. I want to give my big gratefulness to Le Dung, Tan Trung and Le Phong for their help and encouragement during my PhD thesis in Europe. I want to show my gratitude to my former supervisors, Dr. Nguyen Dinh Thuc and Dr. Pham The Bao for our fruitful discussions during my stay in Vietnam. I also would like to give my thankfulness to Anna, Matteo and other Russian friends for their warmness and kindness during my stay in Russia. For my students, let me thank Anh Duc and Van Thach for their supports in one of my projects.

Finally, I want to appreciate my parents, my younger brother, and my girlfriend for their unconditional love.

Nguyen Thanh Binh

Paris, June 2012

Table of Contents

Chapter 1

Motivation

The Laplace eigenvalue problem has always been a golden topic in physics, mathematics and computer science. A classical eigenproblem in a bounded domain $\Omega \in \mathbb{R}^d$ can be formulated as

$$\begin{cases} \triangle u + \lambda u = 0, \text{ in } \Omega, \\ \quad \text{it satisfies a boundary conditon on } \partial\Omega, \end{cases} \tag{1.1}$$

where $\triangle = \nabla \cdot \nabla = \frac{\partial^2}{\partial x_1^2} + \cdots + \frac{\partial^2}{\partial x_d^2}$ is the Laplace operator. The most common boundary conditions are given as following

$$\begin{cases} \text{Dirichlet boundary condition: } u = 0 \text{ on } \partial\Omega, \\ \text{Neumann boundary condition: } \frac{\partial u}{\partial \mathbf{n}} = 0 \text{ on } \partial\Omega, \\ \text{Robin boundary condition: } \frac{\partial u}{\partial \mathbf{n}} + hu = 0 \text{ on } \partial\Omega \ (h > 0), \end{cases} \tag{1.2}$$

where h is a positive constant and $\mathbf{n}$ is the normal vector oriented outwards the domain.

The Laplacian eigenproblem may arise from various problems of mathematical physics, such e.g vibration modes of a thin membrane, vibration of water waves on the ocean surface, standing waves in optical or acoustical cavity resonators, propagation of particles in waveguides, chemical reactors with heterogeneous spatial distributions of catalytic germs, the eigenstates of a single trapped particle in quantum mechanics etc. The properties of Laplacian eigenvalues and eigenfunctions have been investigated in many scientific disciplines, including spectral theory, theory of acoustical, optical, and quantum waveguides, condensed matter physics and quantum mechanics, quantum graphs, spectral theory, image processing, computer graphics, dynamical systems and quantum billiards, biology, etc.

The geometrical structure of Laplacian eigenfunctions has been studied in various directions [4, 51, 52, 80, 108, 109, 111, 116–118, 131, 145, 156, 159, 167, 168, 171, 176, 213, 228–230]. During 1990s, Sapoval and co-workers have formulated and investigated the problem of localization in irregularly-shaped domains through numerical simulations and experiments [71, 76, 104, 106, 187, 188, 191–193]. Localized eigenmodes in bounded planar domains have a special interest in their own right. Qualitatively, an eigenfunction is localized if it is mainly distributed in a fraction of a domain, and decays rapidly outside this region. There are many questions related to localization. How can the geometrical irregularities influence

localization? What is the difference between localized and non-localized eigenmodes? Interestingly, a generic mathematical definition of localization is still unknown. One of the goals of this monograph is to investigate the properties of localization, and more importantly, to find a *mechanism* for explaining this phenomenon.

This chapter serves first to introduce a historical overview about localization of Laplacian eigenfunctions in a bounded domain in $\mathbb{R}^2$ and second to emphasize our contribution and the importance of our works. The chapter ends by giving the outline of the monograph.

1.1 High-frequency localization

1.1.1 History

During 1870*s*, Lord Rayleigh, one of the most famous English physicists, mentioned in his textbook *Theory of Sound* about the study of whispering waves in Saint Paul Cathedral in London. During 1910*s*, he continued by studying the problem of whispering gallery and showing the existence of localized eigenmodes in elliptical domains [179]. Motivated by Rayleigh's works, Raman and Sutherland documented an acoustical observation in the whispering gallery under the dome of Saint Paul Cathedral in London. In this observation, a whisper from a person standing at one position in the whispering gallery will propagate along the curved wall to another person stood near the wall [177, 178]. In 1960, Keller and Rubinow discussed these so-called *whispering gallery modes* (Fig. 1.1a) and also *bouncing ball modes* (Fig. 1.1b), and showed that these modes exist for a two-dimensional domain with arbitrary smooth convex curve as its boundary [128]. Lazutkin and co-workers developed a semiclassical approximation of Laplacian eigenfunctions in convex domains [13, 137–140]. In 1994, Chen and his colleagues used Mathieu and modified Mathieu functions to visualize *whispering gallery modes* and *bouncing ball modes* in elliptical domains [41], and moreover, they also reported another type of localization named *focusing modes* (Fig. 1.1c). All these eigenmodes become more and more localized in a small subdomain when the corresponding eigenvalue increases. In 1997, Bäcker and co-workers investigated the number of these eigenmodes in a class of two-dimensional quantized billiards with two parallel walls [14].

In quantum billiards, a lot of studies are related to the structure of high-frequency Laplacian eigenfunctions [11, 13, 89, 141, 148, 201]. For a bounded domain Ω with an ergodic billiard flow [200], Shnirelman proved one of his well-known theorems (also known as quantum ergodicity theorem [34, 45, 232, 233]) which states that among the set of L^2-normalized Dirichlet (or Neumann) Laplacian eigenfunctions, there is a sequence u_{j_k} of density 1 (i.e., $\lim_{k\to\infty} j_k/k = 1$), such that for any open subset $V \subset \Omega$, one has [198]

$$\lim_{k\to\infty} \int_V |u_{j_k}(\mathbf{r})|^2 d\mathbf{r} = \frac{\mu_d(V)}{\mu_d(\Omega)}, \tag{1.3}$$

where μ_d is the Lebesgue measure.

From Shnirelman's theorem, $\{u_{j_k}\}$ is a sequence of non-localized eigenfunctions which become more and more uniformly distributed over the domain (see [34, 89, 116] for further discussion and references). How-

ever, this theorem does not prevent the existence of localized eigenmodes in Ω. How large the excluded subsequence of "localized" eigenfunctions may be? In a special case of arithmetic hyperbolic manifolds, Rudnick and Sarnak proved that there is no strong localization ("scarring") onto totally geodesic sub-manifolds [186]. This statement is known as the quantum unique ergodicity (QUE). The validity of this statement for other dynamical systems (in particular, ergodic billiards) remains under investigation [17, 65, 105]. The related notion of weak quantum ergodicity was discussed by Kaplan and Heller [125]. A classification of eigenstates to regular and irregular ones was thoroughly discussed (see [175, 219] and references therein).

Related to "scarring" phenomenon, Liu and co-workers investigated the localization of Dirichlet-Laplacian eigenfunctions on classical periodic orbits in a spiral-shaped billiards. Bies and co-workers presented a brief survey on scarring and symmetric effects of eigenfunctions in a stadium billiard [24]. Other references can be found in [95].

It is worth mentioning that there are many physical experiments related to whispering gallery and bouncing ball modes. For instance, Wiersig investigated the structure of whispering gallery modes in optical microdisks perturbed by nanoparticles [227]. Albert and co-workers discussed whispering gallery modes lasing in electrically driven quantum dot micropillars [3]. Sridhar and co-workers performed a series of experiments in microwave cavities in the shape of Sinai's billiard [206, 207]. In particular, they observed bouncing ball modes and modes with quasi-rectangular or quasi-circular symmetry. Bäcker and Schubert briefly studied the rate of quantum ergodicity in Euclidean billiards and visualized theoretical results by numerical computations in three kinds of Euclidean billiards (stadium, cosine, and cardioid billards) using up to 6000 eigenfunctions. They also analyzed the influence of localized eigenfunctions (such as e.g bouncing ball modes or scarred eigenfunctions) on the rate of quantum ergodicity [15].

(a) A whispering gallery mode   (b) A bouncing ball mode   (c) A focusing mode
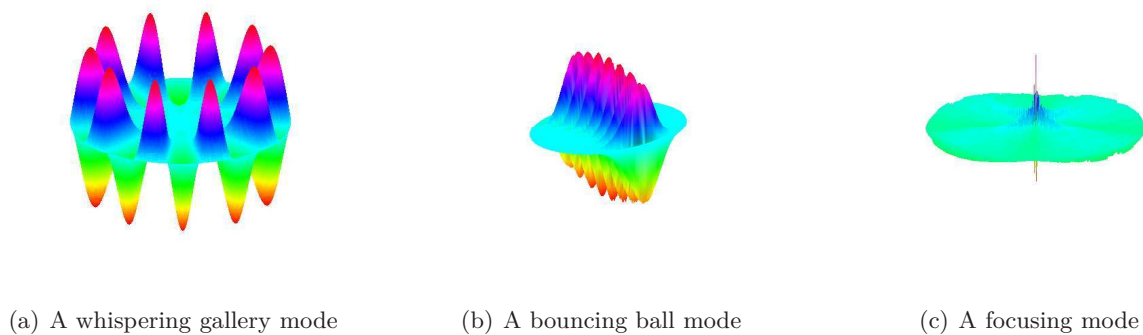
Figure 1.1: Three types of high-frequency localization: (a) - whispering gallery modes, (b) - bouncing ball modes, (c) - focusing modes.

1.1.2 Our research goal and contribution

As mentioned above, there are numerous localized eigenfunctions (such as e.g whispering gallery and bouncing ball modes) in two-dimensional domains with smooth and convex boundaries. We aim at investigating high-frequency localization in several simple domains.

By a method of separating variables, we will revisit three types of high-frequency localizations: whispering gallery, bouncing ball and focusing modes in circular, spherical and elliptical domains. We present rigorous inequalities for better illustration for the existence of such localized eigenmodes in these domains. Using these inequalities, we show the emergence of bouncing ball modes in an elliptical annulus. This is also an example of a non-convex domain in which the high-frequency localization happens.

Note that the unit disk can be regarded as the N-sided polygon in the limit $N \to \infty$. Although there exist various localized eigenmodes in the unit disk, the existence of high-frequency localization in an N-sided regular (equilateral) polygon is still unknown. We guess that there may be no localized eigenmode in any regular polygon. In order to clarify this statement, we consider the eigenfunctions in rectangles or equilateral triangles. We indicate that there is no localization in most rectangular domains. For the equilateral triangle, we prove that all symmetric eigenfunctions of the Dirichlet-Laplace operator are not localized.

(a)

Figure 1.2: A localized vibration in a fractal drum from an experiment of Sapoval and co-workers [191].

1.2   Low-frequency localization

1.2.1   Previous works

The low-frequency localization of Laplacian eigenfunctions in bounded domains has been investigated for a long time. In 1989, when observing low-frequency vibrations of several fractal drums, Sapoval found several localized modes (Fig. 1.5, top), which are mostly distributed near the boundary [190]. These localized modes have infinite derivatives near the re-entrant point of the boundary of the domains. Two years later, by using experimental and numerical approaches, Sapoval and co-workers observed several low-frequency localized vibrations of a membrane bounded by a rigid fractal drum (Fig. 1.2 and 1.3) [191]. Motivated by these results, Sapoval and Gobron continued the study of vibrations in irregular or fractal resonators with Dirichlet boundary condition and concluded that localized modes can emerge at low-frequency eigenvalues if there exist "narrow channels" in the drum geometry [192]. Lapidus and Pang [135] studied Laplacian eigenfunctions with Dirichlet boundary condition in a class of planar domains Ω with fractal boundaries and explained the damping of wave excitations in a fractal drum from previous experiments by Sapoval *et al.*. A numerical evidence for the boundary behavior of eigenfunctions was reported by Lapidus and co-workers in [136], with numerous pictures of eigenfunctions. Later, Daudert

and Lapidus considered more specifically the localization character of eigenfunctions in von Koch domains [58]. In particular, different *measures* of localization were discussed.

(a)   (b)
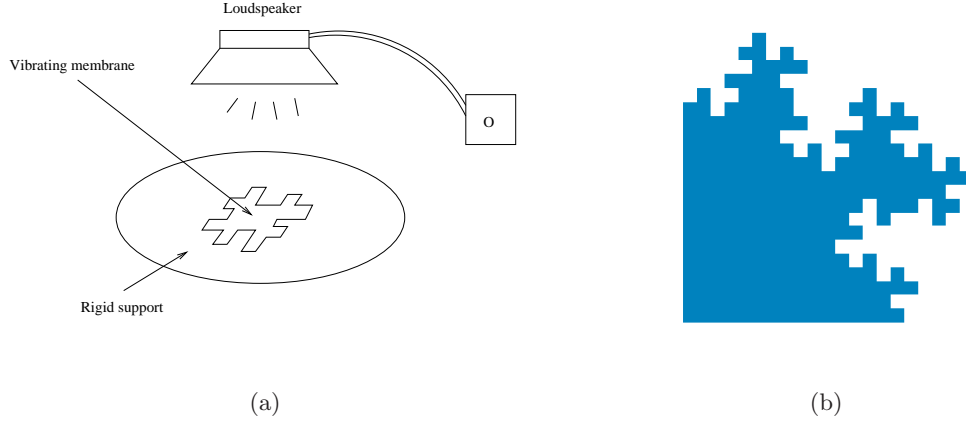
Figure 1.3: An experiment by using the visual observation of low-frequency vibrations of a fractal drum [191]: (a) - The loudspeaker is situated above the fractal drum to excite low-frequency vibration, above $20Hz$, (b)- A prefractal domain.

For Neumann boundary condition, there also exist localized eigenmodes (Fig. 1.5, bottom) in irregular and fractal resonators, which are confined near the boundary [188]. Even and his co-workers [71] experimentally observed acoustical resonances of a fractal-shaped liquid crystal film. For Dirichlet boundary condition, they compared the amplitude distribution of Laplacian eigenfunctions in a fractal domain from numerical and experimental approaches, and more importantly, visualized the emergence of localized modes at various frequencies in fractal geometries. The resonance frequencies from their experiments agree with numerical results. They analyzed two types of localization related to "strong" and "weak" localization mechanisms. In the study of sound attenuation by noise-protective walls, Félix and co-workers have further extended the analysis to the union of two domains with different refraction indices which are separated by an irregular boundary [76]. Many eigenfunctions (Fig. 1.4) of the related second order elliptic operator were shown to be localized on this boundary (so-called "astride localization"). A rigorous mathematical theory of these important phenomena is still missing.

A "definition" of localization was also given in [76] by combining L^2 and L^4 norms to define the "existence area" as

$$S(u) = \frac{\|u\|_{L^2(\Omega)}^4}{\|u\|_{L^4(\Omega)}^4}. \tag{1.4}$$

From this definition, a function u was called localized when its existence area $S(u)$ was much smaller than the area $\mu_2(\Omega)$ [76] (this definition trivially extends to higher dimensions). In fact, if a function is small in a subdomain, the fourth power diminishes it stronger than the second power. For instance, if $\Omega = [0, 1]$ and u is 1 on the subinterval $\Omega_0 = [1/4, 1/2]$ and 0 otherwise, one has $\|u\|_{L^2(\Omega)} = \|u\|_{L^4(\Omega)} = 1/2$ so that $S(u) = 1/4$, i.e. the length of the subinterval Ω_0. Once again, the smallness of $S(u)/\mu_2(\Omega)$ is conventional. Berry and co-workers developed a new method to approximate the Neumann spectrum of the Laplace operator on a planar fractal set Ω as a renormalized limit of the Neumann spectra of the standard Laplacian

(a) u_8	(b) u_8	(c) u_{21}	(d) u_{21}

(e) u_8	(f) u_{10}	(g) u_{12}	(h) u_{16}
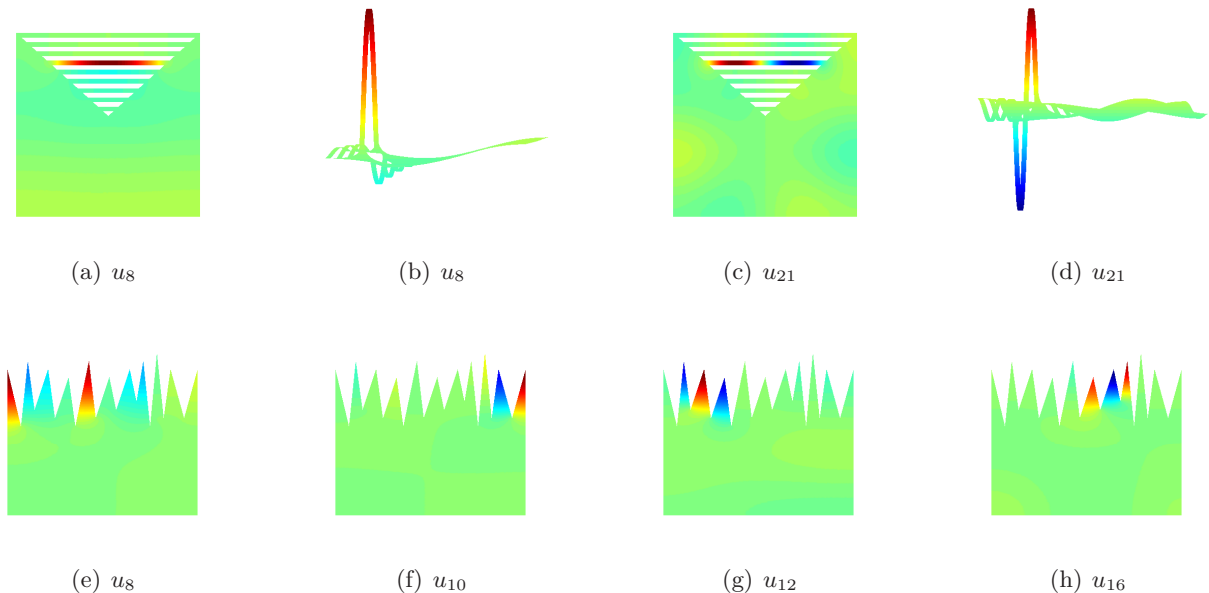
Figure 1.4: Examples of localized Neumann eigenfunctions in two domains adapted from [76]: square with many elongated holes (top) and random sawteeth (bottom). Colors represent the amplitude of eigenfunctions, from the most negative value (dark blue), through zero (green), to the largest positive value (dark red). One can notice that the eigenfunctions on the top are not negligible outside the localization region. This is yet another illustration for the conventional character of localization in bounded domains.

on a sequence of domains that approximate Ω from the outside [23]. They applied this method to compute the Neumann-Laplacian eigenfunctions in several domains, including a sawtooth domain, Sierpinski gasket and carpet, as well as nonsymmetric and random carpets and the octagasket. In particular, they gave a numerical evidence for the localized eigenfunctions for a sawtooth domain, in agreement with the earlier work by Félix *et al.* [76]. Recently, Filoche and Mayboroda have studied the problem of localization for bi-Laplacian in rigid thin plates and discovered that clamping just one point inside such a plate not only perturbs its spectral properties, but essentially divides the plate into two independently vibrating regions [77]. Heilman and Strichartz have reported numerical examples of localized Neumann-Laplacian eigenfunctions in several two-dimensional domains [107].

1.2.2   Our research goal and contribution

Understanding the "mechanism" of low-frequency localization is important first for the theory of Laplacian eigenproblems, and second, from a practical point of view, for the theory of acoustics and quantum waveguides. Motivated by the previous works, we are interested in investigating the low-frequency localization of Laplacian eigenfunctions in bounded domains. We will analyze localization in various kinds of domains, either simple or irregular. We focus on finding rigorous mathematical explanations for the existence of low-frequency localized eigenfunctions.

For better understanding low-frequency localization, we aim at studying the exponential decay of the Dirichlet-Laplacian eigenfunctions in a large class of domains D composed of a basic domain V of arbitrary

(a) u_1 (b) u_8 (c) u_{38}

(d) u_2 (e) u_3 (f) u_{12}
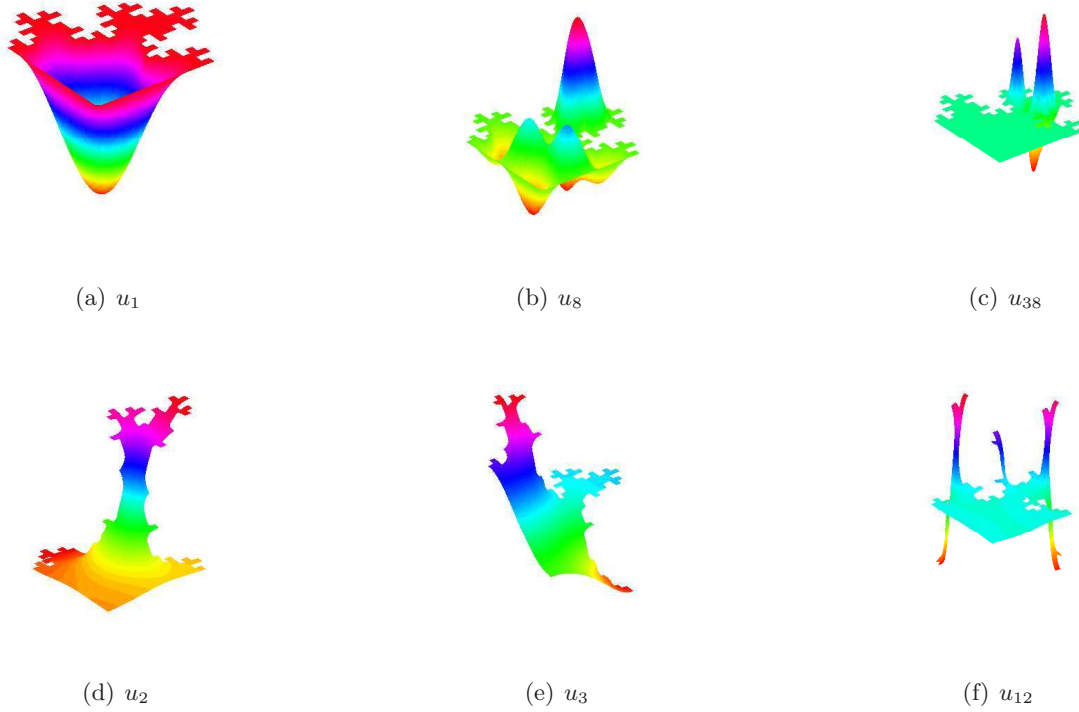
Figure 1.5: Several Dirichlet (top) and Neumann (bottom) eigenfunctions for the prefractal domain on Fig. 1.3b. The 38th Dirichlet and the 12th Neumann eigenfunctions are localized in a small subdomain (located in the upper right corner on Fig. 1.3b), while the first Dirichlet and the third Neumann eigenfunctions are almost zero on this subdomain. Finally, the 8th Dirichlet and the second Neumann eigenfunctions are examples of eigenfunctions extended over the whole domain.

shape and a branch Q of variable cross-sectional profile. We will rigorously prove that under certain conditions, the L^2-norm of an eigenfunction exponentially decays inside the branch with an explicit decay rate. It is important to emphasize that the exponential estimate is applicable in any dimension and for both finite and infinite branches. We show that the exponential estimate is also applicable for any V with arbitrary boundary condition on ∂V for which the Laplace operator is still self-adjoint. Using the theoretical results, one can explain the existence of low-frequency localized eigenmodes in various domains.

We extend our results to the problem of localized eigenmodes of the Laplace operator in resonators with long branches. Using an explicit representation of an eigenfunction in branches, we propose a general variational formalism for checking the existence of localized eigenmodes. We derive sufficient conditions on the branch lengths for getting a localized eigenfunction. We illustrate our approach for several typical waveguides, and in particular, we obtain an upper bound for the minimal branch length which is sufficient for localization. We prove the existence of a trapped mode in finite L-shape, bent strip and cross of two strips provided that their branches are long enough, with an accurate estimate on the required minimal length. Our method can be applied for studying the localization in many other waveguides.

In addition, we will analyze localization in a specific class of planar graphs. We will describe the properties

of localized eigenmodes and visualize them. Using these properties, one can easily distinguish localized and non-localized eigenmodes in these planar graphs. When the number of vertices in the graphs is very large, a traditional computational method becomes too slow so that an efficient algorithm is necessary for numerical computations. To overcome this limitation, we will propose a fast and stable algorithm for solving the eigenproblem in these graphs.

In another approach, we will discuss the low-frequency localization for either Dirichlet or Neumann boundary condition in dumbbell domains (domains with narrows connections). We will indicate that low-frequency localization can occur in numerous elongated polygons. It shows that localization may exist not only in irregular domains but also in a variety of simple domains.

1.3   Applications of Laplacian eigenfunctions

There are numerous applications of Laplacian eigenfunctions, which range from pure and applied mathematics to physics, chemistry, biology and computer sciences. For instance, Laplacian eigenfunctions can be used to investigate the increased damping in irregular acoustics cavities [76, 187]. Using the eigenfunctions of the Laplace operator, one can analyze and represent data recorded on general domains in $\mathbb{R}^d$ [189]. Jones and co-workers studied manifold parameterizations by eigenfunctions of the Laplacian and heat kernels [123]. McGraw and Menzinger used Laplacian spectra as a diagnostic tool for network structure and dynamics [154].

Beside theoretical results on different types of localization, one of the goals in this monograph is to apply Laplacian eigenfunctions to study the survival probabilities in porous media. We will present a spectral approach to investigate the survival probability of reflected Brownian motion in reactive media. Using the spectral approach, the survival probability is represented in the form of spectral decomposition over Laplacian eigenfunctions. We aim at studying the role of the geometrical structure of reactive regions and its influence on the overall reaction rate in the long-time regime. For this purpose, we compute the survival probability in several model reactive media and show how the shape and spatial arrangement of reactive regions affect the overall reaction rate. That can be adapted for designing the geometrical shapes of efficient catalysts or diffusive exchangers.

1.4   Outline of the monograph

The monograph is organized as follows. In Chapter 1, we explain our motivation in this thesis. In Chapter 2, we provide basic properties and definitions of the Laplacian eigenproblem with Dirichlet, Neumann or Robin boundary condition in bounded domains. In Chapter 3, we discuss high-frequency localization in simple domains such as circular, spherical and elliptical domains.

In Chapters 4 and 5, we study the exponential decay of low-frequency eigenfunctions of the Laplace operator in domains with branches of variable cross-sectional profiles and present several applications for finite quantum waveguides. We also discuss low-frequency localization in elongated polygons. In Chapter 6, we analyze the existence of localization in planar spectral graphs. We also propose an efficient and

stable divide-and-conquer algorithm for solving the eigendecomposition of the Laplacian matrix of an undirected and weighted graph.

In Chapter 7, we use a spectral approach for studying the survival probability of reflected Brownian motion in reactive media. Finally, the thesis ends by conclusions and further questions in Chapter 8.

Chapter 2

Preliminary

In this chapter, we give basis definitions and properties of the Laplace eigenvalue problem in bounded domains Ω in $\mathbb{R}^d$, which we will use throughout this monograph. The discussion is adapted for non-experts, so that an experienced reader may skip this chapter and move to the next ones.

2.1 Properties of eigenvalue problems

A function $u \neq 0$ satisfying Eq. (1.1) and one of boundary conditions in (1.2) is called an eigenfunction of the Laplace opertor in Ω, and the corresponding λ is called an eigenvalue with that boundary condition. In this section, we start by recalling several basic properties of Laplacian eigenvalues and eigenfunctions. For each u and v from $L^2(\Omega)$, we denote $(.,.)$ the L^2 inner product on a domain Ω

$$(u, v) = \int_{\Omega} u(\mathbf{r})v(\mathbf{r})d\mathbf{r}. \tag{2.1}$$

The Green formula for all $u, v \in C^2\left(\bar{\Omega}\right)$ is

$$\int_{\Omega} (u\triangle v - v\triangle u)\, d\mathbf{r} = \int_{\partial\Omega} \left(u\frac{\partial v}{\partial \mathbf{n}} - v\frac{\partial u}{\partial \mathbf{n}}\right) ds. \tag{2.2}$$

If both u and v satisfy one of boundary conditions in (1.2), one has

$$\int_{\Omega} u\triangle v d\mathbf{r} = \int_{\Omega} v\triangle u d\mathbf{r}, \tag{2.3}$$

or

$$(u, \triangle v) = (\triangle u, v). \tag{2.4}$$

With the boundary conditions in (1.2), the Laplace operator is thus self-adjoint.

2.1.1 Basic properties

The spectrum of the Laplace operator with one of the boundary condition (1.2) is known to be countably infinite and discrete and the eigenvalues can be ordered in an ascending order by the index $m = 1, 2, 3, \ldots$ (with possible multiplicities) as following $0 \leq \lambda_1 < \lambda_2 \leq \lambda_3 \leq \ldots$, while the set of Laplacian eigenfunctions $\{u_m(x)\}$ form a complete basis in the functional space $L^2(\Omega)$ of measurable and square-integrable functions on Ω [54, 133]:

Theorem 2.1.1. *Suppose that $\{u_k\}_{k=1}^{\infty}$ is the set of all normalized, orthogonal eigenfunctions of the Laplace operator with Dirichlet, Neumann or Robin boundary condition. For any function $f \in L^2(\Omega)$, there exists a sequence $\{c_k\}_{k=1}^{\infty}$ such that*

$$\lim_{n \to \infty} \left\| f - \sum_{k=1}^{n} c_k u_k \right\|_{L^2(\Omega)}^2 = 0, \tag{2.5}$$

where

$$c_k = (f, u_k), \forall k \geq 1. \tag{2.6}$$

In other words, the associated eigenfunctions can be chosen to form an orthonormal eigenbasis in $L^2(\Omega)$.

The eigenfunctions are infinitely differentiable inside the domain Ω [133]. For any open set $V \subset \Omega$, the restriction of an eigenfunction u_m cannot be strictly 0.

When a domain Ω is not connected and separated into several non-overlapping subdomains, the eigenproblem of the Laplace operator in Ω can be reduced into the corresponding problem in each subdomain [54]:

Theorem 2.1.2. *Suppose that Ω is a bounded domain consisting of non-overlapping domains $\Omega_1, \Omega_2, \ldots, \Omega_k$ (Fig. 2.1), then the set of Laplacian eigenvalues and eigenfunctions in Ω with Dirichlet, Neumann or Robin boundary condition includes all Laplacian eigenvalues and eigenfunctions in each subdomain $\Omega_1, \Omega_2, \ldots, \Omega_k$, where each eigenfunction vanishes identically in all except one of the separate subdomains.*

2.1.2 Minimum - Minimax principle

Two of the most crucial properties of Laplacian eigenvalues and eigenfunctions are the minimum and minimax principles. Many important properties can be derived from these principles. In this section, we introduce the minimum and minimax principles for Laplacian eigenvalues in a bounded domain Ω with Dirichlet boundary condition.
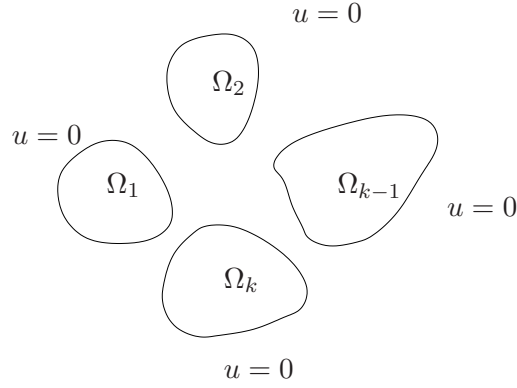
Figure 2.1: The Laplacian eigenvalue problem in a domain Ω with k non-overlapping components $\Omega_1, \Omega_2, \ldots, \Omega_k$ with Dirichlet boundary condition.

2.1.2.1 Minimum principle

For a given function u in Ω, we define the Rayleigh quotient $R(u; \Omega)$ as

$$R(u; \Omega) = \frac{\int\limits_{\Omega} |\nabla u|^2 \, d\mathbf{r}}{\int\limits_{\Omega} u^2 d\mathbf{r}}. \tag{2.7}$$

The following theorems hold [54]:

Theorem 2.1.3. *(Minimum principle for the first eigenvalue) The first eigenvalue λ_1 with Dirichlet boundary condition satisfies*

$$\lambda_1 = \min_{v \in A_1} R(v; \Omega), \tag{2.8}$$

where A_1 is the set of all admissible functions v such that

$$A_1 = \left\{ v \in C^2(\Omega), v \neq 0, \ v = 0 \text{ on the boundary } \partial\Omega \right\}. \tag{2.9}$$

A function u that minimizes the Rayleigh quotient $R(v; \Omega)$ in (2.8) is the corresponding eigenfunction.

Similarly, one can extend the minimum principle for general eigenvalues:

Theorem 2.1.4. *(Minimum principle for λ_{n+1}) For a given positive integer n, we suppose that $u_1, u_2, \ldots, u_n$ are the first n eigenfunctions of the Laplace operator with Dirichlet boundary condition in a domain Ω and can be chosen to be orthogonal. We define*

$$A_n = \left\{ v \in C^2(\Omega), v \not\equiv 0, \ v = 0 \text{ on } \partial\Omega, v \perp u_i, \forall i = 1, 2, \ldots, n \right\}. \tag{2.10}$$

Then,

$$\lambda_{n+1} = \min_{v \in A_n} R(v; \Omega), \tag{2.11}$$

Moreover, a function u which minimizes the above Rayleigh quotient is an eigenfunction associated to the eigenvalue λ_{n+1}.

2.1.2.2 Minimax principle

For any n linearly independent continuous and piecewise differential functions $\phi_1, \phi_2, \ldots, \phi_n \in A_1$, we denote

$$L(\phi_1, \ldots, \phi_n) = \left\{ u \in C^2(\Omega) : u = \sum_{i=1}^{n} c_i \phi_i, \ c_1, c_2, \ldots, c_n \in \mathbb{R} \right\}. \tag{2.12}$$

The Laplacian eigenvalues with Dirichlet boundary conditon satisfy the minimax principle [54, 133].

Theorem 2.1.5. *(Minimax principle) For any positive integer n, the nth eigenvalue λ_n with Dirichlet boundary condition can be computed by*

$$\lambda_n = \min_{\phi_1, \phi_2, \ldots, \phi_n \in A_1} \max_{u \in L(\phi_1, \ldots, \phi_n)} R(u; \Omega) \tag{2.13}$$

where $R(u; \Omega)$ is the Rayleigh quotient of u in the domain Ω.
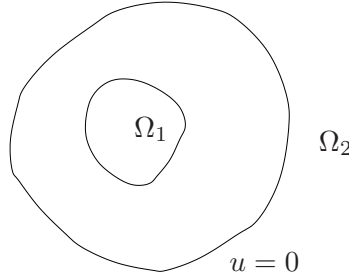
Figure 2.2: The *domain monotonicity* of Dirichlet-Laplace eigenproblem: when $\Omega_1 \subset \Omega_2$, $\lambda_n(\Omega_2) \leq \lambda_n(\Omega_1)$.

For Robin boundary condition with $h > 0$, the minimax principle becomes

$$\lambda_n = \min \max \frac{\|\nabla v\|_{L^2(\Omega)}^2 + h\|v\|_{L^2(\partial\Omega)}^2}{\|v\|_{L^2(\Omega)}^2}, \tag{2.14}$$

where the maximum is over all linear combinations of the form

$$v = a_1\phi_1 + \ldots + a_n\phi_n,$$

and the minimum is over all choices of n linearly independent continuous and piecewise-differentiable

functions ϕ_1, ..., ϕ_n (said to be in the functional space $C^1(\Omega)$) [54]. It is important to note that the minimum is reached exactly on the eigenfunction u_n.

2.1.3   Domain monotonicity

The minimax principle implies the property of domain monotonicity for Dirichlet boundary condition:

Theorem 2.1.6. *Suppose that $\Omega_1 \subset \Omega_2$ are two bounded domains (Fig. 2.2). We denote $\lambda_k(\Omega_i)$ the kth eigenvalue of the Laplace operator with Dirichlet boundary condition in the domain Ω_i, $i = 1, 2$. Then, $\lambda_k(\Omega_2) \leq \lambda_k(\Omega_1), \forall k$.*

However, this property is not applicable for Neumann or Robin boundary condition. We present the following theorem about the relation of Laplacian eigenvalues with Dirichlet and Robin boundary condition [54]:

Theorem 2.1.7. *Suppose that $\{\lambda_k\}_{k=1}^{\infty}$ is the set of Laplacian eigenvalues with Dirichlet boundary condition (1.2) and $\{\mu_k\}_{k=1}^{\infty}$ is the set of Laplacian eigenvalues with Robin boundary condition (1.2) in a bounded domain Ω. Then, $\mu_k \leq \lambda_k$, $\forall k$.*

From the domain monotonicity theorem, one can prove that

Theorem 2.1.8. *Let $\{\lambda_k\}_{k=1}^{\infty}$ be the set of Laplacian eigenvalues with Dirichlet boundary condition (1.2) in a bounded domain $\Omega \in \mathbb{R}^n$. Then, $\lim_{k \to \infty} \lambda_k = +\infty$.*

The above theorem ensures that the spectrum of the Laplace operator with Dirichlet boundary condition has an infinite number of eigenvalues.

2.1.4   Weyl's law

The Weyl's law is one of the first connections between the spectral properties of the Laplace operator and the geometrical structure of a bounded domain Ω. In 1911, Hermann Weyl derived the asymptotic behavior of the Laplacian eigenvalues [225, 226]:

$$\lambda_m \sim \frac{4\pi^2}{(\omega_d \mu_d(\Omega))^{2/d}} \, m^{2/d} \qquad (m \to \infty), \tag{2.15}$$

where $\mu_d(\Omega)$ is the Lebesgue measure of Ω (its area in 2D and volume in 3D), and

$$\omega_d = \frac{\pi^{d/2}}{\Gamma(d/2 + 1)} \tag{2.16}$$

is the volume of the unit ball in d dimensions ($\Gamma(z)$ being the Gamma function). As a consequence, plotting eigenvalues versus $m^{2/d}$ allows one to extract the area in 2D or the volume in 3D. This result can equivalently be written for the counting function $N(\lambda) = \#\{m \, : \, \lambda_m < \lambda\}$ (i.e., the number of eigenvalues smaller than λ):

$$N(\lambda) \sim \frac{\omega_d \mu_d(\Omega)}{(2\pi)^d} \, \lambda^{d/2} \qquad (\lambda \to \infty). \tag{2.17}$$

2.1.5 Several basic inequalities

The "amplitudes" of eigenfunctions can be characterized either globally by their L^p norms

$$\|u\|_p \equiv \left(\int_\Omega |u(\mathbf{r})|^p \, d\mathbf{r} \right)^{1/p} \qquad (p \geq 1), \tag{2.18}$$

or locally by pointwise estimates. Since eigenfunctions are defined up to a multiplicative constant, one often uses $L^2(\Omega)$ normalization: $\|u\|_2 = 1$. Note also the limiting case of L^∞-norm

$$\|u\|_\infty = \max_{x \in \Omega} |u(x)|. \tag{2.19}$$

It is worth recalling the Hölder's inequality for any two measurable functions u and v and for any positive p, q such that $1/p + 1/q = 1$:

$$\|uv\|_1 \leq \|u\|_p \|v\|_q. \tag{2.20}$$

In addition, for a bounded domain $\Omega \subset \mathbb{R}^d$ (with a finite Lebesgue measure $\mu_d(\Omega)$), the Jensen's inequality for convex functions yields

$$\|u\|_p \leq [\mu_d(\Omega)]^{\frac{1}{p} - \frac{1}{p'}} \|u\|_{p'} \qquad (1 \leq p \leq p'). \tag{2.21}$$

2.1.6 Nodal sets, nodal domains

There are numerous studies on nodal sets and nodal domains of Laplacian eigenfunctions with Dirichlet, Neumann and Robin boundary conditions [4, 51, 52, 80, 108, 109, 111, 118, 145, 156, 159, 171, 176, 213]. In an open, bounded domain $\Omega \in \mathbb{R}^d$ with one of boundary condition in (1.2), the nodal set of an eigenfunction can be determined by the following definition:

Definition 2.1.1. *The nodal set $N(u)$ of an eigenfunction $u(\mathbf{r})$ is the set of all points in Ω at which the eigenfunction u vanishes:*

$$N(u) = \{ \mathbf{r} \in \Omega : u(\mathbf{r}) = 0 \} . \tag{2.22}$$

For each eigenfunction, its nodal set divides the domain Ω into non-overlapping subdomains (called *nodal domains*) with piecewise smooth boundaries. In other words, the nodal domains of an eigenfunction u are the connected components of $\Omega \setminus N(u)$.

Theorem 2.1.9. *(Courant Nodal Domains Theorem)*
a. The first Laplacian eigenfunction u_1 with Dirichlet boundary condition has no nodal domains in the interior of the domain Ω. It also means that u_1 does not change sign in Ω.
b. For any integer $k \geq 2$, an eigenfunction u_k corresponding to the eigenvalue λ_k (counting multiplicity) has at least two and at most k nodal domains.

A simple proof can be found in [54]. An example on Fig. 2.3 illustrates that the eigenfunction u_k has at most k nodal domains for $k = 1, 3, 4, 5$.

Theorem 2.1.10. *A nodal set of a Dirichlet-Laplacian eigenfunction u is not open in Ω.*

(a) u_1 (b) u_3 (c) u_4 (d) u_5
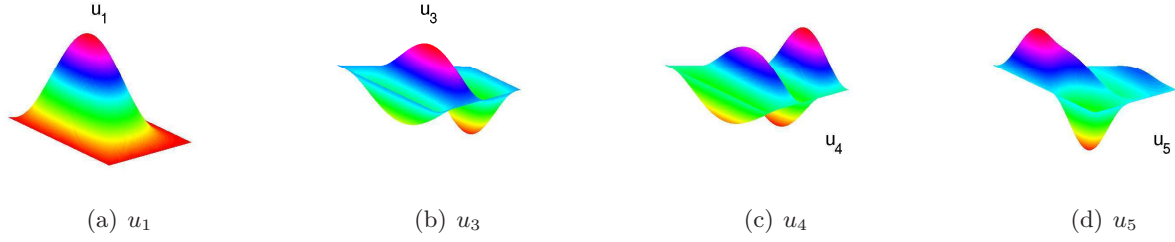
Figure 2.3: Several Dirichlet eigenmodes in a trapeze Ω. The first eigenfunction has only one nodal domain while the 3rd/5th eigenfunctions have three nodal domains. The fourth eigenfunction u_4 has 4 nodal domains.

From the above theorems, it is not difficult to get the following theorems:

Theorem 2.1.11. *Suppose that a Dirichlet-Laplace eigenfunction u_n with its corresponding eigenvalue λ_n has k nodal domains $\Omega_1, \Omega_2, \ldots, \Omega_k$ in Ω ($k \leq n$). Then, for any $1 \leq i \leq k$, the function $u_n|_{\Omega_i}$ is the first eigenfunction of the Laplace operator and λ_n is the smallest Laplacian eigenvalue in the subdomain Ω_i.*

Theorem 2.1.12. *Let Ω be an open bounded domain, and $\{u_n\}$ be the set of all Dirichlet eigenfunctions of the Laplace operator in Ω. For any open set $\Omega_1 \subset \Omega$ and any positive integer n,*

$$\int_{\Omega_1} u_n^2 d\mathbf{r} > 0 \tag{2.23}$$

2.2 Eigenproblem in simple domains

2.2.1 Intervals

All eigenfunctions of the Laplace operator in an arbitrary interval $\Omega = [a, b]$ with Neumann boundary condition can be determined by

$$\lambda_m = \left(\frac{\pi m}{b-a}\right)^2, \quad u_m(x) = \sqrt{\frac{2}{b-a}} \cos\left(\pi m \left(\frac{x-a}{b-a}\right)\right) \quad (m = 1, 2, \ldots), \tag{2.24}$$

and $u_0(x) = \sqrt{\frac{1}{b-a}}$.

For Dirichlet boundary condition,

$$\lambda_m = \left(\frac{\pi m}{b-a}\right)^2, \quad u_m(x) = \sqrt{\frac{2}{b-a}} \sin\left(\pi m \left(\frac{x-a}{b-a}\right)\right) \quad (m = 1, 2, \ldots). \tag{2.25}$$

For Robin boundary condition, all normalized Laplacian eigenfunctions in the interval $\Omega = [0, 1]$ can be given by

$$u_m(x) = A_m \cos(\alpha_m x) + B_m \sin(\alpha_m x) \quad (m = 0, 1, 2, \ldots), \tag{2.26}$$

and the corresponding eigenvalues $\lambda_m = \alpha_m^2$. Here, α_m is the positive zero of the following transcendental equation

$$\left(h^2 - z^2\right) \sin z + 2hz \cos z = 0. \tag{2.27}$$

Two parameters A_m and B_m are the normalization coefficients that satisfy $A_m = \alpha_m y_m$, $B_m = h y_m$, where $y_m = \sqrt{\frac{2}{\alpha_m^2 + h^2 + 4h \cos^2 \alpha_m}}$. In practice, both eigenfunction $u_m(x)$ and its eigenvalue λ_m are computed from Eq.(2.26).

Lemma 2.2.1. *Suppose that* $\Omega = [0, 1]$. *For* $0 \le a < b \le 1$, *there exists* $\epsilon(a, b) > 0$ *such that for any positive integer* m *and any boundary condition (Dirichlet, Neumann, Robin), the Laplacian eigenfunction* $u_m(x)$ *in the domain* Ω *satisfies that*

$$\int_a^b u_m^2(x)dx \ge \epsilon(a, b) > 0, \tag{2.28}$$

Proof. The following proof is given for Robin boundary condition $(h > 0)$ and the other cases are similar. Eq.(2.26) implies

$$\int_a^b u_m^2(x)dx = \left(\frac{b-a}{2}\right) \left(\frac{2\left(\alpha_m^2 + h^2\right)}{\alpha_m^2 + h^2 + 4h \cos^2 \alpha_m}\right) \left(1 + \right.$$
$$\left. \frac{\sin\left(\alpha_m(b-a)\right)}{\alpha_m(b-a)} \cos\left(\alpha_m(b+a) + 2\varphi\right)\right), \tag{2.29}$$

where

$$\cos \varphi = \frac{\alpha_m}{\sqrt{\alpha_m^2 + h^2}}, \sin \varphi = \frac{h}{\sqrt{\alpha_m^2 + h^2}}. \tag{2.30}$$

Using the inequality

$$\left(\frac{\alpha_m^2 + h^2}{\alpha_m^2 + h^2 + 4h \cos^2 \alpha_m}\right) \ge \frac{h^2}{h^2 + 4h}, \tag{2.31}$$

one can get the conclusion with

$$\epsilon(a, b) = \frac{b-a}{2} \times \left(\frac{2h}{h+4}\right) \times \min\left\{\frac{1}{2}, 1 + \frac{\sin\left(\alpha_m(b-a)\right)}{\alpha_m(b-a)} : \alpha_m \in \left(0, \frac{2}{b-a}\right)\right\} > 0, \tag{2.32}$$

$\square$

2.2.2 Circular domains

2.2.2.1 Disks

a. Neumann/Robin boundary condition

The rotation symmetry of a disk $\Omega = \{\mathbf{r} \in \mathbb{R}^2 \; : \; |\mathbf{r}| < R\}$ of radius R (see Fig. 2.4a) leads to an explicit representation of the eigenfunctions with Neumann boundary condition in polar coordinates:

$$
\begin{aligned}
u_{nk1}(r,\varphi) &= \frac{\sqrt{2}}{\sqrt{\pi}} \frac{\beta_{nk}}{J_n(\alpha_{nk})} J_n\left(\alpha_{nk}\frac{r}{R}\right) \cos(n\varphi) \\
u_{nk2}(r,\varphi) &= \frac{\sqrt{2}}{\sqrt{\pi}} \frac{\beta_{nk}}{J_n(\alpha_{nk})} J_n\left(\alpha_{nk}\frac{r}{R}\right) \sin(n\varphi) \qquad (n > 0), \\
u_{0k1}(r,\varphi) &= \frac{1}{\sqrt{\pi}} \frac{\beta_{0k}}{J_0(\alpha_{0k})} J_0\left(\alpha_{0k}\frac{r}{R}\right) \qquad\qquad (n = 0).
\end{aligned}
\tag{2.33}
$$

For each $n \geq 0$, α_{nk} $(k = 1, 2, ...)$ denote all the positive roots of the equation:

$$
J_n'(z) = 0,
\tag{2.34}
$$

where $J_n(z)$ is the Bessel function of the first kind, and prime denotes the derivative. The eigenvalues are $\lambda_{nk} = \alpha_{nk}^2/R^2$, while the normalization constants β_{nk} are defined as [96]

$$
\beta_{nk} = \sqrt{\frac{\lambda_{nk}}{(\lambda_{nk} - n^2)}}.
$$

The eigenfunctions are enumerated by the triple index nki, with $n = 0, 1, 2, ...$ counting the order of Bessel functions, $k = 1, 2, 3, ...$ counting the positive zeros, and $i = 1, 2$. Since $u_{0k2}(r,\varphi)$ are trivially zero (as $\sin(n\varphi) = 0$ for $n = 0$), they are not counted as eigenfunctions. The eigenvalues $\lambda_{nk} = \alpha_{nk}^2/R^2$, which are independent of the last index i, are simple for $n = 0$ and twice degenerate for $n > 0$. In the latter case, the eigenfunction is any nontrivial linear combination of u_{nk1} and u_{nk2}.

For Robin boundary condition, the Laplacian eigenfunctions in the disk Ω can be determined by the same representation as Eq. (2.33). However, the normalization coefficients β_{nk} have the following formula

$$
\beta_{nk} = \sqrt{\frac{\lambda_{nk}}{(\lambda_{nk} - n^2 + h^2)}},
$$

and the eigenvalues $\lambda_{nk} = \alpha_{nk}^2$, where α_{nk} are positive zeros of the functions

$$
z J_n'(z) + h J_n(z) = 0.
$$

b. Dirichlet boundary condition

For Dirichlet boundary condition, the Laplacian eigenfunctions in the disk Ω can be determined by the

(a) A disk   (b) A sector   (c) A circular annulus
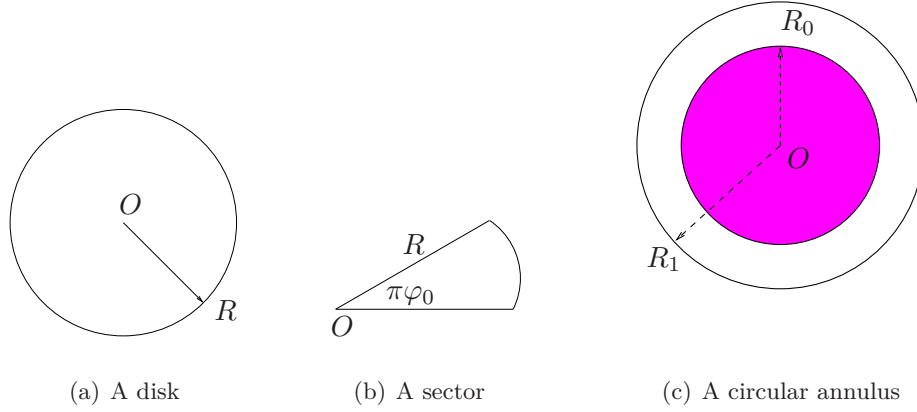
Figure 2.4: Several types of circular domains in $\mathbb{R}^2$: (a) - a disk of radius R, (b) - a circular sector Ω of the radius R and the angle $\pi\varphi_0$, and (c) - a circular annulus Ω.

(a) u_{00} (b) u_{10} (c) u_{01} (d) u_{40}
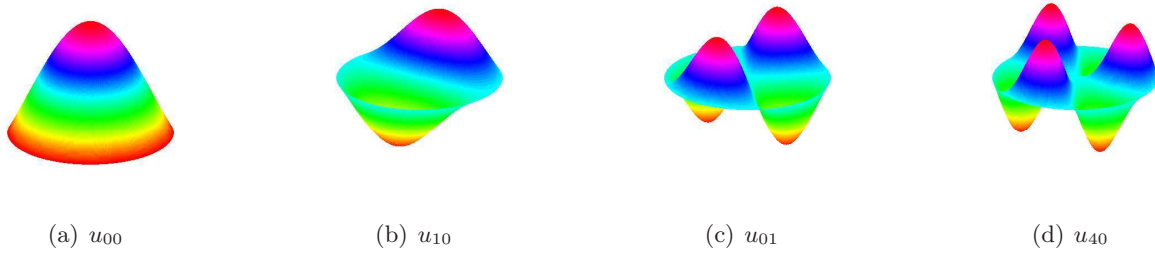
Figure 2.5:   Several Laplacian eigenfunctions with Dirichlet boundary condition in the unit disk Ω in $\mathbb{R}^2$.

following representation

$$
\begin{aligned}
u_{nk1}(r,\varphi) &= \frac{\sqrt{2}}{\sqrt{\pi}}\frac{\beta_{nk}}{J_n'(\alpha_{nk})}J_n\left(\alpha_{nk}\frac{r}{R}\right)\cos(n\varphi) \\
u_{nk2}(r,\varphi) &= \frac{\sqrt{2}}{\sqrt{\pi}}\frac{\beta_{nk}}{J_n'(\alpha_{nk})}J_n\left(\alpha_{nk}\frac{r}{R}\right)\sin(n\varphi) \qquad (n>0), \\
u_{0k1}(r,\varphi) &= \frac{1}{\sqrt{\pi}}\frac{\beta_{0k}}{J_0'(\alpha_{0k})}J_0\left(\alpha_{0k}\frac{r}{R}\right) \qquad\qquad (n=0),
\end{aligned}
\tag{2.35}
$$

where the coefficients β_{nk} satisfy that $\beta_{nk} = 1$. Fig. 2.5 shows several eigenfunctions in the unit disk satisfying Dirichlet boundary condition.

2.2.2.2   Circular sectors

We consider a sector Ω (see Fig. 2.4b) such that

$$
\Omega = \{(r\cos(\varphi), r\sin(\varphi)), 0 \le r \le R, 0 \le \varphi \le \pi\varphi_0\}
\tag{2.36}
$$

The Laplacian eigenfunctions satisfying Dirichlet boundary condition are given by

$$u_{nk}(r,\varphi) = \beta_{nk} J_{n/\varphi_0}\left(\frac{\alpha_{nk}r}{R}\right)\sin\left(\frac{n\varphi}{\varphi_0}\right),\tag{2.37}$$

where $J_{n/\varphi_0}(x)$ is the Bessel function of fractional order $\dfrac{n}{\varphi_0}$ and β_{nk} are the normalization constants

$$\beta_{nk} = \frac{2}{R\sqrt{\pi\varphi_0}\left|J'_{n/\varphi_0}(\alpha_{nk})\right|}.\tag{2.38}$$

The corresponding eigenvalue $\lambda_{nk} = \alpha_{nk}^2/R^2$. Here, α_{nk} is the kth zero of the equation: $J_{n/\varphi_0}(z) = 0$ for any positive integer n.

Example 2.2.1. *Suppose that Ω is the sector of radius $R = 1$ and angle $\dfrac{\pi}{6}$ (Fig. 2.4b). We consider the Laplace eigenvalue problem with Dirichlet boundary condition in Ω. In this case, all eigenvalues $\lambda_{nk} = \alpha_{nk}^2$, where α_{nk} are the zeros of the Bessel functions*

$$J_{6n}(z) = 0.\tag{2.39}$$

In Appendix A2, one can find several first zeros of the Bessel functions $J_{6n}(z)$, $n = 1, 2, 3$. In Fig. 2.6, we plot Laplacian eigenfunctions corresponding to four smallest eigenvalues: $\lambda_{10} = 98.7263$, $\lambda_{11} = 184.6688$, $\lambda_{21} = 278.8316$, and $\lambda_{13} = 289.1299$.

(a) u_{10} (b) u_{11} (c) u_{21} (d) u_{13}
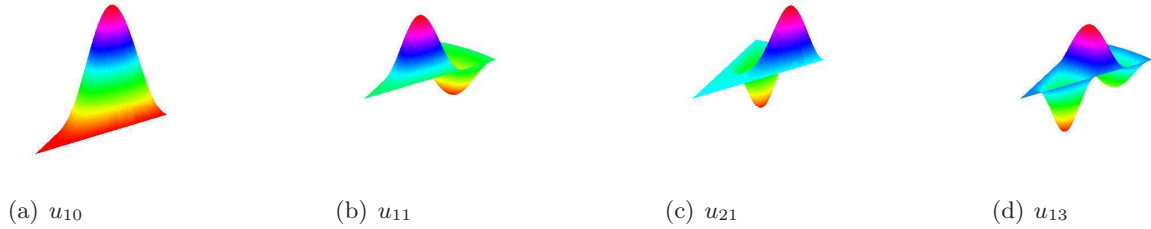
Figure 2.6: The first 4 Laplacian eigenfunctions in a circular sector Ω of the radius $R_0 = 1$ and the angle $\dfrac{\pi}{6}$ in $\mathbb{R}^2$.

2.2.2.3 Circular annuli

a. Dirichlet-Neumann boundary condition

We consider the Laplacian eigenproblem in a circular annulus $\Omega = \{\mathbf{r} \in \mathbb{R}^2 \; : \; R_0 < |\mathbf{r}| < R_1 = 1\}$ with the inner radius R_0 and the outer radius R_1, $0 < R_0 < R_1$ (Fig. 2.4c). The normalized Laplacian

eigenfunctions in Ω have the following forms [96]

$$
\begin{aligned}
u_{nk1}(r, \varphi) &= \frac{\sqrt{2}}{\sqrt{\pi}} \beta_{nk} \frac{v_{nk}(r)}{v_{nk}(R_1)} \cos(n\varphi) \\
u_{nk2}(r, \varphi) &= \frac{\sqrt{2}}{\sqrt{\pi}} \beta_{nk} \frac{v_{nk}(r)}{v_{nk}(R_1)} \sin(n\varphi) \qquad (n > 0), \\
u_{0k1}(r, \varphi) &= \frac{1}{\sqrt{\pi}} \beta_{0k} \frac{v_{0k}(r)}{v_{0k}(R_1)} \qquad\qquad (n = 0).
\end{aligned}
\tag{2.40}
$$

For each non-negative integer n, the functions $v_{nk}(r)$ satisfy the Bessel equation

$$
r^2 v'' + r v' + \left(\alpha^2 r^2 - n^2 \right) v = 0,
\tag{2.41}
$$

then it has the following representation

$$
v_{nk}(r) = c_1 J_n(\alpha_{nk} r) + c_2 Y_n(\alpha_{nk} r).
\tag{2.42}
$$

Depending on the boundary condition and the normalization of the eigenfunction u_{nkl}, one can determine the parameters c_1, c_2, α_{nk} and the normalization coefficients β_{nk}. For example, if the eigenfunction satisfies Dirichlet boundary condition at the inner circle and Neumann boundary condition at outer circle, these parameters can be computed by the following equations

$$
\begin{aligned}
c_1 J_n(\alpha_{nk} R_0) + c_2 Y_n(\alpha_{nk} R_0) &= 0, \tag{2.43} \\
c_1 J_n'(\alpha_{nk} R_1) + c_2 Y_n'(\alpha_{nk} R_1) &= 0. \tag{2.44}
\end{aligned}
$$

Here, the eigennvalue $\lambda_{nk} = \alpha_{nk}^2$, and α_{nk} is the kth positive zero of the equation

$$
Y_n(\alpha R_0) J_n'(\alpha R_1) - Y_n'(\alpha R_0) J_n(\alpha R_1) = 0
\tag{2.45}
$$

The normalization coefficients β_{nk} can be obtained as

$$
\beta_{nk} = \left(\frac{\lambda_{nk}}{\lambda_{nk} - n^2 - \lambda_{nk} \left[\frac{J_n'(\alpha_{nk})}{J_n(\alpha_{nk} R_0)} \right]^2} \right)^{\frac{1}{2}}
\tag{2.46}
$$

b. Robin-Robin boundary condition

In this section, we consider the eigenproblem of the Laplace operator in a circular annulus $\Omega = \{ \mathbf{r} \in \mathbb{R}^2 \ : \ R_0 < |\mathbf{r}| < R_1 = 1 \}$ (Fig. 2.4c) satisfying Robin boundary condition at both inner and outer circle: $\frac{\partial u_m}{\partial n} + h u_m = 0$. The Laplacian eigenfunctions have the same representation as Eq.(2.40). For each non-negative integer n, the corresponding eigenvalues $\lambda_{nk} = \alpha_{nk}^2$, where α_{nk} is the kth positive solution

of the equation [100]

$$
\begin{aligned}
&\left[\alpha J_n'(\alpha R_0) - h J_n(\alpha R_0)\right]\left[\alpha Y_n'(\alpha R_1) + h Y_n(\alpha R_1)\right] \\
&- \left[\alpha J_n'(\alpha R_1) + h J_n(\alpha R_1)\right]\left[\alpha Y_n'(\alpha R_0) - h Y_n(\alpha R_0)\right] = 0
\end{aligned}
\tag{2.47}
$$

The normalization coefficients β_{nk} can be obtained as follows [100]

$$
\beta_{nk} = \left(\frac{\lambda_{nk}}{\left[(\lambda_{nk} + h^2)\,R_1^2 - n^2\right] - \left[(\lambda_{nk} + h^2)\,R_0^2 - n^2\right]\xi_{nk}^2}\right)^{\frac{1}{2}}
\tag{2.48}
$$

with

$$
\xi_{nk} = \frac{v_{nk}(R_0)}{v_{nk}(R_1)}.
\tag{2.49}
$$

In the special case $h = 0$ (Neumann boundary condition at both inner and outer circles), the equation Eq.(2.47) can be reduced as

$$
Y_n'(\alpha R_1) J_n'(\alpha R_0) - Y_n'(\alpha R_1) J_n'(\alpha R_0) = 0.
\tag{2.50}
$$

2.2.3   Ball

In the unit ball Ω, the normalized eigenfunctions (with Robin boundary condition) are

$$
u_{nkl}(r, \theta, \varphi) = \frac{1}{\sqrt{2\pi}} \frac{\beta_{nk}}{j_n(\alpha_{nk})} j_n(\alpha_{nk} r) P_n^l(\cos\theta) e^{il\varphi},
\tag{2.51}
$$

where $0 \le r \le 1$, $0 \le \theta \le \pi$, and $0 \le \varphi \le 2\pi$ [96, 97]. Here, $j_\nu(z) = \sqrt{\frac{\pi}{2z}} J_{\nu+1/2}(z)$ are the spherical Bessel functions, and $P_n^l(x)$ are the associated Legendre polynomials. The corresponding eigenvalue $\lambda_{nkl} = \alpha_{nk}^2$ is expressed through the positive zeros α_{nk} of the equation

$$
z j_n'(z) + h j_n(z) = 0.
\tag{2.52}
$$

One can express the normalization coefficients β_{nk} by [96, 97]

$$
\beta_{nk} = \left(\frac{(2n+1)\lambda_{nk}}{\lambda_{nk} - n(n+1) + h(h-1)}\right)^{\frac{1}{2}},
\tag{2.53}
$$

and $\beta_{00} = \sqrt{\frac{3}{2}}$.

2.2.4   Rectangular domains

We consider a rectangular domain $\Omega = \{(x, y) : 0 \le x \le a, 0 \le y \le b\}$ with two sides a and b. The normalized Laplacian eigenfunctions with Dirichlet boundary condition are

$$
u_{mn}(x, y) = \frac{2}{\sqrt{ab}} \sin\left(\frac{\pi m x}{a}\right) \sin\left(\frac{\pi n y}{b}\right), \ \forall\, 0 \le x \le a, 0 \le y \le b,
\tag{2.54}
$$
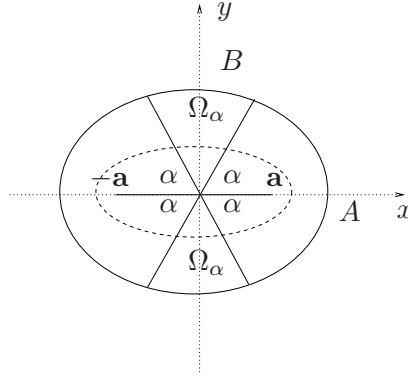
Figure 2.7: Two ellipses of radii $R = 0.5$ (dashed line) and $R = 1$ (solid line), with the focal distance $a = 1$. The major and minor semi-axes, $A = a \cosh R$ and $B = a \sinh R$, are shown by black dotted lines. The horizonal thick segment connects the foci.

and the corresponding eigenvalues are

$$\lambda_{mn} = \pi^2 \left[\left(\frac{m}{a} \right)^2 + \left(\frac{n}{b} \right)^2 \right], \quad m, n = 1, 2, \ldots \tag{2.55}$$

which can be degenerated if a, b are commensurable.

2.2.5 Elliptical domains

2.2.5.1 Ellipses

It is convenient to introduce the elliptic coordinates as

$$\begin{cases} x_1 &= a \cosh r \cos \theta, \\ x_2 &= a \sinh r \sin \theta, \end{cases} \tag{2.56}$$

where $a > 0$ is the prescribed distance between the origin and the foci, $r \geq 0$ is the radial coordinate that fixes the major and minor semi-axes: $A = a \cosh r$ and $B = a \sinh r$, and $0 \leq \theta < 2\pi$ is the angular coordinate (Fig. 2.7). An ellipse of radius $R > 0$ is the curve of constant $r = R$ whose points (x_1, x_2) satisfy $x_1^2/A^2 + x_2^2/B^2 = 1$. Note that the eccentricity $e = a/A = 1/\cosh r$ is strictly positive. A filled ellipse Ω (i.e., the interior of a given ellipse) can be characterized in elliptic coordinates as $0 \leq r < R$ and $0 \leq \theta < 2\pi$. The elliptic coordinates yield the separation of the radial and angular variables as

$$u(x, y) = f(r)g(\theta).$$

Substituting this formula into the eigenvalue problem $-\Delta u = \lambda u$, one gets

$$\left(\frac{f''}{f} + \frac{g''}{g} \right) + \frac{a^2 \lambda}{2} \left(\cosh 2r - \cos 2\theta \right) = 0.$$

Letting

$$c = \left(\frac{f''}{f} \right) + \frac{a^2 \lambda}{2} \cosh 2r = - \left(\frac{g''}{g} \right) + \frac{a^2 \lambda}{2} \cos 2\theta,$$

the angular and radial parts, $g(\theta)$ and $f(r)$, become solutions of the Mathieu equation and the modified Mathieu equation, respectively [41]

$$g''(\theta) + (c - 2q \cos 2\theta)\, g(\theta) \;=\; 0, \tag{2.57}$$

$$f''(r) - (c - 2q \cosh 2r)\, f(r) \;=\; 0, \tag{2.58}$$

where c is the characteristic value of the corresponding Mathieu function, and

$$q = \frac{a^2}{4} \lambda. \tag{2.59}$$

Periodic solutions of the Mathieu equation are possible for specific values of c. They are denoted as $\mathrm{ce}_n(\theta, q)$ and $\mathrm{se}_{n+1}(\theta, q)$ (with $n = 0, 1, 2, ...$) and called the angular Mathieu functions of the first and second kind. Each function $\mathrm{ce}_n(\theta, q)$ and $\mathrm{se}_{n+1}(\theta, q)$ corresponds to its own characteristic value c (the relation being implicit, see [155]).

For the radial part, there are two linearly independent solutions for each characteristic value c: two modified Mathieu functions $\mathrm{Mc}_n^{(1)}(r, q)$ and $\mathrm{Mc}_n^{(2)}(r, q)$ correspond to the same c as $\mathrm{ce}_n(\theta, q)$, and two modified Mathieu functions $\mathrm{Ms}_{n+1}^{(1)}(r, q)$ and $\mathrm{Ms}_{n+1}^{(2)}(r, q)$ correspond to the same c as $\mathrm{se}_{n+1}(\theta, q)$. As a consequence, there are four families of eigenfunctions (distinguished by the index $i = 1, 2, 3, 4$) in a filled ellipse:

$$
\begin{aligned}
u_{nk1} &= \mathrm{ce}_n(\theta, q_{nk1}) \mathrm{Mc}_n^{(1)}(r, q_{nk1}), \\
u_{nk2} &= \mathrm{ce}_n(\theta, q_{nk2}) \mathrm{Mc}_n^{(2)}(r, q_{nk2}), \\
u_{nk3} &= \mathrm{se}_{n+1}(\theta, q_{nk3}) \mathrm{Ms}_{n+1}^{(1)}(r, q_{nk3}), \\
u_{nk4} &= \mathrm{se}_{n+1}(\theta, q_{nk4}) \mathrm{Ms}_{n+1}^{(2)}(r, q_{nk4}),
\end{aligned}
\tag{2.60}
$$

where the parameters q_{nki} are determined by the boundary condition. For instance, for a filled ellipse of radius R with Dirichlet boundary condition, there are four individual equations for the parameter q_{nki}, for each $n = 0, 1, 2, ...$:

$$
\begin{aligned}
\mathrm{Mc}_n^{(1)}(R, q_{nk1}) = 0, &\quad \mathrm{Mc}_n^{(2)}(R, q_{nk2}) = 0, \\
\mathrm{Ms}_{n+1}^{(1)}(R, q_{nk3}) = 0, &\quad \mathrm{Ms}_{n+1}^{(2)}(R, q_{nk4}) = 0,
\end{aligned}
\tag{2.61}
$$

each of them having infinitely many positive solutions q_{nki} enumerated by $k = 1, 2, \ldots$ [1, 155]. The

associated eigenvalues λ_{nki} can be determined by Eq. (2.59) as

$$\lambda_{nki} = \frac{4q_{nki}}{a^2}. \tag{2.62}$$

For solving Eqs. (2.61), one needs an efficient approximation of the modified Mathieu functions $\mathrm{Mc}_n^{(1,2)}(z,q)$ and $\mathrm{Ms}_{n+1}^{(1,2)}(z,q)$ [160]. In chapter 3, we calculate these functions by using truncated recurrence relations [234] (see Appendix C for details). The accurate approximation for Mathieu and modified Mathieu functions is one of the most time-consuming steps in the numerical approach.

2.2.5.2 Elliptical annuli

The above analysis can be applied almost directly to an elliptical annulus Ω, i.e. a domain between an inner ellipse Ω_1 and an outer ellipse Ω_2, with the same foci. In elliptic coordinates, Ω can be defined by two inequalities: $R_1 < r < R_2$ and $0 \le \theta < 2\pi$, where the prescribed radii R_1 and R_2 determine Ω_1 and Ω_2, respectively.

In chapter 3, we consider two families of eigenfunctions in Ω as

$$\begin{aligned}
u_{nk1} &= \mathrm{ce}_n(\theta, q_{nk1})\left[a_{nk1}\mathrm{Mc}_n^{(1)}(r, q_{nk1}) + b_{nk1}\mathrm{Mc}_n^{(2)}(r, q_{nk1})\right], \\
u_{nk2} &= \mathrm{se}_{n+1}(\theta, q_{nk2})\left[a_{nk2}\mathrm{Ms}_{n+1}^{(1)}(r, q_{nk2}) + b_{nk2}\mathrm{Ms}_{n+1}^{(2)}(r, q_{nk2})\right].
\end{aligned} \tag{2.63}$$

The parameters a_{nki}, b_{nki} and q_{nki} $(i = 1, 2)$ are set by boundary conditions and the normalization of eigenfunctions. For Dirichlet boundary condition, one solves the following equations [160]

$$\begin{aligned}
\mathrm{Mc}_n^{(1)}(R_1, q_{nk1})\mathrm{Mc}_n^{(2)}(R_2, q_{nk1}) - \mathrm{Mc}_n^{(1)}(R_2, q_{nk1})\mathrm{Mc}_n^{(2)}(R_1, q_{nk1}) = 0, \\
\mathrm{Ms}_{n+1}^{(1)}(R_1, q_{nk2})\mathrm{Ms}_{n+1}^{(2)}(R_2, q_{nk2}) - \mathrm{Ms}_{n+1}^{(1)}(R_2, q_{nk2})\mathrm{Ms}_{n+1}^{(2)}(R_1, q_{nk2}) = 0.
\end{aligned} \tag{2.64}$$

For each $n = 0, 1, 2, ...$, each of these equations has infinitely many solutions denoted as $\{q_{nk1}\}$ and $\{q_{nk2}\}$, and enumerated by $k = 1, 2, 3, ...$ [155].

2.2.6 Equilateral triangle

In 1852, by using reflections and the related symmetries, Lamé discovered the Dirichlet eigenvalues and eigenfunctions of the Laplace operator in the equilateral triangle

$$\Omega = \left\{(x, y) \in \mathbb{R}^2 : 0 < x < 1, 0 < y < x\sqrt{3}, y < \sqrt{3}(1 - x)\right\}, \tag{2.65}$$

as following

$$\lambda_{mn} = \left(\frac{16\pi^2}{27}\right)\left(m^2 + n^2 - mn\right), m, n = 0, \pm 1, \dots, \tag{2.66}$$

$$u_{mn}(x, y) = \sum_{(m', n')} \pm \exp\left(\frac{2\pi i}{3}\right)\left(m'x + \frac{(2n' - m')y}{\sqrt{3}}\right), \tag{2.67}$$

with the following conditions:

(A) $m + n$ is a multiple of 3,

(B) $m \neq 2n$,

(C) $n \neq 2m$,

and (m', n') range over $\wp \subset Z^2$, where $|\wp| = 6$, and $\pm$ is determined by the following rules:

$$(-n, m - n) \to (-n, -m) \to (n - m, -m) \to (n - m, n) \to (m, n) \to (m, m - n) \qquad (2.68)$$

Each translation induces a change of sign in the (m, n) entry of the above rule. Pinsky showed that this set of eigenfunctions is complete in $L^2(\Omega)$ [173, 174].

The Dirichlet eigenfunctions can be separated into two families of eigenfunctions: symmetric and complex eigenfunctions. In particular, an eigenvalue corresponds to a symmetric eigenfunction if and only if m is multiple of 3, and the associated eigenfunction u_{mn} is enumerated by the index $(m, 0)$ where $m = 3q$.

The eigenfunctions for Neumann boundary condition are

$$u_{mn}(x, y) = \sum_{(m', n')} \exp\left(\frac{2\pi i}{3}\right)\left(m'x + \frac{(2n' - m')y}{\sqrt{3}}\right), \qquad (2.69)$$

where the only condition is that $(m + n)$ are multiples of 3, and no sign change.

Chapter 3

High-frequency localization of Laplacian eigenfunctions

A mathematician is a blind man in a dark room looking for a black cat which isn't there.
- Charles Robert Darwin

What is the simplest two-dimensional shape for getting localized eigenfunctions? This is one of the first questions we asked ourselves. In this chapter, we revisit the existence of high-frequency localization in several simple domains.

In the first part of this chapter, we investigate Laplacian eigenfunctions in circular, spherical and elliptical domains and then discuss three kinds of high-frequency localization: whispering gallery modes, bouncing ball modes and focusing modes. Although the existence of these modes was known for a class of convex domains with piece-wise smooth boundary [128, 137, 138], the seperation of variables for the aforementioned domains helps us to prove more precisely the high-frequency localization of Laplacian eigenfunctions, i.e how an eigenfunction is getting distributed in a small region of the domain, and decays rapidly outside this region. Basing on the properties of Bessel and Mathieu functions, we derive the inequalities which imply and clearly illustrate localization. Moreover, we will provide an example of a non-convex domain (an elliptical annulus) for which the high-frequency localized modes are still present.

In the second part of this chapter, we discuss the high-frequency localization in convex polygons. In most rectangles, we can prove that there is no localized eigenmode. Interestingly, the existence of some localized eigenmode in regular polygons (such as e.g. equilateral triangle, square, etc) is still an open question. Several numerical results are given in Appendix C6 for future references.

The results of this chapter are reported in [160].

3.1   Introduction

We call an eigenfunction u of the Laplace operator in a bounded domain $\Omega \subset \mathbb{R}^d$ L^p-*localized* ($p \geq 1$) if it is essentially supported by a small subdomain $\Omega_\alpha \subset \Omega$, i.e.

$$\frac{\|u\|_{L^p(\Omega \setminus \Omega_\alpha)}}{\|u\|_{L^p(\Omega)}} \ll 1, \qquad \frac{\mu_d(\Omega_\alpha)}{\mu_d(\Omega)} \ll 1, \tag{3.1}$$

where $\|.\|_{L^p}$ is the L^p-norm, and μ_d is the Lebesgue measure. We stress that this "definition" is qualitative as there is no objective criterion for deciding how small these ratios have to be. This is the major problem in defining the notion of localization.

For circular, spherical and elliptical domains, we will show in Sect. 3.2 and 3.3 that the ratios can be made arbitrarily small. In other words, for any prescribed threshold ε, there exist a subdomain Ω_α and infinitely many eigenfunctions for which both ratios are smaller than ε. Most importantly, we will provide a simple example of a non-convex domain for which the high-frequency localization is still present. At the same time, we will show in Sect. 3.4 that there is no localization in most of rectangle-like domains. Finally, using this terminology, we prove that all symmetric eigenfunctions of the Dirichlet-Laplace operator in equilateral triangles are non-localized. This observation will help us formulating an open problem of localization in polygonal domains.

3.2   Localization in circular and spherical domains

In circular and spherical domains, all Laplacian eigenvalues and eigenfunctions can be explicitly determined as shown in Section 2.2.2 and 2.2.3. These eigenvalues and eigenfunctions can be easily found by a numerical computation implemented in Matlab. In this section, we will discuss high-frequency localization in these domains.

3.2.1   Whispering gallery modes

The disk is the simplest shape for illustrating the whispering gallery modes and focusing modes. The explicit form (2.33) of eigenfunctions allows one to derive accurate bounds, as shown below. When the index k is fixed, while n increases, the Bessel functions $J_n(\alpha_{nk} r/R)$ become strongly attenuated near the origin (as $J_n(z) \sim (z/2)^n/n!$ at small z) and essentially localized near the boundary, yielding whispering gallery modes. In turn, when n is fixed while k increases, the Bessel functions highly oscillate, the amplitude of oscillations decreasing towards to the boundary. In that case, the eigenfunctions are mainly localized at the origin, yielding focusing modes. These qualitative arguments are rigorously formulated in the following theorem

Theorem 3.2.1. *Let $D = \{\mathbf{r} \in \mathbb{R}^2 \;:\; |\mathbf{r}| < R\}$ be a disk of radius $R > 0$, and $D_{nk} = \{\mathbf{r} \in \mathbb{R}^2 \;:\; |\mathbf{r}| < Rd_n/\alpha_{nk}\}$, where $d_n = n - n^{2/3}$, and α_{nk} are the positive zeros of $J_n(z)$ (Dirichlet), $J_n'(z)$ (Neumann) or $J_n'(z) + hJ_n(z)$ for some $h > 0$ (Robin), with $n = 0, 1, 2, \ldots$ denoting the order of Bessel function $J_n(z)$ and $k = 1, 2, 3, \ldots$ counting zeros. Then for any $p \geq 1$, there exists a universal constant $C_p > 0$ such that for*

any $k = 1, 2, 3, ...$, there exists $N_{p,k} > 0$ such that for any integer $n > N_{p,k}$, the Laplacian eigenfunction u_{nk} for Dirichlet, Neumann or Robin boundary condition satisfies

$$\frac{\|u_{nk}\|_{L^p(D_{nk})}}{\|u_{nk}\|_{L^p(D)}} < C_p n^{\frac{1}{3} + \frac{2}{3p}} 2^{-n^{1/3}/3}. \tag{3.2}$$

This estimate implies that

$$\lim_{n \to \infty} \frac{\|u_{nk}\|_{L^p(D_{nk})}}{\|u_{nk}\|_{L^p(D)}} = 0, \tag{3.3}$$

while

$$\lim_{n \to \infty} \frac{\mu_2(D_{nk})}{\mu_2(D)} = 1. \tag{3.4}$$

Proof. One can find the proof in Appendix B1. □

The theorem shows the existence of infinitely many Laplacian eigenmodes which are L^p-localized near the boundary ∂D. In fact, for any prescribed thresholds for both ratios in (3.1), there exists n_0 such that for all $n > n_0$, the eigenfunctions u_{nk} are L^p-localized. These eigenfunctions are called "whispering gallery eigenmodes" and illustrated on Fig. 3.1.

A simple consequence of the above theorem is

Theorem 3.2.2. *For any $p \geq 1$ and any open subset V compactly included in D (i.e., $\bar{V} \cap \partial D = \emptyset$), one has*

$$\lim_{n \to \infty} \frac{\|u_{nk}\|_{L^p(V)}}{\|u_{nk}\|_{L^p(D)}} = 0. \tag{3.5}$$

As a consequence,

$$C_p(V) \equiv \inf_{nk} \left\{ \frac{\|u_{nk}\|_{L^p(V)}}{\|u_{nk}\|_{L^p(\Omega)}} \right\} = 0. \tag{3.6}$$

In fact, for any open subset V compactly included in D, there exists n_0 such that for all $n > n_0$, $V \subset D_{nk}$ so that $\|u_{nk}\|_{L^p(V)} \leq \|u_{nk}\|_{L^p(D_{nk})}$ yielding Eq. (3.5).

In the same way, the localization also happens for any circular sector (as illustrated on Fig. 3.2):

Theorem 3.2.3. *Let*

$$S = \left\{ (r \cos \varphi, r \sin \varphi) \in \mathbb{R}^2 \; : \; 0 \leq r < R, 0 < \varphi < \phi \right\}, \tag{3.7}$$

be a circular sector of radius $R > 0$, and $S_{nk} = \left\{ \mathbf{r} \in S_0 \; : \; |\mathbf{r}| < \frac{d_n}{\alpha_{nk}} R \right\}$, where $d_n = n - n^{2/3}$ and α_{nk} are the positive zeros of $J_{n\pi/\phi}(z)$ (Dirichlet), $J'_{n\pi/\phi}(z)$ (Neumann) or $J'_{n\pi/\phi}(z) + h J_{n\pi/\phi}(z)$ for some $h > 0$ (Robin), with $n = 0, 1, 2, ...$ and $k = 1, 2, 3, ...$ counting zeros. Then for any $p \geq 1$, there exists a universal constant $C_p > 0$ such that for any $k = 1, 2, 3, ...$, there exists $N_{p,k} > 0$ such that for any integer $n > N_{p,k}$, the Laplacian eigenfunction u_{nk} for Dirichlet, Neumann or Robin boundary condition satisfies

$$\frac{\|u_{nk}\|_{L^p(S_{nk})}}{\|u_{nk}\|_{L^p(S)}} < C_p n^{\frac{1}{3} + \frac{2}{3p}} 2^{-(n\phi/\pi)^{1/3}/3}. \tag{3.8}$$
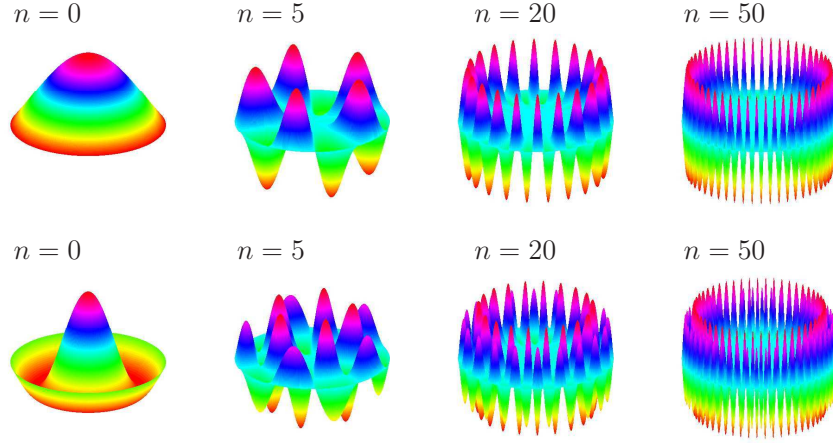
Figure 3.1: Formation of whispering gallery modes u_{nk} in the unit disk with Dirichlet boundary condition: for a fixed k ($k = 0$ for top figures and $k = 1$ for bottom figures), an increase of the index n leads to stronger localization of the eigenfunction near the boundary.

It also implies that, for any positive integer k,

$$\lim_{n \to \infty} \frac{\|u_{nk}\|_{L^p(S_{nk})}}{\|u_{nk}\|_{L^p(S)}} = 0, \tag{3.9}$$

while

$$\lim_{n \to \infty} \frac{\mu_2(S_{nk})}{\mu_2(S)} = 1. \tag{3.10}$$

Proof. The proof is completely similar to that of Theorem 3.2.1.   □

In three dimensions, the existence of whispering gallery modes in a ball follows from the following

Theorem 3.2.4. *Let $B = \{\mathbf{r} \in \mathbb{R}^3 \ : \ |\mathbf{r}| < R\}$ be a ball of radius R, and $B_{nk} = \{\mathbf{r} \in B \ : \ 0 < |\mathbf{r}| < Rs_n/\alpha_{nk}\}$, where $s_n = (n + 1/2) - (n + 1/2)^{2/3}$ and α_{nk} are the positive zeros of $j_n(z)$ (Dirichlet), $j_n'(z)$ (Neumann) or $j_n'(z) + hj_n(z)$ for some $h > 0$ (Robin), with $n = 0, 1, 2, ...$ denoting the order of spherical Bessel function $j_n(z)$ and $k = 1, 2, 3, ...$ counting zeros. Then, for any $p \geq 1$, there exists a universal constant $\tilde{C}_p > 0$ such that for any $k = 1, 2, 3, ...$, there exists $N_{p,k} > 0$ such that for any integer $n > N_{p,k}$, the Laplacian eigenfunction u_{nk} with Dirichlet, Neumann or Robin boundary condition satisfies*

$$\frac{\|u_{nk}\|_{L^p(B_{nk})}}{\|u_{nk}\|_{L^p(B)}} < \tilde{C}_p(n + 1/2)^{\frac{1}{3} + \frac{2}{3p}} \exp\left(-\frac{1}{3}\left(n + \frac{1}{2}\right)^{1/3}\right) \qquad (n \gg 1). \tag{3.11}$$

As a consequence, for any positive integer k,

$$\lim_{n \to \infty} \frac{\|u_{nk}\|_{L^p(B_{nk})}}{\|u_{nk}\|_{L^p(B)}} = 0, \tag{3.12}$$

while

$$\lim_{n \to \infty} \frac{\mu_3(B_{nk})}{\mu_3(B)} = 1. \tag{3.13}$$

(a) $n = 1$ (b) $n = 6$ (c) $n = 11$ (d) $n = 36$

(e) $n = 1$ (f) $n = 6$ (g) $n = 11$ (h) $n = 36$
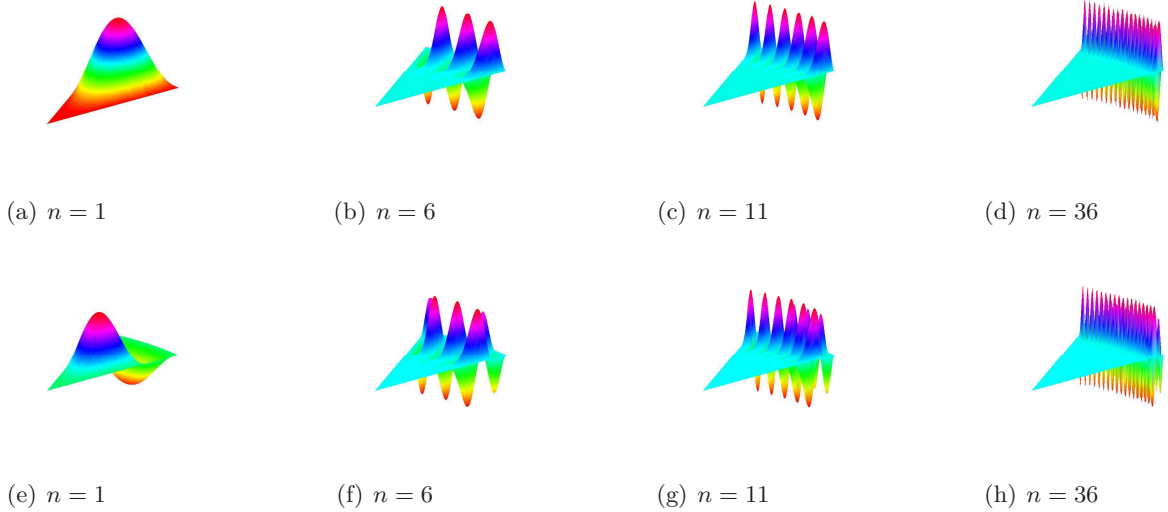
Figure 3.2: Formation of whispering gallery modes u_{nk} in the sector of radius $R = 1$ and angle $\frac{\pi}{6}$ with Dirichlet boundary condition: for a fixed k ($k = 0$ for top figures and $k = 1$ for bottom figures), an increase of the index n leads to stronger localization of the eigenfunction near the boundary.

Proof. See Appendix B2 for details.   □

As for the disk, the above results show that infinitely many high-frequency eigenfunctions are L^p-localized near the boundary of the ball. This is the well-known whispering gallery phenomenon.

3.2.2   Focusing modes

The localization of focusing modes at the origin is described by

Theorem 3.2.5. *For each $R_0 \in (0,1)$, let $D(R_0) = \{\mathbf{r} \in \mathbb{R}^2 \ : \ R_0 < |\mathbf{r}| < 1\}$, and D be the unit disk. Then, for any $n = 0, 1, 2, \ldots$ and $p > 4$, the Laplacian eigenfunction u_{nk} with Dirichlet, Neumann or Robin boundary condition satisfies*

$$\lim_{k \to \infty} \frac{\|u_{nk}\|_{L^\infty(D(R_0))}}{\|u_{nk}\|_{L^\infty(D)}} = 0, \tag{3.14}$$

$$\lim_{k \to \infty} \frac{\|u_{nk}\|_{L^p(D(R_0))}}{\|u_{nk}\|_{L^p(D)}} = 0 \tag{3.15}$$

and

$$\lim_{k \to \infty} \frac{\|u_{nk}\|_{L^2(D(R_0))}}{\|u_{nk}\|_{L^2(D)}} = \sqrt{1 - R_0} > 0. \tag{3.16}$$

Proof. See Appendix B1.   □

This theorem states that for each non-negative integer n, when the index k increases, the eigenfunctions u_{nk} become localized more and more near the origin. These eigenfunctions are called "focusing eigenmodes" and illustrated on Fig. 3.3. This theorem shows that the definition of localization is sensitive to
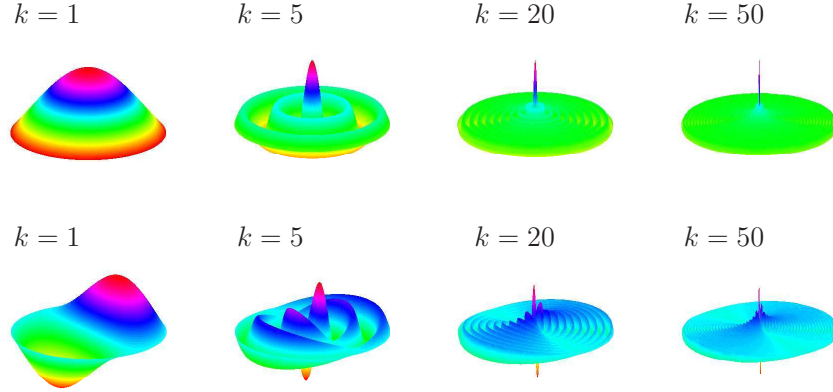
Figure 3.3:   Formation of focusing modes u_{nk} in the unit disk with Dirichlet boundary condition: for a fixed n ($n = 0$ for top figures and $n = 1$ for bottom figures), an increase of the index k leads to stronger localization of the eigenfunction at the origin.

the norm: the above focusing modes are L^p-localized (for all $p > 4$, including $p = \infty$), but they are not L^2-localized.

Remark 3.2.1. *It is interesting to understand the limit value of* $\dfrac{\|u_{nk}\|^p_{L^p(D(R_0))}}{\|u_{nk}\|^p_{L^p(D)}}$ *when* $k \to \infty$*, for* $1 \le p < 2$ *and* $2 < p \le 4$*. We expect that*

$$\lim_{k\to\infty} \frac{\|u_{nk}\|^p_{L^p(D(R_0))}}{\|u_{nk}\|^p_{L^p(D)}} \quad > \quad 0, \forall 1 \le p \le 2, \tag{3.17}$$

$$\lim_{k\to\infty} \frac{\|u_{nk}\|^p_{L^p(D(R_0))}}{\|u_{nk}\|^p_{L^p(D)}} \quad = \quad 0, \forall 2 \le p \le 4. \tag{3.18}$$

(see Appendix B1 for further discussions).

One can generalize the above theorem for a circular sector in two dimensions (Fig. 3.4):

Theorem 3.2.6. *For each $R_0 \in (0,1)$, let S_0 is the circular sector of radius $R = 1$, defined in (3.7), and $S(R_0) = \{\mathbf{r} \in S \ : \ R_0 < |\mathbf{r}| < 1\}$. Then, for any $n = 1, 2, \dots$ and $p > 4$, the Laplacian eigenfunction u_{nk} with Dirichlet, Neumann or Robin boundary condition satisfies*

$$\lim_{k\to\infty} \frac{\|u_{nk}\|_{L^\infty(S(R_0))}}{\|u_{nk}\|_{L^\infty(S)}} = 0, \tag{3.19}$$

$$\lim_{k\to\infty} \frac{\|u_{nk}\|_{L^p(S(R_0))}}{\|u_{nk}\|_{L^p(S)}} = 0 \tag{3.20}$$

and

$$\lim_{k\to\infty} \frac{\|u_{nk}\|_{L^2(S(R_0))}}{\|u_{nk}\|_{L^2(S)}} = \sqrt{1 - R_0} > 0. \tag{3.21}$$

Proof. Similar to Theorem 3.2.5. □

(a) $k = 0$ (b) $k = 5$ (c) $k = 20$ (d) $k = 100$

(e) $k = 0$ (f) $k = 5$ (g) $k = 20$ (h) $k = 100$
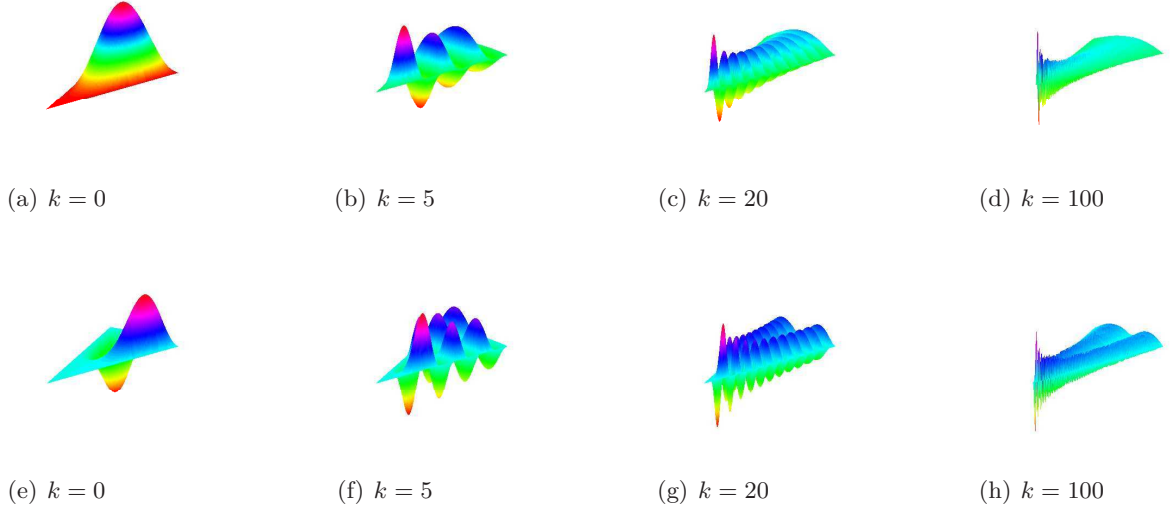
Figure 3.4: Formation of focusing modes u_{nk} in the sector of radius $R = 1$ and angle $\frac{\pi}{6}$ with Dirichlet boundary condition: for a fixed n ($n = 1$ for top figures and $n = 2$ for bottom figures), an increase of the index k leads to stronger localization of the eigenfunction near the origin.

A similar theorem can be reformulated for a ball in three dimensions.

Theorem 3.2.7. *For each $R_0 \in (0, 1)$, let $B(R_0) = \{\mathbf{r} \in \mathbb{R}^3 : R_0 < |\mathbf{r}| < 1\}$, and B be the unit ball. Then, for any $n = 0, 1, 2, \ldots$ and $p > 3$, the Laplacian eigenfunction u_{nk} with Dirichlet, Neumann or Robin boundary condition satisfies*

$$\lim_{k \to \infty} \frac{\|u_{nk}\|_{L^\infty(B(R_0))}}{\|u_{nk}\|_{L^\infty(B)}} = 0, \tag{3.22}$$

$$\lim_{k \to \infty} \frac{\|u_{nk}\|_{L^p(B(R_0))}}{\|u_{nk}\|_{L^p(B)}} = 0 \tag{3.23}$$

and

$$\lim_{k \to \infty} \frac{\|u_{nk}\|_{L^2(B(R_0))}}{\|u_{nk}\|_{L^2(B)}} = \sqrt{1 - R_0} > 0. \tag{3.24}$$

Proof. See Appendix B2. □

Remark 3.2.2. *For other cases $1 \leq p < 2$ and $2 < p \leq 3$, we expect that*

$$\lim_{k \to \infty} \frac{\|u_{nk}\|^p_{L^p(B(R_0))}}{\|u_{nk}\|^p_{L^p(B)}} > 0, \forall 1 \leq p < 2, \tag{3.25}$$

$$\lim_{k \to \infty} \frac{\|u_{nk}\|^p_{L^p(B(R_0))}}{\|u_{nk}\|^p_{L^p(B)}} = 0, \forall 2 < p \leq 3, \tag{3.26}$$

which still requires a rigorous proof.

3.3 Localization in elliptical domains

3.3.1 Eigenfunctions for an ellipse or elliptical annuli

In Section 2.2.5, we introduced four families of Laplacian eigenfunctions in an ellipse and two families of Laplacian eigenfunctions in an elliptical annuli. One can first solve Eqs. (2.61) or (2.64) for values of q_{nki}, and then compute the corresponding eigenvalues and eigenfunctions by using the numerical algorithms from Appendix C.

3.3.2 Bouncing ball modes

For each $\alpha \in \left(0, \frac{\pi}{2}\right)$, we consider the elliptical sector Ω_α inside an elliptical domain Ω (Fig. 2.7)

$$\Omega_\alpha = \{R_1 < r < R_2, \ \theta \in (\alpha, \pi - \alpha) \cup (\pi + \alpha, 2\pi - \alpha)\}.$$

Theorem 3.3.1. *Let Ω be an ellipse or an elliptical annulus (with a focal distance $a > 0$), defined in Section 2.2.5. For any $\alpha \in \left(0, \frac{\pi}{2}\right)$, $n \geq 0$, $p \geq 1$ and $i = 1, 2, 3, 4$ (for ellipse) or $i = 1, 2$ (for elliptical annulus), there exists $\Lambda_{\alpha,n} > 0$ such that for any $\lambda_{nki} > \Lambda_{\alpha,n}$,*

$$\frac{\|u_{nki}\|_{L^p(\Omega \backslash \Omega_\alpha)}}{\|u_{nki}\|_{L^p(\Omega)}} < D_n \left(\frac{16\alpha}{\pi - \alpha/2}\right)^{1/p} \exp\left(-a\sqrt{\lambda_{nki}} \left[\sin\left(\frac{\pi}{4} + \frac{\alpha}{2}\right) - \sin\alpha\right]\right), \qquad (3.27)$$

where

$$D_n = 3\sqrt{\frac{1 + \sin\left(\frac{3\pi}{8} + \frac{\alpha}{4}\right)}{\left[\tan\left(\frac{\pi}{16} - \frac{\alpha}{8}\right)\right]^n}}. \qquad (3.28)$$

Proof. See Appendix B5. □

Given that $\lambda_{nki} \to \infty$ as k increases (for any fixed n and i), while the area of Ω_α can be made arbitrarily small by sending $\alpha \to \pi/2$, the theorem implies that there are infinitely many eigenfunctions u_{nki} which are L^p-localized (in the elliptical sector Ω_α)

$$\lim_{k \to \infty} \frac{\|u_{nki}\|_{L^p(\Omega \backslash \Omega_\alpha)}}{\|u_{nki}\|_{L^p(\Omega)}} = 0. \qquad (3.29)$$

These eigenfunctions are called "bouncing ball modes" and illustrated on Fig. 3.5. We note that the existence of bouncing ball modes was already known for an ellipse and, more generally, for convex planar domains with smooth boundary [41, 128]. Although our estimates are specific to elliptical shapes, they are simpler and also applicable to elliptical annuli, i.e. non-convex domains.

The quality of the above estimates was checked numerically. Fig. 3.6 shows the ratio $\frac{\|u_{nk1}\|_{L^2(\Omega \backslash \Omega_\alpha)}}{\|u_{nk1}\|_{L^2(\Omega_\alpha)}}$ and its upper bound for two families of eigenfunctions in a filled ellipse and an elliptical annulus, respectively. One can clearly see the rapid exponential decay of this ratio when k increases that implies the localization in a thin sector around the vertical (minor) axis. Note that the upper bound is not sharp and can be further improved.
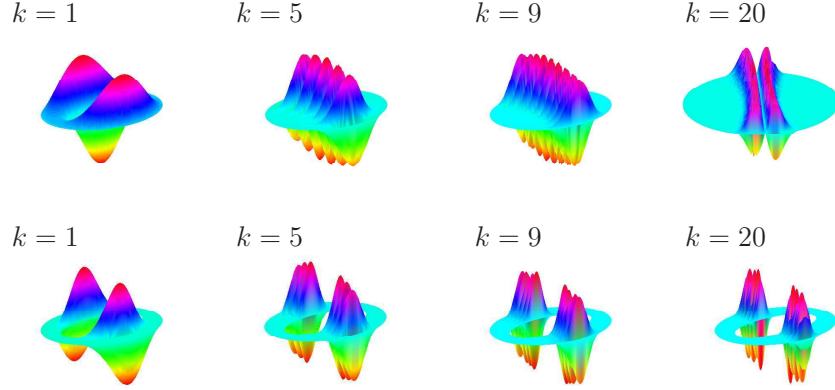
Figure 3.5: Formation of bouncing ball modes u_{nki} in a filled ellipse of radius $R = 1$ (top) and an elliptical annulus of radii 0.5 and 1 (bottom), with the focal distance $a = 1$ and Dirichlet boundary condition. For fixed $n = 1$ and $i = 1$, an increase of the index k leads to stronger localization of the eigenfunction near the vertical semi-axis ($K_{max} = 200$, see Appendix C1).
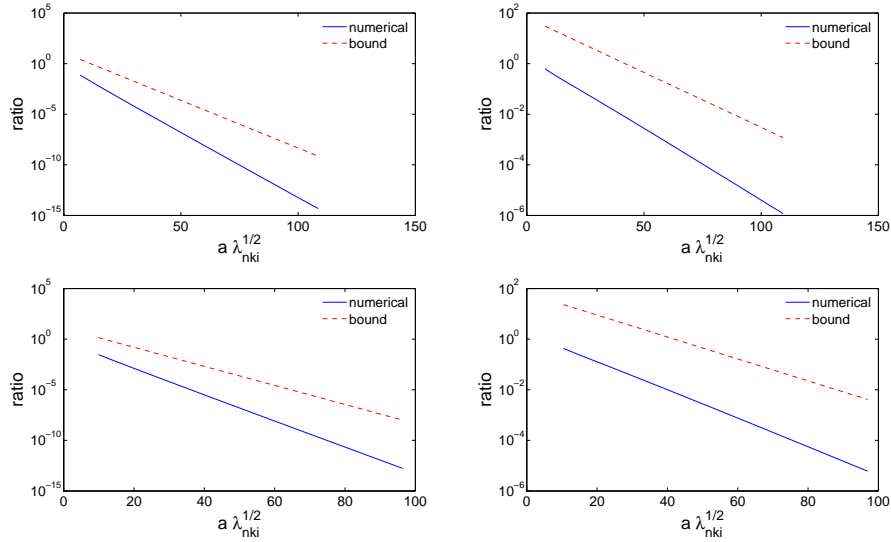
Figure 3.6: The ratio $\dfrac{\|u_{nk1}\|_{L^2(\Omega \setminus \Omega_\alpha)}}{\|u_{nk1}\|_{L^2(\Omega_\alpha)}}$ (solid blue line) and its upper bound (3.27) (dashed red line) in a filled ellipse of radius $R = 1$ and focal distance $a = 1$ (top) and in an elliptical annulus of radii $R_0 = 0.5$ and $R = 1$ and focal distance $a = 1$ (bottom), with $n = 0$ and $\alpha = \pi/4$ (left) and $n = 1$ and $\alpha = \pi/3$ (right). For numerical computation of Mathieu functions, we used $K_{max} = 200$ (see Appendix C).

The explicit estimates from previous sections provide us with simple examples of domains for which there are infinitely many L^p-localized eigenfunctions, according to the definition (3.1). Most importantly, the high-frequency localization may occur in both convex and non-convex domains. This observation relaxes, at least for elliptical domains, the condition of convexity that was significant for the construction of whispering gallery and bouncing ball modes by Keller and Rubinow [128] and for semiclassical approximations by Lazutkin [138–140]. At the same time, these approximations suggest the existence of L^p-localized eigenfunctions for a large class of domains. How large is this class? What are the relevant conditions on the domain? To our knowledge, these questions are open. In order to highlight the relevance of these questions, it is instructive to give an example of domains for which there is no localization.

3.4 Localization in rectangular domains

The study of localization in rectangle-like domains, $\Omega = (0, \ell_1) \times ... \times (0, \ell_d) \subset \mathbb{R}^d$ (with the sizes $\ell_i > 0$), may seem to be the simplest case because the Laplacian eigenfunctions are factored and expressed through sines (Dirichlet), cosines (Neumann) or their combination (Robin):

$$u_{n_1,...,n_d}(x_1, ..., x_d) = u_{n_1}^{(1)}(x_1) \ldots u_{n_d}^{(d)}(x_d), \qquad \lambda_{n_1,...,n_d} = \lambda_{n_1}^{(1)} + ... + \lambda_{n_d}^{(d)}, \tag{3.30}$$

with the multiple index $n_1...n_d$, and $u_{n_i}^{(i)}(x_i)$ and $\lambda_{n_i}^{(i)}$ ($i = 1, ..., d$) corresponding to the one-dimensional problem on the interval $(0, \ell_i)$:

$$u_n^{(i)}(x) = \sin(\pi n x/\ell_i), \quad \lambda_n^{(i)} = \pi^2 n^2/\ell_i^2, \quad n = 1, 2, 3, ... \qquad \text{(Dirichlet)},$$
$$u_n^{(i)}(x) = \cos(\pi n x/\ell_i), \quad \lambda_n^{(i)} = \pi^2 n^2/\ell_i^2, \quad n = 0, 1, 2, ... \qquad \text{(Neumann)}$$

(Robin boundary condition will not be considered here). The situation is indeed elementary for rectangle-like domains for which all eigenvalues are simple.

Theorem 3.4.1. *Let $\Omega = (0, \ell_1) \times ... \times (0, \ell_d) \subset \mathbb{R}^d$ be a rectangle-like domain with sizes $\ell_1 > 0$, ..., $\ell_d > 0$ such that*

$$\ell_i^2/\ell_j^2 \notin \mathbb{Q} \qquad \forall \, i \neq j. \tag{3.31}$$

($\mathbb{Q}$ denoting the set of rational numbers). Then for any $p \geq 1$ and any open subset $V \subset \Omega$,

$$C_p(V) = \inf_{n_1,...,n_d} \left\{ \frac{\|u_{n_1,...,n_d}\|_{L^p(V)}}{\|u_{n_1,...,n_d}\|_{L^p(\Omega)}} \right\} > 0. \tag{3.32}$$

The proof is elementary (see Appendix B3) and relies the fact that all the eigenvalues are simple due to the condition (3.31). The fact that $C_p(V) > 0$ for any open subset V means that there is no eigenfunction that could fully "avoid" any location inside the domain, i.e., there is no L^2-localized eigenfunction. Since the set of rational numbers has zero Lebesgue measure, the condition (3.31) is fulfilled almost surely, if one would choose a rectangle-like domain randomly. In other words, for most rectangle-like domains, there is no L^2-localized eigenfunctions.

Remark 3.4.1. *When at least one ratio ℓ_i^2/ℓ_j^2 is rational, certain eigenvalues are degenerate, and the associated eigenfunctions become linear combinations of products of sines or cosines. For instance, for the square with $\ell_1 = \ell_2 = \pi$ and Dirichlet boundary condition, the eigenvalue $\lambda_{1,2} = 1^2 + 2^2$ is twice degenerate, and $u_{1,2}(x_1, x_2) = c_1 \sin(x_1)\sin(2x_2) + c_2 \sin(2x_1)\sin(x_2)$, with arbitrary constants c_1 and c_2 ($c_1^2 + c_2^2 \neq 0$). Although the computation is still elementary for each eigenfunction, it is unknown whether the infimum $C_p(V)$ from Eq. (3.32) is strictly positive or not, for arbitrary rectangle-like domain Ω and any open subset V. For instance, the most general known result for a rectangle $\Omega = (0, \ell_1) \times (0, \ell_2)$ states that $C_2(V) > 0$ for any $V \subset \Omega$ of the form $V = (0, \ell_1) \times \omega$, where ω is any open subset of $(0, \ell_2)$ [34]. Even for the unit square, the statement $C_p(V) > 0$ for any open subset V seems to be an open problem. More generally, one may wonder whether $C_p(V)$ is strictly positive or not for any open subset V in polygonal convex domains or in piecewise smooth convex domains. Following an approach of Zelditch and Zworski [232], Marlof and Rudnick proved that among an orthogonal basis $\{u_n\}$ of Laplacian eigenfunctions in a rational polygon Ω (satisfying Dirichlet boundary condition), there exists a density-one subsequence $\{u_{n_j}\}$ such that for any subset $V \subset \Omega$ with boundary of Lebesgue measure zero, [151]*

$$\lim_{j \to \infty} \left\{ \frac{\|u_{n_j}\|_{L^2(V)}}{\|u_{n_j}\|_{L^2(\Omega)}} \right\} = \frac{\mu_2(V)}{\mu_2(\Omega)}$$

where $\mu_2(.)$ is the Lebesgue measure in $\mathbb{R}^2$. This remarkable result shows that in a rational polygon, the set of localized eigenfunctions of the Laplace operator with Dirichlet boundary condition has measure zero. The study for localization in polygonal convex domains is still interesting and requires further investigations.

3.5 Localization in equilateral triangles

Let Ω be the equilateral triangle

$$\Omega = \left\{ (x, y) : 0 < y < x\sqrt{3}, 0 < y < \sqrt{3}(1 - x) \right\} \tag{3.33}$$

The Dirichlet eigenvalues and eigenfunctions in this domain can be computed explicitly as shown in Section 2.2.6. For symmetric eigenvalues $\lambda_{3p,0}$, the associated eigenfunction can be represented as

$$u_{3p,0}(x, y) = \sin\left(2\pi p \overline{d_1}\right) + \sin\left(2\pi p \overline{d_2}\right) + \sin\left(2\pi p \overline{d_3}\right), \ p = 1, 2, \ldots \tag{3.34}$$

where $\overline{d_1} = \frac{2y}{\sqrt{3}}$, $\overline{d_2} = x - \frac{y}{\sqrt{3}}$ and $\overline{d_3} = 1 - x - \frac{y}{\sqrt{3}}$. Here, $\overline{d_1}, \overline{d_2}, \overline{d_3}$ are the normalized altitudes of the point (x, y) in the triangle Ω, which satisfy the normalization $\overline{d_1} + \overline{d_2} + \overline{d_3} = 1$. The following theorem concerns the high-frequency localization of symmetric eigenfunctions in Ω:

Theorem 3.5.1. *Let $\{u_{3p,0}(x, y)\}$ be the set of all symmetric Laplacian eigenfunctions (Fig. 3.7) with Dirichlet boundary condition in Ω. Then, for any open set $V \subset \Omega$, there exists a universal constant $C_V > 0$, such that*

$$\int_V u_{3p,0}^2(x, y) dx dy \geq C_V \int_\Omega u_{3p,0}^2(x, y) dx dy, \ \forall p = 1, 2, \ldots \tag{3.35}$$

Proof. See Appendix B6. □

(a) u_1 (b) u_2 (c) u_3 (d) u_4

(e) u_5 (f) u_6 (g) u_7 (h) u_8
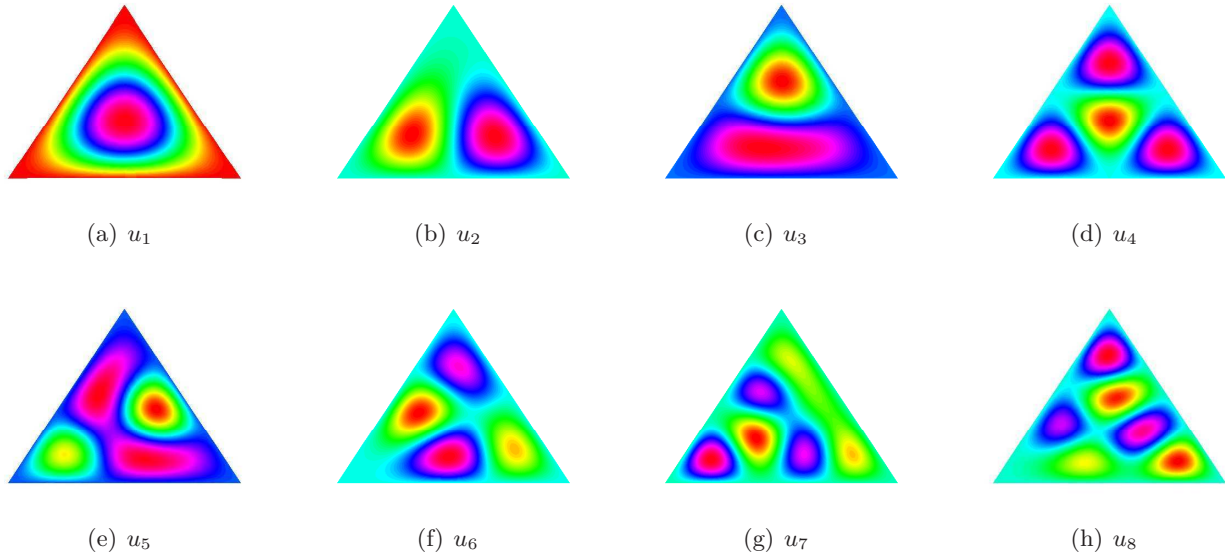
Figure 3.7: Several eigenmodes of the Laplace operator in the equilateral triangles. The first/fourth eigenfunctions are symmetric eigenmodes while the remaining shown eigenfunctions are complex eigenmodes.

Remark 3.5.1. *From the above theorem, all symmetric eigenfunctions in the triangle Ω are not localized. In turn, the existence of localized eigenmodes among complex eigenfunctions is still an open question.*

3.6   Conclusion

In this chapter, we revived the classical problem of high-frequency localization of Laplacian eigenfunctions. For circular, spherical and elliptical domains, we derived the inequalities for L^p-norms of the Laplacian eigenfunctions that clearly illustrate the emergence of whispering gallery, bouncing ball and focusing eigenmodes. We gave an alternative proof for the existence of bouncing ball modes in elliptical domains. This proof relies on the properties of modified Mathieu functions and is as well applicable to elliptical annuli. As a consequence, we showed that bouncing ball modes also exist in non-convex domains. At the same time, we proved that there is no localization in most rectangle-like domains that led us to formulating the problem of how to characterize the class of domains admitting high-frequency localization. The non-localization of symmetric eigenfunctions in equilateral triangles was proven. In particular, the roles of convexity and smoothness have to be further investigated. The problem of localization in polygonal convex domains or, more generally, in piecewise smooth convex domains, remains open.

Chapter 4

Exponential decay of Laplacian eigenfunctions in domains with branches

In this chapter, we study the behavior of Laplacian eigenfunctions in domains with branches of variable cross-sectional profile. If an eigenvalue is below a threshold which is determined by the shape of the branch, the associate eigenfunction is proved to exponentially decay inside the branch. The decay rate is twice the square root of the difference between the threshold and the eigenvalue. The derived exponential estimate is applicable for arbitrary domains in any spatial dimension. It allows us to explain the existence of low-frequency localized eigenmodes in various domains. In particular, we show the existence of localized eigenmodes in elongated polygons.

The results of this chapter up to Section 4.7 are reported in a joint-work with A. Delitsyn [60].

4.1 Introduction

We investigate the behavior of Laplacian eigenfunctions in domains with branches. We show that certain eigenfunctions are "expelled" from the branch, i.e., their amplitude along the branch decays exponentially fast. A similar "expulsion" effect is well known in optics and acoustics: a wave of wavelength ℓ cannot freely propagate inside a rectangular channel of width b smaller than $\ell/2$ because of the exponential attenuation $\sim e^{-x\pi/b}$ along the channel [115, 191]. We extend this classical result to arbitrary domains with branches of arbitrary shape. We derive a rigorous exponential estimate for the L^2-norm of the eigenfunction in cross-sections of the branch. We obtain the sharp decay rate which generalizes and refines the classical rate π/b. Although this problem is remotely related to localization of waves in optical or acoustical waveguides (e.g., infinite bent tubes [36, 91, 115]), we mainly focus on bounded domains.

It is worth noting that the exponential decay of eigenfunctions of Schrödinger operators in free space (so-called strong localization) has been thoroughly investigated in physical and mathematical literature (see, e.g., [2, 152, 153, 166, 194]). The first exploration of this problem for arbitrary Schrödinger potential bounded from below was given by Schnol' [194] who proved an exponential decay of eigenfunctions in which the decay rate was related to the distance between the corresponding eigenvalue and the essential spectrum. This result is of remarkable generality because the essential spectrum may be arbitrary, for
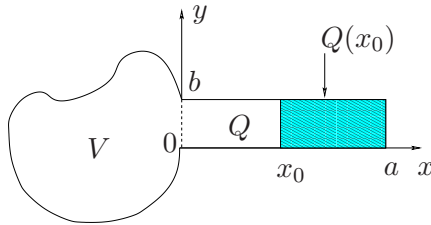
Figure 4.1:   A bounded domain D is the union of a basis domain V of arbitrary shape and a rectangular branch Q.

example with gaps, and may not consist of the positive axis. A sharp estimate for the decay rate was made by Maslov who reduced the problem to a differential inequality [152, 153]. Anderson discovered the exponential decay of eigenfunctions of the Schrödinger operator with random potentials [6]. This phenomenon, known as the Anderson localization, has been intensively investigated (see reviews [19, 72]). Although the Laplace operator in a bounded domain is a much simpler mathematical object, the properties of its eigenfunctions are still poorly understood.

The chapter is organized as follows. In Sec. 4.2, we start by considering a two-dimensional domain with a rectangular branch. In this special case, the estimates are derived in a rather elementary and straightforward way that helps to illustrate many properties of eigenfunctions. Section 4.3 presents the analysis for domains with branches of arbitrary shape in any spatial dimension. We provide a sufficient condition on the eigenvalue, under which the related eigenfunction decays exponentially inside the branch. In Sections 4.4 and 4.5, we discuss the exponential decay for domains with infinite branches and higher-dimensional domains. Sec. 4.6 presents numerical examples which illustrate the theoretical results and suggest new perspectives for further investigations. In Sec. 4.7, we show the existence of localized eigenfunctions in elongated polygons. The chapter ends by conclusions, in which the main results are summarized and their consequences are discussed.

4.2   Rectangular branches

In order to describe our approach, we consider the Dirichlet eigenproblem

$$\begin{cases} \triangle u + \lambda u = 0, \text{ in } D, \\ \quad u = 0 \text{ on } \partial D, \end{cases} \tag{4.1}$$

in a planar bounded domain $\bar{D} = \bar{V} \cup \bar{Q}$, which is decomposed into a basic domain V of arbitrary shape and a rectangular branch Q of side a and b (see on Fig. 4.1) such that

$$Q = \left\{ (x, y) \in \mathbb{R}^2 : 0 < x < a, 0 < y < b \right\}.$$

Assuming an eigenvalue λ is smaller than the first eigenvalue of the Laplace operator in the cross-section of

the branch Q (i.e the interval $[0,b]$), $\lambda < \frac{\pi^2}{b^2}$, we aim at showing the classical result that the corresponding eigenfunction u decays exponentially along this branch. The general case of variable cross-sectional profiles will be presented below.

One can easily check that a general solution of Eq. (4.1) in the rectangular branch Q can be determined by the following form

$$u(x,y) = \sum_{n=1}^{\infty} c_n \sinh(\tilde{\gamma}_n(a-x)) \sin(\pi n y/b), \tag{4.2}$$

where $\tilde{\gamma}_n = \sqrt{(\frac{\pi}{b}n)^2 - \lambda}$, and c_n are constants. We now consider the energetic norm of the eigenfunction u in the subdomain $Q(x_0) = \{(x,y) \in \mathbb{R}^2 \ : \ x_0 < x < a, \ 0 < y < b\}$ which is defined as

$$||\nabla u||^2_{L^2(Q(x_0))} \equiv \int_{Q(x_0)} (\nabla u, \nabla u) dx dy. \tag{4.3}$$

We substitute Eq.(4.2) into Eq.(4.3):

$$||\nabla u||^2_{L^2(Q(x_0))} = \sum_{n=1}^{\infty} c_n^2 \frac{b}{2} \int_{x_0}^{a} \left[(\frac{\pi}{b}n)^2 \sinh^2(\tilde{\gamma}_n(a-x)) + \gamma_n^2 \cosh^2(\tilde{\gamma}_n(a-x)) \right] dx. \tag{4.4}$$

Using elementary inequalities for the integral (see Appendix D1), one gets

$$||\nabla u||^2_{L^2(Q(x_0))} \leq C e^{-2\tilde{\gamma}_1 x_0} \sum_{n=1}^{\infty} n c_n^2 \sinh^2(\tilde{\gamma}_1 a), \tag{4.5}$$

where C is an explicit constant.

By the trace theorem, one can estimate the upper bound of the above series (see Appendix D1)

$$||\nabla u||^2_{L^2(Q(x_0))} \leq C_1 e^{-2\tilde{\gamma}_1 x_0},$$

with another explicit constant C_1 that does not depend on x_0 (and the L^2-norm of u in D was set to 1). As a result, we established the exponential decay of the energy $||\nabla u||^2$ along the branch Q with the decay rate $2\tilde{\gamma}_1 = 2\sqrt{\mu - \lambda}$ where $\mu = (\frac{\pi}{b})^2$.

From the above estimate, it is not difficult to deduce a similar estimate in L^2-norm,

$$||u||^2_{L^2(Q(x_0))} \equiv \int_{Q(x_0)} u^2 dx dy \leq C_2 e^{-2\tilde{\gamma}_1 x_0}, \tag{4.6}$$

where C_2 is another constant. The derivation implies that this estimate is sharp, i.e. the decay rate cannot be improved in general.

Remark 4.2.1. *It is worth noting no information about the basic domain V was used. In particular, the Dirichlet boundary condition on $\partial V \cup \partial D$ can be replaced by arbitrary boundary condition on ∂V under which the Laplace operator is still self-adjoint.*
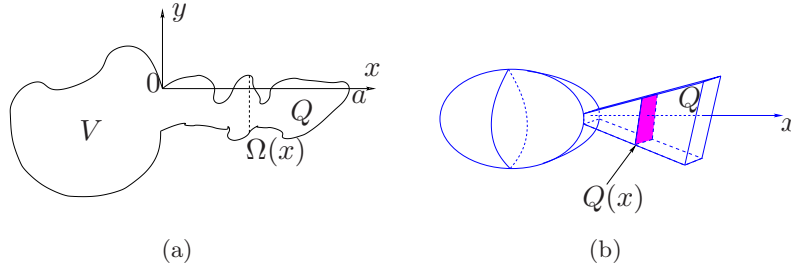
Figure 4.2: A bounded domain D is the union of a basic domain V of arbitrary shape and a branch Q of a variable cross-sectional profile $\Omega(x) \subset \mathbb{R}^n$: (a) - two-dimensional domains, (b) - three-dimensional domain.

4.3 Branch of arbitrary shape

In this section, we show that the above estimate is still valid for Dirichlet eigenfunctions in a much more general case with a branch of arbitrary shape in $\mathbb{R}^{n+1}(n = 1, 2, 3, \dots)$. We consider again the eigenvalue problem

$$\begin{cases} \triangle u + \lambda u = 0, \text{ in } D, \\ \qquad u = 0 \text{ on } \partial D, \end{cases} \tag{4.7}$$

where $\bar{D} = \bar{V} \cup \bar{Q}$ is decomposed into a basic bounded domain $V \in \mathbb{R}^{n+1}$ of arbitrary shape and a branch $Q \subset \mathbb{R}^{n+1}$ of a variable cross-sectional profile $\Omega(x) \subset \mathbb{R}^n$ (Fig. 4.2) such that

$$Q = \{(x, \mathbf{y}) \in \mathbb{R}^{n+1} \ : \ \mathbf{y} \in \Omega(x), \ 0 < x < a\}.$$

Each cross-section $\Omega(x)$ is a bounded domain which is parameterized by x from 0 to a. The boundary of the branch Q is assumed to be piecewise smooth [102].

For a fixed $x \in (0, a)$, we call $\mu_1(x)$ the first eigenvalue of the problem

$$- \Delta_\perp \phi(\mathbf{y}) = \mu_1(x)\phi(\mathbf{y}) \quad \mathbf{y} \in \Omega(x), \qquad \phi|_{\partial\Omega} = 0, \tag{4.8}$$

where $\Delta_\perp$ is the n-dimensional Laplace operator. We denote

$$\mu = \inf_{0 < x < a} \mu_1(x) \tag{4.9}$$

the smallest first eigenvalue among all cross-sections of the branch. For example, if $\Omega(x) = [0, b]$ (independent of x), one has $\mu = \pi^2/b^2$ and retrieves the example from previous section.

Now, we formulate our main result as

Theorem 4.3.1. *If the basic domain V is large enough such that there exists an eigenvalue*

$$\lambda < \mu, \tag{4.10}$$

the squared L^2-norm of the associated eigenfunction u in the cross-section $\Omega(x_0)$,

$$I(x_0) \equiv \int\limits_{\Omega(x_0)} u^2(x_0, \mathbf{y}) d\mathbf{y}, \tag{4.11}$$

has an upper bound which decays exponentially with x_0:

$$I(x_0) \leq I(0) e^{-\beta x_0} \quad (0 \leq x_0 < a), \tag{4.12}$$

with the decay rate

$$\beta = \sqrt{2} \ \sqrt{\mu - \lambda}. \tag{4.13}$$

Moreover, if the branch profile $\Omega(x)$ satisfies the condition

$$(\mathbf{e}_x, \mathbf{n}(x, \mathbf{y})) \geq 0 \quad \forall (x, \mathbf{y}) \in \partial Q, \tag{4.14}$$

where $\mathbf{e}_x$ is the unit vector along the x coordinate, and $\mathbf{n}(x, \mathbf{y})$ the unit normal vector at the boundary point $(x, \mathbf{y})$ directed outwards the domain, then the decay rate is improved:

$$\beta = 2\sqrt{\mu - \lambda}. \tag{4.15}$$

Proof. We will prove the theorem by three steps.

(i) First, we derive the inequality

$$I''(x_0) \geq c\gamma^2 I(x_0), \tag{4.16}$$

where $c = 2$ for arbitrary branch and $c = 4$ for branches satisfying the condition (4.14), and $\gamma = \sqrt{\mu - \lambda}$. This type of inequalities was first established by Maslov for Schrödinger operators in free space [152, 153]. For this purpose, we consider the first two derivatives of $I(x_0)$:

$$I'(x_0) \;=\; 2 \int\limits_{\Omega(x_0)} u \frac{\partial u}{\partial x} \, d\mathbf{y}, \tag{4.17}$$

$$I''(x_0) \;=\; 2 \int\limits_{\Omega(x_0)} u \frac{\partial^2 u}{\partial x^2} \, d\mathbf{y} + 2 \int\limits_{\Omega(x_0)} \left(\frac{\partial u}{\partial x} \right)^2 d\mathbf{y}, \tag{4.18}$$

where the boundary condition $u|_{\partial Q} = 0$ cancels the integrals over the "lateral" boundary of $Q(x_0)$. One can estimate the first integral in Eq. (4.18) by

$$\int\limits_{\Omega(x_0)} u \frac{\partial^2 u}{\partial x^2} d\mathbf{y} = \int\limits_{\Omega(x_0)} u[\Delta u - \Delta_\perp u] \, d\mathbf{y} = \int\limits_{\Omega(x_0)} (\nabla_\perp u, \nabla_\perp u) d\mathbf{x} - \lambda \int\limits_{\Omega(x_0)} u^2 d\mathbf{y} \tag{4.19}$$

Using the Friedrichs-Poincaré inequality for the cross-section $\Omega(x_0)$ (see Appendix D2), one has

$$\int\limits_{\Omega(x_0)} (\nabla_\perp u, \nabla_\perp u) d\mathbf{y} \geq \mu_1(x_0) \int\limits_{\Omega(x_0)} u^2 d\mathbf{y}. \tag{4.20}$$

Since $\mu_1(x_0) \geq \mu$ by definition of μ in Eq. (4.9), one gets

$$\int\limits_{\Omega(x_0)} (\nabla_\perp u, \nabla_\perp u) d\mathbf{y} \geq \mu \int\limits_{\Omega(x_0)} u^2 d\mathbf{y}.$$

Bringing the above results together, it is easy to see that

$$\int\limits_{\Omega(x_0)} u \frac{\partial^2 u}{\partial x^2} d\mathbf{y} \geq (\mu - \lambda) \int\limits_{\Omega(x_0)} u^2 d\mathbf{y}. \tag{4.21}$$

Since the second term in Eq. (4.18) is always positive, it implies that

$$I''(x_0) \geq 2 \int\limits_{\Omega(x_0)} u \frac{\partial^2 u}{\partial x^2} d\mathbf{y} \geq 2(\mu - \lambda) \int\limits_{\Omega(x_0)} u^2 d\mathbf{y},$$

from which follows the inequality (4.16) with $c = 2$.

If the condition (4.14) is satisfied, one can get a more accurate estimate of the second term in Eq. (4.18) from the Rellich's identity (see Appendix D3):

$$\int\limits_{\Omega(x_0)} \left(\frac{\partial u}{\partial x}\right)^2 d\mathbf{y} = \int\limits_{\Omega(x_0)} (\nabla_\perp u, \nabla_\perp u) d\mathbf{y} - \lambda \int\limits_{\Omega(x_0)} u^2 d\mathbf{y} + \int\limits_{\partial Q(x_0) \backslash \Omega(x_0)} \left(\frac{\partial u}{\partial n}\right)^2 (\mathbf{e}_x, \mathbf{n}(S)) dS, \tag{4.22}$$

where $Q(x_0)$ denotes the "right" part of the branch Q delimited by $\Omega(x_0)$:

$$Q(x_0) = \left\{ (x, \mathbf{y}) \in \mathbb{R}^{n+1} \; : \; \mathbf{y} \in \Omega(x), \; x_0 < x < a \right\}. \tag{4.23}$$

It is easy to see that the condition (4.14) implies the positivity of the last term in Eq. (4.22), which can therefore be dropped off in order to get the following estimate:

$$\int\limits_{\Omega(x_0)} \left(\frac{\partial u}{\partial x}\right)^2 d\mathbf{y} \geq \int\limits_{\Omega(x_0)} (\nabla_\perp u, \nabla_\perp u) d\mathbf{y} - \lambda \int\limits_{\Omega(x_0)} u^2 d\mathbf{y} \geq (\mu - \lambda) \int\limits_{\Omega(x_0)} u^2 d\mathbf{y}.$$

Combining this result with (4.21), one gets the inequality (4.16) with $c = 4$.

(ii) Secondly, we prove that

$$I(a) = 0, \quad I'(a) = 0, \quad I(x_0) \neq 0, \quad I'(x_0) < 0, \forall x_0 \in [0, a). \tag{4.24}$$

By using Eq.(4.17) and applying the Green's formula in the subdomain $Q(x_0)$, one gets

$$
\begin{aligned}
I'(x_0) &= -2 \int\limits_{Q(x_0)} u\Delta u \, dxd\mathbf{y} - 2 \int\limits_{Q(x_0)} (\nabla u, \nabla u) dxd\mathbf{y} - 2 \int\limits_{\partial Q(x_0)\backslash\Omega(x_0)} u\frac{\partial u}{\partial x} \, d\mathbf{y} \\
&= -2 \int\limits_{Q(x_0)} u\Delta u \, dxd\mathbf{y} - 2 \int\limits_{Q(x_0)} (\nabla u, \nabla u) dxd\mathbf{y} = -2\lambda \int\limits_{Q(x_0)} u^2 \, dxd\mathbf{y} - 2 \int\limits_{Q(x_0)} (\nabla u, \nabla u) dxd\mathbf{y}.
\end{aligned}
\tag{4.25}
$$

Using again the Friedrichs-Poincaré inequality (4.20), one can estimate the second term in Eq.(4.25):

$$
\begin{aligned}
\int\limits_{Q(x_0)} (\nabla u, \nabla u) dxd\mathbf{y} &= \int\limits_{Q(x_0)} \left[\left(\frac{\partial u}{\partial x}\right)^2 + (\nabla_\perp u, \nabla_\perp u) \right] dxd\mathbf{y} \\
&\geq \int\limits_{x_0}^{a} dx \int\limits_{\Omega(x)} (\nabla_\perp u, \nabla_\perp u) d\mathbf{y} \geq \mu \int\limits_{x_0}^{a} dx \int\limits_{\Omega(x)} u^2 dxd\mathbf{y} = \mu \int\limits_{Q(x_0)} u^2 dxd\mathbf{y}.
\end{aligned}
\tag{4.26}
$$

From the above inequality, one obtains

$$
-I'(x_0) = -2\lambda \int\limits_{Q(x_0)} u^2 dxd\mathbf{y} + 2 \int\limits_{Q(x_0)} (\nabla u, \nabla u) dxd\mathbf{y} \geq 2(\mu - \lambda) \int\limits_{Q(x_0)} u^2 dxd\mathbf{y} \geq 0,
$$

i.e the function $I(x_0)$ monotonously decays in the interval $(0, a)$.

Substituting x_0 by a in Eq. (4.25), it is easy to see that $I'(a) = 0$ and $I(a) = 0$.

Finally, we prove that $I(x_0) \neq 0$ for $0 \leq x_0 < a$. Conversely, if one can find some x_0 such that $I(x_0) = 0$, then the restriction of u to the subdomain $Q(x_0)$ is a solution of the eigenvalue problem in $Q(x_0)$:

$$
-\Delta u = \lambda u \quad (x, \mathbf{y}) \in Q(x_0), \qquad u|_{\partial Q(x_0)} = 0.
$$

Multiplying this equation by u and integrating over the domain $Q(x_0)$ lead to

$$
\lambda \int\limits_{Q(x_0)} u^2 dxd\mathbf{y} = \int\limits_{Q(x_0)} (\nabla u, \nabla u) dxd\mathbf{y}.
$$

On the other hand, the Friedrichs-Poincaré inequality (4.26) yields

$$
\int\limits_{Q(x_0)} (\nabla u, \nabla u) dxd\mathbf{y} \geq \mu \int\limits_{Q(x_0)} u^2 dxd\mathbf{y},
$$

from which $\lambda \geq \mu$, in contradiction to the condition (4.10).

(iii) Thirdly, we establish the exponential decay (4.12) following the Maslov's method [152, 153]. The multiplication of the inequality (4.16) by $I'(x_0)$ yields

$$
((I')^2)' \leq c\gamma^2 (I^2)'.
$$

After integrating from x_0 to a, one gets

$$-(I'(x_0))^2 \leq -c\gamma^2 I^2(x_0),$$

where $I(a) = I'(a) = 0$ from Eq. (4.24). Taking in account that $I' < 0$, one deduces

$$-I'(x_0) \geq \sqrt{c}\gamma I(x_0).$$

Dividing by $I(x_0)$ and integrating from 0 to x_0 lead to Eq. (4.12) that completes the proof.

□

As in Sec. 4.2, no information about the basic domain V was used so that the Dirichlet boundary condition on ∂V can be replaced by arbitrary boundary condition on ∂V under which the Laplace operator in D remains self-adjoint.

4.4   Infinite branches

For an infinite branch, the exponential decay is still valid if the condition (4.10) is satisfied. However, it is worth noting that when the branch Q is infinite, the eigenspectrum of the Laplace operator is not necessarily discrete, and L^2-normalized eigenfunctions may not exist. For example, in a semi-infinite strip $D = [0,\infty) \times [0,\pi]$, the functions $f_n(x) = \sinh(\sqrt{n^2 - \lambda x})\sin(ny)$ satisfy the Laplacian eigenproblem (4.7), but their $L^2(D)$-norms are infinite.

As shown by Rellich, if the first eigenvalue $\mu_1(x)$ in the cross-section $\Omega(x)$ of an infinite branch Q goes to infinity as $x \to \infty$, then there exist infinitely many L^2-normalized eigenfunctions [181]. In two dimensions, the bound $\mu_1(x) = \pi^2/\ell(x)^2$ is related to the length $\ell(x)$ of the largest interval in the cross-section $\Omega(x)$. It is easy to see that the condition $\mu_1(x) \to \infty$ requires $\ell(x) \to 0$.

For infinite decreasing branches, eigenfunctions can be shown to decay *faster* than an exponential with any decay rate. We assume that the domain D can be separated into a basic domain V and an infinite decreasing branch Q so that the separation happens at $x = x_0$. The norm of Laplacian eigenfunctions satisfies

$$I(x) \leq I(x_0)\exp\left[-2\sqrt{\mu(x_0) - \lambda}\,(x - x_0)\right] \quad x \geq x_0,$$

where the new threshold $\mu(x_0) = \inf_{x_0 < x}\left[\frac{\pi}{\ell(x)}\right]^2$ increases with x_0, while the prefactor $I(x_0)$ also decays exponentially with x_0 according to Eq. (4.12). We assume that $\lim_{x \to \infty} \ell(x) = 0$. One can easily see that the value $\mu(x_0)$ tends to ∞ as $x_0 \to \infty$. Since the above estimate is applicable for any x_0, for a given decay rate, one can choose an appropriate value of x_0 so that the function $I(x)$ decays faster than the exponential with this rate along the branch $Q(x_0)$.

4.5 Three-dimensional domains

Our exponential estimate is also valid in three or higher dimensional domains (Sec. 4.3). For an example shown on Fig. 4.2, one can see that the shape of the cross-section $\Omega(x)$ can vary significantly. Whatever the shape of the branch is, the only relevant information for the exponential decay is the smallest eigenvalue μ in all cross-sections $\Omega(x)$.

For example, if $\Omega(x) = [0, b(x)] \times [0, c(x)]$, the first eigenvalue of the Laplace operator in $\Omega(x)$ is $\mu_1(x) = \frac{\pi^2}{b(x)^2} + \frac{\pi^2}{c(x)^2}$. One can bound the value of $\mu_1(x)$ from below by some μ ($\mu_1(x) > \mu, \forall x$) even if one of two sides $b(x)$ and $c(x)$ is extremely large ($b(x) \gg 1$ or $c(x) \gg 1$). As a consequence, when the basic domain V is large enough, there may exist some eigenvalues λ smaller than μ, whose eigenfunctions exponentially decay even along extremely-long-growing branches.

4.6 Discussion

From the main results in Section 4.3, if an eigenvalue λ with Dirichlet boundary condition in the domain D is below the smallest eigenvalue μ in all cross-sections $\Omega(x)$, the corresponding eigenfunction u decays exponentially along the branch Q. One can replace this condition on the eigenvalue λ in D by a stronger condition,

$$\kappa < \mu \tag{4.27}$$

on the eigenvalue κ in the basic domain V:

$$-\Delta\phi = \kappa\phi, \quad (x, \mathbf{y}) \in V, \qquad \phi|_{\partial V} = 0. \tag{4.28}$$

Using the *domain monotonicity* property of Dirichlet-Laplacian eigenfunctions (Theorem 2.1.6), the condition (4.27) is sufficient for the existence of the eigenvalue λ lying below μ (see Appendix D2). In practice, one can use the condition (4.27) for studying different branches Q attached to the same basic domain V so that the eigenvalue κ is computed only once.

In the next subsections, we will present several numerical simulations to show the accuracy of our exponential estimate and the behavior of the associated eigenfunctions u.

4.6.1 Numerical simulations

For numerical simulations, we consider several planar bounded domains D which are all composed of the unit square V as the basic domain and a branch Q of different shapes (See Fig. 4.3 for details) and make the computation by the following steps:

- *Step* 1:
  We solve the eigenproblem (4.7) with Dirichlet boundary condition in these domains by the package PDETools in Matlab.

- *Step* 2:
  After computing the eigenvalues and the corresponding eigenfunctions, we approximate the squared
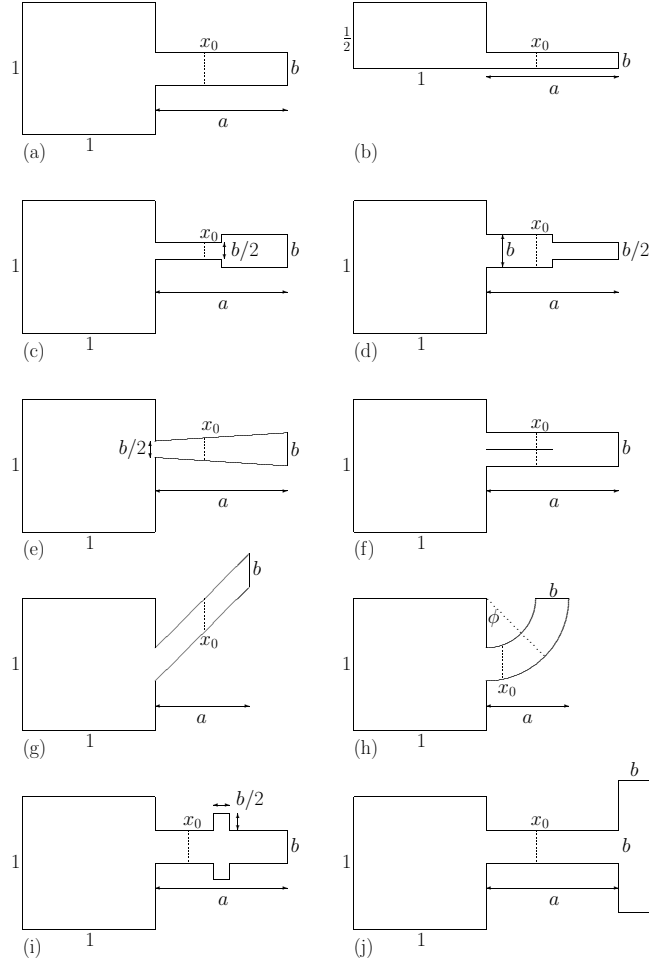
Figure 4.3:   The unit square (basic domain V) and several shapes of the branch Q: **(a)** rectangular branch;   **(b)** half of the domain 'a';   **(c)** narrow-then-wide channel;   **(d)** wide-then-narrow channel;   **(e)** increasing branch with the width linearly changing from $b/2$ to b;   **(f)** branch with a partial cut at the middle;   **(g)** parallelogram branch;   **(h)** circular branch;   **(i)** branch with a small broadening in the middle; **(j)** bifurcating branch. We set $a = 1$ and $b = 1/4$ in all cases, except 'g' and 'h', for which $a = 1/\sqrt{2}$ and $a = 5/8$, respectively. For shapes 'c', 'd', 'e', 'f', 'i' and 'j', the branching is up-shifted by $1/8$ in order to break the reflection symmetry (for cases 'g' and 'h', there is no shift because the branch itself has no reflection symmetry).

n	2a	2c	2d	2e	2f	2g	2h	2i	2j
1	19.33	19.66	19.39	19.64	19.58	19.39	19.33	19.39	19.39
2	47.53	48.95	47.58	48.94	48.59	47.86	47.54	47.58	47.58
3	49.32	49.35	49.33	49.35	49.33	49.32	49.32	49.33	49.33
4	78.83	78.75	77.85	78.90	78.54	78.85	78.84	77.85	77.85
5	93.12	97.87	94.41	97.69	97.09	94.48	93.12	94.40	94.41
6	98.70	98.71	98.67	98.71	98.66	98.71	98.71	98.67	98.67
7	126.1	127.8	125.2	127.9	127.3	126.9	126.1	125.2	125.2
8	128.0	128.3	128.0	128.3	128.0	128.1	128.0	128.0	127.7
9	151.7	166.1	154.1	165.8	164.6	158.5	151.6	150.4	128.0
10	167.7	167.8	167.8	167.8	167.8	167.7	167.7	156.8	153.6
11	167.8	177.5	176.5	177.1	177.0	175.8	171.8	167.8	167.8
12	175.3	193.9	182.3	196.9	183.4	196.5	176.1	176.7	167.8
13	191.7	196.1	196.1	197.5	195.3	197.4	196.4	185.3	176.7
14	196.4	197.5	197.4	239.6	197.4	229.6	197.4	197.1	185.4
15	197.4	245.1	229.1	244.4	244.1	245.9	204.5	197.4	195.2
16	218.8	246.8	246.0	246.8	246.2	250.7	235.5	218.5	195.5
17	245.7	254.3	249.2	254.1	252.4	256.7	245.8	242.8	197.4
18	246.7	256.7	256.6	256.7	256.6	284.6	250.5	246.1	214.8
19	252.5	284.7	269.6	285.8	259.3	285.5	256.7	250.6	229.0
20	256.6	286.3	285.9	286.3	283.2	304.1	278.7	256.6	245.9

Table 4.1:   First 20 eigenvalues of the Laplace operator in domains shown on Fig. 4.3.

L^2-norm of the eigenfunction u_n in the subregion $Q(x_0) = \{(x,y) \in Q \; : \; x_0 < x < a\}$ of the branch Q as

$$J_n(x_0) \equiv \int_{Q(x_0)} u_n^2(x,y)dxdy \simeq \sum_T \frac{S(T)}{3} \sum_{j=1}^3 u_n^2(x_j^T, y_j^T), \qquad (4.29)$$

where the sum runs over all triangles T of the mesh, $S(T)$ being the area of the triangle T, and $\{(x_j^T, y_j^T)\}_{j=1,2,3}$ its three vertices.

- *Step* 3:

  For checking whether the results are accurate or not, we firstly compute the function $J_n(x_0)$ at different levels k of mesh refinement (once the initial triangular mesh is generated by Matlab, each level of refinement consists in dividing each triangle of the mesh into four triangles of the same shape). Then, we checked the exponential decay of the function $J_n(x_0)$ as shown in the inequality (4.31).

Taking into account the exponential decay (4.12) for $I(x_0)$, one checks

$$J_n(x_0) = \int_{x_0}^a I_n(x) \; dx \le \int_{x_0}^a I_n(0)e^{-2\gamma_n x} \; dx \le \frac{I_n(0)}{2\gamma_n}e^{-2\gamma_n x_0}, \qquad (4.30)$$
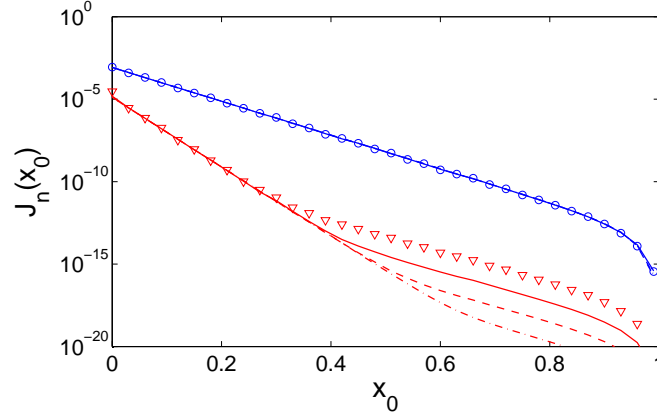
Figure 4.4:   Computation of $J_n(x_0)$ at different levels k of mesh refinement of the rectangular branch on Fig. 4.3a: $k = 3$ (symbols, 6848 triangles in the mesh), $k = 4$ (solid lines, 27392 triangles), $k = 5$ (dashed lines, 109568 triangles) and $k = 6$ (dash-dotted lines, 438272 triangles). For $n = 1$, all these curves fall onto each other, confirming the accurate computation which is independent of the mesh size. In turn, the curves for $n = 3$ coincide only for small x_0 but deviate from each other for larger x_0. The higher k, the closer the curve to the expected exponential decay (Fig. 4.5).

where

$$\gamma_n = \sqrt{\mu - \lambda_n},$$

and we take $c = 4$ even if the sufficient condition (4.14) is not satisfied. In what follows, we will check numerically the stronger inequality

$$J_n(x_0) \leq J_n(0)e^{-2\gamma_n x_0}, \tag{4.31}$$

from which (4.30) follows, because

$$J_n(0) = \int_0^a I_n(x) \ dx \leq I_n(0) \int_0^a e^{-2\gamma_n x} \ dx \leq \frac{I_n(0)}{2\gamma_n}.$$

It is worth stressing that the inequality (4.31) for the squared L^2-norm $J_n(x_0)$ in the subregion $Q(x_0)$ is a *weaker* result than the inequality (4.12) for the squared L^2-norm $I_n(x_0)$ in the cross-section $\Omega(x_0)$. However, the analysis of $I_n(x_0)$ would require an accurate computation of the restriction of an eigenfunction u_n, which was computed on a triangular mesh in D, onto the cross-section $\Omega(x_0)$. The resulting $I_n(x_0)$ would be less accurate than $J_n(x_0)$. For this reason, we will focus on checking the exponential decay of $J_n(x_0)$.

We have the following remarks about the error of the computation in Matlab.

Remark 4.6.1. *Since the eigenfunctions are analytic inside the domain, the error of the above approximation is mainly determined by the areas of triangles.*

Remark 4.6.2. *The higher k, the closer the resulting curve to the expected exponential decay.*

For illustrating the above remark, we give the following example.

Figure 4.5: The squared L^2-norm, $J_n(x_0)$, of four eigenfunctions with $n = 1, 8, 9, 13$ (symbols) for the rectangular branch on Fig. 4.3a. The estimate (4.31) with $\mu = \pi^2/(1/4)^2$ is plotted by dashed ($n = 1$), solid ($n = 8$) and dash-dotted ($n = 9$) lines. The estimate with $\mu = \pi^2/(1/8)^2$ is shown for $n = 8$ by dotted line.

Example 4.6.1. *In Fig. 4.4, we show the resulting curves for the rectangular branch (Fig. 4.3a). For the first eigenfunction, all the curves fall onto each other, i.e. $J_1(x_0)$ is independent of k, as it should be. In turn, the curves for $n = 3$ coincide only for small x_0 but deviate from each other for larger x_0.*

It means that even 6 levels of mesh refinement (i.e., a mesh with 438272 triangles) is not enough for an accurate computation of the integral $J_3(x_0)$. Among the 20 first eigenfunctions, similar deviations were observed for $n = 3, 4, 8, 10, 14, 15, 17$. The specific behavior of these eigenfunctions seems to be related to their reflection symmetry.

Remark 4.6.3. *For all following data sets, we checked the accuracy by performing computations with different k and presented only the reliable data with $k = 5$ (such meshes contain between 100000 and 170000 triangles, except for the case on Fig. 4.3f with 671744 triangles).*

4.6.2   Rectangular branch

In this domain, we consider the rectangular branch of width $b = \frac{1}{4}$ (see Fig. 4.3a). Since the value $\mu = 16\pi^2 \approx 157.91$, among the first 20 Dirichlet-Laplacian eigenvalues in Table 4.1, there are 9 eigenvalues λ_n below μ.

a. *Case $\lambda < \mu$:*

Among these eigenvalues, for the eigenmodes with $n = 1, 2, 5, 7, 9$ (illustrated by $n = 1, 9$), the estimate is very accurate. In this case, the decay rate $2\gamma_n$ is sharp and cannot be improved.

In turn, for the remaining eigenfunctions with $n = 3, 4, 6, 8$ (illustrated by $n = 8$), the function $J_n(x_0)$ is significantly smaller than the estimate.

For $x_0 < 0.4$, $J_8(x_0)$ decays as $J_8(0)\exp[-2\gamma_8' x_0]$, where $2\gamma_8' = 2\sqrt{4\mu - \lambda_8}$ is the improved decay rate

(for larger x_0, the computation is inaccurate as explained earlier and its result is not shown). For better understanding this behavior, we analyze the shape of the eigenfunction $u_8(x,y)$ as shown in Fig. 4.5b. This eigenfunction is anti-symmetric with respect to the horizontal line which splits the domain D into two symmetric subdomains. As a result, $u_8(x,y)$ is 0 along this line and it is thus a solution of the Dirichlet eigenvalue problem for each subdomain (Fig. 4.3b). The width of the branch in each subdomain is twice smaller so that one can apply the general estimate with $\mu' = 4\mu$. This is a special feature of all symmetric domains.

If we shift the branch upwards or downwards, the reflection symmetry would be broken, and the decay rate $2\gamma'_n$ would not be applicable any more. This example shows that the estimate (4.12) may not be sharp for certain eigenfunctions.

b. *Case $\lambda > \mu$:*

For the eigenfunction u_{13}, the corresponding eigenvalue λ_{13} is greater than μ and the exponential decay estimate (4.31) is not applicable (Fig. 4.3a) along the branch Q. One can expect this behavior from the shape of this eigenfunction u_{13} (Fig. 4.3b).

4.6.3 Narrow/wide and wide/narrow branches

In this section, the branch Q consists of two channels as shown on Fig. 4.3c and 4.3d. Any cross-section $\Omega(x)$ of the branch Q is a union of intervals. The first eigenvalue $\mu(x)$ in this cross-section is equal to $\frac{\pi^2}{l(x)^2}$, where $l(x)$ is the length of the largest interval in $\Omega(x)$. If we put $b = \max\limits_{x \in (0,a)} l(x)$, the bound μ of the exponential decay can be easily determined by $\mu = \frac{\pi^2}{b^2}$.

In Fig. 4.3c, the narrow channel of width $\frac{b}{2}$ is placed first for which $\mu = 16\pi^2$. Although the narrow channel strongly attenuates the amplitude of an eigenfunction u, it does not imply the exponentially decay with a hypothetical rate $2\sqrt{4\mu - \lambda}$ along the next wider channel of width b. For example, in Fig. 4.6, one can see that the theoretical estimate with the decay rate $2\sqrt{\mu - \lambda}$ is applicable for $n = 1$. However, with the rate $2\sqrt{4\mu - \lambda}$, the function $J_1(x)$ only decays exponentially up to $x_0 \approx 0.5$ and then starts to slow down in the interval $(0.5, 1)$. We also get the same behavior for $n = 9$.

In turn, if one puts the wider channel first, the eigenfunction decays exponentially with the decay rate $2\sqrt{\mu - \lambda}$ on the whole branch Q. Here, the value μ is still equal to $16\pi^2$. Moreover, if one consider a basic domain including both the unit square and the wider channel, the decay rate $2\sqrt{4\mu - \lambda}$ can be applicable along the narrow one (see details on Fig. 4.7).

Remark 4.6.4. *If the branch $Q = Q_1 \cup Q_2 \cup \cdots \cup Q_k$ can be decomposed into k channels $Q_1, Q_2, \ldots, Q_k$ with the corresponding widths $b_1, b_2, \ldots, b_k$ such that $b_1 \geq b_2 \geq \cdots \geq b_k$, the eigenfunction will exponentially decay with the rate $2\sqrt{\frac{\pi^2}{b_i^2} - \lambda}$ along the sub-branch $Q_i \cup Q_{i+1} \cup \cdots \cup Q_k$ for all $i = 1, \ldots, k$ when $\lambda < \frac{\pi^2}{b^2}$. Here, $b = \max\limits_{1 \leq i \leq k} b_i$.*

4.6.4 Increasing branch

Let us consider the branch Q as shown on Fig. 4.3e. One can see that $l(x)$ is an increasing function for $x \in (0, a)$. Although the condition (4.14) is not satisfied in Q, one can obtain the sharp exponential decay

Figure 4.6:   The squared L^2-norm, $J_n(x_0)$, of three eigenfunctions with $n = 1, 9, 12$ (symbols) for the narrow-than-wide branch on Fig. 4.3c. The estimate (4.31) with $\mu = \pi^2/(1/4)^2 = 16\pi^2$ is plotted for $n = 1$ by solid line. The hypothetical estimate with $\mu = \pi^2/(1/8)^2 = 64\pi^2$ is shown by dash-dotted ($n = 1$) and dashed ($n = 9$) lines. The vertical dotted line indicates the connection between two parts of the branch.

Figure 4.7:   The squared L^2-norm, $J_n(x_0)$, of three eigenfunctions with $n = 1, 3, 12$ (symbols) for the wide-than-narrow branch on Fig. 4.3d. The estimate (4.31) with $\mu = \pi^2/(1/4)^2 = 16\pi^2$ is plotted by dotted lines for $n = 1$ and $n = 3$. The combined estimate (for the wide part with $\mu = \pi^2/(1/4)^2$ and for the narrow part with $\mu = \pi^2/(1/8)^2 = 64\pi^2$) is shown by solid ($n = 1$), dashed ($n = 3$) and dash-dotted ($n = 12$) lines. The vertical dotted line indicates the connection between two parts of the branch.
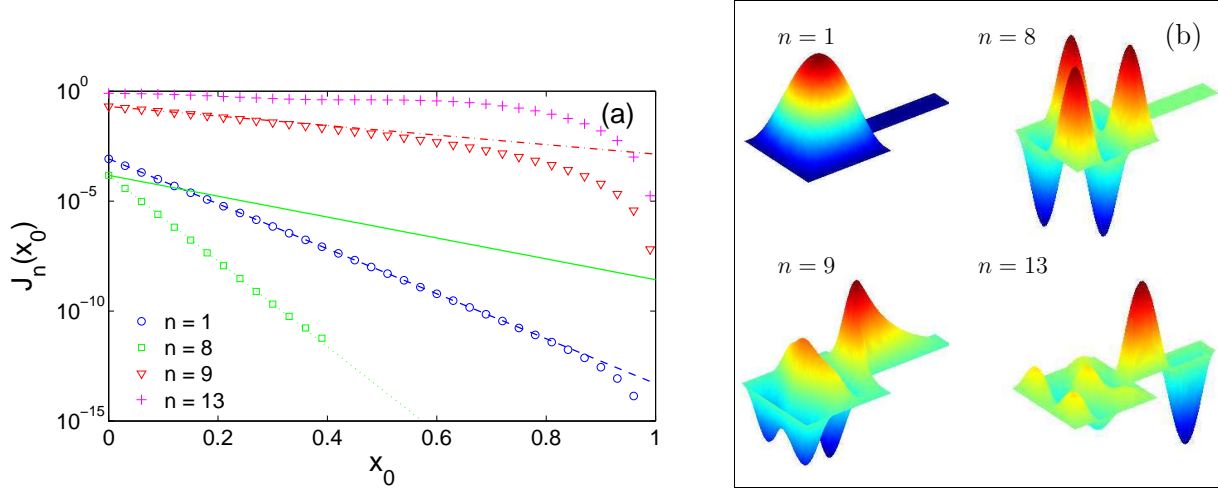
Figure 4.8: The squared L^2-norm, $J_n(x_0)$, of two eigenfunctions with $n = 1, 8$ (symbols) for the increasing branch on Fig. 4.3e. The estimate (4.31) with $\mu = \pi^2/(1/4)^2$ is plotted by solid ($n = 1$) and dash-dotted ($n = 8$) lines. The hypothetical estimate with $\mu = \pi^2/(1/8)^2$ is shown by dashed ($n = 1$) and dotted ($n = 8$) lines.

with the rate $2\sqrt{\mu - \lambda}$ (Fig. 4.8) for which $\mu = 16\pi^2$.

4.6.5 Branch with a cut

In this example, the rectangular branch Q has a horizontal cut at the middle of this branch. This branch is useful to check the robustness of the exponential estimate (4.31).

If the cut goes along the whole branch, Q can be decomposed into two similar rectangular branch of width $\frac{b}{2}$. In this case, one can apply the theoretical estimate (4.31) individually to each branch with the bound $\mu = \frac{4\pi^2}{b^2}$ of the exponential estimate.

If the cut goes partially on the branch with the length $a_{cut} \in (0, a)$, the value of μ is equal to $\frac{\pi^2}{b^2}$, and when $\lambda < \mu$, the theoretical estimate with the rate $2\sqrt{\mu - \lambda}$ is applicable along the branch Q.

In Fig. 4.9a, we show the squared L^2-norm $J_n(x)$ of three eigenfunctions u_n with $n = 1, 11, 12$ for $x \in (0, a)$. In case $n = 1$, we compare the exponential decay of $J_1(x)$ with the theoretical bound $\mu = \frac{\pi^2}{b^2} = 16\pi^2$ and another hypothetical bound $\mu = \frac{4\pi^2}{b^2} = 64\pi^2$. In this case, one can see that the theoretical bound is applicable but not sharp for all $x \in (0, a)$. In turn, the hypothetical bound is sharp but it works only up to $x = 0.4$, and the decay of the function $J_1(x)$ starts to slow down from 0.4 to 1. For cases $n = 11, 12$, the eigenvalues are greater than the theoretical bound $\mu = 16\pi^2$, and the exponentially decaying estimate is not applicable.

4.6.6 Tilted and circular branches

In this section, we consider two kinds of branches Q: tilted and circular branches.

In Fig. 4.3g, the branch Q is a rectangular branch tilted by the angle $\frac{\pi}{4}$. One may apply the exponential decay (4.31) with the bound $\mu = \frac{\pi^2}{b^2}$ in this case. Figure 4.10 shows the exponential decay of $J_1(x)$ for the first eigenfunction with $\mu = 16\pi^2$. However, since the branch Q was turned clockwise by $\frac{\pi}{4}$, the accurate
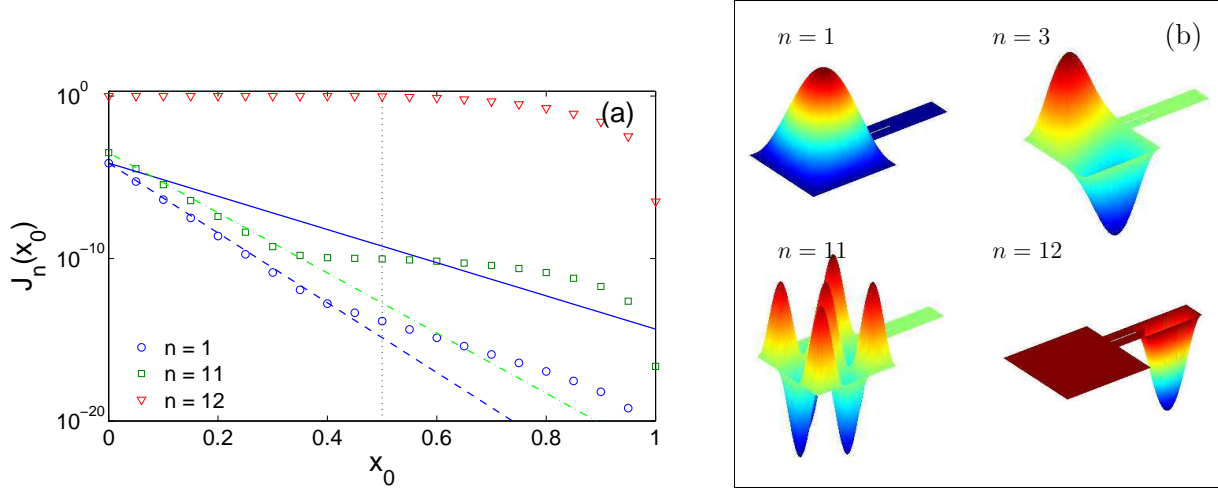
Figure 4.9: The squared L^2-norm, $J_n(x_0)$, of three eigenfunctions with $n = 1, 11, 12$ (symbols) for the branch with a cut on Fig. 4.3f. The estimate (4.31) with $\mu = \pi^2/(1/4)^2$ is plotted by solid ($n = 1$) and dash-dotted ($n = 11$) lines. The hypothetical estimate with $\mu = \pi^2/(1/8)^2$ for $n = 1$ is shown by dashed line. The vertical dotted line indicates the end of the cut.

width of Q is $b_{new} = \frac{b}{\sqrt{2}}$. From the estimate, one can expect the exponential decay of $J_n(x)$ with the new bound $\mu_{new} = 2\mu = 32\pi^2$. It is clear that the behavior of eigenfunctions does not depend neither on rotations of the domain, nor on the parameterization of the branch. Figure 4.10 shows the exponential decay with the latter threshold μ.

Next, we consider a circular branch Q with $b = 1$ and $a = \frac{5}{8}$ (Fig. 4.11). In this branch, the largest cross-section appears at $x = \frac{3}{8}$, and it is equal to $\frac{1}{2}$. For this reason, the bound $\mu = 4\pi^2$. From Table 4.1, one can see that the exponential decay is only applicable for the first eigenfunction (as $\lambda_2 > \mu$).

Naturally, the circular branch Q can be parameterized by the angle ϕ or by an arc, as illustrated in Fig. 4.3h. However, there is an ambiguity in the choice between arcs of various radii (e.g., inner, outer or middle arcs). Although the length of all these arcs is proportional to the angle ϕ, the proportionality coefficient enters in the decay rate. In Fig. 4.11, we made the computation for the inner arc of radius $r = 3/8$. The squared L^2-norm was plotted as a function of the curvilinear coordinate $x'_0 = r\phi$, with ϕ varying between 0 and $\pi/2$. For such a curvilinear parameterization, the width of the branch is constant, $b = 1/4$, so that there are 9 eigenvalues λ_n below $\mu = 16\pi^2$. One can see the exponential decay of the 9th eigenfunction on Fig. 4.11.

4.6.7 Branch with a small broadening

We consider a rectangular branch Q with a small broadening at the middle (Fig. 4.3i). In this case, the largest cross-section has the width $b = \frac{1}{2}$ so that threshold bound μ is equal to $4\pi^2 \approx 39.4784$. As a result, from the Table 4.1, only the first eigenvalue λ_1 is smaller than μ. One can see the exponential decay of the function $J_1(x)$ in Fig. 4.12.

What is the behavior of other eigenfunctions with the bound value $\mu' = 16\pi^2 \approx 157.91$ along the branch?
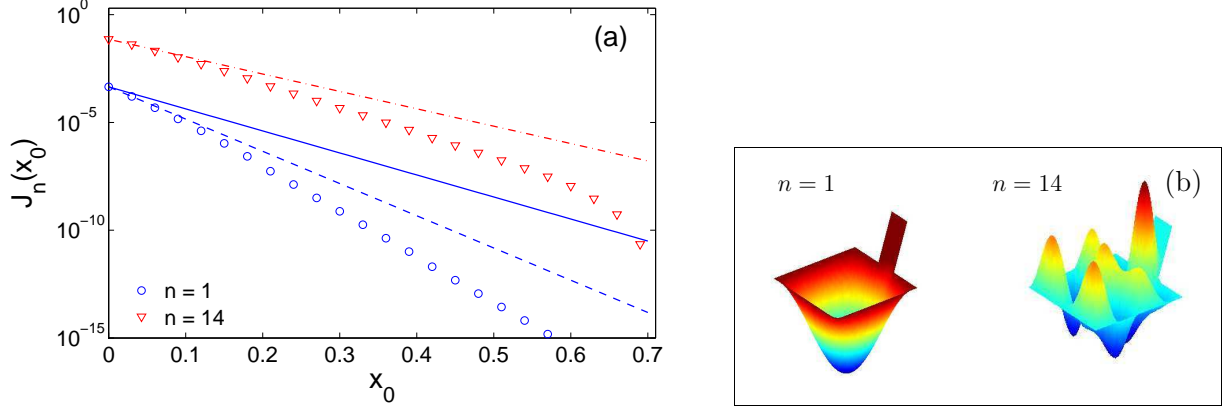
Figure 4.10: The squared L^2-norm, $J_n(x_0)$, of two eigenfunctions with $n = 1, 14$ (symbols) for the tilted branch on Fig. 4.3g. The formal estimate (4.31) with $\mu = \pi^2/(1/4)^2$ is plotted by solid line for $n = 1$. The improved estimate with $\mu = \pi^2/(1/4/\sqrt{2}))^2$ is shown by dashed ($n = 1$) and dash-dotted ($n = 14$) lines.
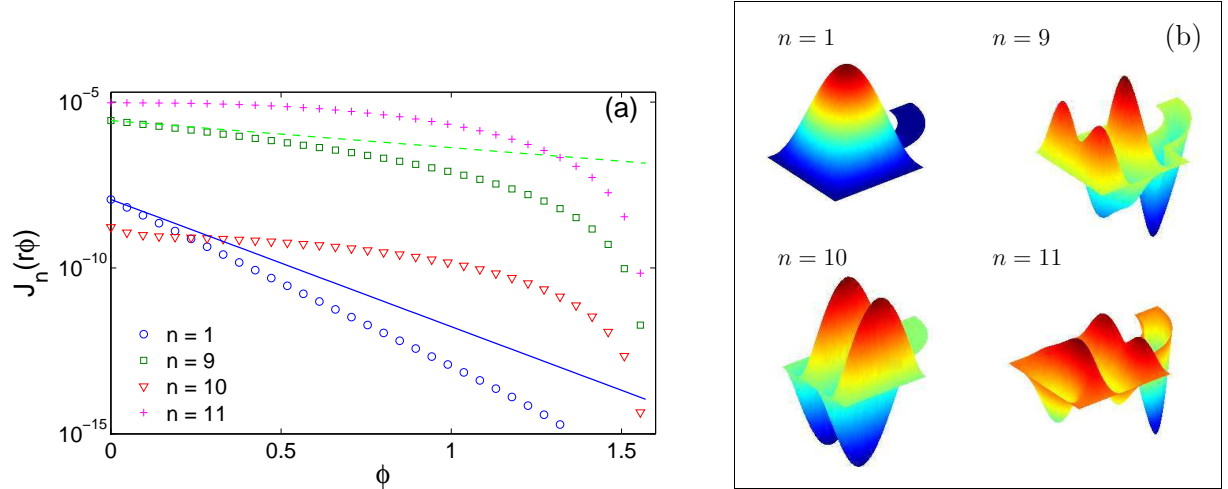
Figure 4.11: The squared L^2-norm, $J_n(x'_0)$, of four eigenfunctions with $n = 1, 9, 10, 11$ (symbols) for the circular branch on Fig. 4.3h. The estimate (4.31) with $\mu = \pi^2/(1/4)^2$ is plotted by solid ($n = 1$) and dashed ($n = 9$) lines. The curvilinear coordinate $x'_0 = r\phi$ with $r = 3/8$ and the angle ϕ varying from 0 to $\pi/2$, was used.
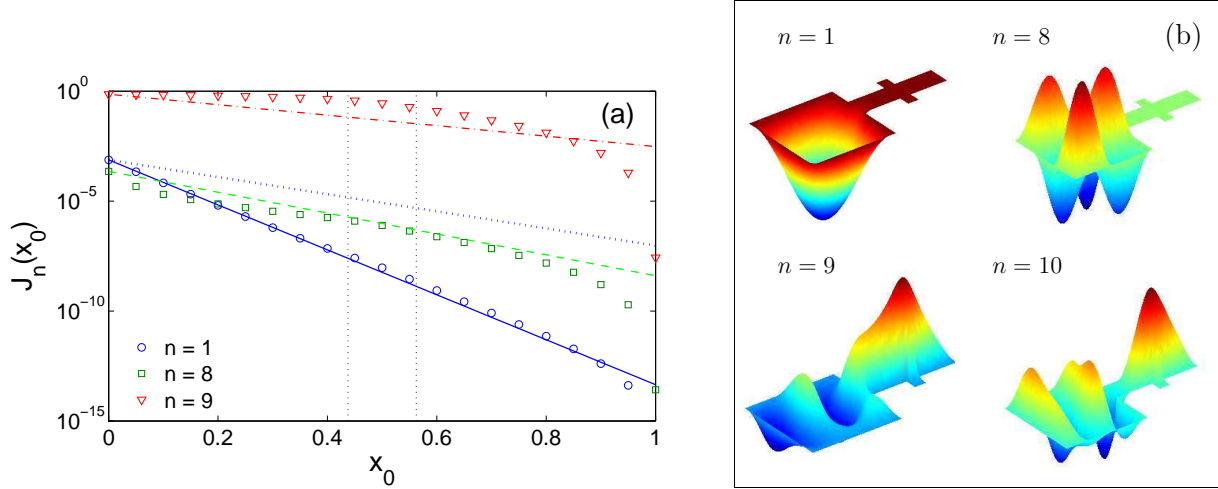
Figure 4.12:   The squared L^2-norm, $J_n(x_0)$, of three eigenfunctions with $n = 1, 8, 9$ (symbols) for the branch with a broadening on Fig. 4.3i. The estimate (4.31) with $\mu = \pi^2/(1/2)^2$ for $n = 1$ is shown by dotted line. The hypothetical estimate (4.31) with $\mu = \pi^2/(1/4)^2$ is plotted by solid ($n = 1$), dashed ($n = 8$) and dash-dotted ($n = 9$) lines. Vertical dotted lines indicate the position of the broadening.

From Table 4.1, only first 10 eigenvalues are smaller than μ'. Among these eigenmodes, the first 8 eigenfunctions u_n still decay exponentially along the branch except for the case $n = 9, 10$. In Fig. 4.12, we plot the function $J_n(0) \exp(-2\sqrt{\mu' - \lambda_n} x_0)$ for three eigenfunctions with $n = 1, 8, 9$. One can see that this function correctly capture the behavior of $J_n(x)$ for $n = 1, 8$, but fails to be its upper bound (there are some sets of $(0, a)$ where $J_n(x)$ exceeds this function).

In conclusion, although the small broadening of the branch does not significantly influence the exponentially decay of the first eigenfunctions, the upper bound may not be valid.

4.6.8   Bifurcating branch

In the last example, we consider a rectangular branch which bifurcates into two rectangular branches (Fig. 4.3j). In this case, the length of the largest cross-section is 1 so that $\mu = \pi^2 = 9.8696$. From the Table 4.1, all eigenvalues exceed μ so that the exponential decay with the theoretical bound μ is not applicable for all eigenfunctions. Now, what does happen for $J_n(x)$ if we use the hypothetical bound $\mu = 16\pi^2$ as for the rectangular branch? In Fig. 4.13, one can see that for the first eigenfunction, the function $J_1(x)$ can be well estimated by the exponential function $J_1(0) \exp(-2\sqrt{\mu' - \lambda_1} x_0)$ practically along the interval $(0, 1)$ except for a small deviation at the bifurcation region ($x_0 > 1$).

Similar behavior can be observed for other eigenfunctions up to $n = 7$. The larger the index n, the earlier the deviation from the exponential estimate appears (e.g., in case $n = 7$, the estimate works only for $x_0 < 0.3$). In turn, the 8th eigenfunction has no exponential decay in the branch as it is localized in the bifurcation region.
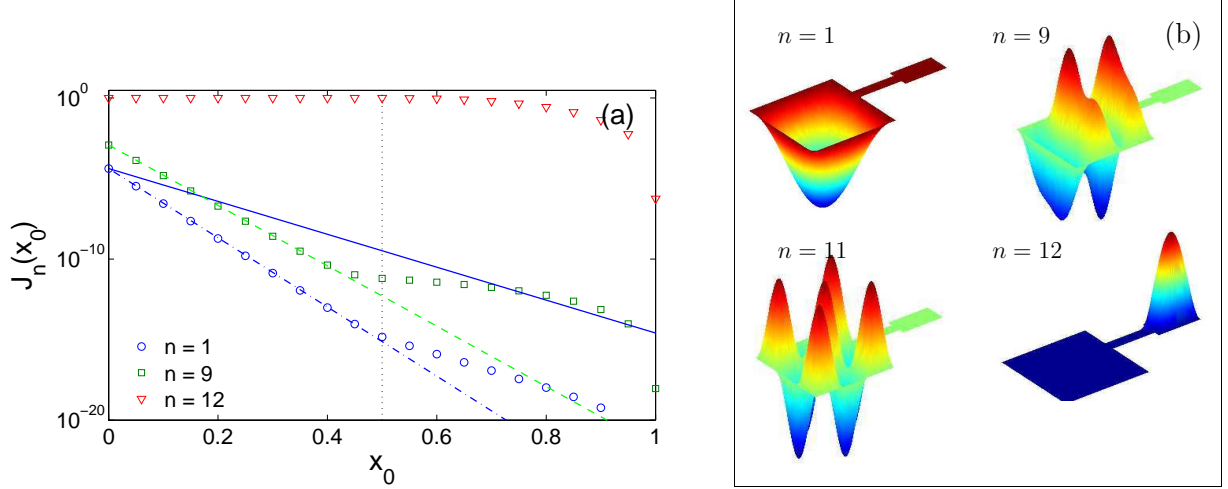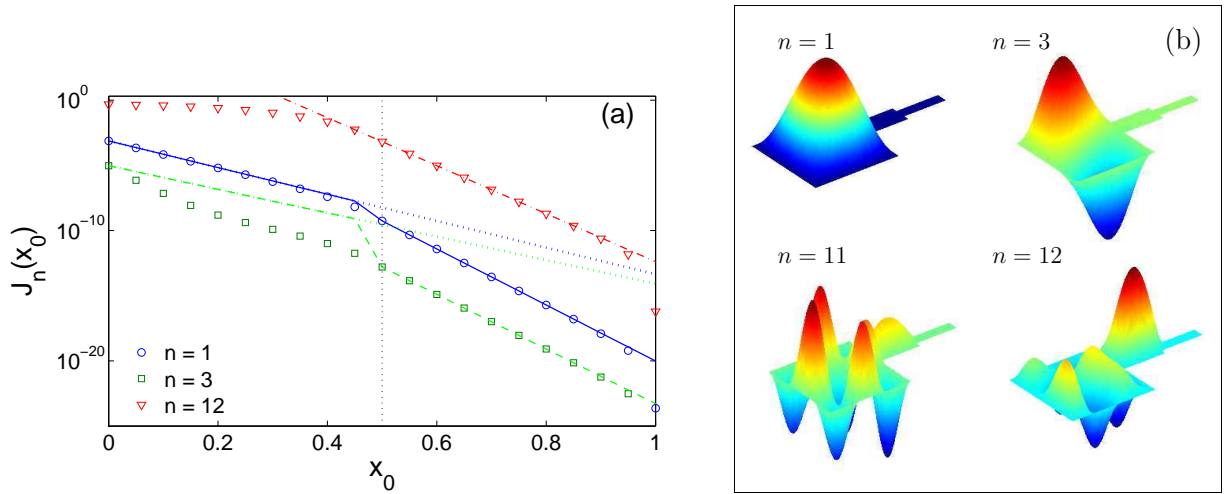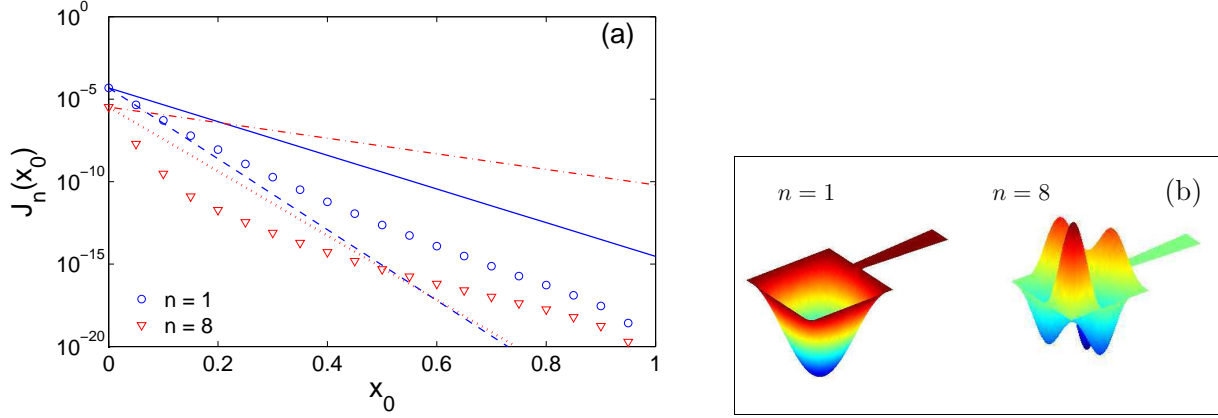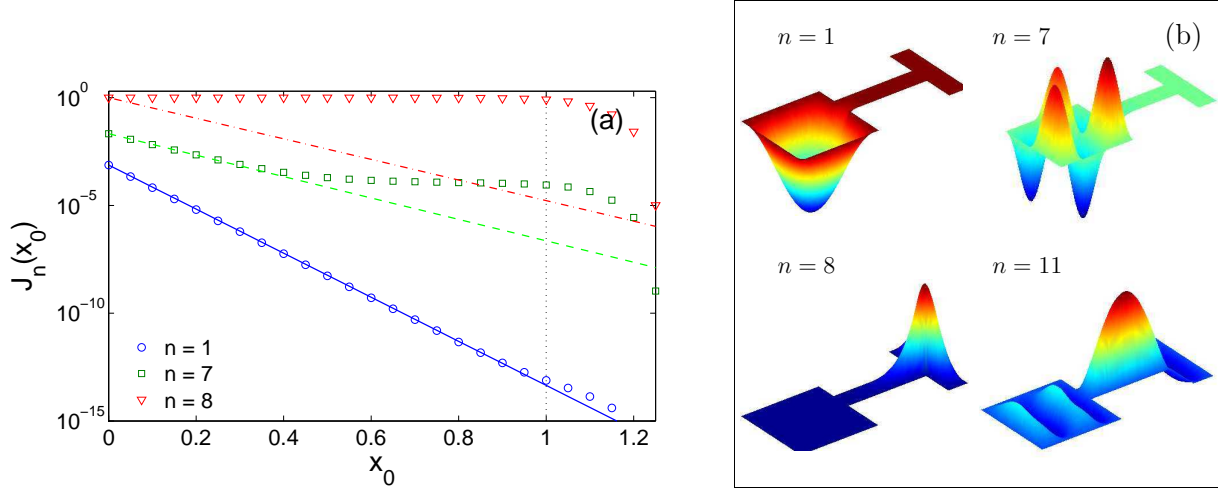
Figure 4.13: The squared L^2-norm, $J_n(x_0)$, of three eigenfunctions with $n = 1, 7, 8$ (symbols) for the bifurcating branch on Fig. 4.3j. The hypothetical estimate (4.31) with $\mu = \pi^2/(1/4)^2$ is plotted by solid ($n = 1$), dashed ($n = 7$) and dash-dotted ($n = 8$) lines. The vertical dotted line indicates the position of bifurcation.

4.6.9 Neumann boundary condition

The theoretical derivation in Sec. 4.3 essentially relies on the Dirichlet boundary condition on the branch boundary: $u|_{\partial Q} = 0$. This condition can be interpreted, e.g., as a rigid fixation of a vibrating membrane at the boundary, or as a perfect absorption of diffusing particles at the boundary. The opposite case of free vibrations of the membrane or a perfect reflection of the particles is described by Neumann boundary condition, $\partial u/\partial n|_{\partial Q} = 0$. Although the eigenvalue problem may look similar, the behavior of eigenfunctions is different. In particular, an extension of the results of Sec. 4.3 fails even in the simplest case of a rectangular branch, as illustrated on Fig. 4.14. Although the 8 first eigenvalues λ_n are below $\mu = 16\pi^2$ (Table 4.1), only some of them decay exponentially (e.g., with $n = 4$). This decay seems to be related to the reflection symmetry of the domain.

In Fig. 4.14, the eigenfunctions with $n = 4, 10$ are anti-symmetric so that they get the value 0 along the horizontal line at the middle of the branch. As a result, one can split Q into two symmetric sub-branches and apply the Dirichlet boundary condition along the splitting line. One can prove that with this mixed Dirichlet-Neumann boundary condition, there may exist the exponential decay of $J_n(x)$ along the whole branch by the following theorem.

Theorem 4.6.1. *Suppose that a bounded domain D can be decomposed into a basic domain V of arbitrary shape and a branch $Q = \{(x, \mathbf{y}) \in \mathbb{R}^{n+1} : 0 \leq x \leq a, |\mathbf{y}| < f(x)\}$ (as illustrated on Fig. 4.15) with a piecewise smooth function $f(x)$. We assume that the branch Q is not increasing i.e $f'(x) \leq 0$, $\forall x \in (0, a)$ and $f(a) = 0$ and denote*

$$J(x_0) = \frac{1}{\omega_n} \int\limits_{Q(x_0)} u(x, \mathbf{y})^2 dx d\mathbf{y} \tag{4.32}$$
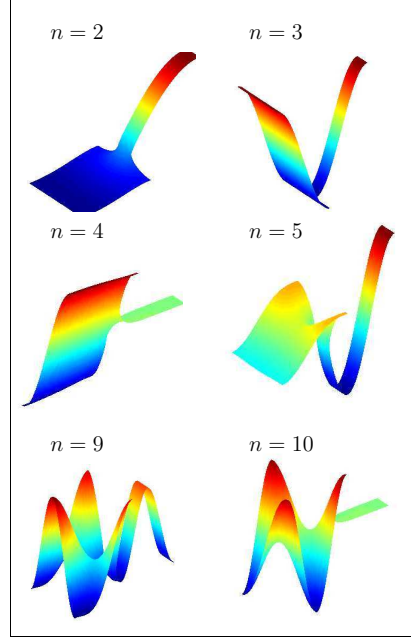
Figure 4.14:   Six eigenfunctions with $n = 2, 3, 4, 5, 9, 10$ for the rectangular branch (Fig. 4.3a) with Neumann boundary condition (the fundamental eigenfunction with $n = 1$ is constant and not shown).
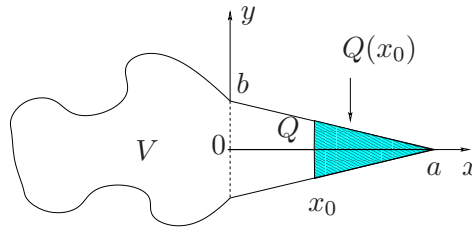
Figure 4.15:   A bounded domain D is the union of a basic domain V of arbitrary shape and a branch $Q = \{(x, \mathbf{y}) \in \mathbb{R}^{n+1} : 0 \leq x \leq a, |\mathbf{y}| < f(x)\}$, where $f'(x) \leq 0$ and $f(a) = 0$. Here, one imposes Neumann boundary condition on the boundary ∂Q.

where $Q(x_0) = \{(x, \mathbf{y}) \in \mathbb{R}^{n+1} : x_0 \leq x \leq a, |\mathbf{y}| < f(x)\}$, and ω_n is the volume of the unit n-dimensional ball. We consider the Laplacian eigenproblem with Neumann boundary condition on the boundary ∂Q. Then, if an eigenvalue λ is smaller than the smallest Dirichlet-Laplacian eigenvalue μ over the cross-section $\Omega(x)$ of Q, the corresponding eigenfunction u exponentially decays along the branch:

$$J(x_0) \leq J(0)\exp(-\sqrt{2}\sqrt{\mu - \lambda}x_0), \quad \forall x \in [0, a). \tag{4.33}$$

Proof. Firstly, from the definition of $J(x)$ and the parameterization of branch Q, one gets

$$J(x_0) = \int_0^a \int_0^{f(x)} r^{n-1}u^2(x, r)dr \tag{4.34}$$

$$J'(x_0) = -\int_0^{f(x_0)} r^{n-1}u^2(x_0, r)dr \tag{4.35}$$

$$J''(x_0) = \int_0^a \int_0^{f(x_0)} r^{n-1}u(x_0, r)dr\frac{\partial u}{\partial x} - u^2(x_0, f(x_0))f'(x_0)f^{n-1}(x_0) \tag{4.36}$$

Using the Green's formula and the boundary condition on ∂Q, one has

$$\int_{Q(x_0)} u\Delta u dx d\mathbf{y} + \int_{Q(x_0)} |\nabla u|^2\, dx d\mathbf{y} = \int_{\partial Q(x_0)} u\frac{\partial u}{\partial n}dS = -\omega_n \int_0^{f(x_0)} r^{n-1}u(x_0, r)\frac{\partial u}{\partial x}dr \tag{4.37}$$

where $\frac{\partial u}{\partial n} = -\frac{\partial u}{\partial x}$ over the cross-section $\Omega(x_0)$. Finally, using Friedrichs-Poincaré again, one can show that

$$\begin{aligned}
J''(x_0) &= \frac{2}{\omega_n}\int_{Q(x_0)}\left(u\Delta u + |\nabla u|^2\right)dx d\mathbf{y} - u^2(x_0, f(x_0))f'(x_0)f^{n-1}(x_0) \\
&\geq \frac{2\,(\mu - \lambda)}{\omega_n}\int_{Q(x_0)} u^2(x, \mathbf{y})dx d\mathbf{y} = 2\,(\mu - \lambda)\,J(x_0).
\end{aligned} \tag{4.38}$$

Secondly, the condition $f(a) = 0$ implies $J(a) = J'(a) = 0$. From the initial assumption that $f(a) = 0$ and $f'(x_0) \leq 0$, one can show that $J(x_0) \neq 0$ and $J'(x_0) < 0$ for all $x_0 \in (0, a)$.

Finally, by applying Maslov's inequalities, one gets the exponential estimate (4.33) of $J(x_0)$ in the same way as in Section 4.3. □

4.6.10 Expelling from the branch

It is important to stress that the "smallness" of an eigenfunction in the branch and its exponential decay are different notions which should not to be confused. In fact, the eigenfunction can be small in the branch either due to a rapid exponential decay, or because of the small constant $I_n(0)$ or $J_n(0)$ in front of the estimate. For instance, Fig. 4.11a shows the behavior of $J_{10}(x_0)$ without an exponential decay, but the

eigenfunction is nevertheless small (Fig. 4.11b). Another example on Fig. 4.5a with $n = 9$ illustrates the opposite situation: the eigenfunction decays exponentially along the branch but it does not look small.

4.7 Localization in elongated polygons

In this section, we show the existence of localized eigenfunctions in elongated polygons for which the ratio between their diameter and their inradius is quite large. We first construct a right triangle in which low-frequency localization happens for Dirichlet boundary condition, and then we extend this idea to general elongated polygons.

4.7.1 Localization in triangles

4.7.1.1 Estimate for the first eigenvalue

We consider a rectangle of sides a and b on which a right triangle with legs c and d is constructed as shown on Fig. 4.16. Without loss of generality, we assume $a \geq b$. Note that the triangle is uniquely defined by one of the legs (e.g., d), while the other leg is given as $c = ad/(d - b)$.

The vertical line at $x = a$ splits the triangle Ω into two subdomains, Ω_1 (a trapeze) and Ω_2 (a triangle). We call λ_1 the first eigenvalue of the Laplace operator in Ω with Dirichlet boundary condition:

$$\Delta u + \lambda_1 u = 0, \qquad u_{|\partial \Omega} = 0. \tag{4.39}$$

For fixed a and b, we are searching for a sufficient condition on d under which

$$\lambda_1 < \pi^2/b^2. \tag{4.40}$$

If this condition is satisfied, from Theorem 4.3.1, the eigenfunction u becomes localized in Ω_1, i.e., it decays exponentially fast in the subdomain Ω_2 (see Fig. 4.16). The condition (4.40) can be replaced by a weaker condition

$$\gamma_1 < \pi^2/b^2. \tag{4.41}$$

where γ_1 is the first eigenvalue of the Laplace operator in Ω_1 with Dirichlet boundary condition. In fact, since $\lambda_1 < \gamma_1$, (4.41) implies (4.40). The eigenvalue γ_1 can be found as

$$\gamma_1 = \inf_{v \in H_0^1(\Omega_1)} \gamma(v) \tag{4.42}$$

where

$$\gamma(v) = \frac{(\nabla v, \nabla v)_{L^2(\Omega_1)}}{(v, v)_{L^2(\Omega_1)}}. \tag{4.43}$$

Using the same technique as in Chapter 5, we search for a trial function v such that $\gamma(v) < \pi^2/b^2$, in
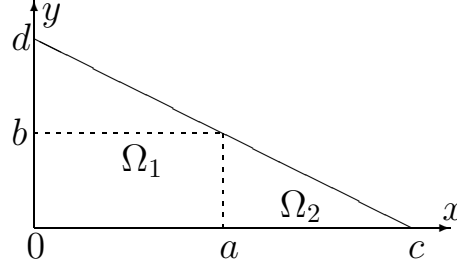
Figure 4.16: A right triangle Ω which can be decomposed into a trapeze Ω_1 and a right triangle Ω_2.

order to get $\gamma_1 < \pi^2/b^2$ and thus $\lambda_1 < \pi^2/b^2$. We consider the trial function

$$v(x,y) = y\left(y - d + \frac{d-b}{a}x\right)\sin(\pi x/a) \tag{4.44}$$

which satisfies Dirichlet boundary condition on the boundary of Ω_1. We consider the conditions under which

$$Q = \frac{\pi^2}{b^2}(v,v)_{L^2(\Omega_1)} - (\nabla v, \nabla v)_{L^2(\Omega_1)} > 0. \tag{4.45}$$

The direct integration yields

$$Q = \frac{b^5}{720\pi^2 a}P(e), \qquad P(x) = \sum_{j=0}^{5}(k^2 A_j - B_j)x^j, \tag{4.46}$$

where $e = (d/b) - 1$, $k = a/b$ and

$$
\begin{aligned}
A_5 &= 2\pi^4 - 15\pi^2 + 45 \approx 91.7741 & B_5 &= 2\pi^4 + 15\pi^2 - 45 \approx 297.8622 \\
A_4 &= 6(2\pi^4 - 10\pi^2 + 15) \approx 666.7328 & B_4 &= 6(2\pi^4 + 10\pi^2 - 15) \approx 1671.0854 \\
A_3 &= 30(\pi^4 - 4\pi^2 + 3) \approx 1827.9202 & B_3 &= 30(\pi^4 + 3\pi^2) \approx 3810.5371 \\
A_2 &= 20(2\pi^4 - 9\pi^2 + 9) \approx 2299.8348 & B_2 &= 20(2\pi^4 + 3\pi^2) \approx 4488.5399 \\
A_1 &= 30(\pi^4 - 6\pi^2) \approx 1145.7439 & B_1 &= 30\pi^4 \approx 2922.2727 \\
A_0 &= 12(\pi^4 - 10\pi^2) \approx -15.4434 & B_0 &= 12\pi^4 \approx 1168.9091
\end{aligned}
\tag{4.47}
$$

Note that all $B_j > 0$ and $A_j > 0$ except for $A_0 < 0$. From the fact that $A_j < B_j$, one has $P(x) < 0$ for all $x > 0$ when $k = 1$ (i.e., $a = b$). The sign of Q is determined by the sign of $P(e)$. We have therefore two parameters, e and k, which determine the localization. The condition $Q > 0$ can be rewritten as

$$P(e) = k^2 P_A(e) - P_B(e) > 0, \tag{4.48}$$

where $P_A(e)$ and $P_B(e)$ are two polynomials of the fifth order determined by the coefficients A_j and B_j, respectively:

$$P_A(e) = \sum_{j=0}^{5} A_j e^j, \qquad P_B(e) = \sum_{j=0}^{5} B_j e^j, \tag{4.49}$$

Since $P_B(e) > 0$ for all $e \geq 0$, the above condition is equivalent to two inequalities:

$$P_A(e) > 0, \quad k^2 > \frac{P_B(e)}{P_A(e)}. \tag{4.50}$$

One can check that $P_A(e_0) = 0$ at $e_0 \approx 0.0131$ and $P_A(e) > 0$ iff $e > e_0$. We get therefore a explicit *sufficient* condition for low-frequency localization in right triangles

$$e > 0.0131, \quad k^2 > \frac{P_B(e)}{P_A(e)}. \tag{4.51}$$

We remind that this condition is not necessary (as we deal with an estimate for the first eigenvalue). For a given a and b (i.e., k), the above inequalities determine the values of e (and thus the leg d) for which localization occurs. Alternatively, one can express a and b from the legs c and d (and parameter e) as

$$a = \frac{ce}{e + 1}, \qquad b = \frac{d}{e + 1} \tag{4.52}$$

from which $k = ce/d$. For given c and d, one can vary e to get a family of inclosed rectangles (of sides a and b). The above inequalities can be reformulated as

$$e > e_0 \quad \Leftrightarrow \quad b < \frac{d}{e_0 + 1}, \quad k^2 > \frac{P_B(e)}{P_A(e)} \quad \Leftrightarrow \quad \frac{c}{d} > \frac{\sqrt{P_B(e)}}{\sqrt{P_A(e)}\, e} = f(e) \tag{4.53}$$

Since the function $f(e)$ turns out to be monotonously decreasing (checked numerically), the last inequality yields

$$e > f^{-1}(c/d) \quad \Leftrightarrow \quad b < \frac{d}{f^{-1}(c/d) + 1} \tag{4.54}$$

where f^{-1} denotes the inverse of the function $f(e)$. This condition determines the choice of the inscribed rectangle (the size b) for a given triangle.

Let us now consider the "worst" case $c = d$, for which a numerical computation yields $f^{-1}(1) \approx 1.515$ so that

$$b < \frac{d}{2.515} \approx 0.3976 \, d \tag{4.55}$$

This example shows that one can always inscribe a rectangle in such a way that $\lambda < \pi^2/b^2$. Of course, the "branch" Ω_2 in which an exponential decay of the eigenfunction is expected, is small. For this reason, this decay will not be "visible".

4.7.1.2   Numerical computation

We visualize our theoretical results by two following examples.

a. Example 1

In this example, we take $b = 1$ and $a = 2$ (i.e, $k = 2$), for which the inequalities (4.51) allow us to estimate the threshold e for localization as $e \approx 0.3352$ (see on Fig. 4.17). A direct numerical solution of the eigenvalue problem in Ω_1 gives a smaller threshold 0.32 for which $\gamma_1 = \pi^2$. The comparison shows
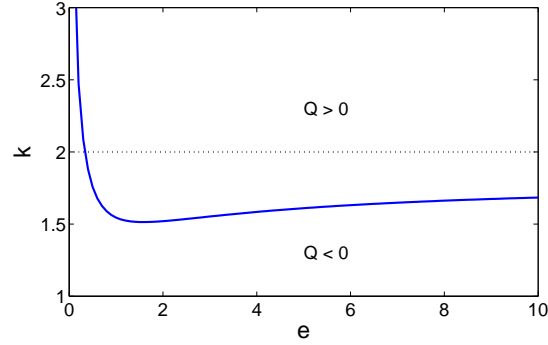
Figure 4.17: The diagram in the space of parameters e and k for positive and negative signs of Q which correspond to localization and non-localization regions. For a given k (e.g., $k = 2$ shown by horizontal dotted line), one can determine the values of e, for which localization occurs.

that our estimate is indeed accurate.

For $e = 0.32$, the numerical solution yields $\lambda_1 \approx 9.2719$ while $\gamma_1 \approx 9.8405$. As expected, the eigenvalue λ_1 is smaller than γ_1. On Fig. 4.18, the first eigenfunction u_1 is shown to be localized in the domain Ω_1.

(a) u_1 (b) u_2 (c) u_3 (d) u_4
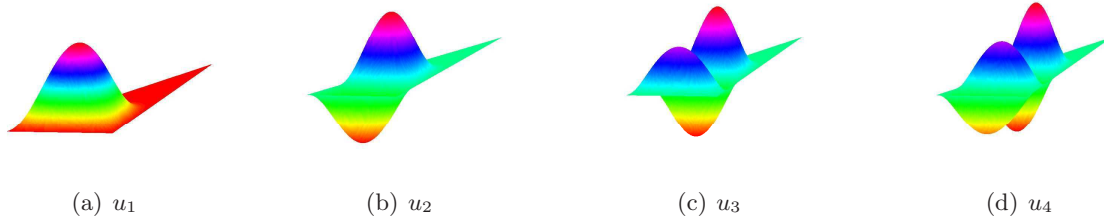
Figure 4.18: Several Dirichlet eigenfunctions in the right triangle Ω with $a = 2$, $b = 1$ and $e = 0.32$ for which $c = 8.25$ and $d = 1.32$. The four first eigenvalues are $\lambda_1 \approx 9.2719$, $\lambda_2 \approx 12.9094$, $\lambda_3 \approx 16.6383$ and $\lambda_4 \approx 20.5730$. The first eigenfunction u_1 is localized in the trapeze Ω_1 and decays exponentially along the subdomain Ω_2.

b. Example 2

Another example is $a = 4$, $b = 1$, for which we can estimate the threshold as $e \approx 0.0782$. Using the numerical computation in Matlab, one can get the direct solution $e \approx 0.07$ for $\gamma_1 = \pi^2$ and $e \approx 0.025$ for $\lambda_1 = \pi^2$. The first Dirichlet eigenfunction u_1 decays exponentially along the triangle Ω_2 and becomes localized in the subdomain Ω_1 (Fig. 4.19).

The above numerical computation confirms theoretical results. Although our technique is applicable for the first eigenfunction u_1, one can generalize the idea to other eigenfunctions. In particular, one can explain the existence of localized eigenmodes in elongated isosceles triangles (Fig. 4.20).

(a) u_1 (b) u_2 (c) u_3 (d) u_4
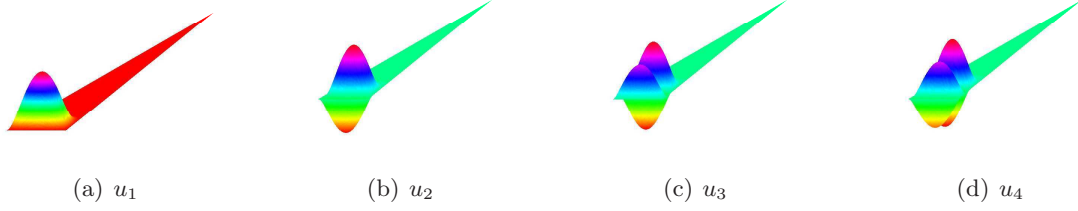
Figure 4.19: Several Dirichlet eigenfunctions in the right triangle Ω with $a = 4$, $b = 1$ and $e = 0.07$ for which $c = 61.1429$ and $d = 1.07$. First 4 eigenvalues are $\lambda_1 \approx 9.6834$, $\lambda_2 \approx 10.5395$, $\lambda_3 \approx 11.2851$ and $\lambda_4 \approx 11.9796$. Since $\lambda_1 < \pi^2$, the first eigenfunction u_1 is localized in the trapeze Ω_1 and decays exponentially along the subdomain Ω_2. The eigenfunctions u_2, u_3 and u_4 are also concentrated in Ω_1.

(a) u_1 (b) u_2 (c) u_3 (d) u_4
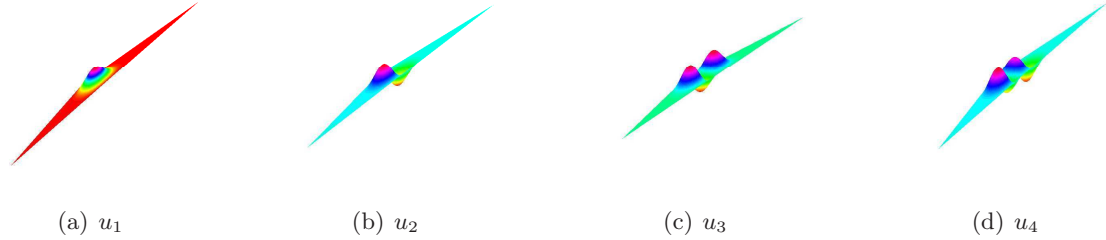
Figure 4.20: Localized modes in an elongated isosceles triangle.

4.7.2   Localization in elongated polygons

Motivated by the above results, we construct elongated polygons of n vertices for each positive integer n ($n \geq 3$) for which there exist low-frequency localized eigenfunctions.

We fix a positive integer $n \geq 3$. If $n = 3$, one can construct an elongated triangle as shown in the previous section. Without loss of generality, we suppose that $n > 3$ and a, b are given parameters.

We consider an elongated polygon $P^{(n)}$ as shown in Fig. 4.21 such that k points P_i do not depend on two parameters c and d. The parameter d varies in the interval (b, ∞) and $c = ad/(d - b)$.

By the domain monotonicity theorem (Theorem 2.1.6), the first Dirichlet eigenvalue of the Laplace operator in the polygon $P^{(n)}$ is smaller than the first Dirichlet eigenvalue in the right triangle $\Omega = \Omega_1 \cup \Omega_2$. Using the results of the previous section, one can estimate a threshold for the parameter e by condition (4.51) for which the first Dirichlet eigenvalue in $P^{(n)}$ does not exceed π^2/b^2 and the associated eigenfunction decays exponentially along the subdomain Ω_2.

For instance, on Figs. 4.22 and 4.23, we illustrate low-frequency localization in elongated quadrangles and hexagons. In agreement with our results, the first eigenfunction u_1 is localized in the polygons $P^{(4)}$ and $P^{(6)}$.

In summary, we have already shown how to construct an elongated polygon of n vertices for arbitrary positive integer $n \geq 3$. It shows that low-frequency localization can occur in very simple domains such as elongated polygons. In the above examples, localization depends on the ratio between the inradius and the diameter of an elongated polygon (see more on Fig. 4.24). The larger this ratio is, more localized
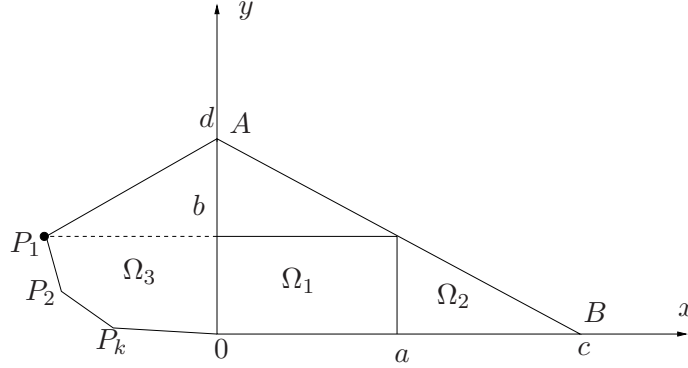
Figure 4.21: An elongated polygon P with n vertices $\{0, B, A, P_1, P_2, \ldots, P_k\}$, where $k = n - 3$. Here, Ω_3 is the polygon including $n - 1$ vertices $\{0, A, P_1, P_2, \ldots, P_k\}$. Ω_1 and Ω_2 are a trapeze and a right triangle as shown in Fig. 4.16.

(a) u_1 (b) u_2 (c) u_3 (d) u_4
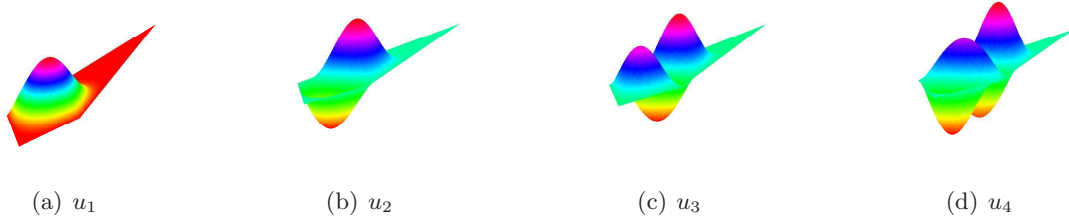
Figure 4.22: Low-frequency localization in an elongated quadrangle $P^{(4)}$.

eigenfunctions are.

4.8 Conclusion

We have studied the behavior of the Laplace operator eigenfunctions in a large class of domains composed of a basic domain of arbitrary shape and a branch Q which can be parameterized by a variable profile $\Omega(x)$. We have rigorously proved that each eigenfunction whose eigenvalue λ is smaller than the threshold $\mu = \inf\{\mu_1(x)\}$, exponentially decays inside the branch, where $\mu_1(x)$ is the first eigenvalue of the Laplace operator in the cross-section $\Omega(x)$. In general, the decay rate was shown to be at least $\sqrt{2}\sqrt{\mu - \lambda}$. For non-increasing branches, the decay rate $2\sqrt{\mu - \lambda}$ was derived and shown to be sharp for an appropriate parameterization of the branch. The exponential estimate is applicable in any dimension and for finite and infinite branches. In the latter case, the condition $\mu_1(x) \to \infty$ as $x \to \infty$ is imposed to ensure the existence of L^2-normalized eigenfunctions. Since the derivation did not involve any information about the basic domain V, the exponential estimate is applicable for arbitrary V with any boundary condition on ∂V for which the Laplace operator in D is still self-adjoint. In turn, the Dirichlet boundary condition on the branch boundary was essential.

(a) u_1 (b) u_2 (c) u_3 (d) u_4
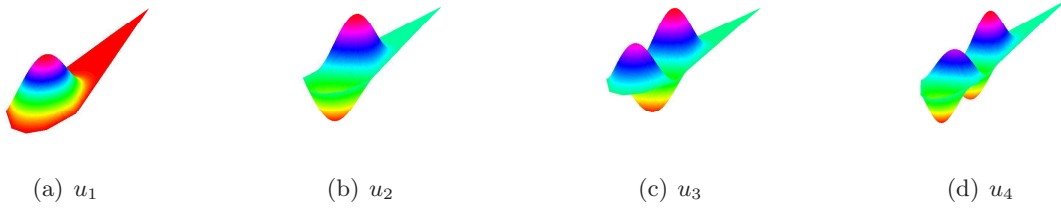
Figure 4.23: Low-frequency localization in an elongated hexagon $P^{(6)}$.

The numerical simulations have been used to illustrate and extend the theoretical results. It was shown that the sufficient condition $\lambda < \mu$ is not necessary, i.e., the eigenfunctions may exponentially decay even if $\lambda > \mu$. However, in this case, the decay rate and the range of its applicability strongly depend on the specific shape of the branch. For all numerical examples, the sharp decay rate $2\sqrt{\mu - \lambda}$ was correct, even if the condition (4.14) for non-increasing branches was not satisfied. In future, it is tempting either to relax this condition, or to find counter-examples, for which the sharp decay is not applicable.

For any positive integer $n \geq 3$, one can construct many elongated polygons of n vertices in which there exist low-frequency localized eigenfunctions. This localization depends on the ratio between the inradius and the diameter of elongated polygons. Although our approach was focused on the first Dirichlet eigenmode, these results can be extended to other eigenfunctions.

Basing on our approach in this chapter, we will study in chapter 5 trapped modes of the Laplace operator in finite quantum waveguides. Some other discussions can be found in [60, 161].

(a) u_1 (b) u_2 (c) u_3 (d) u_4

(e) u_1 (f) u_2 (g) u_3 (h) u_4

(i) u_1 (j) u_2 (k) u_3 (l) u_4
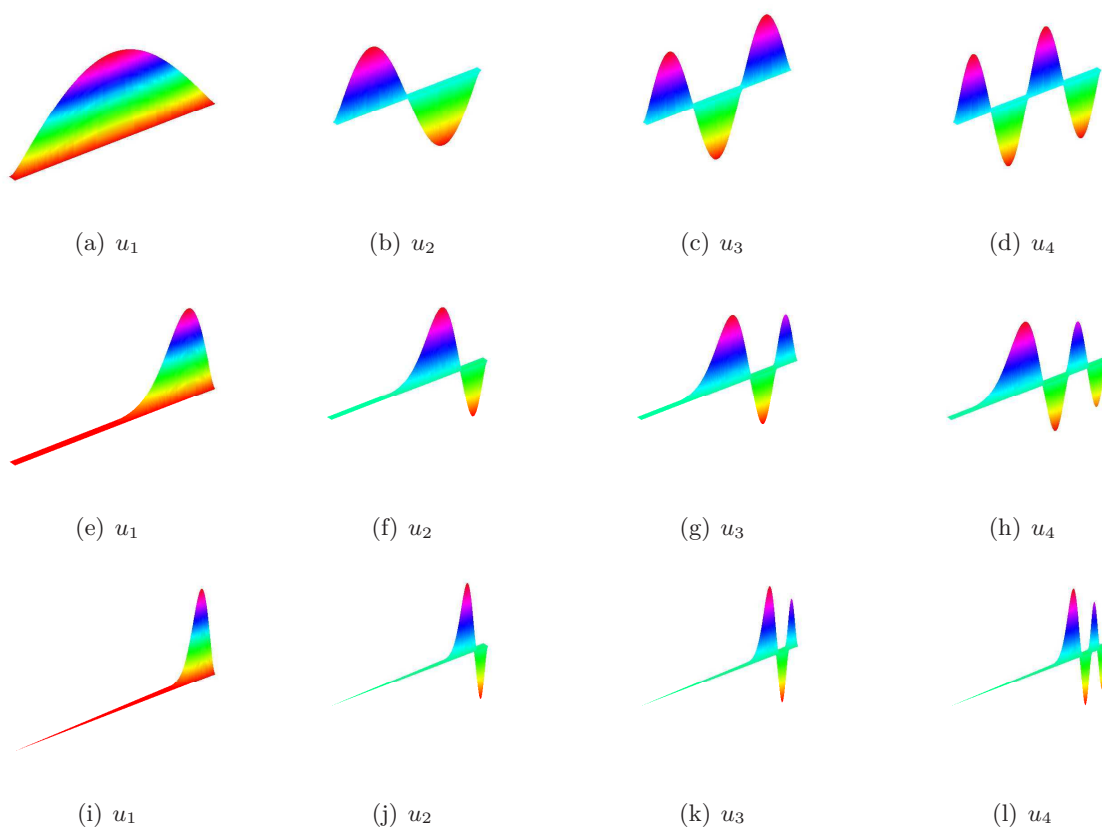
Figure 4.24: The first four Dirichlet eigenfunctions for three elongated domains: (first row) rectangle of size 25×1; (second row) right trapezoid with bases 1 and 0.9 and height 25 which is very close to the above rectangle; (last row) right triangle with edges 25 and 1 (half of the rectangle). There is no localization for the first shape, while the first eigenfunctions for the second and third domains tend to be localized.

Chapter 5

Trapped modes in finite waveguides

In the previous chapter, we have discussed the exponential decay of Laplacian eigenfunctions in a domain with branches when the corresponding eigenvalue is smaller than some threshold. In this chapter, we will analyze sufficient conditions for trapping an eigenfunction.

The eigenstates of an electron in an infinite quantum waveguide (e.g., a bent strip or a twisted tube) are often trapped or localized in a bounded region that prohibits the electron transmission through the waveguide at the corresponding energies. We revisit this statement for resonators with long but finite branches that we call "finite waveguides". Although the Laplace operator in bounded domains has no continuous spectrum and all eigenfunctions have finite L^2 norm, the trapping of an eigenfunction can be understood as its exponential decay inside the branches. We describe a general variational formalism for detecting trapped modes in such resonators. For finite waveguides with general cylindrical branches, we obtain a sufficient condition which determines the minimal length of branches for getting a trapped eigenmode. Varying the branch lengths may switch certain eigenmodes from non-trapped to trapped or, equivalently, the waveguide state from conducting to insulating. These concepts are illustrated for several typical waveguides (L-shape, bent strip, crossing of two strips, etc.).

The results of this chapter up to Section 5.3 are reported in a joint-work with A. Delitsyn [61].

5.1   Introduction

The theory of quantum waveguides has been often employed to describe and model microelectronic devices [35–37, 149, 195, 208]. In a high purity crystallic semiconductor, the electron mean free path can be orders of magnitude larger than the size of the structure that allows one to consider the electron as a free particle [67]. In this approximation, the original many-body Schrödinger equation is replaced by the Helmholtz equation with Dirichlet boundary condition. The latter mathematical problem also describes the electromagnetic waves in microwave and optical waveguides [115]. The transmission properties of a waveguide are characterized by its resonance frequencies, i.e. by the spectrum of the Laplace operator. In general, the Laplacian spectrum consists in two parts: (i) the discrete (or point-like) spectrum, with eigenfunctions of finite L^2 norm that are necessarily "trapped" or "localized" in a bounded region of the waveguide, and (ii) the continuous spectrum, with associated functions of infinite L^2 norm that are

extended over the whole domain. The continuous spectrum may also contain embedded eigenvalues whose eigenfunctions have finite L_2 norm. A wave excited at the frequency of a trapped eigenmode remains in the bounded region and does not propagate. Similarly, an electron at the energy of a trapped eigenmode does not move through the quantum waveguide, strongly reducing its conductivity. Since the presence of such eigenmodes drastically changes the transmission properties of waveguides, their qualitative understanding and quantitative characterization are important for describing microelectronic, microwave and optical devices.

The existence of trapped, bound or localized eigenmodes in classical and quantum waveguides has been thoroughly studied in mathematical and applied physics (see [149], reviews [67, 146] and also references in [163]). In the seminal paper, Rellich proved the existence of a localized eigenfunction in a deformed infinite cylinder [181]. His results were significantly extended by Jones [122]. Ursell reported on the existence of trapped modes in surface water waves in channels [216–218], while Parker observed experimentally the trapped modes in locally perturbed acoustic waveguides [169, 170]. Exner and Seba considered an infinite bent strip of smooth curvature and showed the existence of trapped modes by reducing the problem to Schrödinger operator in the straight strip, with the potential depending on the curvature [74]. Goldstone and Jaffe gave the variational proof that the wave equation subject to Dirichlet boundary condition always has a localized eigenmode in an infinite tube of constant cross-section in two and three dimensions, provided that the tube is not exactly straight [91]. This result was further extended by Chenaud *et al.* to arbitrary dimension [42]. The problem of localization in acoustic waveguides with Neumann boundary condition has also been investigated [69, 70]. For instance, Evans *et al.* considered a straight strip with an inclusion of arbitrary (but symmetric) shape [70] (see [59] for further extension). Such an inclusion obstructed the propagation of waves and was shown to result in trapped modes. The effect of mixed Dirichlet, Neumann and Robin boundary conditions on the localization was also investigated (see [32, 64, 81, 163] and references therein). A mathematical analysis of guided water waves was developed in [27]. Lower bounds for the eigenvalues below the cut-off frequency (for which the associated eigenfunctions are localized) were obtained by Ashbaugh and Exner for infinite thin tubes in two and three dimensions [10]. In addition, these authors derived an upper bound for the number of the trapped modes. More recently, Exner *et al.* considered the Laplacian in finite-length curved tubes of arbitrary cross-section, subject to Dirichlet boundary conditions on the cylindrical surface and Neumann conditions at the ends of the tube. They expressed a lower bound for the spectral threshold of the Laplacian through the lowest eigenvalue of the Dirichlet Laplacian in a torus determined by the geometry of the tube [73].

All the aforementioned works (except the last one) dealt with infinite waveguides for which the Laplace operator spectrum is continuous, with a possible inclusion of isolated or embedded eigenvalues. Since they were responsible for trapped modes, the major question was whether or not such eigenvalues exist. It is worth noting that the localized modes have to decay relatively fast at infinity in order to guarantee the finite L^2 norm. But the same question about the existence of rapidly decaying eigenfunctions may be formulated for bounded domains (resonators) with long branches that we call "finite waveguides" (Fig. 5.1). This problem is different in many aspects. Since all eigenfunctions have now finite L^2 norms, the definition of trapped or localized modes has to be revised. Quite surprisingly, a rigorous definition of

localization in bounded domains turns out to be a challenging problem [71, 76, 191]. In the context of the present paper concerning finite waveguides, an eigenmode is called trapped or localized if it decays exponentially fast in prominent subregions (branches) of a bounded domain. A sufficient condition for the exponential decay of an eigenfunction along the branch can be related to the smallness of the associated eigenvalue in comparison to the cut-off frequency, i.e. the first eigenvalue of the Laplace operator in the cross-section of that branch [115]. In other words, the existence of a trapped mode is related to "smallness" of the eigenvalue, in full analogy to infinite waveguides (here, we focus on isolated eigenvalues below the continuous spectrum; note that the eigenfunctions associated to embedded eigenvalues may also decay exponentially). Using the standard mathematical tools such as domain decomposition, explicit representation of solutions of the Helmholtz equation and variational principle, we aim at formalizing these ideas and providing a sufficient condition on the branch lengths for getting a trapped mode. The dependence of the localization character (i.e., the conductivity) on the length of branches is the main result of the paper and a new feature of finite waveguides which was overseen in the well-established theory of infinite waveguides. It is worth recalling that a physical justification for considering infinite quantum waveguides relied on the fact that their length was typically several orders of magnitude bigger than their width [67]. The recent progress in lithography led to further miniaturization of microelectronic devices for which an approximation by infinite waveguides may be questionable. As a consequence, finite-size effects such as a sensitive dependence of the conductivity of finite waveguides on their length, require new theoretical developments and may have potential applications, as discussed below. These results are also relevant for the theory of classical microwave cavities or resonators.

This chapter is organized as following. In Sec. 5.2, we adapt the method by Bonnet-Ben Dhia and Joly [27] in order to reduce the original eigenvalue problem in the whole domain to the nonlinear eigenvalue problem in the domain without branches. Although the new problem is more sophisticated, its variational reformulation provides a general framework for proving the trapping (or localization) of eigenfunctions. We use it to derive the main result of the paper: a sufficient condition (5.19) on the branch lengths for getting a trapped mode. In sharp contrast to infinite non-straight waveguides of a constant cross-section, for which the first eigenfunction is always trapped and exponentially decaying [91], finite waveguides may *or may not* have such an eigenfunction, depending on the length of branches. In Sec. 5.3, we illustrate our approach by several typical waveguides. For these examples, we estimate the minimal branch length which is sufficient for getting at least one localized mode. At the same time, we provide an example of a waveguide, for which there is no localization for any branch length. We also construct a family of finite waveguides for which the minimal branch length varies continuously. As a consequence, for a given (large enough) branch length, one can construct two almost identical resonators, one with and the other without localized mode. This observation may be used for developing quantum switching devices. In Sec. 5.4, we propose several sufficient conditions related to the basis domain for getting a trapped modes on general shapes of the branches. The chapter ends by conclusions and further works.

5.2 Exponential decay in rectangular domains

To clarify our approach, we start by considering planar bounded domains D with the rectangular branches, and then generalize the problem for any domain in $\mathbb{R}^n$ with cylindrical branches.

We assume that a planar bounded domain D can be decomposed into a basic domain Ω of arbitrary shape and M rectangular branches Q_i of length a_i and width b_i as shown on Fig. 5.1:

$$D = \Omega \cup \bigcup_{i=1}^{M} Q_i.$$

We denote $\Gamma_i = \partial\Omega \cap \partial Q_i$ the inner boundary between the basic domain Ω and the branch Q_i and $\Gamma = \partial\Omega \backslash \bigcup_{i=1}^{M} \Gamma_i$ the exterior boundary of Ω. Now, we study the Laplacian eigenproblem in the domain D with Dirichlet boundary condition on ∂D:

$$\begin{cases} \triangle U + \lambda U = 0, \text{ in } D, \\ U = 0 \text{ on } \partial D, \end{cases} \qquad (5.1)$$

(a)   (b)
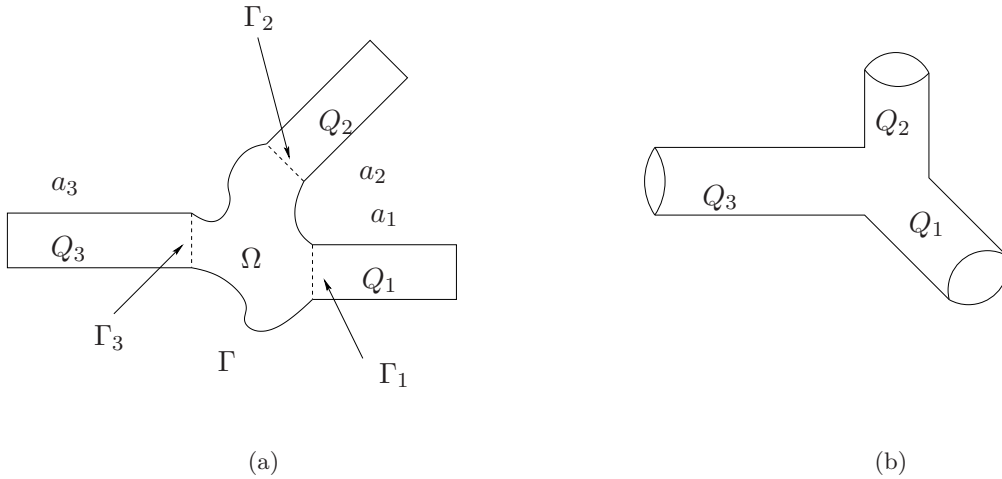
Figure 5.1: Two examples of a finite waveguide: (a) a planar bounded domain D which is composed of a basic domain Ω of arbitrary shape and three rectangular branches Q_i of lengths a_i and width b; (b) a three-dimensional bounded domain with three general cylindrical branches.

5.2.1 Theoretical results

For the sake of convenience, we suppose that $b_i = 1$ and the coordinates x and y can be chosen so that each branch $Q_i = \{(x, y) \in \mathbb{R}^2 : x \in (0, a_i), y \in (0, 1)\}$. For an eigenfunction U of the eigenproblem (5.1), we denote $u_i(x, y)$ the restriction of this function to each branch Q_i. The eigenfunction $u_i(x, y)$ can be represented by the following form:

$$u_i(x, y) \equiv U_{|Q_i} = \sum_{n=1}^{\infty} c_n \sinh(\gamma_n(a_i - x)) \sin(\pi n y), \qquad (5.2)$$

in which $\gamma_n = \sqrt{\pi^2 n^2 - \lambda}$ and c_n are the Fourier coefficients of the function U at the inner boundary Γ_i (at $x = 0$):

$$c_n = \frac{2}{\sinh(\gamma_n a_i)} \int_0^1 u(0, y) \sin(\pi n y) \, dy. \tag{5.3}$$

By substituting the coefficients (5.3) into Eq. (5.2) one gets

$$u_i(x, y) = 2 \sum_{n=1}^{\infty} (U_{|\Gamma_i}, \sin(\pi n y))_{L^2(\Gamma_i)} \frac{\sinh(\gamma_n(a_i - x))}{\sinh(\gamma_n a_i)} \sin(\pi n y). \tag{5.4}$$

Here,

$$(U_{|\Gamma_i}, \sin(\pi n y))_{L^2(\Gamma_i)} = \int_{\Gamma_i} U_{|\Gamma_i}(0, y) \sin(\pi n y) dy.$$

Each rectangular branch Q_i has the same height $b = 1$. For this reason, the smallest Dirichlet-Laplacian eigenvalue in all cross-section along Q_i is equal to π^2 ($\mu = \pi^2$). Using the same technique as in the previous chapter, one can easily prove that the squared L^2-norm of the function $u_i(x, y)$ exponentially decays with the decay rate $2\gamma_1 = 2\sqrt{\pi^2 - \lambda}$ along the branch Q_i whenever its corresponding eigenvalue λ is smaller than μ:

$$I_i(x) \leq I_i(0) \exp(-2\gamma_1 x), \tag{5.5}$$

for any $0 < x < a$, where

$$I_i(x) \equiv \int_0^1 u_i^2(x, y) dy = 2 \sum_{n=1}^{\infty} (U_{|\Gamma_i}, \sin(\pi n y))_{L^2(\Gamma_i)}^2 \frac{\sinh^2(\gamma_n(a_i - x))}{\sinh^2(\gamma_n a_i)}. \tag{5.6}$$

When $\lambda > \pi^2$, several γ_n are purely imaginary so that the function $\sinh(\gamma_i z)$ becomes $\sin(|\gamma_n| z)$, and the above exponential decay is replaced by an oscillating behavior.

The condition $\lambda < \mu$ is only a sufficient but not necessary condition for the existence of exponentially decaying eigenfunctions. In fact, one may find some eigenmodes which has such behavior even when $\lambda > \mu$. However, it is difficult to find these eigenvalues in general.

In this chapter, we will focus on establishing the condition for getting some eigenvalues λ smaller than a given threshold μ that implies that the corresponding eigenfunctions exponentially decay according to the inequality (5.5).

5.2.2   Nonlinear eigenvalue problem

We denote $u = U|_{\Omega}$ the restriction of a solution U onto the basic domain Ω. Then, this restriction satisfies the following equation

$$\begin{aligned}
-\Delta u = \lambda u \quad \text{in } \Omega, \qquad u|_{\Gamma} = 0, \\
u|_{\Gamma_i} = u_i|_{\Gamma_i}, \qquad \left.\frac{\partial u}{\partial n}\right|_{\Gamma_i} = -\left.\frac{\partial u_i}{\partial n}\right|_{\Gamma_i},
\end{aligned} \tag{5.7}$$

Here, $\frac{\partial}{\partial n}$ denotes the normal derivative directed outwards the domains. The last boundary condition in (5.7) ensures the continuity of the eigenfunction u and its derivative at each inner boundary Γ_i. At each Γ_i, the normal derivatives on its both sides are opposite which implies that $\frac{\partial u}{\partial n}|_{\Gamma_i} = -\frac{\partial u_i}{\partial n}|_{\Gamma_i}$. Using Eq. (5.2), the normal derivative of u_i can be explicitly represented as

$$\frac{\partial u_i}{\partial n}\bigg|_{\Gamma_i} = -\frac{\partial u_i}{\partial x}\bigg|_{x=0} = 2\sum_{n=1}^{\infty} \gamma_n \coth(\gamma_n a_i)\big(U_{|\Gamma_i}, \sin(\pi n y)\big)_{L^2(\Gamma_i)} \sin(\pi n y). \tag{5.8}$$

Now, for each i, one denotes an operator $T_i : H^{1/2}(\Gamma_i) \to H^{-1/2}(\Gamma_i)$ (see [147] for details) such that

$$T_i(\lambda)f \equiv 2\sum_{n=1}^{\infty} \gamma_n \coth(\gamma_n a_i)\big(f, \sin(\pi n y)\big)_{L^2(\Gamma_i)} \sin(\pi n y).$$

It is important to remark that T_i is a positive-definite operator for each i. Then, Eq.(5.8) can be represented as

$$\frac{\partial u_i}{\partial n}\bigg|_{\Gamma_i} = T_i(\lambda)U_{|\Gamma_i}.$$

Bringing all above facts together, a solution (u, λ) of Eq. (5.7) satisfies

$$-\Delta u = \lambda u \quad \text{in } \Omega, \quad u|_\Gamma = 0, \quad \frac{\partial u}{\partial n}\bigg|_{\Gamma_i} = -T_i(\lambda)u|_{\Gamma_i}. \tag{5.9}$$

Here, the new eigenvalue problem is more complicated because the eigenvalue appears in the boundary condition through the operators $T_i(\lambda)$ that implies the *nonlinearity* of Eq. (5.9). One can overcome this difficulty by using a standard method originally proposed by Birman and Schwinger [26, 196]. In our approach, we adapt the technique developed in [27]. For a given λ, we solve the following linear eigenvalue problem

$$-\Delta u = \mu(\lambda)u \quad \text{in } \Omega, \quad u|_\Gamma = 0, \quad \frac{\partial u}{\partial n}\bigg|_{\Gamma_i} = -T_i(\lambda)u|_{\Gamma_i}, \tag{5.10}$$

where $\mu(\lambda)$ denotes the eigenvalue which is parameterized by λ. The solution of the original problem is recovered when $\mu(\lambda) = \lambda$.

It is much more difficult to get a numerical solution of the new eigenvalue problem in Eq. (5.10) with the subsequent resolution of the equation $\mu(\lambda) = \lambda$ than that for the original problem. However, it is more convenient to check whether the eigenvalue λ is smaller or greater than the threshold μ, e.g π^2. In the following section, we will provide more details about this technique.

5.2.3   Variational formulation

We denote V the space of functions from the standard Sobolev space $H_0^1(D)$ that are restricted to the basic domain Ω. The Rayleigh quotient corresponding to Eq. (5.10) can be written as [61]

$$\mu(v;\lambda) = \frac{(\nabla v, \nabla v)_{L^2(\Omega)} + \sum_{i=1}^{M}(T_i(\lambda)v, v)_{L^2(\Gamma_i)}}{(v,v)_{L^2(\Omega)}}, \tag{5.11}$$

where $v \in V$ is a trial function. From the Rayleigh's principle, the first eigenvalue $\mu_1(\lambda)$ in Eq. (5.10) can be obtained by

$$\mu_1(\lambda) = \inf_{v \in V, \ v \neq 0} \mu(v;\lambda), \tag{5.12}$$

and the other eigenvalues can be determined by the minimax principle as following

$$\mu_k(\lambda) = \sup_{v_1,...,v_{k-1} \in V} \quad \inf_{\substack{v \in V, \ v \neq 0, \\ v \perp \{v_1,...,v_{k-1}\}}} \mu(v;\lambda), \tag{5.13}$$

where the supremum is taken over $k-1$ linearly independent functions v_1, ..., v_{k-1}, and the infimum is over functions $v \neq 0$ that are orthogonal to the linear span over v_1, ..., v_{k-1}.

Lemma 5.2.1. *For any $k = 1, 2, 3, ...$, $\mu_k(\lambda)$ are positive continuous monotonously decreasing functions of λ on the segment $[0, \pi^2]$.*

Proof. One first computes explicitly the derivative of the function

$$h(\lambda) \equiv \gamma_n \coth(\gamma_n a_i) = \sqrt{\pi^2 n^2 - \lambda} \coth\left(\sqrt{\pi^2 n^2 - \lambda}\, a_i\right)$$

as following

$$h'(\lambda) = \frac{-a_i}{4z \sinh(z)}\left(\sinh(2z) - 2z\right)$$

where $z = a_i\sqrt{\pi^2 n^2 - \lambda}$.

The inequality $\sinh y \geq y$ ($\forall y \geq 0$) implies $h'(\lambda) < 0$ so that $\mu(v, \lambda)$ monotonously decreases with λ for any $v \in V$. Now one can show that $\mu_k(\lambda_1) \leq \mu_k(\lambda_2)$ if $\lambda_1 > \lambda_2$. If some trial functions $v_1, ..., v_{k-1} \in V$ and $v \in V$ orthogonal to the linear span $\{v_1, ..., v_{k-1}\}$, optimize $\mu(v, \lambda_2)$, one has

$$\mu_k(\lambda_1) \leq \mu(v, \lambda_1) \leq \mu(v, \lambda_2) = \mu_k(\lambda_2),$$

where the monotonous decrease of $\mu(v, \lambda)$ was used (the mathematical proof of the continuity for an analogous functional is given in [62]). $\qquad \square$

Since the function $\mu_k(\lambda)$ is positive, continuous and monotonously decreasing, the equation $\mu_k(\lambda) = \lambda$ has a solution $0 < \lambda < \pi^2$ if and only if $\mu_k(\pi^2) < \pi^2$. This solution gives the k-th eigenvalue λ_k of the original eigenvalue problem. In what follows, we focus on the first eigenvalue.

5.2.4 Sufficient condition

In this section, we find a sufficient condition for the equation $\mu_1(\lambda) = \lambda$ to have one solution in $(0, \pi^2)$. From Eq. (5.12), if one can find a trial function $v \in V$ such that $\mu(v, \lambda) < \pi^2$ for some $\lambda \in (0, \pi^2)$, then the first eigenvalue $\mu_1(\pi^2)$ (corresponding to $\lambda = \pi^2$ in Eq. (5.10)) is smaller than π^2.

Following this idea, we set $\lambda = \pi^2$ and denote $\mu(v) \equiv \mu(v, \pi^2)$. The functional $\mu(v)$ can be represented by the following form

$$\mu(v) = (v, v)_{L^2(\Omega)}^{-1} \left\{ (\nabla v, \nabla v)_{L^2(\Omega)} + 2 \sum_{i=1}^{M} \frac{1}{a_i} (v, \sin(\pi y))_{L^2(\Gamma_i)}^2 \right.$$
$$\left. + 2\pi \sum_{n=2}^{\infty} \sqrt{n^2 - 1} \sum_{i=1}^{M} \coth(\pi a_i \sqrt{n^2 - 1})(v, \sin(\pi n y))_{L^2(\Gamma_i)}^2 \right\}.$$

Here, $\gamma_n(\pi^2) = \pi\sqrt{n^2 - 1}$ and $\gamma_1(\pi^2) = 0$.

For any $n \geq 2$, $\coth(\pi a_i \sqrt{n^2 - 1}) \leq \coth(\pi a_i \sqrt{3})$. Using this inequality, we obtain the following theorem

Theorem 5.2.1. *The condition $\mu(v) < \pi^2$ is implied by the following sufficient condition*

$$\sum_{i=1}^{M} \frac{\sigma_i}{a_i} < \beta - \sum_{i=1}^{M} \kappa_i \coth(\pi a_i \sqrt{3}), \tag{5.14}$$

where

$$\beta = \pi^2 (v, v)_{L^2(\Omega)} - (\nabla v, \nabla v)_{L^2(\Omega)}, \tag{5.15}$$

$$\sigma_i = 2(v, \sin(\pi y))_{L^2(\Gamma_i)}^2, \tag{5.16}$$

$$\kappa_i = 2\pi \sum_{n=2}^{\infty} \sqrt{n^2 - 1} \, (v, \sin(\pi n y))_{L^2(\Gamma_i)}^2. \tag{5.17}$$

It is worth noting that the above condition is a sufficient but not necessary condition for the equation $\mu_1(\lambda) = \lambda$ to have a solution smaller than π^2. In the next section, we will illustrate this approach by several examples.

One can extend the above analysis to a bounded domain in $\mathbb{R}^n$ with general cylindrical branches by using the separation of variables (in directions parallel and perpendicular to each branch). In fact, the Fourier coefficients $(U|_{\Gamma_i}, \sin(\pi n y)))_{L^2(\Gamma_i)}$ in Eq. (5.2) have to be replaced by a spectral decomposition over the orthonormal eigenfunctions $\{\psi_n(y)\}_{n=1}^{\infty}$ of the Laplace operator $\Delta_\perp$ in the cross-section Γ_i of the studied branch (in general, Γ_i is a bounded domain in $\mathbb{R}^{n-1}$):

$$\Delta_\perp \psi_n + \nu_n \psi_n = 0 \quad \text{in } \Gamma_i, \qquad \psi_n|_{\partial \Gamma_i} = 0. \tag{5.18}$$

In particular, the operator $T_i(\lambda)$ becomes

$$T_i(\lambda)f = \sum_{n=1}^{\infty} \gamma_n \coth(\gamma_n a_i)(f, \psi_n)_{L^2(\Gamma_i)} \psi_n(y),$$

with $\gamma_n = \sqrt{\nu_n - \lambda}$.

Theorem 5.2.2. *Similar to the above analysis, a sufficient condition for getting a trapped mode can be given by*

$$\sum_{i=1}^{M} \frac{\sigma_i}{a_i} < \beta - \sum_{i=1}^{M} \kappa_i \coth(a_i \sqrt{\nu_2 - \nu_1}), \tag{5.19}$$

with

$$\beta = \nu_1 (v, v)_{L^2(\Omega)} - (\nabla v, \nabla v)_{L^2(\Omega)}, \tag{5.20}$$

$$\sigma_i = (v, \psi_1)_{L^2(\Gamma_i)}^2, \tag{5.21}$$

$$\kappa_i = \sum_{n=2}^{\infty} \sqrt{\nu_n - \nu_1} \, (v, \psi_n)_{L^2(\Gamma_i)}^2. \tag{5.22}$$

and v is a trial function from V.

For example, in the rectangular branches, one has $\psi_n(y) = \sqrt{2} \sin(\pi n y)$ and $\nu_n = \pi^2 n^2$.

Remark 5.2.1. *One should choose the trial function v such that the series in Eq. (5.22) converges for each branch Γ_i. If the boundary of Ω is smooth, the convergence of the series in Eq. (5.22) is ensured for any function v from V according to the trace theorem [147]. In turn, the presence of corners or other singularities may require additional verifications for the convergence, as illustrated in the next section.*
There are several ways to check whether a trial function v satisfies the inequality (5.19) or not. Since $\sigma_i \geq 0, \forall i$, this inequality can only be satisfied if $\beta > 0$. For a given trial function v, the first check concerns the positivity of β.

Remark 5.2.2. *The exponential decay of an eigenfunction in all rectangular branches of width b_i can be ensured if the corresponding eigenvalue λ is smaller than a threshold $\mu = \dfrac{\pi^2}{\max b_i^2}$. In general, similar results can be applicable for any b_i. To apply the above analysis, one can rescale the whole domain D in such a way that $\max\{b_i\} = 1$.*

Remark 5.2.3. *If the branches are long enough, one can see that the value of $\coth\left(a_i \sqrt{\nu_2 - \nu_1}\right)$ is very close to 1 and can be replaced by $1 + \epsilon$ where $\epsilon = \max_{i} \left\{\coth\left(a_i \sqrt{\nu_2 - \nu_1}\right) - 1\right\}$. Then, the condition (5.19) can be substituted by the following inequality*

$$\sum_{i=1}^{M} \frac{\sigma_i}{a_i} < \beta - (1 + \epsilon) \sum_{i=1}^{M} \kappa_i. \tag{5.23}$$

Especially, when all σ_i are the same, one can introduce the threshold value η such that

$$\sum_{i=1}^{M} \frac{1}{a_i} < \eta, \qquad \eta \equiv \frac{\beta}{\sigma_1} - \frac{(1 + \epsilon)}{\sigma_1} \sum_{i=1}^{M} \kappa_i. \tag{5.24}$$

For domains with identical branches (of the same length $a_i = a$), one can use the above condition to determine the minimal length $a_{th} = \frac{M}{\eta}$ for the existence of trapped modes. If $\eta > 0$ and $a > a_{th}$, there exists at least one localized eigenmode. However, when $a < a_{th}$, the emergence of localization is not clear. Once again, the above condition is only a sufficient but not necessary condition to ensure that the first eigenfunction is localized in the waveguide.

Remark 5.2.4. *The estimate $\mu(v)$ is not an upper bound for the eigenvalue λ. On one hand, one has $\lambda = \mu_1(\lambda) \geq \mu_1(\pi^2)$ because the function $\mu_1(\lambda)$ is monotonously decreasing. On the other hand, $\mu(v) \geq \mu_1(\pi^2)$ according to the definition of $\mu_1(\pi^2)$ as the infimum of the functional $\mu(v)$. As a consequence, λ can be larger or smaller than $\mu(v)$. In turn, the inequality $\mu(v) < \pi^2$ implies $\mu_1(\pi^2) < \pi^2$ which in turn implies $\lambda < \pi^2$ and ensures the localization of the corresponding eigenfunction.*

Remark 5.2.5. *The above analysis was focused on the first eigenvalue. In particular, the sufficient condition (5.19) ensures that the first eigenmode is localized. At the same time, the examples of waveguides with numerous localized states were reported in the literature. For instance, Avishai et al. demonstrated the existence of many localized states for a sharp "broken strip", i.e. a waveguide made of two channels of equal width intersecting at a small angle θ [12]. Carini and co-workers reported an experimental confirmation of this prediction and its further extensions [36, 149]. Bulgakov et al. considered two straight strips of the same width which cross at an angle $\theta \in (0, \pi/2)$ and showed that, for small θ, the number of localized states is greater than $(1 - 2^{-2/3})^{3/2}/\theta$ [31]. Even for the simple case of two strips crossed at the right angle $\theta = \pi/2$, Schult et al. showed the existence of two localized states, one lying below the cut-off frequency and the other being embedded into the continuous spectrum [195]. The latter state is localized only because it has odd parity with respect to the fourfold rotational symmetry of this waveguide. The above variational approach allows one to investigate the localization of the second and higher-order eigenfunctions that correspond to isolated eigenvalues lying below the continuous spectrum (here, $\lambda_k < \pi^2$). While this is an interesting perspective for future work, we keep considering the first eigenvalue in the following examples.*

5.3   Examples

In this section, we will illustrate our approach by several examples. As we mentioned before, there is no recipe for choosing a trial function v in a general domain D. The best choice of the trial function v makes $\mu(v)$ reaching the minimal value in the Rayleigh quotient. Except for some domains (e.g circular, elliptical, spherical, rectangular domains, etc) in which Laplacian eigenfunctions are analytically determined, the eigenfunctions are not known. In the following examples (L-shape, cross, bent strip, etc), we will show how to guess a possible trial function v and get sufficient conditions for a trapped mode in these domains.

5.3.1 L-shape

The first domain we consider here is an L-shape with two rectangular branches of length a_1 and a_2 as shown in Fig. 5.2a. In this case, the basic domain Ω is simply a unit square.

When $a_1 = a_2 = 0$, the domain D has no branches ($D = \Omega$), and the first eigenvalue λ_1 is equal to $2\pi^2$ so that there is no localization of this eigenfunction (since $\lambda > \pi^2$).

(a)   (b)   (c)
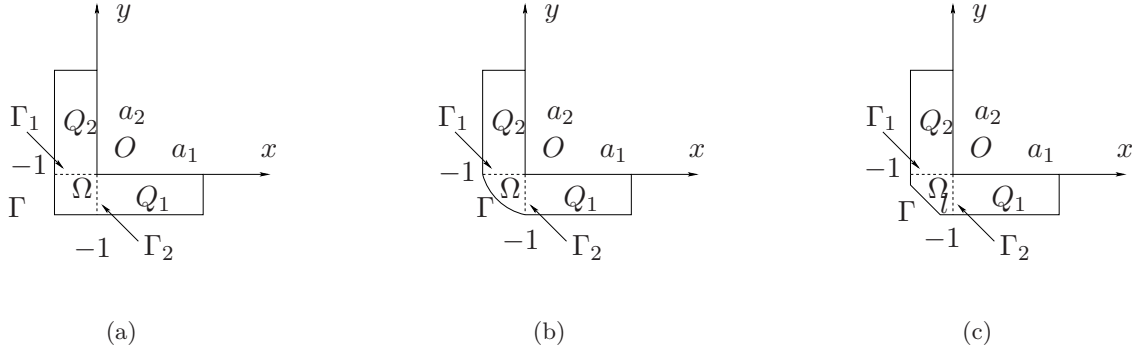
Figure 5.2:   Three types of a bent waveguide: (a) L-shape, (b) bent strip, and (c) truncated L-shapes parameterized by the length ℓ varying from 0 (triangular basic domain) to 1 (the original L-shape).

When $a_1 = a_2 = a$, the first eigenvalue λ_1 is a continuous function of variable a so that the inequality $\lambda_1 > \pi^2$ still remains true for relatively short branches. For infinitely long branches ($a = \infty$), the first eigenvalue becomes smaller than π^2. As a consequence, there exists the minimal length a_{min} such that the corresponding $\lambda_1 = \pi^2$, and more importantly, from the domain monotonicity theorem, the first eigenfunction passes from the non-localized state ($a < a_{min}$) to the localized state ($a > a_{min}$). We aim at getting the upper bound a_{th} of this a_{min}.

From the special structure of the basic domain (the unit square), the simplest choice for a trial function v is $v(x, y) = \sin(\pi x) \sin(\pi y)$ for which one can easily check that $\beta = 0$. Following the remark (5.2.1), this trial function does not satisfy the inequality (5.7) so that it is not a good choice in this case.

One can choose the following trial function v:

$$v(x, y) = (1 + x) \sin(\pi y) + (1 + y) \sin(\pi x). \tag{5.25}$$

Computing explicitly the values of β, σ_i and κ_i from Eqs. (5.15-5.17), one gets

$$\beta = 1, \quad \sigma_1 = \sigma_2 = \frac{1}{2}, \quad \kappa_1 = \kappa_2 = 0.$$

The inequality (5.19) becomes

$$\frac{1}{a_1} + \frac{1}{a_2} < 2. \tag{5.26}$$

From the above inequality, when two branches have the same length $a_1 = a_2 = a$, an upper bound of the theoretical minimal branch length a_{min} for getting the transition from a non-localized mode to localized mode is given by $a_{th} = 1$.

For comparison, we solved the Laplacian eigenproblem in a *L*-shape with $a_1 = a_2 = a$ with Dirichlet boundary condition by using a finite element method implemented by PDETools package in Matlab. For each a, we computed the first eigenvalue in the corresponding domain. In Fig. 5.3, the first eigenvalue λ_1 is shown as a function of the branch length a. The theoretical minimal branch length can be estimated as $a_{min} \approx 0.84$. One can obtain similar results for *L*-shape in three dimensions as shown in Section 5.3.2.
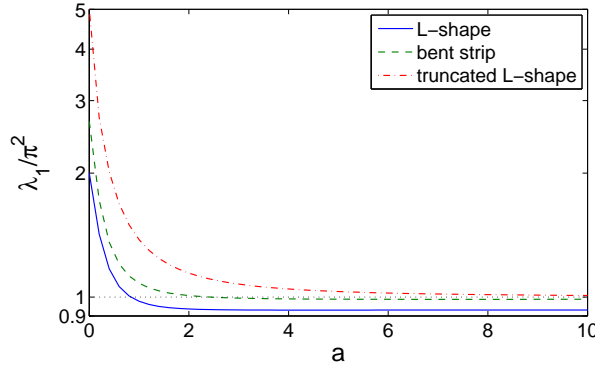
Figure 5.3:   The first eigenvalue λ_1 divided by π^2, as a function of the branch length a ($a_1 = a_2 = a$), for three bent waveguides shown on Fig. 5.2: L-shape (solid line), bent strip (dashed line) and truncated L-shape with $\ell = 0$ (dash-dotted line). For the first two cases, the curves cross the level 1 at $a_{\min} \approx 0.84$ and $a_{\min} \approx 2.44$, respectively. In turn, the third curve always remains greater than 1 (see explanations in Sec. 5.3.5). For $a = 0$, λ_1 is respectively equal to $2\pi^2$, $4j_{0,1}^2$ and $5\pi^2$, where $j_{0,1} \approx 2.4048$ is the first positive zero of the Bessel function $J_0(z)$.
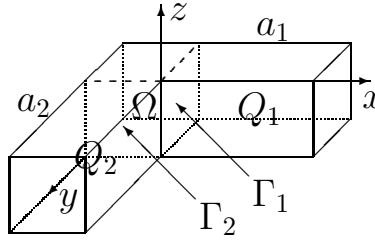
Figure 5.4:   L-shape in three dimensions for which the basic domain $\Omega = [-1,0]^3$ is the unit cube.

5.3.2   L-shape in three dimensions

As we mentioned at the end of Sec. 5.2, an extension of the presented approach to other types of branches is straightforward. We illustrate this point by considering the L-shape in three dimensions, i.e. two connected parallelepipeds of cross-section in the form of the unit square, for which the basic domain Ω is the unit cube (Fig. 5.4). For each branch, the eigenvalues and eigenfunctions in Eq. (5.18) for the cross-section can be parameterized by two indexes m and n:

$$\nu_{m,n} = \pi^2(m^2 + n^2), \quad \psi_{m,n}(y,z) = 2\sin(\pi m y)\sin(\pi n z)$$

(similar for the second branch).
We take the trial function

$$v(x,y,z) = [(1+x)\sin(\pi y) + (1+y)\sin(\pi x)]\sin(\pi z),$$

which satisfies the Dirichlet boundary condition. The coefficients β, σ_i and κ_i can be found from Eqs.

(5.20 - 5.22), for which the explicit integration yields

$$(v, v)_{L^2(\Omega)} = \int\limits_{-1}^{0} \int\limits_{-1}^{0} \int\limits_{-1}^{0} v^2 \ dz \ dy \ dx = \frac{1}{6} + \frac{1}{\pi^2},$$

$$(\nabla v, \nabla v)_{L^2(\Omega)} = \int\limits_{-1}^{0} \int\limits_{-1}^{0} \int\limits_{-1}^{0} (\nabla v, \nabla v) \ dz \ dy \ dx = \frac{\pi^2}{3} + \frac{3}{2},$$

so that $\beta = 2\pi^2 (\nabla v, \nabla v)_{L^2(\Omega)} - (v, v)_{L^2(\Omega)} = 1/2$, and

$$(v, \psi_{1,1})_{L^2(\Gamma_1)} = \int\limits_{-1}^{0} \int\limits_{-1}^{0} v(0, y, z) \ 2 \sin(\pi y) \sin(\pi z) \ dz \ dy = \frac{1}{2},$$

while $(v, \psi_{m,n})_{L^2(\Gamma_1)} = 0$ for $m \neq 1$ or $n \neq 1$, from which $\sigma_1 = \sigma_2 = 1/4$ and $\kappa_1 = \kappa_2 = 0$. The condition (5.19) reads as

$$\frac{1}{a_1} + \frac{1}{a_2} < 2.$$

If the branches have the same length, $a_1 = a_2 = a$, then the upper bound of the minimal branch length for getting a localized eigenfunction is given by $a_{\text{th}} = 1$, as in two dimensions.

5.3.3 Cross

We continue by considering a crossing of two perpendicular rectangular branches (see Fig. 5.5). Here, the basic domain Ω is again the unit square. What is a sufficient condition to get a trapped mode in this domain?

From Eq. (5.12), one can easily see that any increase of the basic domain will decrease the eigenvalue $\mu_k(\lambda)$ on Eq. (5.10). Using this fact, if one considers the basic domain as the unit square with two rectangular branches Q_3 and Q_4 of lengths a_3 and a_4, the condition (5.26) in the previous section is enough for the existence of localized eigemodes in this domain. A similar argument is applicable when the basis domain is the union of the unit square and two arbitrary consecutive rectangular branches in $(Q_1, Q_2), (Q_2, Q_3), (Q_3, Q_4), (Q_4, Q_1)$. For example, the first eigenfunction in the domain D is localized in $\Omega = [-1, 0] \times [-1, 0] \cup Q_1 \cup Q_4$ if $1/a_2 + 1/a_3 < 2$ for any a_1 and a_4, etc. However, the condition $1/a_4 + 1/a_2 < 2$ or $1/a_1 + 1/a_3 < 2$ is not sufficient for getting some trapped modes in this domain. For instance, if $1/a_4 + 1/a_2 < 2$ and $a_1 = a_3 = 0$, the domain D becomes a rectangle and no localization happens.

Another choice of a trial function is as follows

$$v(x, y) = x(1 + x) + y(1 + y). \tag{5.27}$$

One can easily see that this trial function satisfies Dirichlet boundary condition at four corners of the

(a)   (b)   (c)
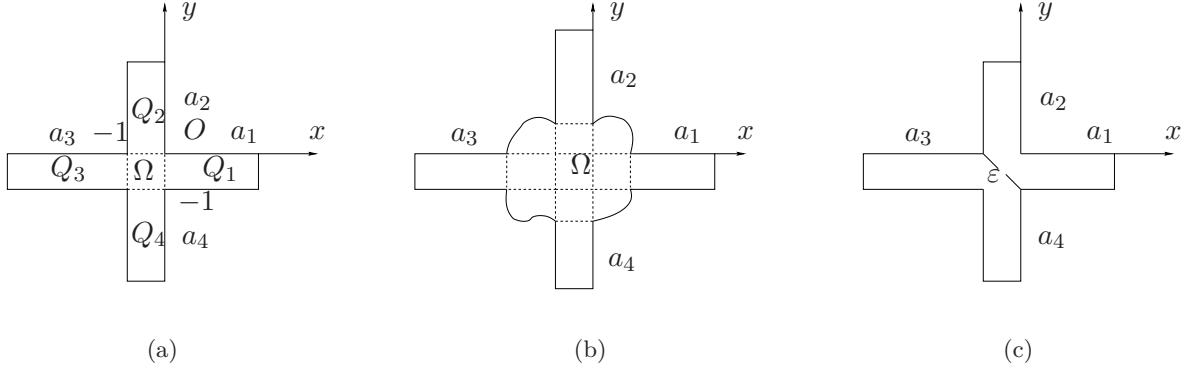
Figure 5.5: (a) Crossing of two rectangular branches; (b) an extension of the related basic domain Ω; and (c) coupling between two waveguides from Fig. 5.2c ($\ell = 0$) with an opening of size ε.

basic domain. The explicit integration yields

$$\beta \;=\; \frac{11}{90}\pi^2 - \frac{2}{3}, \qquad \sigma_i = \frac{32}{\pi^6}, \qquad \kappa_i = 2\pi \sum_{n=2}^{\infty} \sqrt{n^2-1}\left(2\frac{1-(-1)^n}{\pi^3 n^3}\right)^2 \approx 4.4768 \cdot 10^{-4}.$$

The sufficient condition (5.14) for getting a trapped mode becomes

$$\sum_{i=1}^{4} \frac{1}{a_i} < \frac{\beta}{\sigma_1} - \frac{\kappa_1}{\sigma_1} \sum_{i=1}^{4} \coth(\pi a_i \sqrt{3}). \tag{5.28}$$

When all branches have the same lengths $a_1 = a_2 = a_3 = a_4 = a$, the above condition yields the following equation for the upper bound a_{th} of the theoretical minimal length a_{min}:

$$\frac{4}{a_{\text{th}}} = \frac{\beta}{\sigma_1} - \frac{4\kappa_1}{\sigma_1} \coth(\pi a_{\text{th}} \sqrt{3}).$$

Solving this equation, one can estimate a_{th} as $a_{th} \approx 0.2458$. It is worth noting that this result proves and further extends the prediction of localized eigenmodes in the crossing of infinite rectangular strips which was made by Schult *et al.* by numerical computation [195]. In that reference, the importance of localized electron eigenstates in four terminal junctions of quantum wires was discussed.

In [82], Freitas and Krejčiřík estimated the upper bound for the first eigenvalue λ_1 of the Laplace operator with Dirichlet boundary condition in a cross with equal branches which reads in our notations as

$$\lambda_1 \leq 4j_{0,1}^2 \frac{1+2a+4a^2}{1+6a+8a^2},$$

where $j_{0,1} \approx 2.4048$ is the first zero of the Bessel function $J_0(z)$. However, one can easily check that

$$4j_{0,1}^2 \frac{1+2a+4a^2}{1+6a+8a^2} \geq 4j_{0,1}^2 \left(2\sqrt{3}-3\right) \approx 10.7357 > \pi^2, \;\; \forall a \geq 0.$$

For this reason, this inequality is not sufficient to determine the localization character of the first eigen-

$$n = 1 \qquad n = 3 \qquad n = 4 \qquad n = 5$$
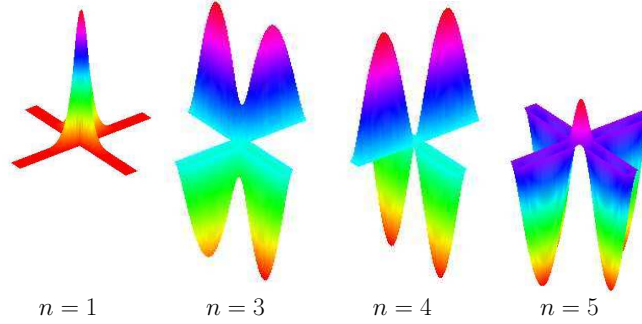
Figure 5.6: First eigenfunctions for the crossing of two rectangular branches ($a_i = 5$). The associated eigenvalues are $\lambda_1 \approx 0.661\pi^2$, $\lambda_2 = \lambda_3 \approx 1.032\pi^2$, $\lambda_4 \approx 1.036\pi^2$ and $\lambda_5 \approx 1.044\pi^2$.

function in this example.

In Fig. 5.6, we present the first eigenfunctions for the cross of two perpendicular rectangular branches with $a_i = a = 5$. Using the sufficient condition (5.28), one can see that $a > a_{th}$ so that the first eigenvalue should be smaller than π^2. As predicted, the first eigenvalue λ_1 in this case is found to be $\lambda_1 \approx 0.66\pi^2$, and the first eigenfunction is clearly localized in the basic domain and decays exponentially along the branches. The other eigenvalues are greater than π^2 so that the corresponding eigenfunctions are not localized (Fig. 5.6).

Remark 5.3.1. *It is important to emphasize that any increase of the basic domain as shown in Fig. 5.5b decreases the eigenvalues so that the similar sufficient condition, as in (5.28), can be obtained for getting localization in a larger domain.*

5.3.4 Bent strip

In this example, we consider the basic domain Ω as a sector of the unit disk as shown on Fig. 5.2b. This basic domain can be seen as the connector between two parts of a bent strip.

Goldstone and Jaffe proved the existence of a localized eigenmode for any bending of an infinite strip (except for the straight strip) [91]. However, for a finite bent strip, there is a minimal branch length required for the emergence of a localized eigenfunction. For this example, we compute an upper bound a_{th} of the minimal branch length in a bent strip.

Let us consider the domain D consisting of the basic domain Ω and two rectangular branches Q_1 and Q_2 of length a_1 and a_2, respectively. A family of trial functions v is

$$v_\alpha(r) = \frac{\sin \pi r}{r^\alpha} \qquad (0 < \alpha < 1). \tag{5.29}$$

The coefficients β, σ_i, and κ_i ($i = 1, 2$) are found in Appendix E (see Eqs. (E.1 - E.3)). Using the numerical computation, one can estimate that the maximum value of η occurs at $\alpha \approx 1/3$ which implies $\eta \approx 0.7154$. As a consequence, if the branches have the same lengths $a_1 = a_2 = a$, one obtains an upper

bound a_{th} of the minimal branch length as

$$a_{th} \approx \frac{2}{\eta} \approx 2.7956. \tag{5.30}$$

It ensures that when $a > a_{th}$, the first eigenfunction becomes localized in the basic domain Ω. Using the numerical computation of the first eigenvalue in the bent strip for each a (by Matlab PDETools), we estimate the minimal branch length as $a_{min} \approx 2.44$. This value is smaller (as expected) but relatively close to the upper bound a_{th}. It means that the chosen trial function is quite good.

5.3.5 Waveguide without localization

As discussed in previous sections, any increase of the basic domain decreases the eigenvalue and favors the localized eigenfunction. In turn, a decrease of the basic domain may lead to the suppression of localization. In this example, we will illustrate this point by considering a L-shape domain D as shown in Fig. 5.2c ($l = 0$) with the triangular basic domain Ω:

$$\Omega = \{(x, y) \in \mathbb{R}^2 \; : \; -1 < x < 0, \; -1 < y < 0, \; x + y > -1\}. \tag{5.31}$$

Lemma 5.3.1. *All Laplacian eigenvalues in the above domain D with Dirichlet boundary condition is greater than π^2 for any positive a_1 and a_2.*

Proof. It is easy to see that $u(x, y) = \cos(\pi x) + \cos(\pi y)$ is the first eigenfunction of the following eigenvalue problem in Ω:

$$-\Delta u = \tilde{\mu} u \quad \text{in } \Omega, \qquad u|_\Gamma = 0, \qquad \frac{\partial u}{\partial n}\Big|_{\Gamma_i} = 0,$$

with the eigenvalue $\tilde{\mu}_1 = \pi^2$ (since u satisfies the eigenvalue equation and does not change sign on the domain Ω). Using the variational principle (see Theorem 2.1.3), one gets

$$\tilde{\mu}_1 = \inf_{v \in V, v \neq 0} \frac{(\nabla v, \nabla v)_{L^2(\Omega)}}{(v, v)_{L^2(\Omega)}},$$

which implies

$$(\nabla v, \nabla v)_{L^2(\Omega)} \geq \tilde{\mu}_1 (v, v)_{L^2(\Omega)} = \pi^2 (v, v)_{L^2(\Omega)}$$

for all $v \in V$. Moreover, the Friedrichs-Poincaré inequality in the branches Q_i yields [147]

$$(\nabla v, \nabla v)_{L^2(Q_i)} \geq \pi^2 (v, v)_{L^2(Q_i)} \quad \forall v \in H_0^1(Q_i),$$

Bringing the above inequalities together, one gets

$$(\nabla v, \nabla v)_{L^2(D)} \geq \pi^2 (v, v)_{L^2(D)} \quad \forall v \in H_0^1(D).$$

As a consequence, all Laplacian eigenvalues in the domain D with Dirichlet boundary condition exceed π^2. $\qquad \square$

(a)   (b)   (c)
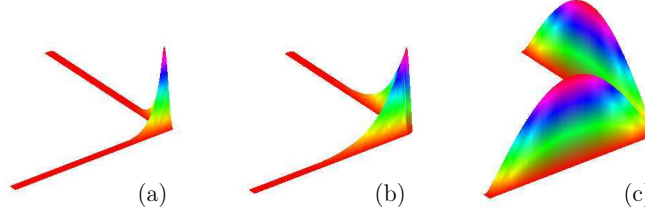
Figure 5.7:   The first eigenfunction for three bent waveguides shown on Fig. 5.2 ($\ell = 0$), with $a = 20$. The associate eigenvalue λ_1 is equal to $0.9302\pi^2$, $0.9879\pi^2$ and $1.0032\pi^2$, respectively. Although the last two values are very close to each other, the behavior of the eigenfunctions is completely different.

On Fig. 5.7, we show the first eigenfunction for three bent waveguides from Fig. 5.2, with $a = 20$. The corresponding eigenvalue λ_1 is equal to $0.9302\pi^2$, $0.9879\pi^2$ and $1.0032\pi^2$, respectively. According the sufficient conditions in previous discussion, the first two eigenfunctions are localized in the basic domain, but the last one is not.

5.3.6   Two coupled waveguides

In the last example, we consider a coupling of two finite crossing waveguides through an opening of small size ε as shown in Fig. 5.5c. When $\varepsilon = 0$, the domain is separated into two bent waveguides, and from Section 5.3.5, there is no trapped modes in this case. When $\varepsilon = \sqrt{2}$, the domain is a crossing as discussed in Section 5.3.3.

In Fig. 5.8, two coupled waveguides have identical branch lengths with $a_i = a = 5, 1 \leq i \leq 4$ and the opening ε varies from 0 to $\sqrt{2}$. When $\varepsilon = 0$ and $\varepsilon = 0.4\sqrt{2}$, the corresponding eigenvalues λ_1 are equal to $1.05\pi^2$ and $1.02\pi^2$ so that no localization happens. When $\varepsilon = 0.5\sqrt{2}$, the first eigenvalue λ_1 is equal to $0.97\pi^2$, and the associate eigenfunction becomes trapped in the basic domain. Finally, when $\varepsilon = \sqrt{2}$, as already expected as $a > a_{th} \approx 0.84$ (from Section 5.3.1), the first eigenfunction is clearly localized in Ω. Since the first eigenvalue λ_1 is a continuous function of ε, there exists $\varepsilon_{trapped}$ for which $\lambda_1 = \pi^2$ and there is a transition from a non-localized state to a localized state at $\varepsilon_{trapped}$. For example, for $a_i = a = 5$, one can estimate $\varepsilon_{trapped} \in \left(0.4\sqrt{2}, 0.5\sqrt{2}\right)$. As a result, the existence of localization in two couple waveguides seems to be very sensitive to the opening ε and the branch lengths. An estimation of $\varepsilon_{trapped}$ depending on the structure of the waveguides, can have useful applications in quantum switching devices. For two coupled infinite waveguives, a fruitful discussion can be found in [75].

5.4   Exponential decay in variable branches

In Section 5.2, we obtained a sufficient conditions (5.19) for getting trapped modes in a finite waveguide with several rectangular branches Q_i. In this section, we assume that a finite waveguide D consists of a basic domain V and the branches Q_i of length a_i and width b_i such that

$$Q_i = \left\{ (x, y) \in \mathbb{R}^2 : y \in (f_i(x), f_i(x) + b_i), x \in (0, a_i) \right\}, \tag{5.32}$$
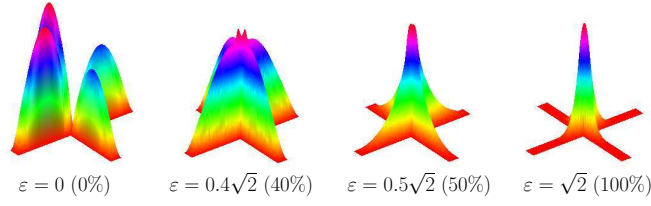
Figure 5.8:   The first eigenfunction for two coupled waveguides shown on Fig. 5.5c, with $a_i = 5$ and different coupling (opening ε): $\varepsilon = 0$ (fully separated waveguides, zero coupling), $\varepsilon = 0.4\sqrt{2}$ (opening 40% of the diagonal), $\varepsilon = 0.5\sqrt{2}$ (opening 50% of the diagonal) and $\varepsilon = \sqrt{2}$ (fully coupled waveguides, no barrier). The associate eigenvalue λ_1 is equal to $1.05\pi^2$, $1.02\pi^2$, $0.97\pi^2$, and $0.67\pi^2$, respectively. In the first two cases, the eigenmodes is not localized. Changing the opening ε, one passes from non-localized to localized eigenmodes.

where $f_i \in C^2([0, a_i])$ and $a_i, b_i > 0$. In what follows, we will derive a sufficient condition for the existence of localized eigenmodes in the waveguide D. Note that when f_i is a constant function, one gets back to the problem in Section 5.2.

First, we prove the following lemma:

Lemma 5.4.1. *For any $f_i \in C^2([0, a_i])$ and $a_i, b_i > 0$, all eigenvalues of the Laplace operator in the domain Q_i (defined in Eq. (5.32)) with Dirichlet boundary condition are always greater or equal to $\frac{\pi^2}{b_i^2}$.*

Proof. By changing the coordinates

$$
\begin{aligned}
x &= t, \ t \in (0, a_i), \\
y &= s - f(t), \ s \in (0, b_i),
\end{aligned}
\tag{5.33}
$$

one can map the original Laplacian eigenvalue problem (5.1) in Q_i onto the following eigenvalue problem in the rectangle $R_0 = [0, a_i] \times [0, b_i]$:

$$
\begin{cases}
\frac{\partial^2 v}{\partial^2 t} + \frac{\partial^2 v}{\partial^2 s} + \lambda v + [f'(t)]^2 \frac{\partial^2 v}{\partial^2 s} - 2f'(t)\frac{\partial^2 v}{\partial t \partial s} - f''(t)\frac{\partial v}{\partial s} = 0 \text{ in } R_0, \\
v = 0 \text{ on } \partial R_0.
\end{cases}
\tag{5.34}
$$

From the Rayleigh's principle, one gets

$$
\lambda_1 = \inf_{v \in H_0^1(R_0), v \neq 0} \frac{I_0 + I_1 + I_2 + I_3}{\int\limits_0^{a_i} \int\limits_0^{b_i} v^2 ds dt},
\tag{5.35}
$$

where

$$
I_0 = \int\limits_0^{a_i} \int\limits_0^{b_i} \left(\frac{\partial^2 v}{\partial^2 s} + \frac{\partial^2 v}{\partial^2 t} \right) v ds dt, \qquad I_1 = \int\limits_0^{a_i} \int\limits_0^{b_i} [f'(t)]^2 \frac{\partial^2 v}{\partial^2 s} v ds dt,
\tag{5.36}
$$

$$
I_2 = \int\limits_0^{a_i} \int\limits_0^{b_i} f'(t) \frac{\partial^2 v}{\partial t \partial s} v ds dt, \qquad I_3 = \int\limits_0^{a_i} \int\limits_0^{b_i} f''(t) \frac{\partial v}{\partial s} v ds dt.
\tag{5.37}
$$

Integrating by parts and using Dirichlet boundary conditions, one gets

$$I_1 = -\int_0^{a_i}\int_0^{b_i}\left[f'(t)\frac{\partial v}{\partial s}\right]^2 dsdt, \qquad I_2 = -\int_0^{a_i}\int_0^{b_i}f'(t)\frac{\partial v}{\partial t}\frac{\partial v}{\partial s}dsdt, \qquad I_3 = 0. \tag{5.38}$$

Then, one gets

$$\lambda_1 = \inf_{v\in H_0^1(R_0),v\neq 0}\frac{\int_0^{a_i}\int_0^{b_i}\left(\frac{\partial v}{\partial s}\right)^2 dsdt + \int_0^{a_i}\int_0^{b_i}\left(f'(t)\frac{\partial v}{\partial s}-\frac{\partial v}{\partial t}\right)^2 dsdt}{\int_0^{a_i}\int_0^{b_i}v^2 dsdt}. \tag{5.39}$$

Basically, one can decompose the function v

$$v(t,s) = \sum_{n=1}^{\infty}\sum_{k=1}^{\infty}c_{nk}\varphi_{nk}(t,s), \tag{5.40}$$

over the set $\{\varphi_{nk}(t,s)\}$ of L^2-normalized Laplacian eigenfunctions with Dirichlet boundary condition in the rectangle R_0

$$\varphi_{nk}(t,s) = \frac{2}{\sqrt{a_ib_i}}\sin\left(\frac{\pi nt}{a_i}\right)\sin\left(\frac{\pi ks}{b_i}\right). \tag{5.41}$$

Then,

$$\int_0^{a_i}\int_0^{b_i}v^2 dsdt = \sum_{n=1}^{\infty}\sum_{k=1}^{\infty}c_{nk}^2. \tag{5.42}$$

It is easy to see that

$$\int_0^{a_i}\int_0^{b_i}\left(\frac{\partial v}{\partial s}\right)^2 dsdt = \frac{\pi^2}{b_i^2}\sum_{n=1}^{\infty}\sum_{k=1}^{\infty}k^2 c_{nk}^2 \geq \frac{\pi^2}{b_i^2}\sum_{n=1}^{\infty}\sum_{k=1}^{\infty}c_{nk}^2 = \frac{\pi^2}{b_i^2}\int_0^{a_i}\int_0^{b_i}v^2 dsdt, \tag{5.43}$$

that implies the conclusion. □

(a) Domain D (b) u_1 (c) u_2 (d) u_3
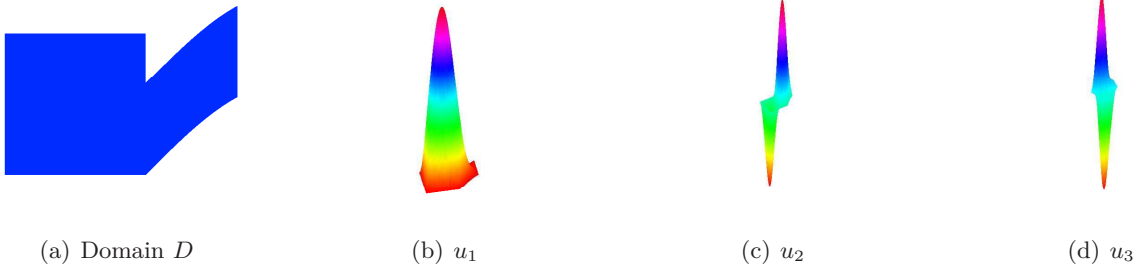
Figure 5.9:   The domain D consists of a basic domain V and one branch $Q =$ $\{(x,y)\in\mathbb{R}^2 : y\in(f(x),f(x)+1), x\in(0,a)\}$ where $b = 1$, $a = 1$, $f(x) = \sin x$ and V is a square of side $L = 1.54$. Here, the first eigenfunction exponentially decays along the branch Q, while the second and third eigenfunctions are not localized.

Now, we give a sufficient condition for the emergence of localized modes in the waveguide D:

Theorem 5.4.1. *Suppose that a waveguide D has a basic domain V and M branches Q_i of width b. Then, if the inradius of V is greater than $\dfrac{j_{0,1}b}{\pi}$, for any $f_i \in C^2([0, a_i])$ and arbitrary $a_i > 0$, there exists at least one eigenmode localized in the basic domain V and exponentially decaying along each branch Q_i with the decay rate $2\sqrt{\pi^2/b_i^2 - \lambda}$. Here, $\dfrac{j_{0,1}b}{\pi} \approx 0.7665b$ and $j_{0,1}$ is the first zero of the Bessel function $J_0(x)$.*

(a) Domain D (b) u_1 (c) u_2 (d) u_3

Figure 5.10:   The domain D consists of a basic domain V and one branch $Q = \{(x, y) \in \mathbb{R}^2 : y \in (f(x), f(x) + 1), x \in (0, a)\}$ where $b = 1$, $a = 5$, $f(x) = \sin x$ and V is a square of side $L = 1.54$. In this domain, the first eigenfunction is localized in V, while the third eigenfunction is localized in Q.

Proof. Suppose that r_0 is the inradius of the domain D. The first eigenvalue $\lambda_1(D)$ in the whole domain D is smaller than the first eigenvalue λ_{1,r_0} of the Laplace operator with Dirichlet boundary condition in a disk of radius r_0. Since $r_0 > \dfrac{j_{0,1}b}{\pi}$, one has

$$\lambda_1(D) \leq \lambda_{1,r_0} = \frac{j_{0,1}^2}{r_0^2} < \frac{\pi^2}{b^2}. \tag{5.44}$$

From Theorem 4.3.1, the first eigenfunction becomes localized in the basic domain V. □

Remark 5.4.1. *According to the theorem, for any geometrical structure (defined by function f_i) of each branch Q_i of width b_i and for any basic domain V satisfying the condition of Theorem 5.4.1, there exists at least one eigenfunction localized in V while the ratio $\dfrac{\mu_2(V)}{\mu_2(D)}$ may be made arbitrarily small by taking $a_i \to \infty$.*

5.4.1   Examples

To clarify the above results, we consider several examples.

Suppose that the domain D has only one branch Q of length a and width b such that

$$Q = \left\{(x, y) \in \mathbb{R}^2 : y \in (f(x), f(x) + b), x \in (0, a)\right\}, \tag{5.45}$$

where $f(x) = \sin x$ and the basic domain is a square of side L. In this example, we fix $b = 1$ and $L = 1.54$.

n	a=1	a=5	a=20
1	7.4787	7.4782	7.4781
2	15.8260	12.5005	12.4969
3	20.5826	15.3153	12.4991
4	23.1802	15.6921	12.5029
5	29.5236	17.5366	12.5075
6	33.7590	20.3117	12.5119

Table 5.1:   The first 6 eigenvalues of the Laplace operator in domains shown on Fig. 5.9, 5.10 and 5.11 with $a = 1, 5, 20$.

In Table 5.1, we compute numerically first 6 eigenvalues in the domain D when $a = 1, 5, 20$. Since the inradius of the square V is greater than $\frac{j_{0,1}}{\pi}$, from Theorem 5.4.1, the first eigenvalue in these domains should be smaller than π^2. Table 5.1 confirms this result.

When $a = 1$, the first eigenfunction decays exponentially along the branch Q, while the next two eigenfunctions are not localized (see Fig. 5.9).

When $a = 5$, the first eigenfunction becomes clearly localized in the basic domain V as shown on Fig. 5.10.

When $a = 20$ (Fig. 5.11), although the basic domain is about 7.15% of the area of the whole domain, the first eigenfunction is localized in V.

(a) Domain D (b) u_1 (c) u_2 (d) u_3
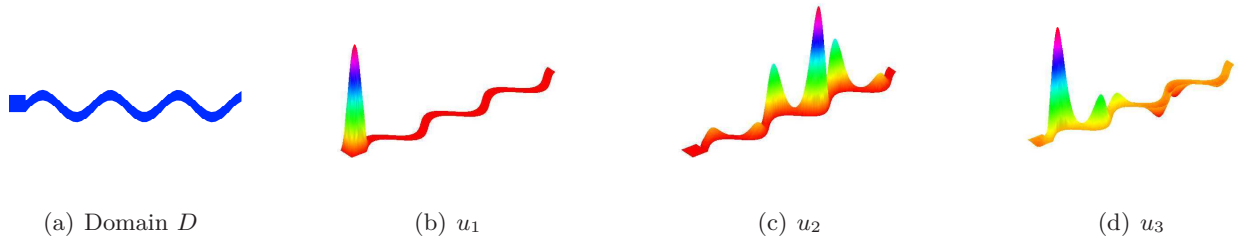
Figure 5.11:   The domain D consists of a basic domain V and one branch $Q =$ $\{(x, y) \in \mathbb{R}^2 : y \in (f(x), f(x) + 1), x \in (0, a)\}$ where $b = 1$, $a = 20$, $f(x) = \sin x$ and V is a square of side $L = 1.54$. One can clearly see that the first eigenfunction is mainly localized in the basic domain V although the ratio $\frac{\mu_2(V)}{\mu_2(D)} = 0.0715$.

5.5   Conclusion

We have studied the problem of localized eigenmodes of the Laplace operator in resonators with long branches. In this chapter, an eigenfunction u is called *localized* if it decays exponentially "in some L^2-sense" inside the branches. According to the results of Chapter 4, if the associated eigenvalue λ is smaller than the theoretical bound $\mu = \frac{\pi^2}{b^2}$, where b is the length of the largest cross-section $\Omega(x)$ of the branch Q, the L^2-norm of the eigenfunction u exponentially decay with rate $c\sqrt{\mu - \lambda}$. Using the explicit

(a) Domain D (b) u_1 (c) u_2

(d) u_3 (e) u_4 (f) u_5
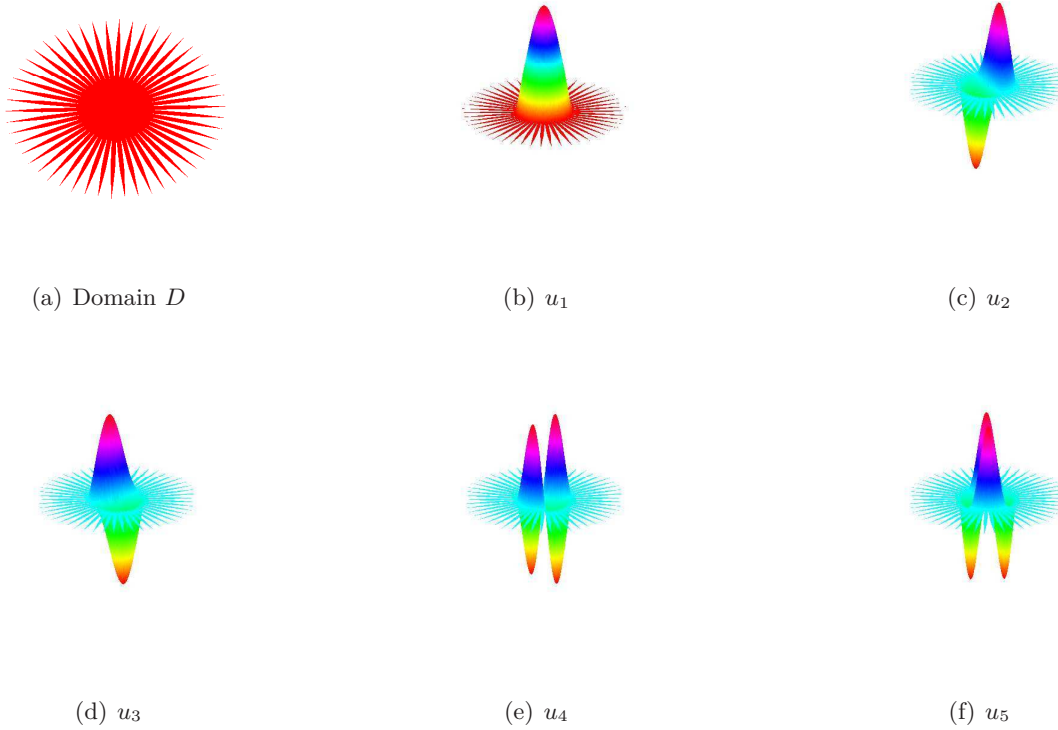
Figure 5.12: Localization of Dirichlet eigenmodes in a domain D with 51 branches.

representation of an eigenfunction in branches, we proposed a general variational formalism for checking the existence of localized eigenmodes. We derived a sufficient condition (5.14) on the branch lengths for getting a trapped mode. A practical use of the sufficient condition relies on an intuitive choice of a trial function in the basic domain (without branches). The trial function should be chosen as close as possible to the (unknown) eigenfunction. Although there is no general recipe for choosing a *good* trial function, one can often guess an appropriate choice basing on the geometry of the basic domain.

If the basic domain V satisfies the condition of Theorem 5.4.1, for any shape of branches Q_i defined in (5.32), there exist Dirichlet eigenfunctions of the Laplace operator which are mainly *localized* in V. Using this result, one can explain the emergence of localized eigenmodes in various domain, such as e.g on Figs. 5.12 and 5.13. An extension of our theoretical approach to study localization of the second and higher-order eigenmodes presents an interesting perspective.

We illustrated our approach for several typical waveguides, including 2D and 3D L-shapes, crossing of the rectangular strips, and bent strips. For all these cases, the basic domain was simple enough to guess an appropriate trial function in order to derive an explicit sufficient condition for getting at least one localized mode. In particular, we obtained an upper bound for the minimal branch length which is sufficient for localization. We proved the existence of a trapped mode in finite L-shape, bent strip and cross of two strips provided that their branches are long enough, with an accurate estimate on the required minimal length. These results were confirmed by a direct numerical resolution of the original eigenvalue problem

(a) Domain D

(b) u_1

(c) u_2

(d) u_3

(e) u_4

(f) u_5
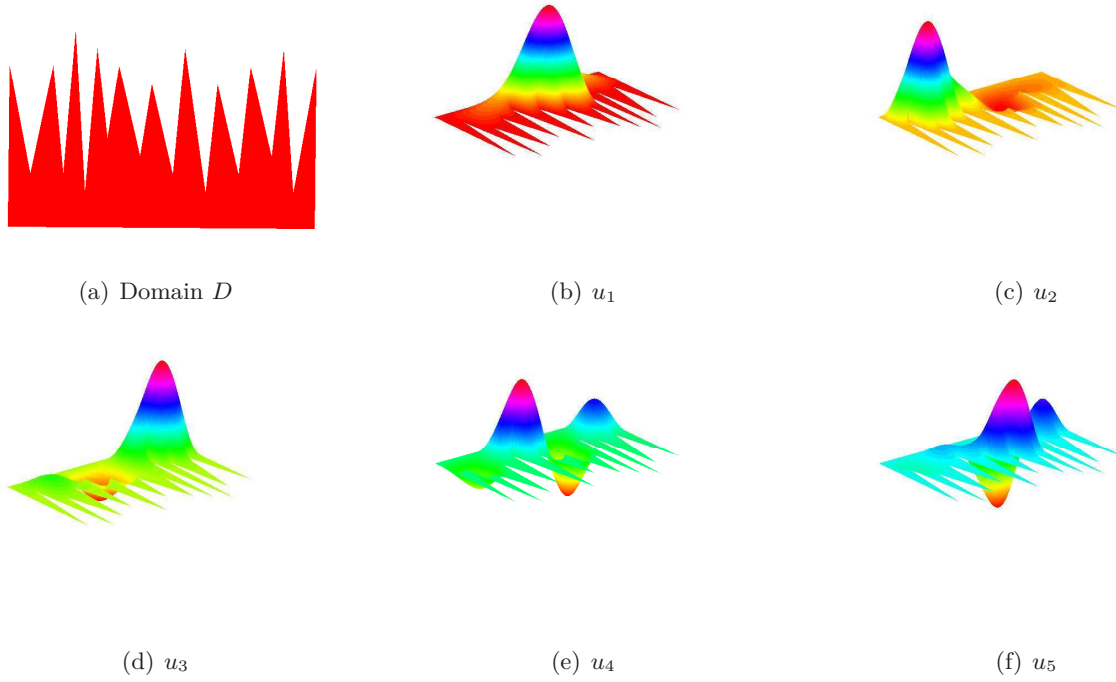
Figure 5.13: Localization of Dirichlet eigenmodes in a sawtooth domain D.

by finite element method implemented in Matlab PDEtools. The presented method can be applied for studying the localization in many other waveguides, e.g. smooth bent strip [163], sharply bent strip [12, 36], Z-shapes [37] or two strips crossing at arbitrary angle [31].

It is worth emphasizing that the distinction between localized and non-localized modes is much sharper in infinite waveguides than in finite ones. Although by definition the localized eigenfunction in a finite waveguide decays exponentially, the decay rate may be arbitrarily small. If the branch is not long enough, the localized mode may be visually indistinguishable from a non-localized one, as illustrated on Fig. 5.7. In turn, the distinction between localized and non-localized modes in infinite waveguides is always present, whatever the value of the decay rate.

The main practical result is an explicit construction of two families of waveguides (truncated L-shapes on Fig. 5.2c and coupled waveguides on Fig. 5.5c), for which the minimal branch length $a_{\min}$ for getting a trapped mode continuously depends on the parameter ℓ or ε of the basic domain. For any prescribed (long enough) branch length, one can thus construct two almost identical finite waveguides, one with and the other without a trapped mode. The high sensitivity of the localization character to the shape of the basic domain and to the length of branches may potentially be used for switching devices in microelectronics and optics.

Chapter 6

Localization in undirected graphs

As mentioned before, for two-dimensional domains, localization can happen in convex domains with smooth boundary (such as circular, spherical, elliptical domains, etc) and in many irregular domains [71, 76, 104, 106, 187, 188, 191–193]. In practice, one can solve Laplacian eigenproblem in a bounded domain by creating a "fine" mesh (or a spectral graph) that approximates the geometrical structure of the domain, and then using a standard finite element method to compute eigenvalues and eigenfunctions. For each localized eigenfunction in the original domain, one can get an approximated Laplacian eigenfunction in the spectral graph which has similar properties of localization. The problem of localized eigenmodes in a spectral graph would be an interesting approach for better understanding the "mechanism" of low-frequency localization.

In this chapter, we aim at studying the existence of localized modes in a class of planar graphs. We also describe some properties of the Laplace eigenvalue problem in these domains. For numerical simulations, we propose an efficient algorithm for solving the Laplacian eigenvalue problem not only in these graphs, but also in the general case. The results of this chapter are reported in [161].

6.1   Introduction

In the first part of this chapter, we discuss the existence of localized eigenmodes in some planar graphs. In Sec. 6.2, we analyze the properties of these localized eigenmodes and visualize them by several numerical computations.

In the remaining part of this chapter, we describe an efficient divide-and-conquer algorithm for solving the eigensystem for the Laplacian matrix L_G of an undirected and weighted graph G. Using numerical computations, we compare our approach with other algorithms (Sec. 6.3). It confirms that our algorithm runs faster than traditional approaches. This chapter ends by conclusions and further questions.

6.2   Localization in a special class of graphs

We consider the Laplace eigenvalue problem with Dirichlet boundary condition in a graph Ω, which can be decomposed into K identical vertical lines A_1B_1, A_2B_2, $\ldots$, A_KB_K and one horizontal line C_1C_2
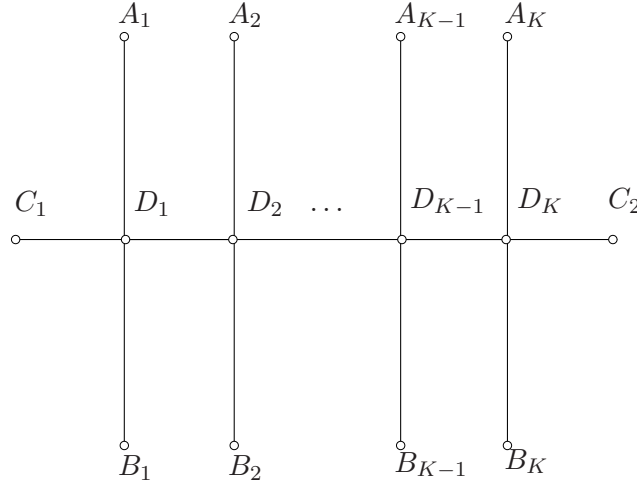
Figure 6.1: A planar graph Ω combining K vertical lines A_1B_1, A_2B_2, ..., A_KB_K and one horizontal line C_1C_2.

(Fig. 6.1). The set of points $\{A_1, \ldots, A_K, B_1, \ldots, B_K, C_1, C_2\}$ is the boundary of Ω. We call D_i the midpoint of A_iB_i with $A_iD_i = D_iB_i = d_1$ and $C_1D_1 = D_iD_{i+1} = \cdots = D_KC_2 = d_2$. Throughout this section, $E_1 = \left\{\frac{k^2\pi^2}{d_1^2}, k = 1, 2, \ldots\right\}$, $E_2 = \left\{\frac{m^2\pi^2}{d_2^2}, m = 1, 2, \ldots\right\}$, $E = E_1 \cup E_2$, and we assume that each eigenfunction U satisfies the Kirckhoff boundary condition at each midpoint D_i:

$$\begin{cases} U(D_i) = \lim_{D \to D_i} U(D) \\ \frac{\partial U(D_i)}{\partial x} + \frac{\partial U(D_i)}{\partial y} = 0 \end{cases} \tag{6.1}$$

Lemma 6.2.1. *Any $\lambda \in E$ is an eigenvalue of the Dirichlet-Laplace operator in the graph Ω.*

Proof. For each $i \in \{1, 2, \ldots, K\}$, the eigenvalues of the Dirichlet-Laplace operator in the interval A_iD_i are

$$\lambda = \frac{k^2\pi^2}{d_1^2}, \ k = 1, 2, 3, \ldots \tag{6.2}$$

We denote $u_1(\mathbf{r})$ the corresponding eigenfunction in A_iD_i and define

$$U(\mathbf{r}) = \begin{cases} u_1(\mathbf{r}) &, \quad \mathbf{r} \in A_iD_i \\ -u_1(\mathbf{r}) &, \quad \mathbf{r} \in D_iB_i \\ 0 &, \quad \mathbf{r} \notin A_iB_i \end{cases} \tag{6.3}$$

where $\mathbf{r} = (x, y)$ is a point in $\mathbb{R}^2$. For this reason, $U(\mathbf{r})$ is an eigenfunction in Ω that implies λ is the associate eigenvalue.

Similarly, one can prove that $\lambda = \dfrac{m^2\pi^2}{d_2^2}$ is an eigenvalue of the Dirichlet-Laplace operator in Ω for any positive integer m. $\qquad\square$

Lemma 6.2.2. *We consider the Laplace eigenvalue problem in an interval (c,d):*

$$u" + \lambda u = 0 \ \ in \ (c,d), \tag{6.4}$$

$$u(c) = x_0, \ \ u(d) = y_0. \tag{6.5}$$

If there exists an eigenvalue λ_0 such that $\lambda_0 = \dfrac{k^2\pi^2}{(d-c)^2}$ for some integer k, then $x_0 = \pm y_0$.

Proof. Suppose that $u(x)$ is an eigenfunction associated to λ_0, then $u(x)$ can be represented by the following form

$$u(x) = c_1 \cos\left(k\pi\frac{x-c}{d-c}\right) + c_2 \sin\left(k\pi\frac{x-c}{d-c}\right).$$

One can see that $u(c) = c_1, u(d) = c_1(-1)^k$ that implies the conclusion. □

Theorem 6.2.1. *Let $U(\mathbf{r})$ be an eigenfunction of the Dirichlet-Laplace operator in Ω. Then, $\exists i \in \{1, 2, \ldots, K\}$, $U(D_i) = 0$ if and only if the corresponding eigenvalue λ belongs to E. In addition, if $\exists i \in \{1, 2, \ldots, K\}$ such that $U(D_i) = 0$, then $U(D_j) = 0, \forall j$.*

Proof. We prove the above theorem for $K = 2$, while other cases are similar.

Without loss of generality, we assume that $i = 1$.

($\rightarrow$) If $U(\mathbf{r})$ is an eigenfunction of the Dirichlet-Laplace in Ω such that $U(D_1) = 0$, it is also an eigenfunction of the Dirichlet-Laplace at least in one of the intervals: $A_1 D_1$, $D_1 B_1$, $C_1 D_1$ and $D_1 D_2$. As a result, the corresponding eigenvalue λ belongs to E.

($\leftarrow$) Suppose that the corresponding eigenvalue λ of $U(\mathbf{r})$ is equal to $\frac{k^2\pi^2}{d_1^2}$ for some positive integer k and $U(D_1) = a$. If $a \neq 0$, from the continuity of the eigenfunction $U(\mathbf{r})$, $U(\mathbf{r}) \neq 0$ in the sub-interval $A_1 D_1$. For this reason, $U(\mathbf{r})$ is an eigenfunction of the Laplace operator in $A_1 D_1$ and satisfies $U(A_1) = 0$ and $U(D_1) = a$. Using Lemma 6.2.2, it only occurs when $a = 0$. It is contradictory to our initial assumption. So, $U(D_1) = 0$. Similarly, $U(D_2) = 0$.

If λ is equal to $\frac{m^2\pi^2}{d_2^2}$ for some positive integer m, one can prove that $U(D_i) = 0$ for all i. □

Theorem 6.2.2. *Suppose that $\Omega_i = \Omega \setminus A_i B_i, \forall i \in \{1, 2, \ldots, K\}$, then*

$$C_p(\Omega_i) \equiv \inf_u \left\{ \frac{\|u\|_{L^p(\Omega_i)}}{\|u\|_{L^p(\Omega)}} \right\} = 0, \tag{6.6}$$

for any $p \geq 1$ and $i = 1, 2, \ldots, K$. Here, u is an eigenfunction of Dirichlet-Laplace operator in Ω.

Proof. From the above theorem, for each $i \in \{1, 2, \ldots, K\}$, one can choose an eigenfunction $U(\mathbf{r})$ such that $U(D_i) = 0$ and $U(\mathbf{r}) = 0$ in Ω_i. It is easy to see that

$$\frac{\|U\|_{L^p(\Omega_i)}}{\|U\|_{L^p(\Omega)}} = 0,$$

for any $p \geq 1$, that implies the conclusion. □

Theorem 6.2.3. *Let $\mathbb{Q}$ be the set of rational numbers and λ is an eigenvalue of the Dirichlet-Laplace operator in Ω. Then,*

a) If $\lambda \notin E$, its multiplicity is 1.

b) If $\dfrac{d_1}{d_2} \notin \mathbb{Q}$ and $\lambda \in E$:

- *If $\lambda \in E_1$, its multiplicity is K and the corresponding eigenfunction $U(\mathbf{r}) = 0$, $\mathbf{r} \in C_1 C_2$.*

- *If $\lambda \in E_2$, its multiplicity is 1 and the corresponding eigenfunction $U(\mathbf{r}) = 0$, $\mathbf{r} \in A_i B_i, \forall i$.*

c) If $\dfrac{d_1}{d_2} = \dfrac{r_1}{r_2} \in \mathbb{Q}$ (the greatest common divisor of two positive integers r_1 and r_2 is 1) and $\lambda = \frac{k^2 \pi^2}{d_1^2} \in E_1$:

- *If k is not a multiple of r_1, the multiplicity of λ is K and the corresponding eigenfunction $U(\mathbf{r}) = 0$, $\mathbf{r} \in C_1 C_2$.*

- *Otherwise, its multiplicity is $2K + 1$.*

d) If $\dfrac{d_1}{d_2} = \dfrac{r_1}{r_2} \in \mathbb{Q}$ (the greatest common divisor of two positive integers r_1 and r_2 is 1) and $\lambda = \frac{m^2 \pi^2}{d_2^2} \in E_2$:

- *If m is not a multiple of r_2, the multiplicity of λ is 1 and the corresponding eigenfunction $U(\mathbf{r}) = 0$, $\mathbf{r} \in A_i B_i, \forall i$.*

- *Otherwise, its multiplicity is $2K + 1$.*

Proof. We prove the above theorem for $K = 2$, while other cases are similar.

a) We assume that $\lambda \notin \mathbb{E}$ and its multiplicity is greater than 1. Then, λ has at least two linearly independent and normalized eigenfunctions U_1 and U_2.

If $U_1(D_1) = a$ and $U_2(D_1) = b$ $(a, b \neq 0)$, one considers the following function

$$U = bU_1 - aU_2. \tag{6.7}$$

Note that $U \neq 0$ and U satisfies the boundary condition in Ω. It is easy to check that U is also an eigenfunction corresponding to λ. Moreover,

$$U(D_1) = ba - ab = 0, \tag{6.8}$$

that implies $\lambda \in E$ (from Theorem 6.2.1). It is contradictory to our initial assumption. Consequently, λ has the multiplicity 1.

b) Using Theorems 6.2.1 and 6.2.2.

c-d) Using Theorems 6.2.1 and 6.2.2 and a similar proof as the above case (a).

$\square$

Remark 6.2.1. *In this section, an eigenfunction is considered to be localized if it is mainly distributed in a small region of the domain, and decays rapidly outside the region.*

- *From Theorem 6.2.3, one can easily find the multiplicities of the Laplacian eigenvalues in the graph Ω.*

- *If $\dfrac{d_1}{d_2} \notin \mathbb{Q}$, a localized eigenfunction is distributed either in vertical lines, or in the horizontal line $C_1 C_2$, but not on both of them.*

- *If $\dfrac{d_1}{d_2} \in \mathbb{Q}$, a localized eigenfunction is distributed either in vertical lines, or in the horizontal line $C_1 C_2$, or in both.*

6.2.1   Numerical implementation

We use a Finite Difference scheme for solving the Laplace eigenvalue problem in Ω. First, we compute the stiffness matrix L of the Laplace operator in the domain, and then solve the eigenvalue problem of the matrix L.

Definition 6.2.1. *For a given N, we define the matrix*

$$
B_N = \begin{pmatrix}
2 & -1 & 0 & 0 & \ldots & 0 & 0 \\
-1 & 2 & -1 & 0 & \ldots & 0 & 0 \\
0 & -1 & 2 & -1 & \ldots & 0 & 0 \\
\ldots & \ldots & \ldots & \ldots & \ldots & \ldots & \ldots \\
0 & 0 & \ldots & -1 & 2 & -1 & 0 \\
0 & 0 & \ldots & 0 & -1 & 2 & -1 \\
0 & 0 & \ldots & 0 & 0 & -1 & 2
\end{pmatrix}_{N \times N}
\tag{6.9}
$$

and

$$
C_N = B_{2N+1} + 2z_0^T z_0, \qquad z_0 = \begin{bmatrix} 0 & \ldots & 0 & 1 & 0 & \ldots & 0 \end{bmatrix}_{1 \times (2N+1)}.
\tag{6.10}
$$

Here, $z_0(N+1) = 1$, otherwise $z_0(i) = 0$.

6.2.1.1   Stiffness matrix

For an easier implementation, we assume that $d_1 = q_1 l_0$, $d_2 = q_2 l_0$, $q_1, q_2 \in \mathbb{N}^*$. For each $M = q_1 p - 1$ and $M = q_2 p - 1$ $(p \in \mathbb{N}^*)$, we divide all vertical lines $A_1 D_1$, $D_1 B_1$, $A_2 D_2$, $D_2 B_2$, $\ldots$, $A_K D_K$, $D_K B_K$ into $M + 1$ identical subintervals and all horizontal lines $C_1 D_1$, $D_1 D_2$, $\ldots$, $D_{K-1} D_K$, $D_k C_2$ into $N + 1$ identical subintervals of length $d_p = \frac{l_0}{p}$ (Fig. 6.2a).

In this mesh, one can approximate the Laplace operator at x_i^k and y_j^k via the following formulas

- $k = 0$

$$
\triangle u(x_i^k) = \begin{cases}
\dfrac{1}{d_p^2} \left[-2u(x_1^k) + u(x_{i+1}^k) \right] & (i = 1), \\[2mm]
\dfrac{1}{d_p^2} \left[u(x_{i-1}^k) - 2u(x_i^k) + u(x_{i+1}^k) \right] & (1 < i < N), \\[2mm]
\dfrac{1}{d_p^2} \left[u(x_{i-1}^k) - 2u(x_i^k) + u(D_{k+1}) \right] & (i = N).
\end{cases}
\tag{6.11}
$$

- $0 < k < K$

$$
\triangle u(x_i^k) = \begin{cases} \dfrac{1}{d_p^2}\left[u(D_k) - 2u(x_1^k) + u(x_{i+1}^k)\right] & (i = 1)\,, \\[2mm] \dfrac{1}{d_p^2}\left[u(x_{i-1}^k) - 2u(x_i^k) + u(x_{i+1}^k)\right] & (1 < i < N)\,, \\[2mm] \dfrac{1}{d_p^2}\left[u(x_{i-1}^k) - 2u(x_i^k) + u(D_{k+1})\right] & (i = N)\,, \end{cases}
$$

$$
\triangle u(y_j^k) = \begin{cases} \dfrac{1}{d_p^2}\left[-2u(y_j^k) + u(x_{j+1}^k)\right] & (j = 1)\,, \\[2mm] \dfrac{1}{d_p^2}\left[u(x_{j-1}^k) - 2u(y_j^k) + u(x_{j+1}^k)\right] & (1 < i < M) \vee (M + 1 < j < 2M)\,, \\[2mm] \dfrac{1}{d_p^2}\left[u(x_{j-1}^k) - 2u(y_j^k) + u(D_k)\right] & (j = M)\,, \\[2mm] \dfrac{1}{d_p^2}\left[u(D_k) - 2u(y_j^k) + u(x_{j+1}^k)\right] & (i = M + 1)\,, \\[2mm] \dfrac{1}{d_p^2}\left[u(x_{j-1}^k) - 2u(y_j^k)\right] & (j = 2M)\,. \end{cases}
$$

(6.12)

- $k = K$

$$
\triangle u(x_i^k) = \begin{cases} \dfrac{1}{d_p^2}\left[u(D_k) - 2u(x_1^k) + u(x_{i+1}^k)\right] & (i = 1)\,, \\[2mm] \dfrac{1}{d_p^2}\left[u(x_{i-1}^k) - 2u(x_i^k) + u(x_{i+1}^k)\right] & (1 < i < N)\,, \\[2mm] \dfrac{1}{d_p^2}\left[u(x_{i-1}^k) - 2u(x_i^k)\right] & (i = N)\,, \end{cases}
$$

$$
\triangle u(y_j^k) = \begin{cases} \dfrac{1}{d_p^2}\left[-2u(y_j^k) + u(x_{j+1}^k)\right] & (j = 1)\,, \\[2mm] \dfrac{1}{d_p^2}\left[u(x_{j-1}^k) - 2u(y_j^k) + u(x_{j+1}^k)\right] & (1 < i < M) \vee (M + 1 < j < 2M)\,, \\[2mm] \dfrac{1}{d_p^2}\left[u(x_{j-1}^k) - 2u(y_j^k) + u(D_k)\right] & (j = M)\,, \\[2mm] \dfrac{1}{d_p^2}\left[u(D_k) - 2u(y_j^k) + u(x_{j+1}^k)\right] & (j = M + 1)\,, \\[2mm] \dfrac{1}{d_p^2}\left[u(x_{j-1}^k) - 2u(y_j^k)\right] & (j = 2M)\,. \end{cases}
$$

(6.13)

Using the above approximation, the eigenvalue equation becomes

$$
Au + \lambda u = 0,
$$

(6.14)
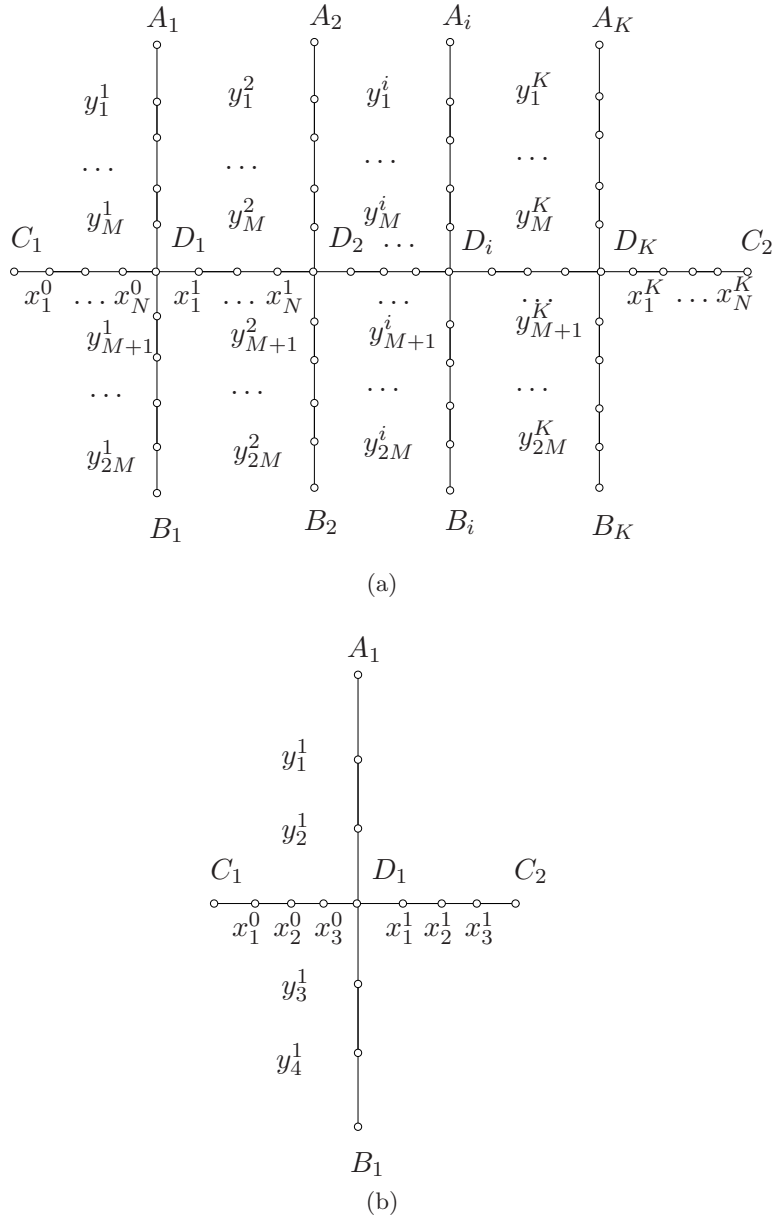
Figure 6.2: A mesh decomposition in a planar graph G: (a) - a general mesh for positive integers K, M and N, (b) - an example with $K = 1$, $M = 2$ and $N = 3$.

where the stiffness matrix A of the Laplace operator has a blocked structure

$$A = \frac{-1}{d_p^2} \begin{pmatrix} B_N & A_{1,2} & 0 & 0 & & \cdots & & 0 & 0 \\ A_{2,1} & C_M & A_{2,3} & 0 & & \cdots & & 0 & 0 \\ 0 & A_{3,2} & B_N & A_{3,4} & & \cdots & & 0 & 0 \\ \cdots & \cdots & \cdots & \cdots & & \cdots & & \cdots & \cdots \\ 0 & 0 & \cdots & A_{2K-1,2K-2} & B_N & & A_{2K-1,2K} & 0 \\ 0 & 0 & \cdots & 0 & & A_{2K,2K-1} & C_M & A_{2K,2K+1} \\ 0 & 0 & \cdots & 0 & & 0 & & A_{2K+1,2K} & B_N \end{pmatrix} \tag{6.15}$$

For $1 \leq i \leq K$, the matrix A has the size $P \times P$, matrices $A_{2i,2i-1} = A_{2i-1,2i}^T$ have the size $P_1 \times P_2$ and matrices $A_{2i+1,2i} = A_{2i,2i+1}^T$ have the size $P_2 \times P_1$, where

$$P = (2M + N + 1)K + N, \qquad P_1 = N, \qquad P_2 = 2M + 1. \tag{6.16}$$

Moreover, $A_{2i,2i-1}(j,k) = 0$, $A_{2i+1,2i}(j,k) = 0$ except

$$A_{2i,2i-1}(M+1, N) = -1, \qquad A_{2i+1,2i}(1, M+1) = -1. \tag{6.17}$$

For a better illustration, we consider the following example.

Example 6.2.1. *When $K = 1$, $M = 2$ and $N = 3$ (Fig. 6.2b),*

$$A = \frac{-1}{d_p^2} \begin{pmatrix} 2 & -1 & 0 & 0 & 0 & 0 & 0 & 0 & 0 & 0 & 0 \\ -1 & 2 & -1 & 0 & 0 & 0 & 0 & 0 & 0 & 0 & 0 \\ 0 & -1 & 2 & 0 & 0 & -1 & 0 & 0 & 0 & 0 & 0 \\ 0 & 0 & 0 & 2 & -1 & 0 & 0 & 0 & 0 & 0 & 0 \\ 0 & 0 & 0 & -1 & 2 & -1 & 0 & 0 & 0 & 0 & 0 \\ 0 & 0 & -1 & 0 & -1 & 4 & -1 & 0 & -1 & 0 & 0 \\ 0 & 0 & 0 & 0 & 0 & -1 & 2 & -1 & 0 & 0 & 0 \\ 0 & 0 & 0 & 0 & 0 & 0 & -1 & 2 & 0 & 0 & 0 \\ 0 & 0 & 0 & 0 & 0 & -1 & 0 & 0 & 2 & -1 & 0 \\ 0 & 0 & 0 & 0 & 0 & 0 & 0 & 0 & -1 & 2 & -1 \\ 0 & 0 & 0 & 0 & 0 & 0 & 0 & 0 & 0 & -1 & 2 \end{pmatrix}$$

6.2.1.2   Eigendecomposition of the matrix A

For solving the eigenvalue problem for the matrix A in Eq. (6.15), one can use classical algorithms for symmetric matrices. For instance, one can find its eigendecomposition in Matlab by one of two functions *eig* or *eigs*.

We propose a fast and efficient divide-and-conquer algorithm to compute the eigensystem of all symmetric

matrices H having similar structures to the matrix A as following [161]:

$$H = \begin{pmatrix} H_{11} & H_{12} & 0 & 0 & \ldots & 0 \\ H_{21} & H_{22} & H_{23} & 0 & \ldots & 0 \\ 0 & H_{32} & H_{33} & H_{34} & \ldots & 0 \\ \ldots & \ldots & \ldots & \ldots & \ldots & \ldots \\ 0 & 0 & 0 & \ldots & H_{K,K-1} & H_{KK} \end{pmatrix} \tag{6.18}$$

where $H_{ij} \in \mathbb{R}^{(2M+1)\times(2M+1)}$, $H_{i,i+1}$ has only one non-zero entry, $H_{i+1,i} = H_{i,i+1}^T$, and $P = (2M+1)K$ is the size of the matrix H. The approach avoids the tridiagonalization step in classical algorithms which mostly costs $O(P^3)$ multiplications, and the algorithm only costs $O(KM^3) + O(P^2)$ i.e. faster than classical algorithms when $K \gg M$. One can see in [161] for details.

In Section 6.3, we will present an algorithm for computing the eigendecomposition of the Laplacian matrix in a weighted, undirected graph $G = (V, E, \omega)$. One can also apply the new algorithm for finding the eigendecomposition of the matrix A.

6.2.2   Numerical results

In this section, we solve the Laplacian eigenproblem in several graphs and visualize some localized eigenmodes in these domains.

Example 6.2.2. *We consider a graph Ω of two vertical lines of sides $d_1 = 0.5$ and $d_2 = \frac{\pi}{5}$. It is easy to see that*

$$E_1 = \left\{4k^2\pi^2 : k = 1, 2, \ldots\right\}, E_2 = \left\{25m^2 : m = 1, 2, \ldots\right\}. \tag{6.19}$$

Since $\dfrac{d_1}{d_2} = \dfrac{5}{\pi} \notin \mathbb{Q}$, from Theorem 6.2.3, all eigenfunctions corresponding to eigenvalues $\lambda \in E_1$ are localized in vertical lines, while if $\lambda \in E_2$, the corresponding eigenfunction is localized in the horizontal line C_1C_2.

Table 6.1 presents the first 10 eigenvalues computed with $M = 300$ and $N = 101$. The numerical values $\lambda_3 = 24.9995 \approx 25 \in E_2$ and $\lambda_{10} = 99.9919 \approx 100 \in E_2$, so that two eigenfunctions u_3 and u_{10} are supported in the horizontal line C_1C_2 (Fig. 6.3).

In addition, $\lambda_6 = \lambda_7 \approx 4\pi^2$ and $\lambda_{13} = \lambda_{14} \approx 16\pi^2$, so that the corresponding eigenfunctions u_6, u_7, u_{13} and u_{14} are localized in vertical lines A_1B_1 and A_2B_2 (Fig. 6.3).

Example 6.2.3. *In this example, we assume that $K = 2$, $d_1 = 0.5$ and $d_2 = \frac{1}{3}$. Then,*

$$E_1 = \left\{4k^2\pi^2 : k = 1, 2, \ldots\right\}, \quad E_2 = \left\{9m^2\pi^2 : m = 1, 2, \ldots\right\}. \tag{6.20}$$

Since $\dfrac{d_1}{d_2} = \dfrac{3}{2}$, from Theorem 6.2.3, the multiplicity of $\lambda \in \{4\pi^2, 16\pi^2, 9\pi^2\}$ is 2, and the multiplicity of $\lambda = 36\pi^2$ is 5.

For computing Laplacian eigenproblem in this graph, we use $M = 300$ and $N = 601$. In Table 6.1, $\lambda_3 = \lambda_4 = 39.4781 \approx 4\pi^2$, $\lambda_{10} = \lambda_{11} = 157.9079 \approx 16\pi^2$ and $\lambda_{14}, \lambda_{15}, \lambda_{16}, \lambda_{17}, \lambda_{18} \approx 36\pi^2$. These

i	$d_2 = \frac{\pi}{5}$	$d_2 = \frac{1}{3}$	i	$d_2 = \frac{\pi}{5}$	$d_2 = \frac{1}{3}$
1	4.8622	9.8805	11	119.8694	157.9079
2	10.7213	24.5008	12	134.9594	193.3879
3	24.9995	39.4781	13	157.8627	247.0077
4	30.1449	39.4781	14	157.8627	355.2767
5	34.0202	45.4036	15	181.4601	355.2767
6	39.4752	55.9341	16	199.0515	355.2801
7	39.4752	88.8262	17	224.9954	355.2847
8	60.5574	129.399	18	267.7518	355.3025
9	75.6610	146.7115	19	299.2119	484.1251
10	99.9919	157.9079	20	355.2767	566.6966

Table 6.1:   The first 15 Laplacian eigenvalues in the graph Ω with $K = 2$, $d_1 = 0.5$ and $d_2 = \frac{\pi}{5}$.

numerical results fit to Theorem 6.2.3.

Since $\lambda_7 \approx 9\pi^2 \in E_2$, u_7 is localized in the horizontal line C_1C_2 (Fig. 6.4). In addition, the eigenfunction u_{18} is also localized in this line.

6.2.3 Discussion

In Section 6.2, we have already studied the Laplacian eigenproblem in several graphs Ω as shown on Fig. 6.1. By Theorem 6.2.3, one can easily obtain the multiplicity of each Laplacian eigenvalue. Moreover, we also give a *mechanism* of localized eigenmodes in this domain. In the next section, we study Laplacian eigenvalue problem in a weighted graph $G = (V, E, \omega)$ and give a fast and efficient algorithm for solving the eigendecomposition of Laplacian matrix in G.

6.3   Laplacian eigenvalue problem in a weighted graph

Motivated from the previous section, we consider a weighted undirected graph $G = (V, E, \omega)$ of n vertices, $n = |V|$, and m edges, $m = |E|$, with a positive function $\omega : E \to \mathbb{R}$ (Fig. 6.6). We suppose that G has K disjoint connected weighted subgraphs $G_1, G_2, \ldots, G_K$ in which $G_i = (V_i, E_i, \omega)$, $n_i = |V_i|$ and $m_i = |E_i|$ and each pair of the consecutive subgraphs $\{G_i, G_{i+1}\}$ can be connected by an edge with weight w_i ($1 \leq i < k$). In the graph G, its adjacency matrix, denoted A_G, is

$$A_G(i,j) = \begin{cases} w(i,j) & \text{if } (i,j) \in E \\ 0 & \text{otherwise,} \end{cases} \tag{6.21}$$

and its degree matrix, denoted D_G, is a diagonal matrix of size $n \times n$ such that

$$D_G(i,i) = \sum_{(i,j) \in E} A_G(i,j). \tag{6.22}$$

(a) u_3

(b) u_6

(c) u_7

(d) u_{10}

(e) u_{13}

(f) u_{14}
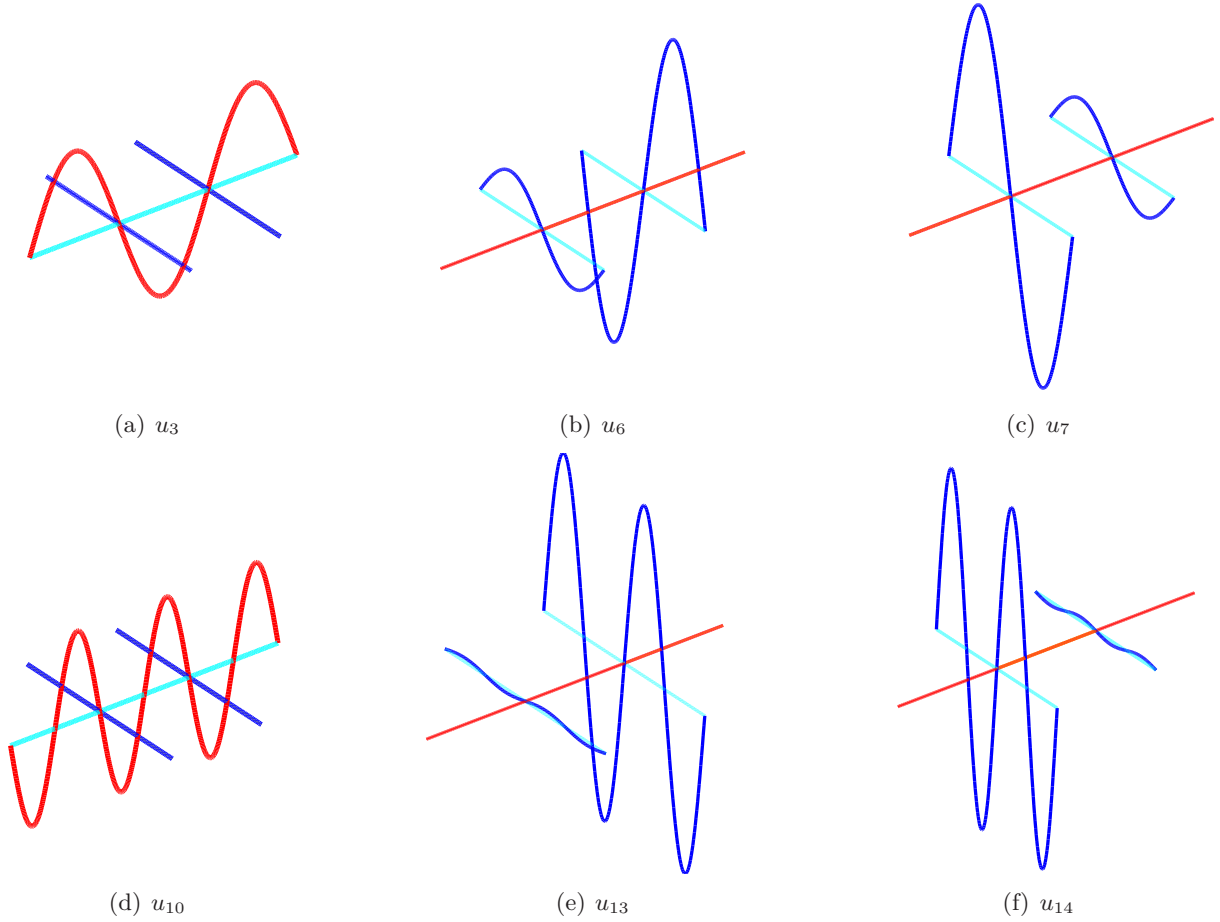
Figure 6.3: Some localized eigenfunctions in the graph Ω with $d_1 = 0.5$ and $d_2 = \frac{\pi}{5}$. The eigenfunctions u_3 and u_{10} are localized in the horizontal line (cases a, d), while the eigenfunctions u_6, u_7, u_{13} and u_{14} are distributed in the vertical lines (cases b, c, e, f). The red and blue lines represent the values of the eigenfunction in the horizontal line $C_1 C_2$ and in vertical lines, respectively.

The Laplacian matrix L_G of the weighted graph G can now be defined by

$$L_G = D_G - A_G. \tag{6.23}$$

For example, if G is a weighted graph as shown in Fig. 6.5, its adjacency, degree and Laplacian matrices are given as follows

$$A_G = \begin{pmatrix} 0 & 1 & 1 \\ 1 & 0 & 1 \\ 1 & 1 & 0 \end{pmatrix}, \; D_G = \begin{pmatrix} 2 & 0 & 0 \\ 0 & 2 & 0 \\ 0 & 0 & 2 \end{pmatrix}, \; L_G = \begin{pmatrix} 2 & -1 & -1 \\ -1 & 2 & -1 \\ -1 & -1 & 2 \end{pmatrix}. \tag{6.24}$$

In this section, we are only interested in finding the eigendecomposition of Laplacian matrices L_G. Classically, one can solve this problem in $O(n^3)$ time. We aim at answering the question "*If one knows all*

(a) u_7 (b) u_{18}
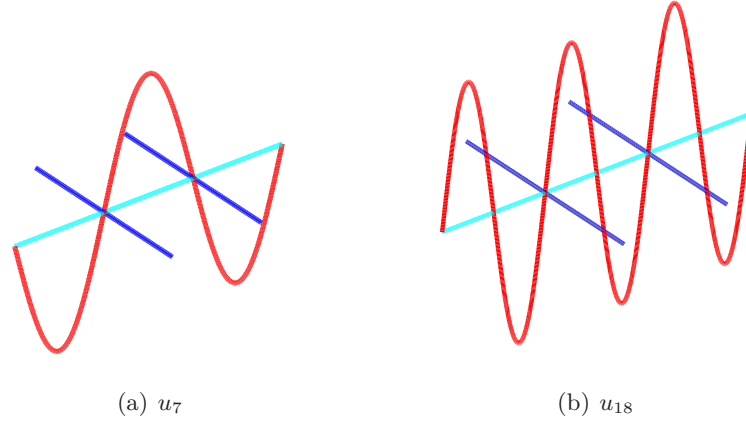
Figure 6.4: Some localized eigenfunctions in the graph Ω with $d_1 = 0.5$ and $d_2 = \frac{1}{3}$. The eigenfunctions u_7 and u_{18} are localized in the horizontal line. The red and blue lines represents the values of the eigenfunction in the horizontal line C_1C_2 and in vertical lines, respectively.
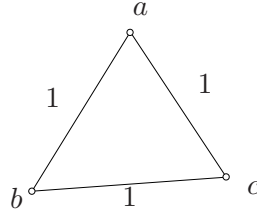
Figure 6.5:   The ring graph R_3 with three vertices $\{a, b, c\}$ and three weighted edges: $w(a,b) = w(a,c) = w(b,c) = 1$.

eigendecompositions of the Laplacian matrices $L_{G_1}, L_{G_2}, \ldots, L_{G_k}$ in subgraphs $G_1, G_2, \ldots, G_k$, can one use this knowledge to reduce the complexity of numerical computation ? "

6.3.1   Description of the problem

For notational convenience, we assume that

- G_i has n_i vertices $V_i = \left\{v_1^{(i)}, v_2^{(i)}, \ldots, v_{n_i}^{(i)}\right\}$ and $p_i = n_1 + \cdots + n_i$, for all $i = 1, 2, \ldots, K$.

- There exist $a_1 \in \{1, 2, \ldots, n_1\}$, $b_2 \in \{1, 2, \ldots, n_2\}$ such that G_1 is connected to G_2 by a weighted undirected edge $v_{a_1}^{(1)} \xrightarrow{w_1} v_{b_2}^{(2)}$, and $D_1, E_{1,2}$ are the matrices of size $n_1 \times n_1$ and $n_2 \times n_1$ respectively,

$$D_1(j,k) = \begin{cases} w_1 & (j,k) \equiv (a_1, a_1) \\ 0 & \text{otherwise} \end{cases}$$

$$E_{1,2}(j,k) = \begin{cases} -w_1 & (j,k) \equiv (a_1, b_2) \\ 0 & \text{otherwise} \end{cases} \qquad (6.25)$$
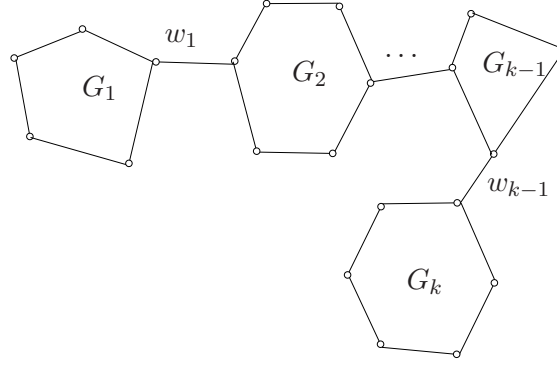
Figure 6.6:   A weighted undirected graph G.

- For each $i = 2, \ldots, K - 2$, there exist $a_i \in \{1, 2, \ldots, n_i\}$, $b_{i+1} \in \{1, 2, \ldots, n_{i+1}\}$ such that G_i is connected to G_{i+1} by a weighted undirected edge $v_{a_i}^{(i)} \xrightarrow{w_i} v_{b_{i+1}}^{(i+1)}$, and D_i, $E_{i,i+1}$ are the matrices of size $n_i \times n_i$ and $n_{i+1} \times n_i$ respectively,

$$D_i(j,k) = \begin{cases} w_{i-1} & (j,k) \equiv (b_i, b_i) \\ w_i & (j,k) \equiv (a_i, a_i) \\ 0 & \text{otherwise} \end{cases}$$

$$E_{i,i+1}(j,k) = \begin{cases} -w_i & (j,k) \equiv (a_i, b_{i+1}) \\ 0 & \text{otherwise} \end{cases} \tag{6.26}$$

When $a_i = b_i$, one has

$$D_i(j,k) = \begin{cases} w_{i-1} + w_i & (j,k) \equiv (b_i, b_i) \\ 0 & \text{otherwise} \end{cases} \tag{6.27}$$

- There exist $a_{K-1} \in \{1, 2, \ldots, n_{K-1}\}$ and $b_K \in \{1, 2, \ldots, n_K\}$ such that G_{K-1} is connected to G_K by a weighted undirected edge $v_{a_{K-1}}^{(K-1)} \xrightarrow{w_{K-1}} v_{b_K}^{(K)}$, and D_{K-1}, $E_{K-1,K}$ are the matrices of size $n_{K-1} \times n_{K-1}$ and $n_K \times n_{K-1}$ respectively,

$$D_{K-1}(j,k) = \begin{cases} w_{K-2} & (j,k) \equiv (b_{K-1}, b_{K-1}) \\ w_{K-1} & (j,k) \equiv (a_{K-1}, a_{K-1}) \\ 0 & \text{otherwise} \end{cases}$$

$$E_{K-1,K}(j,k) = \begin{cases} -w_{K-1} & (j,k) \equiv (a_{K-1}, b_K) \\ 0 & \text{otherwise} \end{cases} \tag{6.28}$$

When $a_{K-1} = b_{K-1}$, one has

$$D_{K-1}(j,k) = \begin{cases} w_{K-2} + w_{K-1} & (j,k) \equiv (b_{K-1}, b_{K-1}) \\ 0 & \text{otherwise} \end{cases} \tag{6.29}$$

- Finally, D_K is the matrix of size $n_K \times n_K$:

$$D_K(j,k) = \begin{cases} w_{K-1} & (j,k) \equiv (b_K, b_K) \\ 0 & \text{otherwise} \end{cases} \tag{6.30}$$

Remark 6.3.1. *It is worth noting that a_i may be equal to b_i for some i.*

From the above assumption, L_G can be represented as

$$L_G = \begin{pmatrix} L_{G_1} & 0 & 0 & \dots & 0 \\ 0 & L_{G_2} & 0 & \dots & 0 \\ 0 & 0 & L_{G_3} & \dots & 0 \\ \dots & \dots & \dots & \dots & \dots \\ 0 & 0 & \dots & 0 & L_{G_K} \end{pmatrix} + \begin{pmatrix} D_1 & E_{1,2} & 0 & \dots & 0 \\ E_{2,1} & D_2 & E_{2,3} & \dots & 0 \\ 0 & E_{3,2} & D_3 & \dots & \dots \\ \dots & \dots & \dots & \dots & E_{K-1,K} \\ 0 & 0 & \dots & E_{K,K-1} & D_K \end{pmatrix}, \tag{6.31}$$

where $E_{i,i+1} = E_{i+1,i}^T, \forall i \in \{1, 2, \dots, K-1\}$.
We can now address the problem:

Problem 6.3.1. *Suppose we have already known the eigendecompositions $L_{G_i} = U_i D_i U_i^T, \forall i \in \{1, 2, \dots, K\}$, can we use this knowledge to compute the eigenvalue problem of the Laplacian matrix L_G in (6.31) more efficiently than by traditional algorithms?*

6.3.2   Description of the method

Laplacian matrices of weighted graphs are symmetric and positive semi-definite. As a consequence, all eigenvalues are non-negative and any algorithm for solving a symmetric eigensystem is applicable. Before showing our approach, we summarize some traditional algorithms.

6.3.2.1   Traditional methods

Traditionally, there are two phases to compute the eigendecomposition of a symmetric matrix A of size n:

- In the first phase, one transforms A into a symmetric tridiagonal matrix T by a sequence of orthogonal similarity transformations:

$$T = Q_k^T \cdots Q_2^T Q_1^T A Q_1 Q_2 \cdots Q_k \tag{6.32}$$

- In the second phase, one computes the corresponding eigendecomposition of the tridiagonal matrix T:

$$T = VDV^T, \tag{6.33}$$

  where V is an orthogonal matrix and D is diagonal.

- Finally, the eigendecomposition of the matrix A is

$$A = UDU^T, \tag{6.34}$$

  where $U = Q_1 Q_2 \cdots Q_k V^T$.

For tridiagonalizing an $n \times n$ symmetric matrix, one can apply Householder algorithm [113], which uses $n-2$ orthogonal reflectors. The total cost in this step is $O(n^3)$ in time. For computing the eigendecomposition of a tridiagonal matrix, one can use one of the most classical algorithms called QR algorithm that costs $O(n^2)$ in time. This algorithm was independently studied by Francis [79] and Kublanovskaja [132] in 1961.

In 1978, Bunch and co-workers [33] presented an efficient algorithm for computing the eigensystem of the rank-one modification of a symmetric matrix with known eigendecompostion. In 1981, motivated in Bunch's paper, Cuppen proposed an efficient divide-and-conquer algorithm of the symmetric tridiagonal eigenproblem [56]. His algorithm could asymptotically be faster than traditional QR algorithm. In 1991, by using arrowhead matrices and fast multiploe method, Gu and his colleagues [87, 88] proposed another fast and stable divide-and-conquer algorithm for computing the eigensystem of a symmetric tridiagonal matrix with improvements on the orthogonality of eigenvectors. In 1997, Dhillon investigated an $O(n^2)$ algorithm for computing both eigenvalues and eigenvectors of a tridiagonal matrix [63]. For the eigenvalue problem of a non-symmetric and tridiagonal matrix, a fast algorithm was proposed by Bini et al. [25], using Ehrlich-Aberth interations. In 2007, Slemons presented, in his thesis [204], a fast and accurate algorithm costing $O(n^2)$ flops for computing both eigenvectors and eigenvalues of a non-symmetric and tridiagonal matrix.

6.3.2.2   Our approach

In the previous section, computing the eigendecomposition of the matrix L_G costs $O(p_K^3)$ in time. In this section, we will consider the case $n_1 = n_2 = \cdots = n_K = N$, $\omega_i \neq 0, \forall i = 1, \ldots, K$, and present an efficient divide-and-conquer algorithm to solve this eigenproblem.

Our algorithm consists of two steps: dividing step and conquering step. In the dividing step, we reduce the eigenproblem from the original matrix into small-size submatrices recursively, and then, we solve the eigenproblem in each submatrix by a classical algorithm. In the conquering step, by using all eigendecompositions computed from these submatrices, we obtain step by step the eigendecomposition of the matrix L_G.

6.3.3 A divide-and-conquer approach for Laplacian matrix L_G

6.3.3.1 Dividing Step

For a better explanation, we denote $M(i,j)$ the entry (i,j) of the matrix M and $a(i)$ the ith element of the vector a. For any $i \leq j$, we also denote $G_{i \to j} = (V_{i \to j}, E_{i \to j}, \omega)$ a subgraph of graph G, where $V_{i \to j} = V_i \cup V_{i+1} \cup \cdots \cup V_j$ and $E_{i \to j} = E_i \cup E_{i+1} \cup \cdots \cup E_j$. Next, we call $L_{G_{i \to j}}$ the Laplacian matrix of the subgraph $G_{i \to j}$.

Now, we represent the matrix L_G as following

$$L_G = \begin{pmatrix} L_{G_{1 \to k}} & 0 \\ 0 & L_{G_{k+1 \to K}} \end{pmatrix} + \begin{pmatrix} B_{11} & B_{12} \\ B_{21} & B_{22} \end{pmatrix}$$

where

$$B_{11}(j,k) = \begin{cases} w_k & (j,k) \equiv (a_k, a_k) \\ 0 & \text{otherwise} \end{cases}$$

$$B_{12}(j,k) = \begin{cases} -w_k & (j,k) \equiv (a_k, b_{k+1}) \\ 0 & \text{otherwise} \end{cases}$$

(6.35)

$$B_{22}(j,k) = \begin{cases} w_k & (j,k) \equiv (b_{k+1}, b_{k+1}) \\ 0 & \text{otherwise} \end{cases}$$

$$B_{12}(j,k) = B_{12}^T$$

(6.36)

and

$$k = \left\lfloor \frac{K}{2} \right\rfloor$$

Using rank-one decomposition, the matrix L_G can be decomposed as following

$$L_G = \begin{pmatrix} L_{G_{1 \to k}} & 0 \\ 0 & L_{G_{k+1 \to K}} \end{pmatrix} + \rho z z^T$$

(6.37)

where $\rho = 2\omega_k$ and z has only two non-zero entries

$$z(i_1) = \frac{1}{\sqrt{2}}, \ z(j_1) = -\frac{1}{\sqrt{2}}.$$

(6.38)

Here, $i_1 = p_{k-1} + a_k$ and $j_1 = p_k + b_{k+1}$.

By this way, we split the original problem for two eigenproblems of two half-size submatrices. Recursively, we continue dividing these matrices until they have only one block L_{G_i} for $i = 1, 2, ..., N$. At this step, we use the eigendecomposition of $L_{G_i} = U_i D_i U_i^T, \forall i = 1, 2, .., N$.

6.3.3.2   Conquering step

In this step, our goal is to compute the eigendecomposition of L_G in Eq. (6.37) given that $Q_1 D_1 Q_1^T$ and $Q_2 D_2 Q_2^T$ are eigendecompositions of $L_{G_{1 \to k}}$ and $L_{G_{k+1 \to K}}$ respectively. We can rewrite Eq. (6.37) as

$$L_G = \begin{pmatrix} Q_1 D_1 Q_1^T & 0 \\ 0 & Q_2 D_2 Q_2^T \end{pmatrix} + \rho z z^T = Q D Q^T + \rho z z^T \tag{6.39}$$

where

$$Q = \begin{pmatrix} Q_1 & 0 \\ 0 & Q_2 \end{pmatrix}, \qquad D = \begin{pmatrix} D_1 & 0 \\ 0 & D_2 \end{pmatrix}. \tag{6.40}$$

For computing the eigendecomposition of L_G in Eq. (6.39), one can use the rank-one modification method of symmetric eigenproblem [33]. The algorithm which was proposed by Bunch et al [33] consists of three steps:

1. Initial deflation.

2. Solving the secular equation to compute the eigenvalues of the matrix L_G.

3. Computing its eigenvectors.

Deflation occurs when $x = Q^T z$ has zero entries or there exists an entry i^{th} of the vector z such that $|z(i)| = 1$. Deflation also happens when D has degenerate eigenvalues. It means that there exist k diagonal entries $\{i_1, i_2, \cdots, i_k\}$ of the matrix D such that $d_{i_1} = \cdots = d_{i_k}$. The details of the initial deflation step were stated explicitly in [33].

After initial deflation step, we suppose that $k \times k$ is the size of the deflated system. One obtains

$$L_G = \tilde{Q}(\tilde{D} + \rho z z^T)\tilde{Q}^T = (\tilde{Q}_1, \tilde{Q}_2) \begin{pmatrix} \tilde{D}_1 & 0 \\ 0 & \tilde{D}_2 + \rho z_2 z_2^T \end{pmatrix} (\tilde{Q}_1, \tilde{Q}_2)^T$$

where $Q = (\tilde{Q}_1, \tilde{Q}_2)$ is the orthogonal matrix with $\tilde{Q}_1 \in \mathbb{R}^{n \times (n-k)}$ and $\tilde{Q}_2 \in \mathbb{R}^{n \times k}$; $\tilde{D}_2 \in \mathbb{R}^{k \times k}$ is the diagonal matrix with distinct values on the diagonal and $z_2 \in \mathbb{R}^{k \times 1}$ is the vector with no zero entry. Next, we need to compute the eigendecomposition of $\tilde{D}_2 + \rho z_2 z_2^T$. The following theorem characterizes the eigenvalues and eigenvectors of the deflated system [33]:

Theorem 6.3.1. *Assume that $d_1 < d_2 < ... < d_n$ and $\rho > 0$. Then the eigenvalues $\{\lambda_i\}_{i=1}^n$ of $D + \rho z z^T$ satisfy the interlacing property*

$$d_1 < \lambda_1 < d_2 < \lambda_2 < ... < d_n < \lambda_n$$

and are the roots of the secular equation

$$f(\lambda) = 1 + \rho \sum_{j=1}^n \frac{z_j^2}{d_j - \lambda} = 0 \tag{6.41}$$

For each eigenvalue λ_i, the corresponding eigenvector is given by

$$u_i = (\frac{z_1}{d_1 - \lambda_i}, ..., \frac{z_n}{d_n - \lambda_i})^T / \sqrt{\sum_{j=1}^{n} \frac{z_j^2}{(d_j - \lambda_i)^2}} \tag{6.42}$$

In [33], Bunch *et al* proposed a rational interpolation method to approximate the roots of the secular equation (6.41) efficiently with the quadratic rate of convergence. The corresponding eigenvector of each computed eigenvalue can be computed directly using Eq. (6.42). Suppose that the eigendecomposition of $\tilde{D}_2 + \rho z_2 z_2^T$ is $\bar{Q}_2 \bar{D}_2 \bar{Q}_2^T$, the matrix whose columns are the eigenvectors of the matrix L_G is $(\tilde{Q}_1, \tilde{Q}_2 \bar{Q}_2)$ and the corresponding diagonal matrix of eigenvalues is $\Lambda = (\tilde{D}_1, \bar{D}_2)$. The bottleneck in our computing overhead is the computation of $\tilde{Q}_2 \bar{Q}_2$ which is $O(nk^2)$. In the next part, we will show that by using the Fast Multipole Method, we can accelerate the computation of the eigenvectors.

6.3.3.3   Acceleration using Fast Multipole Method

In this section, we present the acceleration of our algorithm by using Fast Multipole Method (FMM) which was proposed by Carrier, Greengard and Rokhlin [39, 92], and intensively studied in [88].

Let u_i be the corresponding eigenvector of the eigenvalue λ_i of the deflated system $\tilde{D}_2 + \rho z_2 z_2^T$ and $d_1 < d_2 < ... < d_k$ are the diagonal entries of $\tilde{D}_2$; then, for any vector $q \in \mathbb{R}^{k \times 1}$, one can write the value $u_i^T q$ as

$$u_i^T q = \frac{\sum_{j=1}^{k} \frac{q(j) z_2(j)}{d_j - \lambda_i}}{\sqrt{\sum_{l=1}^{k} \frac{(z_2(l))^2}{(d_l - \lambda_i)^2}}} = \frac{\Phi_1(\lambda_i)}{\sqrt{\Phi_2(\lambda_i)}}$$

where

$$\Phi_1(\lambda) = \sum_{j=1}^{k} \frac{q(j) z_2(j)}{d_j - \lambda}, \tag{6.43}$$

$$\Phi_2(\lambda) = \sum_{l=1}^{k} \frac{(z_2(l))^2}{(d_l - \lambda)^2}. \tag{6.44}$$

For this reason, $\bar{Q}_2^T q$ can be computed by evaluating the functions $\Phi_1(\lambda)$ and $\Phi_2(\lambda)$ at k points $\lambda_1, \lambda_2,$ ..., λ_k. Note also that Eq. (6.43) and (6.44) are of the form $\Phi(x) = \sum_{i=1}^{n} c_j \varphi(x - x_j)$, where $\varphi(x)$ is $1/x$ or $1/x^2$, and the direct computation of $\bar{Q}_2^T q$ takes $O(k^2)$ time. Using Fast Multipole Method (FMM) [39, 92], it only takes $O(k)$ in time to approximate $\Phi_1(x)$ and $\Phi_2(x)$ at these points to a precision specified by the user. Therefore, one can accelerate the computing overhead of the matrix-vector product $\bar{Q}_2^T q$ to $O(k)$. In addition, each row of $\tilde{Q}_2 \bar{Q}_2$ is of the form $(\bar{Q}_2^T q)^T$, which reduces the cost for computing $\tilde{Q}_2 \bar{Q}_2$ to $O(nk)$.

6.3.3.4 Complexity analysis of the proposed algorithm

Let $T(K)$ be complexity of the proposed algorithm for matrix L_G. Tthe complexity for computing the eigendecomposition of each Laplacian matrix L_{G_i} by classical approaches is normally $O(N^3)$ that implies $T(1) = O(N^3)$. In the dividing step, we usually choose $k = \lfloor K/2 \rfloor$. The overhead for the conquering step is $O(P^2) = O(K^2 N^2)$ if FMM is used. One can formulate the complexity $T(K)$ as following:

$$\begin{cases} T(K) = 2T(K/2) + O(K^2 N^2) \\ T(1) = O(N^3) \end{cases} \tag{6.45}$$

Similar to [161], one can prove that

$$T(K) \leq O(KN^3) + 2O(K^2 N^2) = O(KN^3) + O(p_K^2) \tag{6.46}$$

where $p_k = KN$. As a consequence, the complexity of our algorithm is in the order of $T(K) = O(KN^3) + O(p_K^2)$. When $K >> 1$, our algorithm is much faster than a classical algorithm of complexity $O(p_K^3)$.

Remark 6.3.2. *If G_1, G_2, ..., G_K are identical, one only need to solve the eigendecomposition of G_1, and then use this decomposition in the problem (6.3.1). As a result, the complexity of our approach can be reduced to $T(K) = O(N^3) + O(p_K^2)$, and our algorithm becomes very powerful when $K >> 1$.*

Remark 6.3.3. *If one has already known the eigendecomposition $L_{G_i} = U_i D_i U_i^T, \forall i \in \{1, 2, \ldots, K\}$, one only needs $O(p_K^2)$ flops more for obtaining the eigenvalues and eigenvectors of L_G.*

6.3.3.5 Examples

In this section, we illustrate our approach for $K = 2^k$ and $n_i = N$ for $1 \leq i \leq K$ (Fig. 6.7). Using our algorithm, one can find the eigendecomposition of the Laplacian matrix L_G in the graph G by k steps as following:

- Step 1 : Knowing the eigendecomposition of the Laplacian matrices L_{G_i}, for all $i = 1, \ldots, K$, we solve the eigenproblem for the Laplacian matrix $L_{G_{1 \to 2}}, L_{G_{3 \to 4}}, \ldots, L_{G_{K-1 \to K}}$ by the divide-and-conquer method described in Section 6.3.3.1 and 6.3.3.2 , respectively.

- Step i: For each $2 \leq i < k$, using all the knowledge from the previous steps, we find the eigendecomposition of the Laplacian matrices $L_{G_{1 \to 2^i}}, \ldots, L_{G_{2^{k-1} - 2^i + 1 \to 2^k}}$.

- Step k: Using the computed eigendecomposition of the Laplacian matrices $L_{G_{1 \to 2^{k-1}}}$ and $L_{G_{2^{k-1} + 1 \to 2^k}}$, we finally obtain the eigendecomposition of the matrix L_G.

One can see that the computation in this example is much faster than by any traditional algorithm.
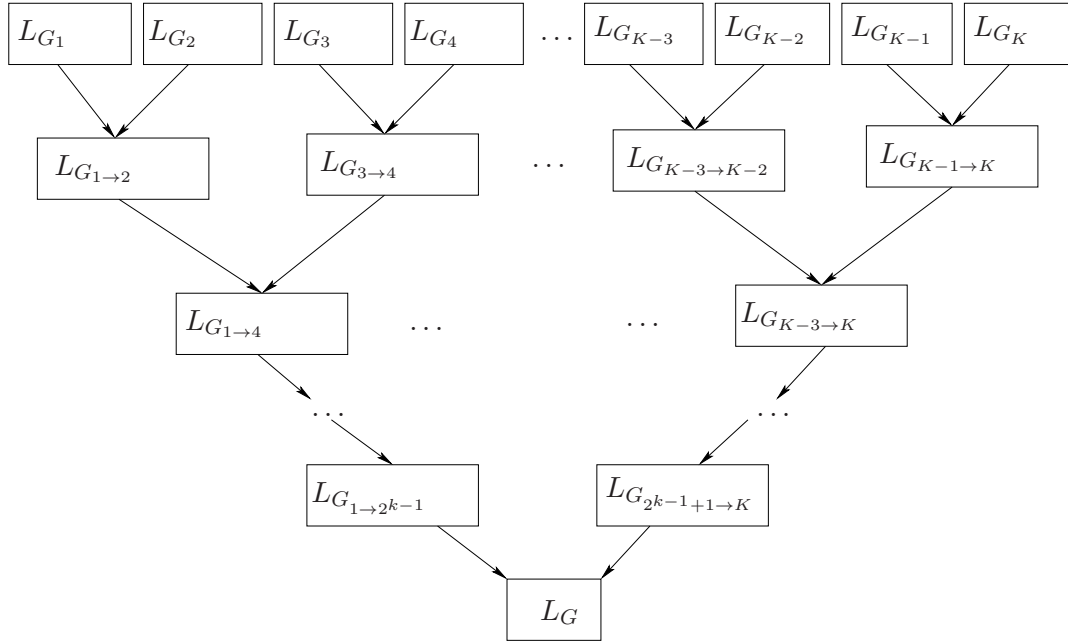
Figure 6.7: Illustration of our algorithm when the graph G has 2^k subgraphs of N vertices.

(a)

(b)
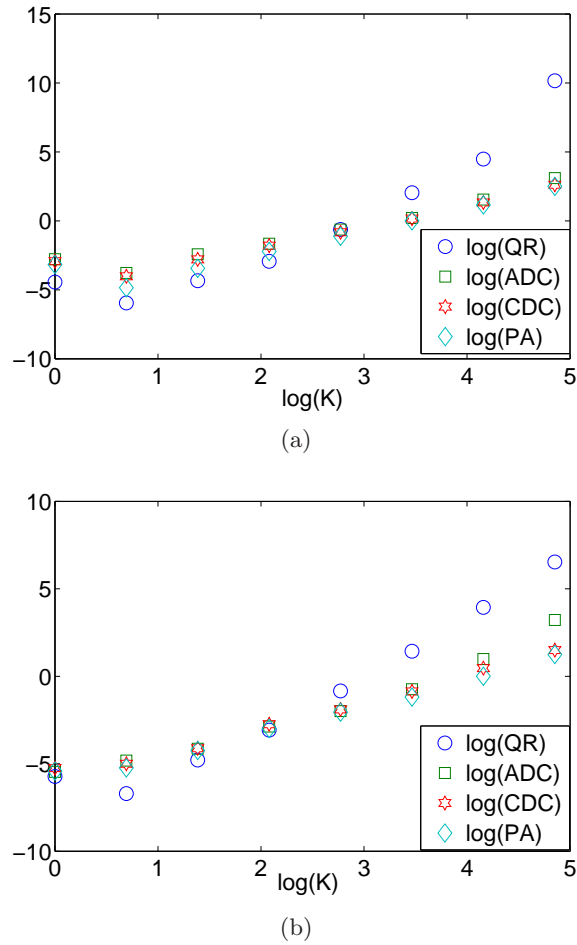
Figure 6.8:   The total computational time comparison (by second) between our algorithm and other algorithms for solving the eigenproblem for the Laplacian matrix L_G of a graph G with K subgraphs G_i: (a) - G_i is a ring graph of 11 vertices, (b) - G_i is a complete graph of 11 vertices. All edges in G have the weight 1 and K varies in the set $\{1, 2, 4, 8, 16, 32, 64, 128\}$.

6.3.4   Numerical experiments

In this section, we start by comparing our divide-and-conquer algorithm (denotes PA below) with three other algorithms for solving the eigenproblem of the Laplacian matrix in a graph G:

- QR: using a sequence of Householder reflectors for tridiagonalization [214, p. 196] and QR algorithm with Wilkinson's shift for a symmetric tridiagonal eigenproblem [79, 132], [214, p. 222]

- CDC: using a sequence of Householder reflectors for tridiagonalization [214, p. 196] and Cuppen's divide-and-conquer algorithm for a symmetric tridiagonal eigenproblem [56]

- ADC: using a sequence of Householder reflectors for tridiagonalization [214, p. 196] and the arrow-head divide-and-conquer algorithm for a symmetric tridiagonal eigenproblem [88]

Since the number of vertices in G was not too large, we did not implement FMM in our computation. In the rank-one modification step, the enhancement of orthogonality of eigenvectors (proposed by Ming Gu and Eisenstat [87]) was implemented in both PA and CDC.

All codes are written in Matlab and all computations were done by a Intel core i3 2.10 GHz computer. The machine precision is $\epsilon = 1.1 \times 10^{-16}$.

It is important to emphasize that in each conquering step, we solve each secular equation (6.41) by the bisection method. As already known, the secular equation has exactly one solution in any interval (d_i, d_{i+1}) $(d_{n+1} = \infty)$. In our computation, we find an approximate solution λ_i^* satisfying that $|\lambda_i - \lambda_i^*| < |d_i - d_{i+1}|\epsilon$ for $1 \le i < n$ and $|\lambda_n - \lambda_n^*| < |d_n - M^*|\epsilon$, in which M^* is large enough in order to get exactly a solution of the associated secular equation in (d_n, M^*). Note that the choice of the value M^* also influences the final error of the numerical computation.

In Tables 6.2 and 6.3, we compare our algorithm (without FMM) with other algorithms by the total computational time, the residual error and the orthogonal error. We suppose that the Laplacian matrix L_G has the eigendecomposition $U\Lambda U^T$ where U is an orthogonal matrix and Λ is a diagonal matrix with eigenvalues on its diagonal. The residual error for the computed eigensystem can be evaluated by the formula $\dfrac{\max_i \|L_G u_i - \lambda_i u_i\|_2}{p_K \epsilon \|L_G\|_2}$ where u_i is the ith column of U and λ_i is the ith entry on the diagonal of Λ.

The orthogonality error for the computed eigensystem can be calculated by the formula $\dfrac{\max_i \|U^T u_i - e_i\|_2}{p_K \epsilon}$ where e_i is unit vector with 1 in its ith entry.

6.3.4.1   Example 1

We consider a graph G which has K subgraphs G_i and each subgraph G_i is a ring graph (Figure 6.9a) of 11 vertices. We assume that all edges in each G_i have the weight 1 and $\omega_i = 1$ for any $1 \le i < K$.

We solve the eigensystem for the Laplacian matrix L_G corresponding to a value $K = 2^i$ where $1 \le i \le 7$. In Table 6.2, one can see the comparison between our algorithm PA and three other algorithms: ADC, CDC and QR. Figure 6.8a shows that as K increases, the algorithm PA runs faster than others and the algorithm QR is the slowest one. In particular, as $K = 128$, our algorithm is about 200 times faster

(a) A ring graph R_4 (b) A complete graph K_6
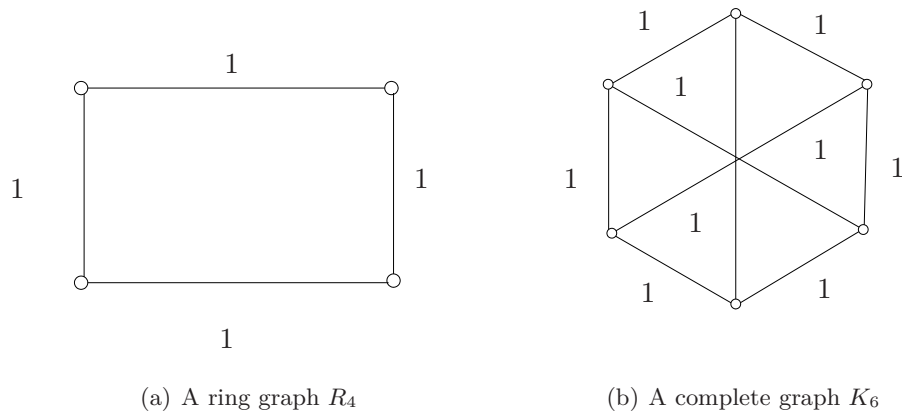
Figure 6.9: An example of ring and complete graphs.

than the traditional QR. The orthogonality error of the algorithm PA is better than ADC, CDC and QR. However, the residual errors in our computation, ADC and CDC are not as good as the algorithm QR.

6.3.4.2   Example 2

In this example, a graph G has K subgraphs, each of them being a complete graph (Figure 6.9b) of 11 vertices. We also assume that all edges have the weight 1, K varies from 1 to 128 and we compute the eigenvalues and eigenvectors of the Laplacian matrix L_G.

The comparison of the total computational time (second), the residual errors and the orthogonality errors is shown on Table 6.3. In this table, one can see that our algorithm runs faster than others when the number of subgraphs increases. In this example, the algorithm ADC seems to be slower than CDC, but still faster than QR (Fig. 6.8b). The residual errors of our algorithm in this example are relatively good, and the corresponding orthogonality errors are better than three other algorithms.

6.3.4.3   Discussion

In two above examples, the algorithm QR is the slowest when the size of the matrix increases. However, it achieves the least errors in comparison with other algorithms. Our algorithm runs faster than ADC, CDC and QR and its orthogonality errors are relatively good. In some cases, the group of three algorithms PA, ADC and CDC has large residual errors in comparison with QR algorithm. One reason is that the strategy for solving the eigensystem in this group is different from that for QR. In QR algorithm, one only uses similar transformation to gradually diagonalize the original matrix while in PA, ADC and CDC algorithms, one computes the eigenvalues first and then construct the corresponding eigenvectors. It indicates that our implementation still has some drawbacks and requires several improvements in future. In what follows, we discuss various aspects of the implementation of our algorithm in Matlab.

Firstly, we present the numerical deflation of a rank-one modification. In other words, we consider the problem of computing the eigendecomposition of $D + \rho z z^T$, where D is a diagonal matrix and z is a vector. As described in [33], the rank-one modification can be deflated whenever $d_i = d_j$ or $z_i = 0$,

(a) Time (second)

K	PA	ADC	CDC	QR
1	0.042	0.062	0.054	0.012
2	0.008	0.023	0.018	0.003
4	0.032	0.089	0.061	0.013
8	0.109	0.190	0.166	0.053
16	0.328	0.309	0.438	0.536
32	1.004	1.226	1.181	7.691
64	3.167	4.692	3.802	88.180
128	12.166	22.122	13.726	$2.6e+04$

(b) Residual Error: $\dfrac{\max_i \|L_G u_i - \lambda_i u_i\|_2}{p_K \epsilon \|L_G\|_2}$

K	PA	ADC	CDC	QR
1	0.586	0.471	0.620	0.586
2	6.341	38.933	8.468	0.504
4	2.945	2029337.7	792800.6	8.697
8	1.444	994882.9	826743.9	2.901
16	0.719	740525.9	193355.5	1.930
32	0.667	305931.8	251122.6	0.971
64	222724.4	266043.3	138472.1	0.593
128	37303.3	1496420.7	90779.9	0.272

(c) Orthogonality: $\dfrac{\max_i \|U^T u_i - e_i\|_2}{p_K \epsilon}$

K	PA	ADC	CDC	QR
1	1.5023	0.6562	0.8107	1.5023
2	0.9807	0.4556	0.3785	1.3046
4	0.5562	0.2504	0.3041	0.9518
8	0.2612	0.1387	0.1730	0.7060
16	0.1272	0.1044	0.1110	0.4783
32	0.0698	0.0611	0.0656	0.4024
64	0.0361	0.0418	0.0382	0.3727
128	0.0209	0.0258	0.0257	0.3224

Table 6.2: The comparison between our algorithm PA and three other algorithms: ADC, CDC and QR. We numerically solve the eigenproblem for the Laplacian matrix in a graph G including K subgraphs. Each subgraph G_i is a complete graph of 11 vertices and each edge in G has weight 1. Tables (a), (b) and (c) show the total time (second), the residual error and the orthogonality error, respectively.

where d_i and d_j are two diagonal entries of the diagonal matrix D and z_i is an element of the vector z. Because of the machine precision, one needs to choose a threshold τ such that $|d_i - d_j| < \tau$ in order to approximate $d_i = d_j$. The choice of the threshold is very important because it can affect the errors of the whole algorithm. More clearly, the orthogonality of eigenvectors can be lost whenever $|d_i - d_j|$ is too small. One can see that there is a trade-off in choosing τ here. If τ is larger, it helps us to avoid the loss of orthogonality of eigenvectors, but the corresponding residual errors can be bigger. On the other hand, if τ is too small, the residual errors are smaller, but the orthogonality of computed eigenvectors can be lost. For this reason, in our implementation, we choose $\tau = 10^{-12}$. This choice of τ is quite conservative because it helps our algorithm to increase the orthogonality of computed eigenvectors in many test cases, but it also allows a bigger residual error.

Similarly, in one deflation case ($z_i = 0$), we also need an appropriate threshold η so that if $|z_i| < \eta$, one can consider $z \approx 0$ in numerical computations. For a better explanation, we give the following example. As already known, the secular equation of the rank-one modification step has the form $f(\lambda) = 1 + \rho \sum_{i=1}^{n} \frac{z_i^2}{d_i - \lambda}$. Here, the roots of the secular equation are the eigenvalues of the original matrix. what happens if one chooses an extremely small η such as e.g $\eta = 10^{-14}$? Practically, sometimes we can get $z_j \approx 10^{-13}$

for some j. In this situation, one gets $z_j^2 \approx 10^{-26}$. However, it is worth emphasizing that when the machine precision ($\epsilon = 1.1 \times 10^{-16}$) is greater than 10^{-26}, z_j^2 may be considered as 0. For this reason, one practically loses the term $\frac{z_j^2}{d_j - \lambda}$ in the above equation, and makes some numerical errors. Therefore, in our implementation, we choose $\eta = 5 \times 10^{-8}$. This choice of η ensures that all terms $\frac{z_i^2}{d_i - \lambda}, i = 1, \ldots, n$ are not omitted. However, it is important to note that this drawback in implementing our algorithm is only related to the machine precision.

6.4   Conclusion

In this chapter, we have studied localization in some specific graphs, and shown how to find a localized eigenmode. An eigenfunction u is localized in these graphs if and only if it has zero value at all connectors. In addition, all non-localized eigenmodes have the multiplicity 1.

We have proposed a divide-and-conquer algorithm for computing the eigendecomposition of the Laplacian matrix for undirected, weighted graphs illustrated in Fig. 6.6. Our algorithm avoids the tridiagonalization step in traditional algorithms which costs $O(p_K^3)$ multiplications. As a consequence, our algorithm only costs $O(KN^3) + O(p_K^2)$, and runs faster than classical algorithms when $K >> 1$. However, there are several drawbacks from the numerical experiments concerning the loss of orthogonality of eigenvectors. In the future, we will improve these points.

(a) Time (second)

K	PA	ADC	CDC	QR
1	0.0044	0.0042	0.0053	0.0033
2	0.0053	0.0081	0.0067	0.0012
4	0.0144	0.0159	0.0163	0.0084
8	0.0508	0.0564	0.0644	0.0461
16	0.1287	0.1372	0.1506	0.4328
32	0.3040	0.4765	0.4199	4.1831
64	1.0021	2.6853	1.5929	51.4558
128	3.4667	24.9412	4.4832	686.4115

(b) Residual Error: $\dfrac{\max\limits_{i}\|L_G u_i - \lambda_i u_i\|_2}{p_K \epsilon \|L_G\|_2}$

K	PA	ADC	CDC	QR
1	1.0376	0.5191	1.0408	1.0376
2	0.5066	553005.2343	5.7516	6.1564
4	0.2581	1556777.655	8.1779	0.7666
8	0.1340	2855.3081	75102.1883	0.7844
16	0.2428	397826.8293	4991.9984	0.9220
32	0.3142	249097.7777	2165343.645	0.4851
64	0.6839	371122.5186	24122499.93	0.3039
128	0.6921	530522.3532	8534774.75	$1.06e + 09$

(c) Orthogonality: $\dfrac{\max\limits_{i}\|U^T u_i - e_i\|_2}{p_K \epsilon}$

K	PA	ADC	CDC	QR
1	1.2288	0.7341	0.8250	1.2288
2	0.9300	0.4720	0.4965	0.7349
4	0.3806	0.2552	0.3629	0.8896
8	0.2037	0.2417	0.2455	0.4977
16	0.1019	0.1223	0.1144	0.4704
32	0.0516	0.0933	0.0938	0.3849
64	0.0252	0.1082	0.1082	0.3097
128	0.0143	0.0542	0.0564	0.2282

Table 6.3: The comparison between our algorithm PA and three other algorithms: ADC, CDC and QR. We numerically solve the eigenproblem for the Laplacian matrix in a graph G including K subgraphs. Each subgraph G_i is a ring graph of 11 vertices and each edge in G has weight 1. Tables (a), (b) and (c) show the total time (second), the residual error and the orthogonality error respectively.

Chapter 7

A spectral approach to survival probabilities in porous media

In this chapter, we consider a diffusive process in a bounded domain with heterogeneously distributed traps, reactive regions or relaxing sinks. This is a mathematical model for chemical reactors with heterogeneous spatial distributions of catalytic germs, for biological cells with specific arrangements of organelles, and for mineral porous media with relaxing agents in NMR experiments. Using a spectral approach, we compute the survival probabilities which are represented in the form of spectral decomposition over Laplacian eigenfunctions. We illustrate the performances of the approach by considering diffusion inside the unit disk filled with reactive regions of various shapes and reactivities. The role of the spatial arrangement of these regions and its influence on the overall reaction rate are investigated in the long-time regime. When the reactivity is finite, a uniform filling of the disk is shown to provide the highest reaction rate. Although the heterogeneity tends to reduce the reaction rate, reactive regions can still be heterogeneously arranged to get nearly optimal performances.

The results of this chapter are reported in [162].

7.1 Introduction

Diffusion is a fundamental transport mechanism in physics, chemistry and biology [114, 180, 223]. During the diffusive exploration, particles may encounter traps, reactive regions or relaxing sinks which are distributed either in the bulk, or on the interface. While staying inside or in vicinity of these specific zones, particles may disappear with a given rate. This is a common mathematical model for many biological and industrial systems, e.g.

1. chemical reactors with heterogeneous spatial distributions of catalytic germs [53, 224];

2. biological cells with specific arrangements of organelles [112, 235];

3. mineral porous media with relaxing agents in nuclear magnetic resonance (NMR) experiments [30].

If the system is isolated (no new particle is injected), the survival probability, as well as the concentration of the survived particles that diffuse in such a medium, decays in time. In the long-time regime, the survival probability exhibits an exponential decay, and the decay constant (i.e the average "lifetime" of a diffusing particle) is expected to be proportional to the total amount of traps, relaxing sinks or reactive regions. This is a consequence of the classical Smoluchowski formula $\Phi \approx 4\pi DRc_0$ for the diffusive flux Φ of particles which are uniformly distributed with concentration c_0 and react on a single absorbing sphere of radius R, D being the diffusion coefficient of particles [205]. In particular, the diffusive flux is proportional to the size R of the sphere, not to its surface area $4\pi R^2$, as one could naively expect for reaction on a surface. For n well-separated absorbing spheres (a diluted suspension), the overall reaction rate k of a single diffusing particle is then $k \approx n\Phi/N \approx 3D\phi/R^2$, where $N = c_0 V$ is the number of diffusing particles and $\phi = n(4\pi R^3/3)/V$ is the volume fraction of absorbing spheres, V being the volume of the medium. It means that the overall reaction rate k (i.e., the decay constant) is proportional to the volume fraction ϕ of reactive grains (i.e., their total amount or "strength").

Since this seminal result, the survival probability of Brownian motion in reactive porous media was studied by different mathematical and numerical tools [114, 180, 223]. The asymptotic behavior of the survival probability in randomly located traps and the role of averaging over trap configurations were analyzed in a series of publications [16, 94, 126, 127]. In the long-time limit, the survived particles reside in large voids, and the statistics of these voids leads to a stretched-exponential decay of the survival probability. Torquato and co-workers performed numerous Monte Carlo simulations in order to investigate how the reaction rate κ depends on the volume fraction ϕ, the shape of individual grains, their polydispersity, overlapping and reactivity, etc. [124, 142, 157, 158, 209]. Using the mean-field approximation, Richards proposed an explicit formula for the survival probability which was shown to be accurate for a wide range of times [182, 183]. Upper and lower bounds for the reaction rate were derived in a series of papers by Torquato and co-workers [184, 185, 210–212]. Singer et al. dealt with the narrow escape problem to find an asymptotic expansion of the expected lifetime of Brownian motions as the absorbing part of the boundary shrinks to zero [202, 203]. Another insight onto this problem was brought by Bénichou and Voituriez [22]. The case of small traps was considered by Ward and co-workers who derived a number of rigorous asymptotic results [43, 44, 130, 172, 221]. Finally, the survival probability is closely related to first-passage and residence times which have been actively studied during the last years [20, 21, 46–50, 144, 231].

Among various theoretical approaches for describing diffusive motion in confined domains, a spectral theory involving the Laplace operator eigenbasis provides perhaps the most fundamental insight onto this process. For instance, Brownstein and Tarr used this technique to explain multiexponential relaxation for water in biological cells [30]. Recently, a matrix formalism was applied for computing the residence times and other functionals of reflected Brownian motion by Grebenkov [97]. In diffusion-reaction equations, reactive regions or relaxing sinks are represented through a spatially heterogeneous trapping reaction or relaxation rate $B(\mathbf{r})$. In this chapter, the survival probability is expressed in a matrix form involving two infinite-dimensional matrices: the diagonal matrix Λ representing the Laplace operator in its own basis, and a matrix $\mathcal{B}$ representing the reaction rate $B(\mathbf{r})$ in the Laplacian basis. After computing these two

matrices analytically and numerically, the survival probability takes an explicit multi-exponential form. In this chapter, we aim at revealing the role of a spatial heterogeneity $B(\mathbf{r})$ of traps, reactive regions or relaxing sinks onto the survival probability in the long-time regime (see more discussions and references in [162]). We study several model arrangements of reactive regions in order to increase the overall reaction performance of a medium, aiming in future at design of efficient catalysts or diffusive exchangers via optimization of their geometrical shapes. In other words, we address the question: for a fixed total amount or "strength" of reactive regions, what is the "optimal" shape and arrangement of these regions? Although the spectral approach is applicable to any bounded confining domain, we illustrate its concepts and performances by considering diffusion inside the unit disk which is filled with reactive grains. The explicit form of the Laplace operator eigenfunctions in the disk significantly simplifies computation and allows one to grasp the main features of the spectral approach. It is worth stressing that, in contrast to works by Ward and co-workers [43, 44, 130, 172, 221], our approach is not limited to small reactive regions and is in fact more accurate when these regions are extended. As a consequence, the spectral approach and perturbative techniques turn out to be complementary to each other. Other references and discussions can be found in [162].

This chapter is organized as follows. In Section 2, we recall the derivation of a multi-exponential form of the survival probability. Section 3 summarizes the main steps for a numerical implementation of the spectral approach, error estimation and improvements. In Section 4, we presented numerical results for both bulk and surface reactivity. Finally, we give our conclusions and further questions.

7.2   A spectral approach to survival probability

7.2.1   Matrix representation

We consider independent particles diffusing inside a bounded domain Ω with a smooth reflecting boundary $\partial\Omega$. At time $t = 0$, the particles are distributed with a given initial density $\rho(\mathbf{r}_0)$. For a given function $B(\mathbf{r})$, a random variable

$$\phi_t = \int\limits_0^t B(X_s)\ ds$$

is associated to a random trajectory X_s of the reflected Brownian motion in Ω. Intuitively, the function $B(\mathbf{r})$ can be thought of as a distribution of "markers" for distinguishing different points and regions of the confining domain. When a diffusing particle passes through these regions, the random variable ϕ_t accumulates the corresponding "marks". In other words, different parts of the trajectory are weighted according to the function $B(\mathbf{r})$, encoding thus the whole stochastic process. For instance, if the bulk contains reactive regions, the function $B(\mathbf{r})$ can represent the distribution of their reaction rates, respectively, while ϕ_t is the cumulant factor penalizing the trajectories that pass through these regions. When $B(\mathbf{r})$ is an applied magnetic field, ϕ_t is the total dephasing of the nuclei in a pulsed-gradient spin-echo NMR experiment [98].

We recall that the probability distribution of the random variable ϕ_t can be found in two steps [97]. The

first step is based on the classical Kac formula relating the expectation $\mathbb{E}\{e^{-h\phi_t}\}$ to the solution of a diffusion equation with bulk relaxation [150, 215]. This expectation includes the average of the functional $e^{-h\phi_t}$ over all random trajectories $\{X_s\}_{0\leq s\leq t}$ of the reflected Brownian motion between the starting point $\mathbf{r}_0$ at time 0 and the arrival point $\mathbf{r}$ at time t, as well as the average over all $\mathbf{r}_0$ and $\mathbf{r}$ with given initial density $\rho(\mathbf{r}_0)$ and weighting function $\tilde{\rho}(\mathbf{r})$ respectively; in this case, Kac formula reads as [97]

$$\mathbb{E}\{e^{-h\phi_t}\} = \int_\Omega c(\mathbf{r}, t)\tilde{\rho}(\mathbf{r})\, d\mathbf{r}, \tag{7.1}$$

where $c(\mathbf{r}, t)$ obeys the equation

$$\frac{\partial c(\mathbf{r}, t)}{\partial t} - D\Delta c(\mathbf{r}, t) + hB(\mathbf{r})c(\mathbf{r}, t) = 0, \tag{7.2}$$

with the initial condition $c(\mathbf{r}_0, t = 0) = \rho(\mathbf{r}_0)$, and $\Delta = \frac{\partial^2}{\partial x_1^2} + \cdots + \frac{\partial^2}{\partial x_d^2}$ is the Laplace operator in d dimensions. The reflected character of Brownian motion is represented by Neumann boundary condition, when the normal derivative $\partial/\partial n$ at the boundary vanishes: $\partial c(\mathbf{r}, t)/\partial n = 0$ on $\partial\Omega$. If $B(\mathbf{r})$ is the distribution of bulk sinks (or their absorption rates), $c(\mathbf{r}, t)$ can be interpreted as the probability density for a Brownian particle, started according to the initial density $\rho(\mathbf{r}_0)$, to arrive in an infinitesimal vicinity of the point $\mathbf{r}$ at time t, without being trapped, reacted, absorbed or relaxed during its motion. The weighting function $\tilde{\rho}(\mathbf{r})$ allows one to delimit the region of interest inside the confining domain. Since $c(\mathbf{r}, t)$ is weighted by $\tilde{\rho}(\mathbf{r})$ in Eq. (7.1), only those Brownian trajectories that arrived into the "pickup" regions at time t do contribute to the expectation in Eq. (7.1).

At the second step, one uses the Laplace operator eigenfunctions $u_m(\mathbf{r})$ $(m = 0, 1, 2, ...)$ that satisfy

$$D\Delta u_m(\mathbf{r}) + \lambda_m u_m(\mathbf{r}) = 0 \quad (\mathbf{r} \in \Omega),$$
$$\frac{\partial u_m(\mathbf{r})}{\partial n} = 0 \quad (\mathbf{r} \in \partial\Omega),$$

λ_m being the Laplace operator eigenvalues. Since the eigenfunctions $u_m(\mathbf{r})$ form a complete orthonormal basis, the solution $c(\mathbf{r}, t)$ of Eq. (7.2) can be expanded as

$$c(\mathbf{r}, t) = \sum_{m'} c_{m'}(t)u_{m'}(\mathbf{r}).$$

Substitution of this expansion in Eq. (7.2), multiplication by $u_m^*(\mathbf{r})$, and integration over Ω yield a set of ordinary differential equations for the unknown coefficients $c_m(t)$,

$$\frac{\partial c_m(t)}{\partial t} + \sum_{m'} \left(\Lambda_{m,m'} + h\mathcal{B}_{m,m'}\right) c_{m'}(t) = 0,$$

where the infinite-dimensional matrices $\mathcal{B}$ and Λ are

$$\mathcal{B}_{m,m'} = \int_{\Omega} u_m^*(\mathbf{r}) \ B(\mathbf{r}) \ u_{m'}(\mathbf{r}) \ d\mathbf{r},$$

$$\Lambda_{m,m'} = \delta_{m,m'} \lambda_m.$$

Thinking of $c_m(t)$ as components of an infinite-dimensional vector $C(t)$, one easily finds the solution of the above matrix equation. The expectation $\mathbb{E}\{e^{-h\phi_t}\}$ can thus be written in a form of a scalar product:

$$S_h(t) = \mathbb{E}\{e^{-h\phi_t}\} = \left(U \ e^{-(\Lambda+h\mathcal{B})t} \tilde{U} \right), \tag{7.3}$$

where the infinite-dimensional vectors U and $\tilde{U}$ represent the projections of the initial density $\rho(\mathbf{r})$ and the weighting function $\tilde{\rho}(\mathbf{r})$ onto the eigenfunctions $u_m(\mathbf{r})$:

$$U_m = \int_{\Omega} u_m^*(\mathbf{r}) \ \rho(\mathbf{r}) \ d\mathbf{r},$$

$$\tilde{U}_m = \int_{\Omega} u_m(\mathbf{r}) \ \tilde{\rho}(\mathbf{r}) \ d\mathbf{r}. \tag{7.4}$$

The matrix $e^{-(h\mathcal{B}+\Lambda)t}$ can be thought of as a kind of evolution operator acting on the initial state $\rho(\mathbf{r})$ (represented by the vector U). The resulting density $c(\mathbf{r},t)$ at time t is then projected onto the weighting function $\tilde{\rho}(\mathbf{r})$ (represented by the vector $\tilde{U}$). It is important to note that the matrices $\mathcal{B}$ and Λ do not commute.

For a positive h, the expectation $\mathbb{E}\{e^{-h\phi_t}\}$ can be interpreted as the Laplace transform of the probability density $p_t(\varphi)$ of ϕ_t,

$$\mathbb{E}\{e^{-h\phi_t}\} = \int_0^{\infty} e^{-h\varphi} \ p_t(\varphi) \ d\varphi,$$

allowing one, at least formally, to find the latter by the inverse Laplace transform. Thus, the properties of the expectation $\mathbb{E}\{e^{-h\phi_t}\}$ provides a complete probabilistic description of the random variable ϕ_t.

7.2.2 Multi-exponential decay

Since the matrix $\Lambda + h\mathcal{B}$ is symmetric, all its eigenvalues γ_m^h are real and can be ordered as $\gamma_0^h \leq \gamma_1^h \leq \gamma_2^h \leq \dots$. The associated eigenvectors form an orthogonal matrix V^h such that

$$\Lambda + h\mathcal{B} = V^h \begin{pmatrix} \gamma_0^h & 0 & 0 & 0 & \dots \\ 0 & \gamma_1^h & 0 & 0 & \dots \\ 0 & 0 & \gamma_2^h & 0 & \dots \\ 0 & 0 & 0 & \gamma_3^h & \dots \end{pmatrix} (V^h)T. \tag{7.5}$$

The substitution of Eq. (7.5) into Eq. (7.3) yields

$$S_h(t) = \sum_{m=0}^{\infty} A_m^h e^{-\gamma_m^h t}, \qquad (7.6)$$

where

$$A_m^h = (UV^h)_m ((V^h)^T \tilde{U})_m. \qquad (7.7)$$

The eigenvalues γ_m^h define the "lifetimes", $1/\gamma_m^h$, of the eigenmodes, while A_m^h set their relative contributions to $S_h(t)$. This multi-exponential decay is a generic feature for diffusive processes in bounded reactive media, whatever the spatial heterogeneity $B(\mathbf{r})$ is. For instance, Brownstein and Tarr derived similar relation for surface relaxation in NMR experiments [30].

In the long-time regime, the only significant contribution comes from the smallest eigenvalue λ_0^h which can therefore be interpreted as the overall reaction rate k. In what follows, the focus will be on this spectral characteristics.

7.2.3   Residence and survival times

How long does a diffusing particle reside in a given subset A of a confining domain Ω up to time t? This so-called residence (or occupation) time, ϕ_t, can be computed through the spectral approach by setting $B(\mathbf{r}) = \mathbb{I}_A(\mathbf{r})$, where $\mathbb{I}_A(\mathbf{r})$ is the indicator function of the set $A : \mathbb{I}_A(\mathbf{r}) = 1$ for $\mathbf{r} \in A$, and 0 otherwise [97–100]. This function can be thought of as a "counter" which is turned on whenever the diffusing particle resides in A. The inverse Laplace transform of the survival probability $S_h(t)$ with respect to h gives, at least formally, the probability density of the residence time ϕ_t (here t is a fixed parameter).

In addition, the survival probability allows one to retrieve the first passage time τ at the reactive region A. In fact, if a particle hits A during the time interval $[0, t]$, then $\phi_t > 0$, while $\phi_t = 0$ otherwise. So, the limit of $\mathbb{E}\{e^{-h\phi_t}\}$ as $h \to \infty$ is the probability that a random trajectory X_s does not hit the set A up to time t:

$$S_\infty(t) = \lim_{h \to \infty} \mathbb{E}\{e^{-h\phi_t}\}.$$

This is the survival probability in a medium containing infinitely reactive regions, in which particles react or relax at the first hit, i.e., $S_\infty(t) = \mathbb{P}\{\tau > t\}$. The time derivative, $-dS_\infty(t)/dt$, is then the probability density of the first passage time τ.

In analogy, the survival probability $S_h(t)$ can be interpreted as the cumulative distribution function $\mathbb{P}\{\tau_h > t\}$ where τ_h is the survival time, i.e., a random moment, at which a particle reacts in a medium with finite reactivity h or, equivalently, up to which the particle survives. Since a particle may hit a partially reactive boundary many times without being reacted, the random moment τ_h at which reaction occurs, can also be termed as "the last passage time" [101]. The probability density of τ_h is $-\partial S_h(t)/\partial t$. In summary, the spectral representation (7.6) allows one to study various time statistics of the diffusive process in heterogeneous reactive media. In Sect. 7.4, we analyze the long-time behavior of the survival probability for surface reaction ($A \subset \partial\Omega$) and bulk reaction ($A \subset \Omega$).

7.3 Numerical implementation

In this section, we describe an implementation of the spectral approach for computing the survival probability $S_h(t)$ on the unit interval or the unit disk containing a given reactive region A. The matrix Λ is formed by the Laplace operator eigenvalues which are known explicitly for these confining domains, while the computation of the matrix $\mathcal{B}$ relies on the integration of two explicitly known eigenfunctions over A:

$$\mathcal{B}_{m,m'} = \int_A u_m(\mathbf{r})\, u_{m'}(\mathbf{r})\, d\mathbf{r}. \tag{7.8}$$

In what follows, we recall the form of the Laplace operator eigenbasis, describe the main steps of the numerical algorithm, and discuss accuracy and improvements.

7.3.1 Eigenbasis in 1D and 2D

For the unit interval $\Omega = [0,1]$ with reflecting endpoints, the eigenvalues and eigenfunctions of the Laplace operator are determined explicitly in Eq. (2.24). For this reason, both matrices Λ and $\mathcal{B}$ have explicit forms so that the survival probability in the unit interval with any reactive region A can easily be found. For example, if A is the boundary of Ω, $A = \{0,1\}$, the matrix $\mathcal{B}$ has the following representation

$$\mathcal{B}_{m,m'} = \varepsilon_m \varepsilon_{m'} \left[1 + (-1)^{m-m'}\right].$$

Simple computations for the unit interval allow one to analyze in depth the performances of the spectral approach.

For the unit disk $\Omega = \{\mathbf{r} \in \mathbb{R}^2 : |\mathbf{r}| < 1\}$, the eigenfunctions of the Laplace operator with Neumann boundary condition are given in Eq. (2.33). For the sake of convenience, the eigenfunctions, eigenvalues and other spectral quantities can be enumerated by the triple index nkl. This enumeration is also used for the related vectors and matrices, e.g., $\mathcal{B}_{nkl,n'k'l'}$ is the element of the matrix $\mathcal{B}$ that corresponds to the eigenfunctions $u_{nkl}(\mathbf{r})$ and $u_{n'k'l'}(\mathbf{r})$ (cf. Eq. (7.8)).

7.3.2 Algorithm

In this section, we give our algorithm for computing the survival probability $S_h(t)$. For numerical implementation, the eigenvalues λ_{nk} are sorted in an ascending order to truncate the infinite-dimensional matrices $\mathcal{B}$ and Λ. The position of the eigenmode in such a sequence can be used as its single index m. The numerical algorithm consists of the following steps:

1. For a chosen truncation size N, to determine the first N Laplace operator eigenvalues λ_{nk} in the unit disk by finding the first positive roots of Eq. (2.34) with different values of n by the bisection method. Since the eigenvalues λ_{nk} depend only on the confining domain, this step has to be performed only once, and the stored values of λ_{nk} can then be used in following computations.

2. For a given reactive region A, to compute the truncated matrix $\mathcal{B}$ of size $N \times N$. Except for certain specific cases, for which the integral in Eq. (7.8) can be found explicitly by using the properties

of Bessel functions [28, 55], a numerical integration is required. For this purpose, the region A is conveniently discretized and integrals are approximated by finite sums. This step is time-consuming and is a major source of numerical inaccuracy.

3. For a given reactivity h, to compute the eigenvalues γ_m^h and eigenvectors V_m^h of the matrix $\Lambda + h\mathcal{B}$. This step is the most time-consuming when the size N of the matrix $\Lambda + h\mathcal{B}$ is large.

4. For a chosen initial density $\rho(\mathbf{r})$ and weighting function $\tilde{\rho}(\mathbf{r})$, to find the truncated vectors U and $\tilde{U}$ according to Eqs. (7.4). When the starting and arrival points are irrelevant, the functions $\rho(\mathbf{r})$ and $\tilde{\rho}(\mathbf{r})$ are considered to be uniform, in which case $U_m = \tilde{U}_m = \delta_{m,0}$. In other cases, a numerical integration may be required, as in the step 2.

5. to get the amplitudes A_m^h from Eq. (7.7).

6. if necessary, to extrapolate γ_m^h and A_m^h to the limit of N going to infinity (see below).

As a result, the survival probability $S_h(t)$ is obtained in its explicit spectral form (7.6).

The computation involves two approximations: numerical integration in Eq. (7.8) and truncation of the matrices Λ and $\mathcal{B}$. The first approximation is classical, and its error is relatively easy to control. The second approximation is more subtle, and its accuracy strongly depends on the reactive region A. In order to illustrate this point, we consider A to be a small region. In this case, slowly varying eigenfunctions (i.e., with small eigenvalues) are almost constant on A so that the corresponding elements of the matrix $\mathcal{B}$ are: $\mathcal{B}_{m,m'} \approx u_m(\mathbf{r}_A)u_{m'}(\mathbf{r}_A)S_A$, S_A being the surface area of A, and $\mathbf{r}_A$ a point in A. It means that slowly varying eigenfunctions cannot distinguish the shape of a small region A. In order to reveal small geometrical features of A, highly oscillating eigenfunctions (i.e., with large eigenvalues) have to be included. In this sense, the truncation size N determines how accurate the spatial resolution of a spectral decomposition is. The choice of an appropriate value for N is therefore strongly dependent on the reactive region A. Since the computational time for finding eigenvalues and eigenvectors of a matrix of size $N \times N$ grows typically as $O(N^3)$, this may be a limiting factor for using the spectral approach, especially for small reactive regions. In this specific case, perturbative techniques are preferred [43, 44, 130, 172, 202, 203, 221].

7.3.3 Rotation-invariant reactive regions

The above numerical limitation can be overcome when the reaction rate distribution $B(\mathbf{r})$ is rotation-invariant (i.e., $B(r, \varphi)$ is independent of φ). In this case, the Laplace operator eigenvalues can be grouped in such a way that the matrix $\mathcal{B}$ gets a block structure. In fact, one has

$$\mathcal{B}_{nk0,n'k'0} = \mathcal{B}_{nk1,n'k'1} = 2\delta_{n,n'} \frac{\beta_{nk}\beta_{nk'}}{J_n(\alpha_{nk})J_n(\alpha_{nk'})} \times \int_0^1 J_n(\alpha_{nk}r) \, J_n(\alpha_{nk'}r) \, B(r) \, r \, dr,$$

$$\mathcal{B}_{nk0,n'k'1} = \mathcal{B}_{nk1,n'k'0} = 0.$$

Instead of previously used ascending order, let us now order the first N eigenvalues as

$$\underbrace{\lambda_{00}, \lambda_{01}, ..., \lambda_{0k_0}}_{\text{block } 0}, \ \underbrace{\lambda_{10}, \lambda_{11}, ..., \lambda_{1k_1}}_{\text{block } 1}, \ \ ... \ \ \underbrace{\lambda_{n-1,0}, \lambda_{n-1,1}, ..., \lambda_{n-1,k_{n-1}}}_{\text{block } n-1}, \ \ \underbrace{\lambda_{n0}}_{\text{block } n} \ ,$$

where the indices k_0, k_1, ... are chosen such that $\lambda_{j,k_j+1} > \lambda_{\max}$ $(j = 0, 1, ...)$, and the index n is such that $\lambda_{n+1,0} > \lambda_{\max}$ (here $\lambda_{\max}$ is the maximal eigenvalue among the first N eigenvalues). It is worth stressing that the eigenvalues λ_{nk} with $n > 0$ are twice degenerate and they should appear twice in the above sequence. The matrix $\mathcal{B}$ is then decomposed into block matrices $\mathcal{B}^j$:

$$\mathcal{B} = \begin{pmatrix} \mathcal{B}^0 & & & & 0 \\ & \mathcal{B}^1 & & & \\ & & \mathcal{B}^2 & & \\ & & & ... & \\ 0 & & & & \mathcal{B}^n \end{pmatrix},$$

where $\mathcal{B}^j_{k,k'} = \mathcal{B}_{jk0,jk'0}$ $(j = 0, ..., n)$. Since Λ is a diagonal matrix, it can also be written in a form of blocks. Consequently, the diagonalization of the matrix $\Lambda + h\mathcal{B}$ is reduced to *separate* diagonalizations of the (much) smaller matrices $\Lambda^j + h\mathcal{B}^j$. This gives a tremendous gain in computational time that allowed us to increase the value of N up to 10^5.

When studying the long-time regime, only the smallest eigenvalue γ_0^h is needed, and it turns out to be the smallest eigenvalue of the first block matrix $\Lambda^0 + h\mathcal{B}^0$. Although this statement is not yet proved rigorously, there are strong numerical evidences for its correctness.

7.3.4 Convergence and accuracy

In this section, we analyze the accuracy of the spectral approach for computing γ_0^h. For this purpose, we consider several examples for which the theoretical value of γ_0^h is known. Since large h is expected to be more problematic for computing the eigenvalues of the matrix $\Lambda + h\mathcal{B}$ (because the "perturbation" $h\mathcal{B}$ is large), the value $h = 10^8$ is taken as a proxy for the limit of h going to infinity. This limit corresponds to a perfectly reactive/absorbing/relaxing medium, in which particles are "killed" at the first encounter with A.

7.3.4.1 Example 1

In this example, $\Omega = (0, 1)$ (the unit interval), $A = \{0, 1\}$ (two endpoints).
In Fig. 7.1, one can see the smallest eigenvalue $\gamma_{0,N}^h$ of the matrix $\Lambda + h\mathcal{B}$ truncated to size $N \times N$ as a function of N ranging from 500 to 2500. One gets

$$\gamma_{0,N}^h \approx 9.8696 + \frac{8.0301}{N},$$

where the limiting value 9.8696 is very close to the theoretical value $\gamma_0^\infty = \pi^2 \approx 9.8696...$ (the smallest
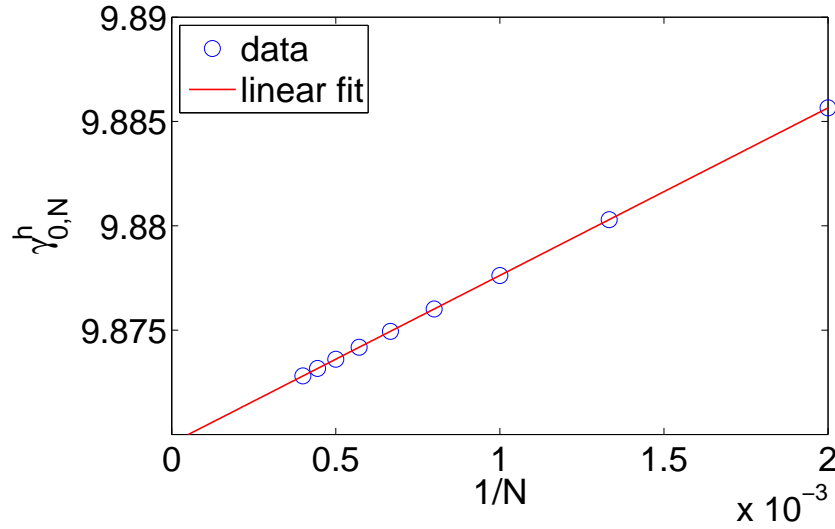
Figure 7.1: The smallest eigenvalue $\gamma_{0,N}^h$ of the truncated matrix $\Lambda + h\mathcal{B}$ (of size $N \times N$) for $\Omega = (0,1)$, $A = \{0,1\}$, $h = 10^8$. The error is almost linear with $1/N$.

eigenvalue of the Laplace operator on the unit interval with Dirichlet boundary conditions).

7.3.4.2 Example 2

We consider the unit interval $\Omega = (0,1)$ and $A = [0.2, 0.8]$ (subinterval).

Fig. 7.2 shows $\gamma_{0,N}^h$ as a function of N ranging from 400 to 1000, which can be fitted as

$$\gamma_{0,N}^h \approx 61.593 + \frac{92.92}{N}.$$

This limit value 61.593 is very close to the theoretical value $\gamma_0^\infty = \pi^2/(2 \cdot 0.2)^2 \approx 61.685...$ (the smallest eigenvalue of the Laplace operator on the interval $[0, 0.2]$ with the reflecting endpoint 0 and the absorbing endpoint 0.2).

Remark 7.3.1. *In general, when A is a compact subset of the unit interval, the error of computation can be estimated in the order of $1/N$:*

$$\gamma_{0,N}^h \approx \gamma_0^h + \frac{const}{N}. \tag{7.9}$$

Knowing the convergence rate, one can compute the value $\gamma_{0,N}^h$ (or other spectral characteristics) for different N, fit them by a linear function of $1/N$ and finally extrapolate the numerical values to the limit. It is worth emphasizing that such supplementary steps do not almost increase the computational time. In fact, one can construct the matrix $\Lambda + h\mathcal{B}$ of the largest available size N and then find eigenvalues of its smaller submatrices.
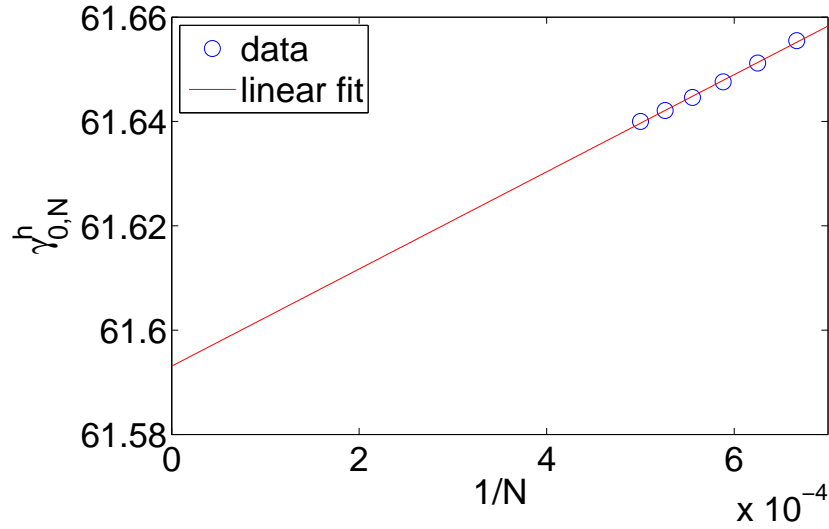
Figure 7.2:   The smallest eigenvalue $\gamma_{0,N}^h$ of the truncated matrix $\Lambda + h\mathcal{B}$ (of size $N \times N$) for $\Omega = (0,1)$, $A = [0.2, 0.8]$, $h = 10^8$. The error is approximately linear with $1/N$.

7.3.4.3   Example 3

In this example, $\Omega = \{\mathbf{r} \in \mathbb{R}^2 \ : \ |\mathbf{r}| < 1\}$ (the unit disk), $A = \partial\Omega$ (its boundary).

On Fig. 7.3, $\gamma_{0,N}^h$ is shown as a function of N ranging from 5000 to 17000 which can be fitted as

$$\gamma_{0,N}^h \approx 5.7829 + \frac{3.732}{\sqrt{N}}.$$

The limiting value 5.7829 is very close to the theoretical value $\gamma_0^\infty = 5.7832...$ (the square of the first positive root α_{00} of the equation $J_0(z) = 0$, which is the smallest eigenvalue of the Laplace operator on the unit disk with Dirichlet boundary condition).

7.3.4.4   Example 4

Let us consider $\Omega = \{\mathbf{r} \in \mathbb{R}^2 \ : \ |\mathbf{r}| < 1\}$ (the unit disk), $A = \{\mathbf{r} \in \mathbb{R}^2 \ : \ |\mathbf{r}| < r_0\}$ (the smaller disk of radius $r_0 = 0.5$ shown on Fig. 7.4a).

Fig. 7.5 shows the value $\gamma_{0,N}^h$ as a function of N ranging from 10^4 to $1.9 \cdot 10^4$ which can be fitted as

$$\gamma_{0,N}^h \approx 7.345 + \frac{81.016}{\sqrt{N}}.$$

The limiting value 7.345 is very close to the theoretical value 7.3474... (the square of the first positive root of Eq. (F.2) from Appendix F2 with $r_0 = 0.5$, which is the smallest eigenvalue of the Laplace operator on the circular layer with inner absorbing circle and outer reflecting circle).
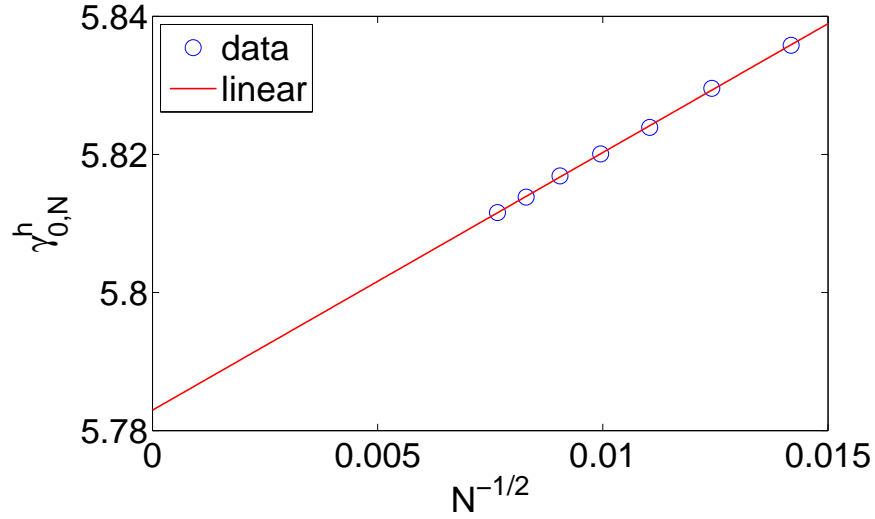
Figure 7.3: The smallest eigenvalue $\gamma_{0,N}^h$ of the truncated matrix $\Lambda + h\mathcal{B}$ (of size $N \times N$) for the unit disk, when A is the unit circle, and $h = 10^8$. The error is almost linear with $1/\sqrt{N}$.
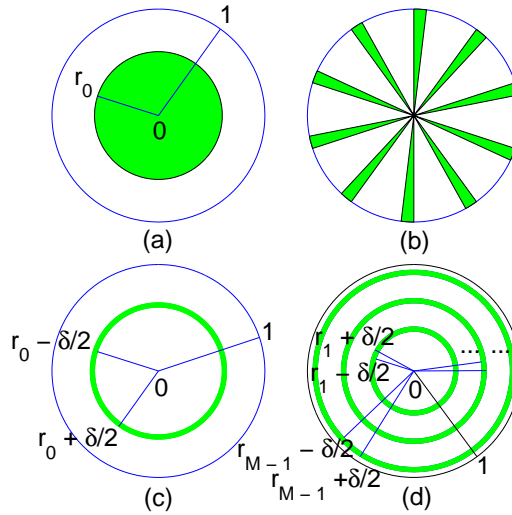
Figure 7.4: Several shapes of the reactive region A inside the unit disk. (a) a smaller disk of radius r_0 centered at the origin; (b) the union of M identical angular sectors of angle β, with the total area $S_A = M\beta/2$ fixed to be $\pi/5$. (c) a circular annulus of the inner and outer radii $r_0 - \delta/2$ and $r_0 + \delta/2$, centered at the origin; (d) the union of $M - 1$ annuli centered at the origin, with the inner and outer radii $r_i - \delta/2$ and $r_i + \delta/2$, and $r_i = i/M$, $i = 1, ..., M - 1$;
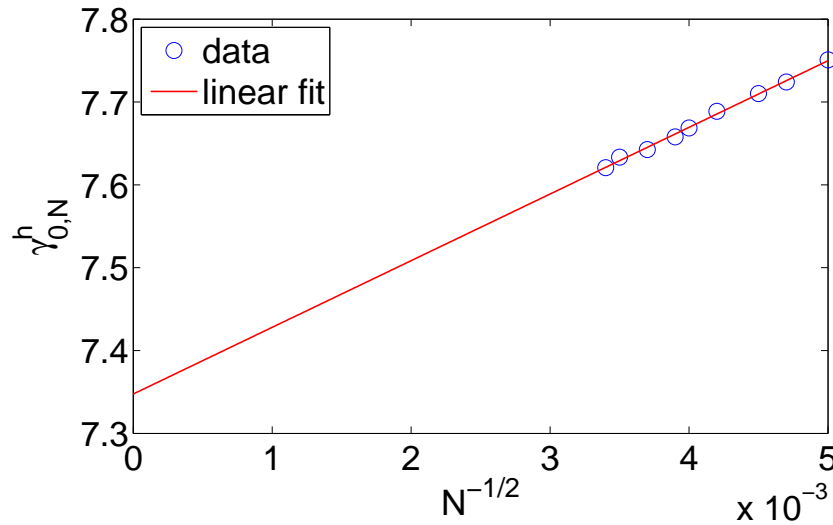
Figure 7.5:   The smallest eigenvalue $\gamma_{0,N}^h$ of the truncated matrix $\Lambda + h\mathcal{B}$ (of size $N \times N$) for the unit disk, when A is a smaller disk of radius $r_0 = 0.5$, and $h = 10^8$. The error is approximately linear with $1/\sqrt{N}$.

Remark 7.3.2. *In general, the error of computation is expected to be in the order of $\frac{1}{\sqrt{N}}$:*

$$\gamma_{0,N}^h \approx \gamma_0^h + \frac{const}{\sqrt{N}}.$$

A slower convergence for two-dimensional domains is expected from Weyl's asymptotic law for the eigenvalues: $\lambda_N \sim N^{2/d}$ [134]. In fact, the error of computation is related to the largest eigenvalue λ_N in the truncated matrix Λ so that Eq. (7.9) implies the error to be in the order of $\lambda_N^{-1/2}$ in the one-dimensional case. Assuming the same behavior of the error in higher dimensions, one gets the error in the order of $N^{-1/d}$, as confirmed by numerical results. Although the convergence is even slower in two dimensions than in one dimension, an extrapolation can still be used to get accurate results (e.g., see Examples 3 and 4).

Remark 7.3.3. *For rotation-invariant functions $B(\mathbf{r})$, one can get a significant improvement. As shown in Sect. 7.3.3, the matrix $\Lambda + h\mathcal{B}$ has a block structure, and the computation is reduced to the diagonalization of each block. We checked numerically that the smallest eigenvalue of a block matrix of size $n \times n$ behaves as*

$$\gamma_{0,n}^h \approx \gamma_0^h + \frac{const}{n},$$

as in the one-dimensional case. The extrapolation is also useful. In summary, the computation for the rotation-invariant case runs faster and uses a smaller number of eigenvalues to estimate more accurately the value of γ_0^h than in the general case.

7.4 Numerical results

7.4.1 Surface reaction on the unit circle

As already mentioned, reactive regions may lie either in the bulk or on the boundary of a confining domain. In the latter case, although the boundary is formally reflecting, particles can eventually react when hitting the boundary. Traditionally, partially reflecting-absorbing surfaces are modeled through Robin boundary condition:

$$\frac{\partial u_m^h(\mathbf{r})}{\partial n} + h u_m^h(\mathbf{r}) = 0 \quad (\mathbf{r} \in \partial\Omega),$$

with a positive constant h. In our approach, the reflecting character of the surface is incorporated through the Laplace operator eigenfunctions with Neumann boundary condition, while the absorbing counter-part is introduced through the matrix $\mathcal{B}$. As discussed in [99], using this separation of the reflection and absorption *mechanisms* has many advantages. First, one can easily introduce heterogeneous reaction rate on the boundary (as illustrated below). Second, the eigenfunctions $u_m^h(\mathbf{r})$ with Robin boundary condition depend on h, and have to be recalculated for each value of h. In turn, here h appears as a constant in the matrix $\Lambda + h\mathcal{B}$ so that one needs to construct the matrices Λ and $\mathcal{B}$ only once.

On Figs. 7.1 and 7.3, we illustrate a numerical validation of the above implementation of the surface reaction mechanism. In these examples, we used the Laplacian eigenfunctions with Neumann boundary condition (reflecting surface) to compute the value γ_0^∞, that is exactly the smallest eigenvalue of the Laplace operator with Dirichlet boundary condition (absorbing boundary). The accuracy of this computation is remarkably good.

In order to illustrate the use of heterogeneous reaction rate on the surface, we consider two cases. First, we take A to be an arc of length 2ε. When ε is small, this is so-called narrow escape problem which was thoroughly studied by Singer *et al.* [202, 203]. In particular, they found the exact formula for the mean exit time from the unit disk. As discussed in Sect. 7.2.3, the survival probability allows one to investigate first passage times and other time statistics of Brownian motion in reactive media. In Appendix F3, we express the mean exit time in terms of the spectral characteristics γ_m^h and A_m^h and compare the numerical results to the exact formula.

Second, we choose A to be the union of M identical arcs of the unit circle:

$$A = \left\{ (x,y) \in \mathbb{R}^2 \ : \ x = \cos\varphi, \ y = \sin\varphi, \ \varphi \in \bigcup_{k=1}^{M} \left(\frac{2\pi k}{M}, \frac{2\pi k + L}{M} \right) \right\}.$$

The total length L of these arcs is fixed. The smallest eigenvalue γ_0^h for $h = 10^8$ is extrapolated to the limit $N \to \infty$ and plotted on Fig. 7.6 as a function of M for $L = 2\pi/5$. One can see that γ_0^h rapidly approaches the limit 5.7829... as M increases. The same behavior was observed for other choices of the total length L (ranging between 0 and 2π). It means that a partly reactive boundary, in which many small reactive grains are equidistributed, has almost the same overall reaction rate as a fully reactive boundary, i.e., a small amount of catalytic grains (here, small length L) works as efficiently as a large amount of catalytic grains. In other words, if the catalytic grains are equidistributed over the surface,
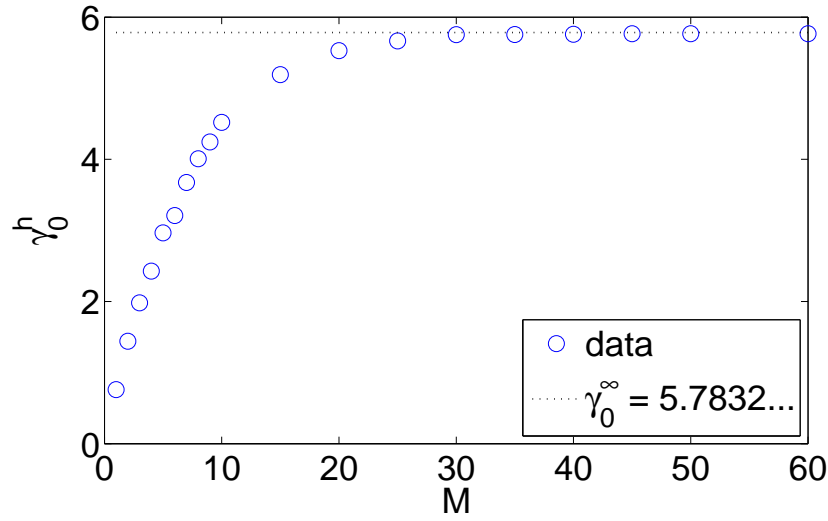
Figure 7.6: The extrapolated smallest eigenvalue γ_0^h for the unit disk, when A is composed of M identical arcs of the unit circle. The total length L is kept to be $2\pi/5$ for different M, and $h = 10^8$. When M increases, the eigenvalue γ_0^h rapidly approaches the limit 5.7832... which corresponds to a perfectly reactive circle (cf. Fig. 7.3).

M	1	5	10	15	20	30	35	50
γ_0^h	2.43	30.26	126.18	626.38	807.15	$1.50 \cdot 10^5$	$2.49 \cdot 10^6$	$2.49 \cdot 10^7$

Table 7.1: The extrapolated smallest eigenvalue γ_0^h for the union of M identical sectors of the unit disk (Fig. 7.4b), with the total surface area $S_A = \pi/4$, and $h = 10^8$. When M increases, γ_0^h approaches the limit $h/4 = 2.5 \cdot 10^7$.

its performance is independent of the amount of catalytic grains (the length L). One can find more probabilistic interpretation of this result in [162].

7.4.2 Infinite reactivity in the bulk

Similar to Sect. 7.4.1, we consider A as the union of M identical sectors of the unit disk (Fig. 7.4b), with the total surface area S_A to be fixed $\pi/4$. For numerical computations, we chose $h = 10^8$ as a proxy for the infinite limit. Table 7.1 shows the values of γ_0^h, which tend to $S_A h/\pi$ for increasing M (see Appendix F1).

If the reactivity h was infinite, one would expect $\gamma_0^\infty \to \infty$ as $M \to \infty$, independently of the total surface area S_A. In what follows, we focus on the case of a finite reactivity which seems to be more relevant for practical situations.
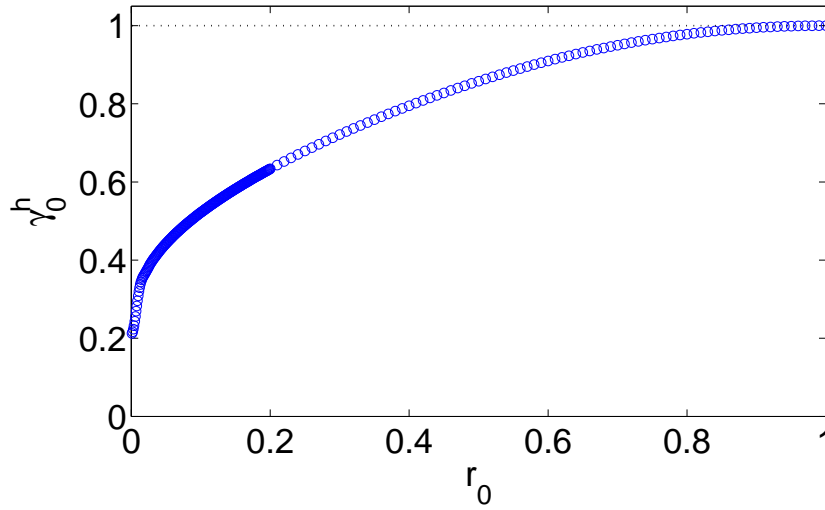
Figure 7.7:   The extrapolated smallest eigenvalue γ_0^h as a function of the radius r_0 of the reactive region (the disk) shown on Fig. 7.4a, with $hS_A = \pi$.

7.4.3   Finite reactivity in the bulk

When the reactivity h is finite, the amount of reactive grains can be naturally characterized by hS_A, S_A being the total area of the reactive region. Fixing hS_A, one may wonder how the reaction performance of the medium depends on the reactivity h and the shape of the reactive region. For instance, what is the shape of the most reactive medium? For the computations of this section, we fix $hS_A = \pi$ and analyze the smallest eigenvalue γ_0^h. We focus on the unit disk as the confining domain.

In the trivial case $A = \Omega$, Eq. (7.8) yields $\mathcal{B}_{m,m'} = \delta_{m,m'}$ due to the orthogonality of the eigenfunctions. The matrix $\mathcal{B}_\Omega$ is just the identity matrix, and γ_0^h is equal to h.

Example 1: $A = \{\mathbf{r} \in \mathbb{R}^2 \ : \ |\mathbf{r}| < r_0\}$ **(the disk of radius r_0)**

The condition $hS_A = \pi$ implies $h = 1/r_0^2$ which varies from 1 to infinity as r_0 goes from 1 to 0. The behavior of γ_0^h is shown on Fig. 7.7.

When r_0 is close to 1, the reactive region is nearly the whole disk so that $\gamma_0^h \approx h \approx 1$. In the opposite limit of r_0 going to 0, the values γ_0^h approach 0, as one may expect for a shrinking reactive region. However, the decay is logarithmically slow, as in the case of a perfectly reactive region ($h = \infty$). In fact, the probability for Brownian motion to find (and then react immediately on) a small disk vanishes logarithmically with its radius r_0 in two dimensions. The asymptotic behavior of γ_0^∞ as $r_0 \to 0$ is given in Appendix F2. On the other hand, for a reactive region with fixed h, a perturbative theory yields

$$\gamma_0^h \approx \lambda_0 + h\mathcal{B}_{0,0} = hr_0^2 \quad (r_0 \to 0)$$

that is a much faster decay. The example shown on Fig. 7.7 is a somewhat intermediate situation, in which the condition $hS_A = \pi$ makes the first-order perturbative term hr_0^2 to be constant. In this case, the whole perturbative series has to be computed for a fixed r_0, and the resulting sum turns out to decay

logarithmically as $r_0 \to 0$.

Since γ_0^h decays logarithmically, even a very small reactive region yields a significant reaction rate γ_0^h as shown on Fig. 7.7 (although the values of γ_0^h seem to approach a positive constant, it is a visual deception).

Example 2: $A = \{\mathbf{r} \in \mathbb{R}^2 \ : \ r_0 - \delta/2 < |\mathbf{r}| < r_0 + \delta/2\}$

Another interesting example is a circular annulus with the inner and outer radii $r_0 - \delta/2$ and $r_0 + \delta/2$ (Fig. 7.4c). When δ is small, the matrix $\mathcal{B}$ can be approximated as

$$\mathcal{B}_{nkl,n'k'l'} = \int\limits_{r_0-\delta/2}^{r_0+\delta/2} \left(\int\limits_{0}^{2\pi} u_{nkl}(r,\varphi) \, u_{n'k'l'}(r,\varphi) \, d\varphi \right) r \, dr \approx r_0\delta \, \mathcal{B}_{nkl,n'k'l'}^{(0,r_0)},$$

where

$$\mathcal{B}_{nkl,n'k'l'}^{(0,r_0)} = \int\limits_{0}^{2\pi} u_{nkl}(r_0,\varphi) \, u_{n'k'l'}(r_0,\varphi) \, d\varphi$$

is the matrix $\mathcal{B}$ for a perfectly reactive circle of radius r_0 (centered at the origin). Since the condition $hS_A = \pi$ implies $hr_0\delta = 1/2$, the matrix $\Lambda + h\mathcal{B}$ becomes

$$\Lambda + h\mathcal{B} \approx \Lambda + hr_0\delta\mathcal{B}^{(0,r_0)} = \Lambda + \frac{1}{2}\mathcal{B}^{(0,r_0)}.$$

The behavior of γ_0^h is shown on Fig. 7.8. Interestingly, there is an optimal radius $r_0 \approx 0.7$ for which a thin circular annulus has the highest reaction rate γ_0^h. The latter is slightly below 1 that is the reaction rate for a uniformly filled unit disk (under the condition of fixed $hS_A = \pi$). This is an example of geometry optimization for reactive media (see below).

Example 3: Multiple equidistant annuli shown on Fig. 7.4d

Next, we consider A be to the union of M thin annuli shown on Fig. 7.4d, each annulus having the width δ. The total area S_A is $\pi\delta(M-1)$, implying $h\delta(M-1) = 1$. When $\delta \to 0$, the matrix $\Lambda + h\mathcal{B}$ converges to

$$\Lambda + h\mathcal{B} \approx \Lambda + h\delta \sum_{i=1}^{M-1} r_i \, \mathcal{B}^{(0,r_i)} = \Lambda + \frac{1}{M(M-1)} \sum_{i=1}^{M-1} i \, \mathcal{B}^{(0,r_i)}.$$

As shown on Fig. 7.9, the value of γ_0^h tends to 1 when the number M of annuli increases.

Our numerical examples suggest that a uniform filling of a medium with reactive grains of finite reactivity h provides the highest overall reaction rate γ_0^h. This seems to be the optimal geometry of the reactive region under the constraint of fixed hS_A. A theoretical argument supporting this suggestion is presented in Appendix F4, while a rigorous proof is still missing. However, such a uniform filling is not available in many practical situations (e.g., when multiple processes have to be maintained in parallel, like in the case of a living cell). In this case, one may wonder whether it is possible to fill the medium heterogeneously nearly as good as uniformly, and what is the optimal shape of the reactive region (perhaps, under some additional constraints).

Two examples of this section illustrate these issues. Fig. 7.8 shows that there is an optimal radius for a
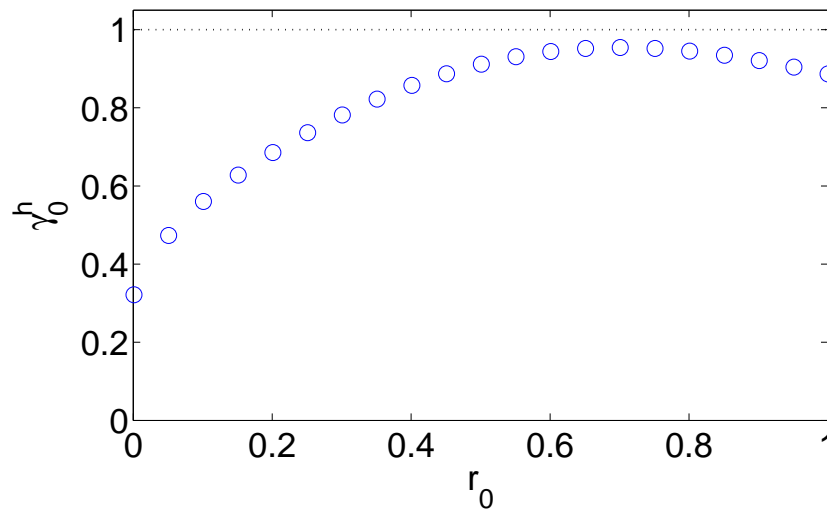
Figure 7.8:   The extrapolated smallest eigenvalue γ_0^h as a function of the radius r_0 of the reactive region (the annulus of width δ) shown on Fig. 7.4c, with $hS_A = \pi$ and $\delta \to 0$.

single thin circular annulus (i.e., under specific geometrical constraint), while Fig. 7.9 confirms that the performance of several thin circular annuli is nearly as good as the best one (for uniform filling). These "toy" models can be considered as the first steps towards geometrical design and engineering of optimal catalysts and diffusive exchangers.

7.5   Conclusion

We have presented a spectral approach to study the survival probability of reflected Brownian motion in reactive media. For arbitrary spatial distribution $B(\mathbf{r})$ of trapping, reaction or relaxation rate, a multi-exponential representation of the survival probability was derived. Its amplitudes A_m^h and characteristic times $1/\gamma_m^h$ were expressed through the spectral properties of the two infinite-dimensional matrices Λ and $\mathcal{B}$ which represent the Laplace operator and the distribution $B(\mathbf{r})$ in the Laplace operator eigenbasis on a chosen confining domain. The advantage of such a representation is that the geometrical complexity of the problem (i.e., the shape of reactive regions) is incorporated through the matrix $\mathcal{B}$, independently of the Laplace operator eigenbasis. In other words, computation of the eigenfunctions, which is often the most time-consuming step, has to be performed only once for a given confining domain. Moreover, in many cases, the shape of the confining domain is irrelevant, and simple confining domains such as a disk or a sphere can be used. In these cases, the Laplace operator eigenfunctions and eigenvalues are known explicitly that significantly simplifies computations. For this reason, we considered the unit disk as a confining domain.

From a numerical point of view, the computational performance of the spectral approach may be inferior to other numerical techniques. It is not surprising because the conventional techniques (such as Monte Carlo simulations or finite difference or finite element methods) search for a single solution of a diffusive
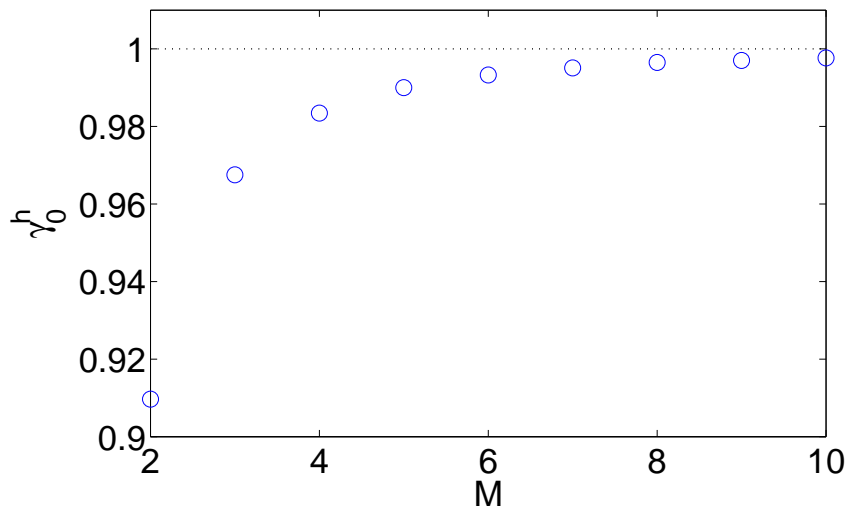
Figure 7.9: The extrapolated smallest eigenvalue γ_0^h as a function of the number M of annuli shown on Fig. 7.4d, with $hS_A = \pi$ and $\delta \to 0$.

problem with a given set of physical parameters. On the contrary, the use of eigenfunctions allows one to find (or, at least, to formally express) all the solutions at once and to analyze the structure of these solutions and their dependence on physical parameters. This much more detailed information comes at the cost of more time-consuming computations. In the general case of any spatial distribution of reactive regions, the accuracy of the algorithm is in the order of $N^{-1/d}$, while the computational time for finding eigenvalues of an $N \times N$ matrix grows as $O(N^3)$, where N is the number of the eigenfunctions used, and d is the space dimension. Nonetheless, an extrapolation to the limit $N \to \infty$ allows one to get reasonably accurate results. In addition, we showed that significant improvements in computational time and accuracy can be achieved for rotation-invariant reactive regions. More importantly, a multi-exponential representation (7.6) of the survival probability provides a much deeper insight onto diffusive processes in reactive media than other numerical techniques. The spectral approach computes separately a large number of terms in Eq. (7.6), while other techniques approximates the whole sum. As a consequence, an accurate determination of rapidly decaying terms (with high eigenvalues) is unfeasible by conventional methods.

Using the spectral approach, we studied the role of the geometrical structure of reactive regions and its influence on the overall reaction rate γ_0^h in the long-time regime. For this purpose, we computed the survival probability in several model reactive media and showed that the shape and spatial arrangement of reactive regions could significantly affect γ_0^h. When the reactivity h was infinite, the confining domain could be filled with numerous reactive regions of arbitrarily small total surface area to make the overall reaction rate arbitrarily high. For the case of finite reactivity h, we discussed the optimization of the geometrical shape of reactive regions under the constraint of having fixed total reactivity (i.e., fixed product hS_A). A uniform filling with $A = \Omega$ appeared as the optimal solution yielding the highest reaction rate. In turn, heterogeneity tends to reduce the reaction rate. However, when such a uniform

filling is not possible (or undesired), one can still arrange the reactive regions heterogeneously in a way to get the reaction rate almost as good as the optimal one. This is an interesting perspective for designing the geometrical shapes of efficient catalysts or diffusive exchangers.

Chapter 8

Conclusion and further works

We have studied localization of Laplacian eigenfunctions in various bounded domains. Localization has been shown to emergence in both simple and irregular domains. An eigenfunction u of the Laplace operator is called "L^p-localized" ($p \geq 1$) in a bounded domain $\Omega \subset \mathbb{R}^d$ if it is essentially supported by a small subdomain $\Omega_\alpha \subset \Omega$, i.e.

$$\frac{\|u\|_{L^p(\Omega \setminus \Omega_\alpha)}}{\|u\|_{L^p(\Omega)}} \ll 1, \qquad \frac{\mu_d(\Omega_\alpha)}{\mu_d(\Omega)} \ll 1, \tag{8.1}$$

where $\|.\|_{L^p}$ is the L^p-norm, and μ_d is the Lebesgue measure. It is worth emphasizing that the above definition of localization remains qualitative. We distinguished two types of localization: high-frequency and low-frequency localization.

High-frequency localization exists in two-dimensional domains with smooth and convex boundary (Chapter 3). For circular, spherical and elliptical domains, we derived the inequalities for the L^p-norm of Laplacian eigenfunctions that clearly illustrate the existence of whispering gallery, bouncing ball and focusing modes. We gave an alternative proof for the emergence of bouncing ball modes in elliptical domains. At the same time, we showed that there is no localization in most rectangular domains that led us to an open problem of characterization of domains admitting high-frequency localization. We also proved that in the equilateral triangle, all symmetric eigenfunctions are not localized.

We investigated the behavior of the Laplacian eigenfunctions in a large class of domains, composed of a basic domain V of arbitrary shape and a branch Q of variable cross-sectional profile $\Omega(x)$ (Chapter 4). We showed that if an eigenvalue λ is smaller than the threshold $\mu = \inf\{\mu_1(x)\}$, the associated eigenfunction exponentially decays inside the branch, where $\mu_1(x)$ is the first eigenvalue of the Laplace operator in the cross-section $\Omega(x)$. The decay rate was shown to be at least $\sqrt{2}\sqrt{\mu - \lambda}$. For non-increasing branches, the larger decay rate $2\sqrt{\mu - \lambda}$ was derived and shown to be sharp for an appropriate parameterization of the branch. The exponential estimate is applicable in any dimension and for finite and infinite branches. Since the derivation did not involve any information about the basic domain V, the exponential estimate is applicable for arbitrary V with any boundary condition on ∂V for which the Laplace operator in $V \cup \Omega$ is still self-adjoint. In turn, the Dirichlet boundary condition on the branch boundary was essential.

We illustrated theoretical results by numerical simulations. It was shown that the sufficient condition $\lambda < \mu$ is not necessary, i.e., the eigenfunctions may exponentially decay even if $\lambda > \mu$. However, in this

case, the decay rate and the range of its applicability strongly depend on the specific shape of the branch. For all numerical examples, the sharp decay rate $2\sqrt{\mu - \lambda}$ was correct, even if the condition (4.14) for non-increasing branches was not satisfied. In future, it would be interesting either to relax this condition, or to find counter-examples, for which the sharp decay rate is not applicable.

It is worth emphasizing that a rigorous upper bound for different norms of Laplacian eigenfunctions in branches of variable cross-sectional profile is a new achievement in the theory of classical and quantum waveguides, with potential applications in microelectronics, optics and acoustics. Using these theoretical results, one can explain the existence of low-frequency localized eigenmodes in various domains. Note that mathematical methods from our approach can be adapted for studying eigenfunctions for other spectral problems or other kinds of domains.

We studied the problem of localized eigenmodes of the Laplace operator in resonators with long branches of constant cross-sectional profile (Chapter 5). The localization here was understood as an exponential decay of an eigenfunction inside the branches. This behavior was related to the smallness of the associated eigenvalue in comparison to the first eigenvalue of the Laplace operator in the cross-section of the branch with Dirichlet boundary condition. Using the explicit representation of an eigenfunction in branches, we proposed a general variational formalism for checking the existence of localized eigenmodes. The main result of this chapter is the sufficient condition (5.14) on the branch lengths for getting a trapped mode. In spite of the generality of the formalism, a practical use of the sufficient condition replies on an intuitive choice of the trial function in the basic domain (without branches). The trial function should be chosen as close as possible to the (unknown) eigenfunction. Although there is no general recipe for choosing a *good* trial function, one can often guess an appropriate choice basing on the geometry of the basic domain.

When the basic domain V and the branch shape satisfy the conditions of Theorem 5.4.1, there exists at least one Dirichlet-Laplacian eigenfunction which is localized in V. Using this result, one can explain the emergence of localized eigenmodes in various domains. We illustrated theoretical results for several typical waveguides, including 2D and 3D L-shapes, crossing of the rectangular strips, and bent trips. In particular, we obtained an upper bound for the minimal branch length which is sufficient for localization. The presented method can be applied for studying the localization in many other waveguides.

It is worth emphasizing that the distinction between localized and non-localized modes is much sharper in infinite waveguides than in finite ones. Although by definition a localized eigenfunction in a finite waveguide decays exponentially, the decay rate may be arbitrarily small. If the branch is not long enough, the localized mode may be visually indistinguishable from a non-localized one. In turn, the distinction between localized and non-localized modes in infinite waveguides is always present, whatever the value of the decay rate. The high sensitivity of the localization character to the shape of the basic domain and to the length of branches may potentially be used for switching devices in microelectronics and optics.

We discussed other kinds of low-frequency localization such as e.g localization in dumbbell domains with narrow connections (Appendix G) and elongated polygons (Chapter 4). In a dumbbell domain, it was shown that low-frequency localization depends on the widths of connectors and may happen for both Dirichlet and Neumann boundary conditions. It is important to emphasize that there may exist only a finite number of low-frequency localized eigenmodes in these domains. We proved the existence

of low-frequency localization in elongated polygons and visualized localized eigenmodes by numerical computations. These results show that even in very simple domains, low-frequency eigenfunctions may be localized.

We studied the existence of localized eigenmodes in a specific class of planar spectral graphs (Chapter 6). We presented several properties of Laplacian eigenvalues and associated eigenfunctions in these domains. Using these properties, one can easily distinguish localized and non-localized eigenmodes in these planar graphs. These points were illustrated by several numerical simulations. We proposed an efficient divide-and-conquer algorithm to solve the eigenvalue problem for Laplacian matrices in a class of undirected and weighted graphs with N vertices. The complexity of our algorithm reduces to $O(N^2)$ by the fast multipole method (FMM) that is much faster than traditional approaches of complexity $O(N^3)$.

Finally, we presented a spectral approach to study the survival probability of reflected Brownian motion in reactive media (Chapter 7). For arbitrary spatial distribution $B(\mathbf{r})$ of trapping, reaction or relaxation rate, we derived a multi-exponential representation of the survival probability. Its amplitudes A_m^h and characteristic times $1/\gamma_m^h$ were expressed through the spectral properties of the two infinite-dimensional matrices Λ and $\mathcal{B}$ which represent the Laplace operator and the distribution $B(\mathbf{r})$ in the Laplace operator eigenbasis on a chosen confining domain. The advantage of such a representation is that the geometrical complexity of the problem (i.e., the shape of reactive regions) is incorporated through the matrix $\mathcal{B}$. Computation of the eigenfunctions, which is often the most time-consuming step, has to be performed only once for a given confining domain. Moreover, if the shape of the confining domain is irrelevant, simple confining domains such as a disk or a sphere can be used. In these cases, the Laplace operator eigenfunctions and eigenvalues are known explicitly that significantly simplifies computations.

Using the spectral approach, we investigated the role of the geometrical structure of reactive regions and its influence on the overall reaction rate in the long-time regime. For this purpose, we computed the survival probability in several model reactive media and showed that the shape and spatial arrangement of reactive regions could significantly affect γ_0^h. When the reactivity h was infinite, the confining domain could be filled with numerous reactive regions of arbitrarily small total surface area to make the overall reaction rate arbitrarily high. For the case of finite reactivity h, we discussed the optimization of the geometrical shape of reactive regions under the constraint of having fixed total reactivity (i.e., fixed product hS_A). A uniform filling with $A = \Omega$ appeared as the optimal solution yielding the highest reaction rate. In turn, heterogeneity tends to reduce the reaction rate. However, when such a uniform filling is not possible (or undesired), one can still arrange the reactive regions heterogeneously in a way to get the reaction rate almost as good as the optimal one. This approach can be adapted for designing the geometrical shapes of efficient catalysts or diffusive exchangers.

8.1   Further works

Localized eigenmodes in bounded planar domains have a special interest in their own right. In future, we plan to study the most interesting open questions related to localization, including the following points.

- **Localization in convex polygons**

Can high-frequency localization happen in a regular polygon or not? As already discussed, even for an equilateral triangle and a square, the rigorous answer is unknown. In the equilateral triangle, all symmetric Dirichlet-Laplace eigenfunctions are not localized. However, it is unclear whether one can find some localized eigenmodes or not among the remaining eigenfunctions.

In Chapter 4, it was shown that localized low-frequency eigenmodes may exist in various elongated polygons. The ratio between the diameter and the inradius of these polygons seems to influence the properties of low-frequency localization. The larger the ratio is, the larger the number of localized eigenfunctions is. At the same time, this ratio can be arbitrary large in irrational rectangles but there is no localization in these domains. It would be interesting to find a "mechanism" of localization in such domains.

- **Counting the number of localized eigenfunctions**

The Weyl's law estimates the counting function $N(\lambda) = \#\{m : \lambda_m < \lambda\}$ of the Laplacian eigenvalues (i.e., the number of eigenvalues smaller than λ) as following [225, 226]

$$N(\lambda) \propto \frac{\omega_d \mu_d(\Omega)}{(2\pi)^d} \lambda^{d/2} \qquad (\lambda \to \infty). \tag{8.2}$$

As mentioned before, Bäcker and co-workers estimated the number of bouncing ball modes of the Laplace operator in a class of two-dimensional quantized billiards Ω with two parallel walls [14]

$$N_{\text{bouncing ball}}(\lambda) = \{n : \lambda_n \leq \lambda, u_n \text{ is a bouncing ball mode}\}. \tag{8.3}$$

It is interesting to investigate the number of localized eigenmodes in a bounded domain in general. In future, we aim at counting the number of localized eigenmodes of the Dirichlet-Laplacian in a bounded domain as following

$$N_{\text{localized}}(\lambda) = \{n : \lambda_n \leq \lambda, u_n \text{ is localized}\}. \tag{8.4}$$

Deriving the asymptotic behavior of $N_{\text{localized}}(\lambda)$ may give a better understanding of localization in a general domain. For this purpose, one can start with both numerical and analytical observations in some simple domains, such as e.g disks, elliptical domains, rectangles, and regular polygons.

- **Localization of the Neumann-Laplacian eigenfunctions**

In previous chapters, we have already illustrated the existence of localized eigenfunctions satisfying the Neumann boundary condition in both irregular and simple domains. A "mechanism" of such localization is still poorly understood.

- **The definition of localization**

Although we provided one possible definition (8.1) of localization, the definition is still qualitative. One of the most important objectives in future is to provide an "appropriate" definition for general kinds of localization in bounded domains. Localized and non-localized eigenfunctions may have

very close eigenvalues. For instance, in a dumbbell domain shown in Fig. G.2, the eigenfunction u_{14} is not localized while the consecutive eigenfunction u_{15} is localized in Ω_1 (Fig. 8.1). Note that the difference between λ_{14} and λ_{15} are small. Although the eigenvalues λ_{19} and λ_{20} are close to each other, the eigenfunction the 19th eigenfunction is localized in Ω_2 while the 20th eigenfunctions is localized in Ω_1. This is one of the difficulties to overcome for getting a generic definition of localization.

(a) u_{14} (b) u_{15} (c) u_{19} (d) u_{20}
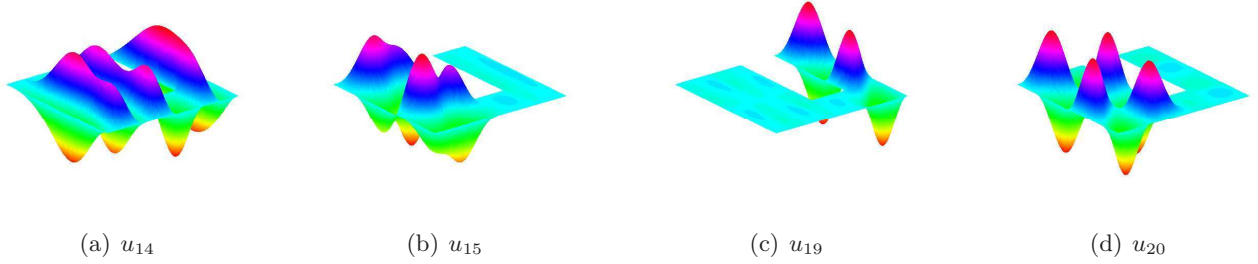
Figure 8.1: Several Dirichlet eigenfunctions in a dumbbell domain Ω_ε shown on Fig. G.2. The 14th, 15th, 19th, and 20th eigenvalues are 165.4611, 167.9188, 197.0922, and 197.3857. The $15^{th}/20^{th}$ eigenfunctions are localized in Ω_1, while the 19th eigenfunction is localized in Ω_2. At the same time, the 14th eigenfunctions is not localized. Note that λ_{14} is relatively close to λ_{15}, while λ_{19} is close to λ_{20}.

Appendix A

Preliminaries

A1 Several lower estimates

In this Appendix, we sketch the proof for the lower estimate, following and extending the ideas by Filoche and Mayboroda [78]. Although the results are formulated for the Laplace operator on domains with smooth boundaries, extensions to other elliptic operators or more general boundaries are possible.

Theorem A1.1. *Let u be an eigenfunction of the Laplace operator in a bounded domain $\Omega \subset \mathbb{R}^d$ with Dirichlet boundary condition, and λ the associated eigenvalue. Let $D \subset \Omega$ is an open subdomain of Ω, and v the harmonic function in D with $v|_{\partial D} = u|_{\partial D}$ on a piecewise smooth boundary ∂D. Then the following inequality holds:*

$$\|u\|_{L^2(D)} \geq \frac{\lambda_1(D)}{\lambda + \lambda_1(D)} \|v\|_{L^2(D)}, \tag{A.1}$$

where $\lambda_1(D)$ is the first Dirichlet-Laplacian eigenvalue in D.

Proof. Following the proof by Filoche and Mayboroda, we consider the function $w = u - v$ which satisfies

$$-\Delta w = \lambda u \quad (\mathbf{r} \in D), \qquad w = 0 \quad (\mathbf{r} \in \partial D).$$

Let $\{\varphi_k^D\}$ denote the set of L^2-normalized eigenfunctions (with eigenvalues λ_k^D) of the Dirichlet-Laplace operator in D that form an orthonormal basis in $L^2(D)$. The function Δw can be expanded over this basis as

$$-\Delta w = \sum_k c_k \varphi_k^D,$$

where the coefficients c_k are

$$c_k = \int_D (-\Delta w(\mathbf{r})) \, \varphi_k^D(\mathbf{r}) = \lambda_k^D \int_D w(\mathbf{r}) \varphi_k^D(\mathbf{r}) d\mathbf{r}.$$

k	$n=0$	$n=1$	$n=2$	$n=3$
1	2.4048	3.8317	5.1356	6.3802
2	5.5201	7.0156	8.4172	9.7610
3	8.6537	10.1735	11.6198	13.0152
4	11.7915	13.3237	14.7960	16.2235
5	14.9309	16.4706	17.9598	19.4094
6	18.0711	19.6159	21.1170	22.5827
7	21.2116	22.7601	24.2701	25.7482
8	24.3525	25.9037	27.4206	28.9084
9	27.4935	29.0468	30.5692	32.0649
10	30.6346	32.1897	33.7165	35.2187

Table A.1: Table of the first 10 positive zeros of the Bessel functions $J_n(z) = 0$.

One gets

$$(\lambda\|u\|_{L^2(D)})^2 = \|\Delta w\|_{L^2(D)}^2 = \sum_k c_k^2 = \sum_k \left(\lambda_k^D \int_D w(\mathbf{r})\varphi_k^D(\mathbf{r})d\mathbf{r}\right)^2$$

$$\geq (\lambda_1^D)^2 \sum_k \left(\int_D w(\mathbf{r})\varphi_k^D(\mathbf{r})d\mathbf{r}\right)^2 \geq \left(\lambda_1^D\|w\|_{L^2(D)}\right)^2,$$

from which

$$\lambda\|u\|_{L^2(D)} \geq \lambda_1^D\|u - v\|_{L^2(D)}.$$

Adding $\lambda_1^D\|u\|_{L^2(D)}$ to both sides, one gets

$$(\lambda + \lambda_1^D)\|u\|_{L^2(D)} \geq \lambda_1^D\left(\|u - v\|_{L^2(D)} + \|u\|_{L^2(D)}\right) \geq \lambda_1^D\|v\|_{L^2(D)},$$

from which the inequality (A.1) follows. □

A2 Zeros of Bessel functions

In this section, we provide some zeros of Bessel functions and its derivative by numerical computations.

k	$n = 0$	$n = 1$	$n = 2$	$n = 3$
1	3.8317	1.8412	3.0542	4.2012
2	7.0156	5.3314	6.7061	8.0152
3	10.1735	8.5363	9.9695	11.3459
4	13.3237	11.7060	13.1704	14.5858
5	16.4706	14.8636	16.3475	17.7887
6	19.6159	18.0155	19.5129	20.9725
7	22.7601	21.1644	22.6716	24.1449
8	25.9037	24.3113	25.8260	27.3101
9	29.0468	27.4571	28.9777	30.4703
10	32.1897	30.6019	32.1273	33.6269

Table A.2: Table of the first 10 positive zeros of the functions $J_n'(z) = 0$.

k	$n = 1$	$n = 2$	$n = 3$
1	9.9361	16.6982	23.2568
2	13.5893	20.7899	27.6979
3	17.0038	24.4949	31.6501
4	20.3208	28.0267	35.3747
5	23.5861	31.4600	38.9654
6	26.8202	34.8300	42.4678
7	30.0337	38.1564	45.9077
8	33.2330	41.4511	49.3011
9	36.4220	44.7219	52.6589
10	39.6032	47.9743	55.9885

Table A.3: Table of the first 10 zeros of the Bessel functions $J_{6n}(z) = 0$.

Appendix B

High-frequency localization of Laplacian eigenfunctions

B1   Proofs for a disk

The proof of Theorem 3.2.1 is based on several estimates for Bessel functions and their roots that we recall in the following lemmas. In this Appendix, $j_{\nu,k}$ and $j'_{\nu,k}$ denote all positive zeros (enumerated by $k = 1, 2, 3, ...$ in an increasing order) of the Bessel function $J_\nu(x)$ and its derivative $J'_\nu(x)$, respectively.

Lemma B1.1. *For any $n = 1, 2, 3, ...$ and any $\varepsilon \in (0, 2/3)$, the Bessel function $J_n(x)$ satisfies [131]*

$$0 < J_n(nz) < 2^{-n^\varepsilon/3} \qquad \forall\ z \in (0, 1 - n^{\varepsilon - \frac{2}{3}}). \tag{B.1}$$

Lemma B1.2. *For the first zeros $j_{n,1}$ and $j'_{n,1}$ with $n = 1, 2, ...$, one has [40, 222]*

$$n < j'_{n,1} < j_{n,1} < \sqrt{n+1}\left(\sqrt{n+2} + 1\right). \tag{B.2}$$

Lemma B1.3. *For large enough n, the asymptotic relations hold [222]:*

$$J_n(n) = C'_1 n^{-1/3} + O(n^{-5/3}) \qquad \left(C'_1 = \frac{\Gamma(1/3)}{2^{2/3}3^{1/6}\pi} \approx 0.4473\right) \tag{B.3}$$

and

$$j'_{n,1} = n + n^{1/3}\ C'_2 + O(n^{-1/3}) \qquad (C'_2 = 0.808618...). \tag{B.4}$$

As a consequence, taking smaller constants (e.g., $C_1 = 0.447$ and $C_2 = 0.8086$), one gets lower bounds for large enough n:

$$J_n(n) > C_1 n^{-1/3} \qquad (n \gg 1) \tag{B.5}$$

and

$$j'_{n,1} > n + C_2 n^{1/3} \qquad (n \gg 1), \tag{B.6}$$

Lemma B1.4. *For fixed k and large ν, the Olver's expansion holds [68, 164, 165]*

$$j_{\nu,k} = \nu + \delta_k \nu^{1/3} + \frac{3}{10}\delta_k^2 \nu^{-1/3} + \frac{5 - \delta_k^3}{350}\nu^{-1} - \frac{479\delta_k^4 + 20\delta_k}{63000}\nu^{-5/3}$$
$$+ \frac{20231\delta_k^5 - 27550\delta_k^2}{8085000}\nu^{-7/3} + O(\nu^{-3}), \tag{B.7}$$

where $\delta_k = -a_k 2^{-1/3} > 0$ and a_k are the negative zeros of the Airy function. Taking $c_k = \delta_k + \epsilon$ (e.g., $\epsilon = 1$), one gets the upper bounds for $j_{\nu,k}$ for ν large enough

$$j_{\nu,k} < \nu + c_k \nu^{1/3} \qquad (\nu \gg 1). \tag{B.8}$$

In particular, $\delta_1 = 1.855757....$

Lemma B1.5. *For fixed ν and large k, the McMahon's expansion holds [222] (p. 506)*

$$j_{\nu,k} = k\pi + \frac{\pi}{2}(\nu - 1/2) - \frac{4\nu^2 - 1}{8(k\pi + \pi(\nu - 1/2)/2)} + O(1/k^3). \tag{B.9}$$

Lemma B1.6. *The absolute extrema of any Bessel function $J_\nu(z)$ progressively decrease [222] (p. 488), i.e.*

$$|J_\nu(j'_{\nu,1})| > |J_\nu(j'_{\nu,2})| > |J_\nu(j'_{\nu,3})| > ... \tag{B.10}$$

Lemma B1.7. *The k-th positive zero α_{nk} of the function $J'_n(z) + hJ_n(z)$ for any $h > 0$ lies between the k-th positive zeros $j_{n,k}$ and $j'_{n,k}$ of the Bessel function $J_n(z)$ and its derivative $J'_n(z)$:*

$$j_{n,k} < \alpha_{nk} < j'_{n,k}. \tag{B.11}$$

Proof. This is a direct consequence of the minimax principle that ensures the monotonous increase of eigenvalues with the parameter h [54]. $\qquad\square$

a. Now, we prove Theorem 3.2.1.

The proof formalizes the idea that the eigenfunction u_{nk} is small in the large subdomain $D_{nk} = \{\mathbf{r} \in D : |\mathbf{r}| < Rd_n/\alpha_{nk}\}$ (with $d_n = n - n^{2/3}$) and large in the small subdomain $A_{nk} = \{\mathbf{r} \in D : Rn/\alpha_{nk} < |\mathbf{r}| < Rj'_{n,1}/\alpha_{nk}\}$. Since $A_{nk} \subset D$, we have

$$\frac{\|u_{nk}\|^p_{L^p(D_{nk})}}{\|u_{nk}\|^p_{L^p(D)}} < \frac{\|u_{nk}\|^p_{L^p(D_{nk})}}{\|u_{nk}\|^p_{L^p(A_{nk})}} = \frac{\int\limits_0^{Rd_n/\alpha_{nk}} dr\, r\, [J_n(r\alpha_{nk}/R)]^p}{\int\limits_{Rn/\alpha_{nk}}^{Rj'_{n,1}/\alpha_{nk}} dr\, r\, [J_n(r\alpha_{nk}/R)]^p} = \frac{\int\limits_0^{d_n} dz z\, [J_n(z)]^p}{\int\limits_n^{j'_{n,1}} dz z\, [J_n(z)]^p}.$$

The numerator can be bounded by the inequality (B.1) with $\epsilon = 1/3$:

$$\int\limits_0^{d_n} dz z\, [J_n(z)]^p < \left(2^{-n^{1/3}/3}\right)^p \frac{d_n^2}{2} < 2^{-pn^{1/3}/3}\frac{n^2}{2} \qquad (n = 1, 2, 3, ...).$$

In order to bound the denominator, we use the inequalities (B.5, B.6) and the fact that $J_n(z)$ increases on the interval $[n, j'_{n,1}]$ (up to the first maximum at $j'_{n,1}$):

$$\int\limits_{n}^{j'_{n,1}} dz z \, [J_n(z)]^p > [J_n(n)]^p \frac{(j'_{n,1})^2 - n^2}{2} > [C_1 n^{-1/3}]^p \, \frac{(n + C_2 n^{1/3})^2 - n^2}{2} > C_1^p C_2 n^{(4-p)/3}$$

for n large enough, from which

$$\frac{\|u_{nk}\|_{L^p(D_{nk})}}{\|u_{nk}\|_{L^p(A_{nk})}} < \frac{n^{\frac{1}{3} + \frac{2}{3p}} 2^{-n^{1/3}/3}}{C_1 (2 C_2)^{1/p}} \qquad (n \gg 1)$$

that implies Eq. (3.2). Finally, from Lemmas B1.4 and B1.7, we have

$$1 > \frac{\mu_2(D_{nk})}{\mu_2(D)} = \left(\frac{d_n}{\alpha_{nk}} \right)^2 > \frac{d_n^2}{j_{n,k}^2} > \frac{(n - n^{2/3})^2}{(n + c_k n^{1/3})^2} \qquad (n \gg 1)$$

so that the ratio of the areas tends to 1 as n goes to infinity.

b. In what follows, let us prove Theorem 3.2.5. Using the explicit representation (2.33) of eigenfunctions, it is easy to see that

$$\frac{\|u_{nk}\|_{L^\infty(D(R_0))}}{\|u_{nk}\|_{L^\infty(D)}} = \frac{\max\limits_{r \in [R_0, 1]} |J_n(\alpha_{nk} r)|}{\max\limits_{r \in [0, 1]} |J_n(\alpha_{nk} r)|} = \frac{\max\limits_{r \in [R_0, 1]} |J_n(\alpha_{nk} r)|}{\left| J_n(j'_{n,1}) \right|}, \qquad (B.12)$$

where we used the fact that the first maximum (at $j'_{n,1}$) is the largest (lemma B1.6). Since $\lim\limits_{k \to \infty} \alpha_{nk} = \infty$, the Bessel function $J_n(\alpha_{nk} r)$ with $k \gg 1$ can be approximated in the interval $[R_0, 1]$ as [1]

$$J_n(\alpha_{nk} r) \approx \sqrt{\frac{2}{\pi \alpha_{nk} r}} \cos \left(\alpha_{nk} r - \frac{n\pi}{2} - \frac{\pi}{4} \right). \qquad (B.13)$$

It also means that there exists a positive integer K_0 and a constant $A_0 > 0$ such that

$$|J_n(\alpha_{nk} r)| < \sqrt{\frac{A_0}{\alpha_{nk} R_0}}, \quad \forall r \in [R_0, 1], \ k > K_0. \qquad (B.14)$$

Given that the denominator in Eq. (B.12) is fixed, while the numerator decays as $\alpha_{nk}^{-1/2}$, one gets Eq. (3.14). Now we prove Eq. (3.16). One has

$$\frac{\|u_{nk}\|_{L^2(D(R_0))}^2}{\|u_{nk}\|_{L^2(D)}^2} = \frac{\int\limits_{R_0}^{1} dr \, r \, [J_n(\alpha_{nk} r)]^2}{\int\limits_{0}^{1} dr \, r \, [J_n(\alpha_{nk} r)]^2}.$$

Using the basic properties of Bessel functions [1],

$$\int_a^b dr \; r \; [J_n(\alpha_{nk}r)]^2 = \left\{ r^2 [J_n'(\alpha_{nk}r)]^2 + \left(r^2 - \frac{n^2}{\alpha_{nk}^2} \right) [J_n(\alpha_{nk}r)]^2 \right\}_a^b, \tag{B.15}$$

one has

$$\frac{\|u_{nk}\|_{L^2(D(R_0))}^2}{\|u_{nk}\|_{L^2(D)}^2} = 1 - R_0^2 \left[\frac{[J_n'(\alpha_{nk}R_0)]^2 + \left(1 - \frac{n^2}{\alpha_{nk}^2 R_0^2} \right) [J_n(\alpha_{nk}R_0)]^2}{[J_n'(\alpha_{nk})]^2 + \left(1 - \frac{n^2}{\alpha_{nk}^2} \right) [J_n(\alpha_{nk})]^2} \right].$$

In order to compute the limit of the expression in large brackets, we write the leading term approximation of the derivative of the Bessel function for $k \gg 1$ from Eq. (B.13):

$$J_n'(\alpha_{nk}R_0) \approx -\sqrt{\frac{2}{\pi \alpha_{nk}R_0}} \sin\left(\alpha_{nk}R_0 - \frac{n\pi}{2} - \frac{\pi}{4} \right). \tag{B.16}$$

In the limit $k \to \infty$, the term n^2/α_{nk}^2 can be neglected as compared to 1, so that for $k \gg 1$

$$\frac{[J_n'(\alpha_{nk}R_0)]^2 + \left(1 - \frac{n^2}{\alpha_{nk}^2 R_0^2} \right) [J_n(\alpha_{nk}R_0)]^2}{[J_n'(\alpha_{nk})]^2 + \left(1 - \frac{n^2}{\alpha_{nk}^2} \right) [J_n(\alpha_{nk})]^2}$$

$$\approx \frac{\frac{2}{\pi \alpha_{nk}R_0} \sin^2\left(\alpha_{nk}R_0 - \frac{n\pi}{2} - \frac{\pi}{4} \right) + \frac{2}{\pi \alpha_{nk}R_0} \cos^2\left(\alpha_{nk}R_0 - \frac{n\pi}{2} - \frac{\pi}{4} \right)}{\frac{2}{\pi \alpha_{nk}} \sin^2\left(\alpha_{nk} - \frac{n\pi}{2} - \frac{\pi}{4} \right) + \frac{2}{\pi \alpha_{nk}} \cos^2\left(\alpha_{nk} - \frac{n\pi}{2} - \frac{\pi}{4} \right)} = \frac{1}{R_0}$$

that completes the proof for Eq. (3.16).

Finally, we prove Eq. (3.15). For $p > 4$, one has

$$\frac{\|u_{nk}\|_{L^p(D(R_0))}^p}{\|u_{nk}\|_{L^p(D)}^p} = \frac{\int_{R_0}^1 dr \; r \; |J_n(\alpha_{nk}r)|^p}{\int_0^1 dr \; r \; |J_n(\alpha_{nk}r)|^p} = \frac{\int_{\alpha_{nk}R_0}^{\alpha_{nk}} dr \; r \; |J_n(r)|^p}{\int_0^{\alpha_{nk}} dr \; r \; |J_n(r)|^p}$$

Using the approximation (B.13), for each positive integer n, there exists a positive integer K_{1n} such that

$$|J_n(z)| < \sqrt{\frac{3}{\pi z}}, \quad \forall z \in [\alpha_{nk}R_0, \alpha_{nk}], \; k > K_{1n}. \tag{B.17}$$

For $k > K_{1n}$, using the approximation (B.17), one gets

$$\int_{\alpha_{nk}R_0}^{\alpha_{nk}} dr \; r \; |J_n(r)|^p \;\; \leq \;\; \left(\frac{3}{\pi} \right)^{p/2} \int_{\alpha_{nk}R_0}^{\alpha_{nk}} dz \; z^{1-p/2} \tag{B.18}$$

$$\leq \;\; \frac{1}{p/2 - 2} \left(\frac{3}{\pi} \right)^{p/2} \left(\left(\frac{1}{\alpha_{nk}R_0} \right)^{p/2-2} - \left(\frac{1}{\alpha_{nk}} \right)^{p/2-2} \right). \tag{B.19}$$

Bringing the above results together, when $k \gg 1$, one has

$$\frac{\|u_{nk}\|_{L^p(D(R_0))}^p}{\|u_{nk}\|_{L^p(D)}^p} < \frac{\frac{1}{p/2-2} \left(\frac{3}{\pi}\right)^{p/2} \left(\left(\frac{1}{\alpha_{nk}R_0}\right)^{p/2-2} - \left(\frac{1}{\alpha_{nk}}\right)^{p/2-2}\right)}{\int\limits_0^1 dr \ r \ |J_n(r)|^p},$$

where the right-hand side tends to 0 as $k \to \infty$, that completes the proof.

Remark B1.1. *In the case $2 < p < 4$, similarly, for $k > K_{1n}$, using the approximation (B.17),one also gets*

$$H_{n,p}(\alpha_{nk}) = \int\limits_{\alpha_{nk}R_0}^{\alpha_{nk}} dr \ r \ |J_n(r)|^p \ \leq \ \left(\frac{3}{\pi}\right)^{p/2} \int\limits_{\alpha_{nk}R_0}^{\alpha_{nk}} dz \ z^{1-p/2} \tag{B.20}$$

$$\leq \ \frac{1}{2-p/2} \left(\frac{3}{\pi}\right)^{p/2} \left((\alpha_{nk})^{2-p/2} - (\alpha_{nk}R_0)^{2-p/2}\right). \tag{B.21}$$

When $k \to \infty$, one expects that

$$I_{n,p}(\alpha_{nk}) = \int\limits_0^{\alpha_{nk}} dr \ r \ |J_n(r)|^p \sim C(n,p)\alpha_{nk}^{\gamma(n,p)}, \tag{B.22}$$

where $C(n,p)$ is a constant, only depending on n and p. It also means that there exist two positive constants $D(n,p)$ and $E(n,p)$, and a positive integer K_{2n} such that

$$D(n,p)\alpha_{nk}^{\gamma(n,p)} \leq I_{n,p}(\alpha_{nk}) \leq E(n,p)\alpha_{nk}^{\gamma(n,p)}, \forall k > K_{2n}. \tag{B.23}$$

If one can prove that

$$\gamma(n,p) > 2 - p/2, \forall n \in \mathbb{N}, p \in (2,4], \tag{B.24}$$

then for $k > max\{K_{1n}, K_{2n}\}$,

$$\frac{\|u_{nk}\|_{L^p(D(R_0))}^p}{\|u_{nk}\|_{L^p(D)}^p} \ < \ \frac{\frac{1}{2-p/2} \left(\frac{3}{\pi}\right)^{p/2} \left((\alpha_{nk})^{2-p/2} - (\alpha_{nk}R_0)^{2-p/2}\right)}{D(n,p)\alpha_{nk}^{\gamma(n,p)}},$$

$$< \ \frac{\frac{1}{2-p/2} \left(\frac{3}{\pi}\right)^{p/2}}{D(n,p)} \left[1 - R_0^{2-p/2}\right] (\alpha_{nk})^{2-p/2-\gamma(n,p)},$$

where the right-hand side tends to zero as $k \to \infty$, or

$$\lim_{k\to\infty} \frac{\|u_{nk}\|_{L^p(D(R_0))}^p}{\|u_{nk}\|_{L^p(D)}^p} = 0, \tag{B.25}$$
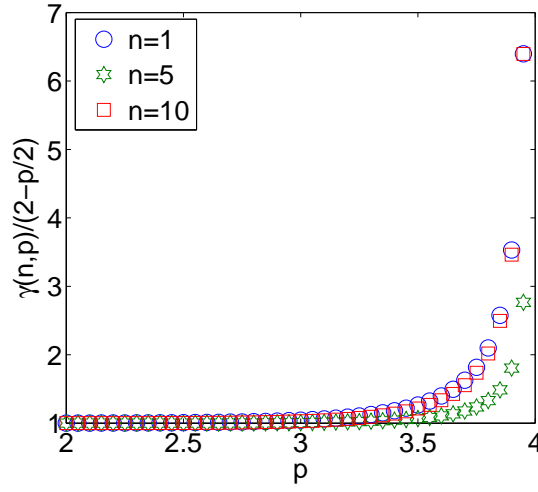
Figure B.1:   The behavior of the function $\dfrac{\gamma(n,p)}{2-\frac{p}{2}}$ in the interval $[2,4]$ for $n=1$ (blue), $n=5$ (green) and $n=10$ (red). In this figure, this function increases everywhere from $p=2$ to $p=4$ and its initial value at $p=2$ is equal to 1.

It is interesting to note that,

$$\lim_{k\to\infty}\frac{\|u_{nk}\|^2_{L^2(D(R_0))}}{\|u_{nk}\|^2_{L^2(D)}}=1-R_0,$$

and one may expect that

$$\lim_{p\to 2}\gamma(n,p)=1.$$

To clarify the inequality (B.24), we will check it by numerical computations. In Fig. B.1, we compute the value of $\gamma(n,p)$ for $n=1$ (blue), $n=5$ (green) and $n=10$ (red). One can see that the function $\dfrac{\gamma(n,p)}{2-\frac{p}{2}}$ is an increasing function in the interval $[2,4]$ for these cases and its value at $p=2$ is equal to 1. The numerical results confirms the inequality (B.24).

Remark B1.2. *In the case $p=4$, for $k>K_{1n}$, using the approximation (B.17), one also gets*

$$\int_{\alpha_{nk}R_0}^{\alpha_{nk}} dr \ r \ |J_n(r)|^p \ \leq \ \left(\frac{3}{\pi}\right)^{p/2}\int_{\alpha_{nk}R_0}^{\alpha_{nk}} dz \ \frac{1}{z} \tag{B.26}$$

$$\leq \ \frac{1}{2-p/2}\left(\frac{3}{\pi}\right)^{p/2}\log\left(\frac{1}{R_0}\right). \tag{B.27}$$

Similarly, from the inequality (B.24), we also expect that

$$\lim_{k \to \infty} \frac{\|u_{nk}\|_{L^4(D(R_0))}^4}{\|u_{nk}\|_{L^4(D)}^4} = 0. \tag{B.28}$$

Remark B1.3. *It is interesting to understand the limit value of* $\dfrac{\|u_{nk}\|_{L^p(D(R_0))}^p}{\|u_{nk}\|_{L^p(D)}^p}$ *when* $k \to \infty$, *for* $1 \leq p < 2$. *When* $k \gg 1$, *one may expect the following asymptotic approximation*

$$H_{n,p}(\alpha_{nk}) \sim F(n,p)\alpha_{nk}^{\beta(n,p)}, \tag{B.29}$$

and from the above discussions, it seems to be true that

$$\beta(n,p) \leq 2 - \frac{p}{2} < \gamma_{n,p}, \forall 2 < p \leq 4. \tag{B.30}$$

In Fig. B.2, we compare the values of $\beta(n,p)$ *and* $\gamma(n,p)$ *in the interval* $[1,4]$ *for* $n = 1$ *and* $R_0 = 0.7$. *One can see that* $\beta(n,p) \leq \gamma(n,p), \forall 1 \leq p \leq 4$, *and especially, for* $1 \leq p \leq 2$,

$$\beta(n,p) \approx 2 - \frac{p}{2} \approx \gamma(n,p). \tag{B.31}$$

Bringing these numerical results together, one can expect that

$$\lim_{k \to \infty} \frac{\|u_{nk}\|_{L^p(D(R_0))}^p}{\|u_{nk}\|_{L^p(D)}^p} \quad > \quad 0, \forall 1 \leq p \leq 2, \tag{B.32}$$

$$\lim_{k \to \infty} \frac{\|u_{nk}\|_{L^p(D(R_0))}^p}{\|u_{nk}\|_{L^p(D)}^p} \quad = \quad 0, \forall 2 \leq p \leq 4, \tag{B.33}$$

which requires a rigorous proof and further investigation.

B2   Proofs for a ball

In this Appendix, we generalize the previous estimates to a ball $B = \{\mathbf{r} \in \mathbb{R}^3 \;:\; |\mathbf{r}| < R\}$ of radius $R > 0$. We start by recalling and extending several classical estimates.

Lemma B2.1. *For any* $\nu \in \mathbb{R}_+$ *and any* $x \in (0,1)$, *the Kapteyn's inequality holds* [199]

$$0 < J_\nu(\nu x) < \frac{x^\nu \exp(\nu\sqrt{1-x^2})}{\left(1 + \sqrt{1-x^2}\right)^\nu}. \tag{B.34}$$

Now we can prove the following
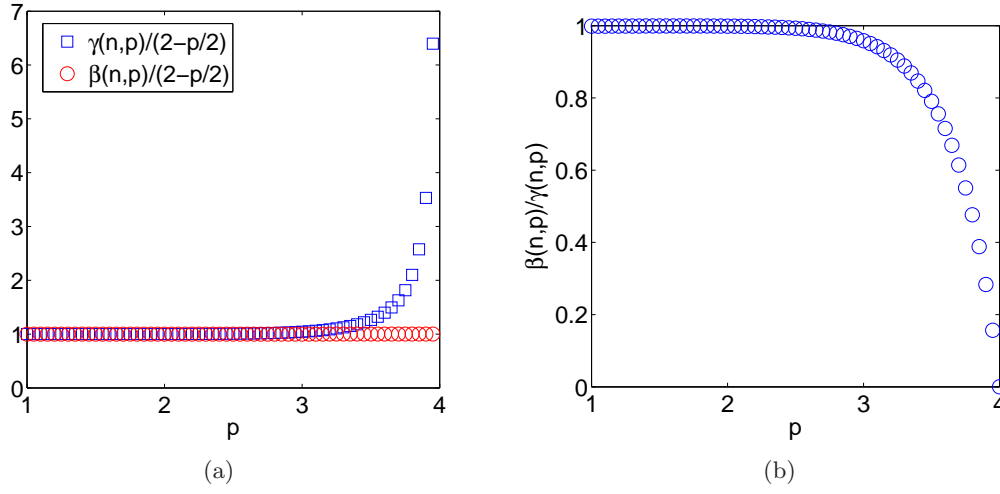
Figure B.2: The behaviors of $\beta(n,p)$ and $\gamma(n,p)$ when p varies in the interval $[1,4]$ ($n=1$ and $R_0 = 0.7$): (a) - The comparison between $\frac{\beta(n,p)}{2-p/2}$ and $\frac{\gamma(n,p)}{2-p/2}$, (b) - The function $\frac{\beta(n,p)}{\gamma(n,p)}$.

Lemma B2.2. *For any $\nu > 1$ and $0 < \epsilon < 2/3$, one has*

$$0 < j_{\nu-\frac{1}{2}}(x) < \sqrt{\frac{\pi}{2\nu}} \, \exp\left(\frac{2}{3} - \frac{1}{3}\nu^\epsilon\right) \qquad \forall \, x \in (0, \nu - \nu^{\epsilon+1/3}). \tag{B.35}$$

Proof. Using the Kapteyn's inequality (B.34) and taking $x = \nu z$ with $z \in (0, 1 - \nu^{\epsilon-2/3})$, one has

$$j_{\nu-1/2}(\nu z) = \sqrt{\frac{\pi}{2\nu}} \frac{J_\nu(\nu z)}{\sqrt{z}} < \sqrt{\frac{\pi}{2\nu}} f(z),$$

where

$$f(z) = \frac{z^{\nu-1/2} e^{\nu\left(1-z^2\right)^{1/2}}}{\left(1 + \sqrt{1-z^2}\right)^\nu}.$$

Substituting $u = \sqrt{1 - z^2} \in (0, 1)$, one gets

$$f(z) = \left(\frac{(1-u^2)^{1-\frac{1}{2\nu}} e^{2u}}{(1+u)^2}\right)^{\nu/2} = \frac{e^{\frac{u}{2}}}{(1+u)^{\frac{1}{2}}} \left[\left(\frac{1-u}{1+u}\right) e^{2u}\right]^{\frac{\nu}{2}-1/4}.$$

Using the inequality

$$\frac{1-u}{1+u} \, e^{2u} < 1 - \frac{2}{3}u^3 \qquad \forall \, u \in (0, 1),$$

one gets

$$f(z) < \frac{e^{\frac{1}{2}}}{(1+0)^{\frac{1}{2}}} \left[1 - \frac{2}{3}u^3\right]^{\frac{\nu}{2}-1/4} < e^{\frac{1}{2}} \left[1 - \frac{2}{3}u^3\right]^{\frac{\nu}{2}-1/4}.$$

Since $z < 1 - \nu^{\epsilon - 2/3}$, one has

$$u = \sqrt{1 - z^2} > \sqrt{1 - z} > \nu^{\frac{\epsilon}{2} - \frac{1}{3}} > \nu^{\frac{\epsilon}{3} - \frac{1}{3}},$$

from which

$$f(z) < e^{\frac{1}{2}} \left[1 - \frac{2}{3} \nu^{\epsilon - 1} \right]^{\frac{\nu}{2} - 1/4} < e^{\frac{1}{2}} \left[\left(1 - \frac{2}{3} \nu^{\epsilon - 1} \right)^{\frac{3}{2} \nu^{1-\epsilon}} \right]^{\frac{\frac{\nu}{2} - 1/4}{\frac{3}{2} \nu^{1-\epsilon}}}.$$

Since

$$(1 - x)^{\frac{1}{x}} < e^{-1}, \quad \forall x \in (0, 1), \quad \text{and} \quad 0 < \frac{2}{3} \nu^{\epsilon - 1} < \frac{2}{3} < 1,$$

one finally gets

$$f(z) < \exp\left(\frac{1}{2} - \frac{\frac{\nu}{2} - 1/4}{\frac{3}{2} \nu^{1-\epsilon}} \right) < \exp\left(\frac{1}{2} + \frac{1}{6} \nu^{\epsilon - 1} - \frac{1}{3} \nu^{\epsilon} \right) < \exp\left(\frac{2}{3} - \frac{1}{3} \nu^{\epsilon} \right),$$

that completes the proof. $\qquad\qquad\qquad\qquad\qquad\qquad\qquad\qquad\qquad\qquad\qquad\qquad$ $\square$

As a consequence, taking $\nu = n + 1/2$ and $\epsilon = 1/3$, one has

Lemma B2.3. *For $n = 1, 2, \ldots$ and any $z \in (0, n + 1/2 - (n + 1/2)^{2/3})$,*

$$j_n(z) < \sqrt{\frac{\pi}{2n+1}} \, \exp\left(\frac{2}{3} - \frac{1}{3} \left(n + \frac{1}{2} \right)^{1/3} \right). \tag{B.36}$$

The lemmas for Bessel functions and their zeros from Appendix B1 allow one to get similar estimates for spherical Bessel functions $j_n(z)$, their positive zeros $\gamma_{n,k}$ and the positive zeros $\gamma'_{n,k}$ of $j'_n(z)$. They are summarized in the following

Lemma B2.4. *For n large enough,*

$$j_n(n + 1/2) > \tilde{C}_1 (n + 1/2)^{-5/6} \qquad (\tilde{C}_1 = \sqrt{\pi/2} C_1), \tag{B.37}$$

$$\gamma_{n,k} < (n + 1/2) + \tilde{c}_k (n + 1/2)^{1/3}, \tag{B.38}$$

$$\gamma'_{n,1} > n + 1/2 + \tilde{C}_2 (n + 1/2)^{1/3} \qquad (\tilde{C}_2 = 0.80), \tag{B.39}$$

$$\gamma'_{n,k} < \alpha_{nk} < \gamma_{n,k}. \tag{B.40}$$

Proof. From Lemma B1.3, we have

$$j_{\nu - 1/2}(\nu) = \sqrt{\frac{\pi}{2\nu}} J_\nu(\nu) > \sqrt{\frac{\pi}{2\nu}} C_1 \nu^{-1/3} = \tilde{C}_1 \nu^{-5/6},$$

from which (B.37) follows by taking $\nu = n + 1/2$.

The zeros $\gamma_{n,k}$ of the spherical Bessel function $j_n(z)$ are also the zeros of the Bessel function $J_{n+1/2}(z)$ so that (B.38) follows directly from Eq. (B.8) for $\nu = n + 1/2$ large enough.

The inequality (B.39) follows from the asymptotic expansion of $\gamma'_{n,1}$ for large n [1] (p. 441)

$$\gamma'_{n,1} = n + 1/2 + 0.8086165(n + 1/2)^{1/3} - 0.236680(n + 1/2)^{-1/3}$$
$$- 0.20736(n + 1/2)^{-1} + 0.0233(n + 1/2)^{-5/6} + \dots \qquad (n \gg 1).$$

Taking $\tilde{C}_2 = 0.80$, one gets the inequality (B.39).

Finally, the inequalities (B.40) follow from the general minimax principle as for the disk. $\qquad\square$

We also prove that the first maximum of the spherical Bessel function at $\gamma'_{n,1}$ is the largest (although this is a classical result, we did not find an explicit reference).

Lemma B2.5. *For an integer $n \geq 0$, one has*

$$\max_{x \in (0,\infty)} j_n(x) = j_n(\gamma'_{n,1}). \qquad (B.41)$$

Proof. The spherical Bessel function $j_n(x)$ satifies

$$x^2 j_n'' + 2x j_n' + [x^2 - (n+1)n]j_n = 0.$$

Denoting $\kappa = n(n+1)$, one can rewrite this equation as

$$j_n''(x) = -\frac{2x j_n'(x) + (x^2 - \kappa) j_n(x)}{x^2},$$

from which

$$
\begin{aligned}
\frac{d}{dx}\left[\frac{x^2}{x^2 - \kappa} \left(j_n'(x)\right)^2 \right] &= \frac{d}{dx}\left[\left(j_n'(x)\right)^2 + \frac{\kappa}{x^2 - \kappa} \left(j_n'(x)\right)^2 \right] \\
&= 2j_n'(x)j_n''(x) + \kappa \left[\frac{2(x^2 - \kappa)j_n'(x)j_n''(x) - 2x \left(j_n'(x)\right)^2}{(x^2 - \kappa)^2} \right] \\
&= \frac{2x^2}{x^2 - \kappa} j_n'(x)j_n''(x) - \frac{2x\kappa}{(x^2 - \kappa)^2} \left(j_n'(x)\right)^2 \\
&= -\frac{2j_n'(x)}{x^2 - \kappa}\left[2x j_n'(x) + \left(x^2 - \kappa\right) j_n(x) \right] - \frac{2x\kappa}{(x^2 - \kappa)^2} \left(j_n'(x)\right)^2 \\
&= -\frac{2x}{(x^2 - \kappa)^2}\left(j_n'(x)\right)^2 \left[2(x^2 - \kappa) + \kappa \right] - 2j_n(x)j_n'(x) \\
&= -\frac{2x}{(x^2 - \kappa)^2}\left(j_n'(x)\right)^2 \left[2x^2 - \kappa \right] - \frac{d}{dx}\left[j_n^2(x) \right].
\end{aligned}
$$

Now, if we put

$$\Lambda_n(x) = j_n^2(x) + \left[\frac{x^2}{x^2 - \kappa} \left(j_n'(x)\right)^2 \right],$$

then

$$\frac{d}{dx}\Lambda_n(x) = -\frac{2x}{(x^2 - \kappa)^2} \left(j_n'(x)\right)^2 \left[2x^2 - \kappa \right] < 0$$

for all $x > \sqrt{\frac{n(n+1)}{2}}$, i.e. $\Lambda_n(x)$ monotonously decreases. Given that $\Lambda_n(\gamma'_{n,k}) = j_n^2(\gamma_{n,k})$ and

$$\sqrt{\frac{n(n+1)}{2}} < \gamma'_{n,1} < \gamma'_{n,2} < \cdots,$$

we get the conclusion. □

a. Now, we can prove Theorem 3.2.4.

As earlier, the proof formalizes the idea that the eigenfunction u_{nk} is small in the large subdomain $B_{nk} = \{\mathbf{r} \in B \ : \ |\mathbf{r}| < Rs_n/\alpha_{nk}\}$ (with $s_n = (n+1/2) - (n+1/2)^{2/3}$) and large in the small subdomain $A_{nk} = \{\mathbf{r} \in B \ : \ R(n+1/2)/\alpha_{nk} < |\mathbf{r}| < R\gamma'_{n,1}/\alpha_{nk}\}$. Since $A_{nk} \subset B$, we have

$$\frac{\|u_{nk}\|_{L^p(B_{nk})}^p}{\|u_{nk}\|_{L^p(B)}^p} < \frac{\|u_{nk}\|_{L^p(B_{nk})}^p}{\|u_{nk}\|_{L^p(A_{nk})}^p} = \frac{\int\limits_0^{Rs_n/\alpha_{nk}} dr \ r^2 \ [j_n(r\alpha_{nk}/R)]^p}{\int\limits_{R(n+1/2)/\alpha_{nk}}^{R\gamma'_{n,1}/\alpha_{nk}} dr \ r^2 \ [j_n(r\alpha_{nk}/R)]^p} = \frac{\int\limits_0^{s_n} dz z^2 \ [j_n(z)]^p}{\int\limits_{n+1/2}^{\gamma'_{n,1}} dz z^2 \ [j_n(z)]^p}.$$

The numerator can be bounded by the inequality (B.36):

$$\int\limits_0^{s_n} dz z^2 \ [j_n(z)]^p < \left(\frac{\pi}{2n+1}\right)^{p/2} \exp\left(\frac{2p}{3} - \frac{p}{3}\left(n+\frac{1}{2}\right)^{1/3}\right) \frac{s_n^3}{3}$$

$$< \frac{(\pi/2)^{p/2}}{3} \exp\left(\frac{2p}{3} - \frac{p}{3}\left(n+\frac{1}{2}\right)^{1/3}\right) (n+1/2)^{3-p/2}$$

$$(n = 1, 2, 3, \ldots).$$

In order to bound the denominator, we use the inequalities (B.37, B.39) and the fact that $j_n(z)$ increases on the interval $[n+1/2, \gamma'_{n,1}]$ (up to the first maximum at $\gamma'_{n,1}$):

$$\int\limits_{n+1/2}^{\gamma'_{n,1}} dz z^2 \ [j_n(z)]^p > [j_n(n+1/2)]^p \frac{(\gamma'_{n,1})^3 - (n+1/2)^3}{3}$$

$$> [\tilde{C}_1(n+1/2)^{-5/6}]^p \frac{(n+1/2 + \tilde{C}_2(n+1/2)^{1/3})^3 - (n+1/2)^3}{3}$$

$$> \tilde{C}_1^p \tilde{C}_2 (n+1/2)^{7/3-5p/6}$$

for n large enough, from which

$$\frac{\|u_{nk}\|_{L^p(B_{nk})}}{\|u_{nk}\|_{L^p(A_{nk})}} < \frac{\sqrt{\pi/2}}{\tilde{C}_1(3\tilde{C}_2)^{1/p}} \exp\left(\frac{2}{3} - \frac{1}{3}\left(n+\frac{1}{2}\right)^{1/3}\right) (n+1/2)^{1/3+2/(3p)} \qquad (n \gg 1)$$

that implies Eq. (3.11). Finally, from Lemma B2.4, we have for n large enough

$$1 > \frac{\mu_3(B_{nk})}{\mu_3(B)} = \left(\frac{s_n}{\alpha_{nk}}\right)^3 > \frac{s_n^3}{\gamma_{n,k}^3} > \frac{(n+1/2 - (n+1/2)^{2/3})^3}{(n+1/2 + \tilde{c}_k(n+1/2)^{1/3})^3}$$

so that the ratio of volumes tends to 1 as n goes to infinity.

b. The proof of Theorem 3.2.7 for a ball is similar to that of Theorem 3.2.5.

Using the explicit representation (2.51) of eigenfunctions, it is easy to see that

$$\frac{\|u_{nk}\|_{L^\infty(B(R_0))}}{\|u_{nk}\|_{L^\infty(B)}} = \frac{\max\limits_{r\in[R_0,1]} |j_n(\alpha_{nk}r)|}{\max\limits_{r\in[0,1]} |j_n(\alpha_{nk}r)|} = \frac{\max\limits_{r\in[R_0,1]} |j_n(\alpha_{nk}r)|}{|j_n(\gamma'_{n,1})|}, \tag{B.42}$$

where we used the fact that the first maximum (at $\gamma'_{n,1}$) is the largest (Lemma B2.5). Since $\lim\limits_{k\to\infty} \alpha_{nk} = \infty$, the spherical Bessel function $j_n(\alpha_{nk}r)$ with $k \gg 1$ can be approximated in the interval $[R_0, 1]$ as [1]

$$j_n(\alpha_{nk}r) = \sqrt{\frac{\pi}{2\alpha_{nk}r}} \, J_{n+1/2}(\alpha_{nk}r) \approx \frac{1}{\alpha_{nk}r} \cos\left(\alpha_{nk}r - \frac{(n+1)\pi}{2}\right). \tag{B.43}$$

It also means that there exists a positive integer K_0 and a constant $A_0 > 0$ such that

$$|j_n(\alpha_{nk}r)| < \frac{A_0}{\alpha_{nk}R_0}, \quad \forall \, r \in [R_0, 1], \; k > K_0.$$

Given that the denominator in Eq. (B.42) is fixed, while the numerator decays as α_{nk}^{-1}, one gets Eq. (3.22).

Now we prove Eq. (3.24). One has

$$\frac{\|u_{nk}\|_{L^2(B(R_0))}^2}{\|u_{nk}\|_{L^2(B)}^2} = \frac{\int\limits_{R_0}^1 dr \, r^2 \, [j_n(\alpha_{nk}r)]^2}{\int\limits_0^1 dr \, r^2 \, [j_n(\alpha_{nk}r)]^2}.$$

Using Eq. (B.15), one gets

$$\int\limits_a^b dr \, r^2 \, [j_n(\alpha_{nk}r)]^2 = \frac{\pi}{2\alpha_{nk}} \left\{ r^2 [J'_{n+1/2}(\alpha_{nk}r)]^2 + \left(r^2 - \frac{(n+1/2)^2}{\alpha_{nk}^2}\right) [J_{n+1/2}(\alpha_{nk}r)]^2 \right\}_a^b,$$

from which

$$\frac{\|u_{nk}\|_{L^2(D(R_0))}^2}{\|u_{nk}\|_{L^2(D)}^2} = 1 - R_0^2 \left[\frac{[J'_{n+1/2}(\alpha_{nk}R_0)]^2 + \left(1 - \frac{(n+1/2)^2}{\alpha_{nk}^2 R_0^2}\right) [J_{n+1/2}(\alpha_{nk}R_0)]^2}{[J'_{n+1/2}(\alpha_{nk})]^2 + \left(1 - \frac{(n+1/2)^2}{\alpha_{nk}^2}\right) [J_{n+1/2}(\alpha_{nk})]^2}\right].$$

In order to compute the limit of the expression in large brackets, we write the leading term approximation

of the derivative of the Bessel function for $k \gg 1$ from Eq. (B.13):

$$J'_{n+1/2}(\alpha_{nk}R_0) \approx -\sqrt{\frac{2}{\pi\alpha_{nk}R_0}} \sin\left(\alpha_{nk}R_0 - \frac{(n+1)\pi}{2}\right).$$

In the limit $k \to \infty$, the term $(n+1/2)^2/\alpha_{nk}^2$ can be neglected as compared to 1, so that for $k \gg 1$

$$\frac{[J'_{n+1/2}(\alpha_{nk}R_0)]^2 + \left(1 - \frac{(n+1/2)^2}{\alpha_{nk}^2 R_0^2}\right)[J_{n+1/2}(\alpha_{nk}R_0)]^2}{[J'_{n+1/2}(\alpha_{nk})]^2 + \left(1 - \frac{(n+1/2)^2}{\alpha_{nk}^2}\right)[J_{n+1/2}(\alpha_{nk})]^2}$$

$$\approx \frac{\frac{2}{\pi\alpha_{nk}R_0}\sin^2\left(\alpha_{nk}R_0 - \frac{(n+1)\pi}{2}\right) + \frac{2}{\pi\alpha_{nk}R_0}\cos^2\left(\alpha_{nk}R_0 - \frac{(n+1)\pi}{2}\right)}{\frac{2}{\pi\alpha_{nk}}\sin^2\left(\alpha_{nk} - \frac{(n+1/2)\pi}{2}\right) + \frac{2}{\pi\alpha_{nk}}\cos^2\left(\alpha_{nk} - \frac{(n+1/2)\pi}{2}\right)} = \frac{1}{R_0}$$

that completes the proof for Eq. (3.24).

Finally, we prove Eq. (3.23). For $p > 3$, one has

$$\frac{\|u_{nk}\|^p_{L^p(D(R_0))}}{\|u_{nk}\|^p_{L^p(D)}} = \frac{\int\limits_{R_0}^{1} dr\; r^2\; |j_n(\alpha_{nk}r)|^p}{\int\limits_{0}^{1} dr\; r^2\; |j_n(\alpha_{nk}r)|^p} = \frac{\int\limits_{\alpha_{nk}R_0}^{\alpha_{nk}} dr\; r^2\; |j_n(r)|^p}{\int\limits_{0}^{\alpha_{nk}} dr\; r^2\; |j_n(r)|^p}$$

Using the approximation (B.43), for each positive integer n, there exists a positive integer K_{1n} such that

$$|j_n(z)| < \frac{2}{z}, \quad \forall z \in [\alpha_{nk}R_0, \alpha_{nk}], \; k > K_{1n}. \tag{B.44}$$

For $k \gg 1$, using the inequality (B.44), one gets

$$\int\limits_{\alpha_{nk}R_0}^{\alpha_{nk}} dr\; r^2\; |j_n(r)|^p \;\le\; 2^p \int\limits_{\alpha_{nk}R_0}^{\alpha_{nk}} dz\; z^{2-p} \tag{B.45}$$

$$\le \left(\frac{2^p}{p-3}\right)\left(\left(\frac{1}{\alpha_{nk}R_0}\right)^{p-3} - \left(\frac{1}{\alpha_{nk}}\right)^{p-3}\right). \tag{B.46}$$

Bringing the above results together, when $k \gg 1$, one has

$$\frac{\|u_{nk}\|^p_{L^p(B(R_0))}}{\|u_{nk}\|^p_{L^p(B)}} < \frac{\left(\frac{2^p}{p-3}\right)\left(\left(\frac{1}{\alpha_{nk}R_0}\right)^{p-3} - \left(\frac{1}{\alpha_{nk}}\right)^{p-3}\right)}{\int\limits_{0}^{1} dr\; r\; |J_n(r)|^p},$$

where the right-hand side tends to 0 as $k \to \infty$, that completes the proof.

B3   No localization in rectangle-like domains

Theorem 3.4.1 relies on the following simple estimate.

Lemma B3.1. *For $0 \le a < b$ and any positive integer m, one has*

$$\int_a^b |\sin(mx)|dx \ge \int_a^b \sin^2(mx)dx \ge \epsilon(a,b) > 0,$$

$$\int_a^b |\cos(mx)|dx \ge \int_a^b \cos^2(mx)dx \ge \epsilon(a,b) > 0,$$

(B.47)

where

$$\epsilon(a,b) = \min\left\{\frac{b-a}{4}, \frac{b-a}{2} - \frac{1}{2}\left|\frac{\sin(n(b-a))}{n}\right| : n = 1, 2, \ldots, \left[\frac{2}{b-a}\right]\right\} > 0,$$

(B.48)

Proof. One has

$$\int_a^b \sin^2(mx)dx \;=\; \frac{b-a}{2} - \frac{\sin\left(m(b-a)\right)\cos\left(m(b+a)\right)}{2m} > \epsilon(a,b),$$

$$\int_a^b \cos^2(mx)dx \;=\; \frac{b-a}{2} + \frac{\sin\left(m(b-a)\right)\cos\left(m(b+a)\right)}{2m} > \epsilon(a,b),$$

that implies the conclusion.   □

It is important to stress that the lower bound $\epsilon(a,b)$ does not depend on m.

The proof of Theorem 3.4.1 is a simple consequence.

Proof. The condition (3.31) ensures that all the eigenvalues are simple so that each eigenfunction is

$$u_{n_1,\ldots,n_d}(x_1, \ldots, x_d) = \begin{cases} \sin(\pi n_1 x_1/\ell_1)\ldots\sin(\pi n_d x_d/\ell_d) & \text{(Dirichlet)}, \\ \cos(\pi n_1 x_1/\ell_1)\ldots\cos(\pi n_d x_d/\ell_d) & \text{(Neumann)}. \end{cases}$$

For any open subset V, there exists a ball included in V and thus there exists a rectangle-like domain $\Omega_V = [a_1, b_1] \times \ldots \times [a_d, b_d] \subset V$, with $0 \le a_i < b_i \le \ell_i$ for all $i = 1, \ldots, d$. The L^1-norm of u in V can be estimated as

$$\|u_{n_1,\ldots,n_d}\|_{L^1(V)} \ge \|u_{n_1,\ldots,n_d}\|_{L^1(\Omega_V)} = \prod_{i=1}^d \int_{a_i}^{b_i} dx_i \begin{cases} |\sin(\pi n_i x_i/\ell_i)| \\ |\cos(\pi n_i x_i/\ell_i)| \end{cases}$$

$$= \frac{\ell_1\ldots\ell_d}{\pi^d} \prod_{i=1}^d \int_{\pi a_i/\ell_i}^{\pi b_i/\ell_i} dx_i \begin{cases} |\sin(n_i x_i)| \\ |\cos(n_i x_i)| \end{cases} \ge \frac{\ell_1\ldots\ell_d}{\pi^d} \prod_{i=1}^d \epsilon(\pi a_i/\ell_i, \pi b_i/\ell_i),$$

where the last inequality results from (B.47). To complete the proof, one uses the Jensen's inequality for L^p-norms and $\mu_d(V) \geq \mu_d(\Omega_V) = (b_1 - a_1)...(b_d - a_d)$

$$\frac{\|u_{n_1,...,n_d}\|_{L^p(V)}}{\|u_{n_1,...,n_d}\|_{L^p(\Omega)}} > \frac{\|u_{n_1,...,n_d}\|_{L^1(V)}(\mu_d(V))^{\frac{1}{p}-1}}{\|u_{n_1,...,n_d}\|_{L_\infty(\Omega)}(\mu_d(\Omega))^{\frac{1}{p}}} \geq \frac{1}{\pi^d} \prod_{i=1}^{d} \left(\frac{b_i - a_i}{\ell_i}\right)^{\frac{1}{p}-1} \epsilon\left(\pi\frac{a_i}{\ell_i}, \pi\frac{b_i}{\ell_i}\right) > 0.$$

Since the right-hand side is strictly positive and independent of $n_1, ... , n_d$, the infimum of the left-hand side over all eigenfunctions is strictly positive. $\qquad\square$

B4 Asymptotic behavior of Mathieu functions for large q

The large-q asymptotic expansions of $\mathrm{ce}_n(z,q)$ and $\mathrm{se}_{n+1}(z,q)$ for $z \in [0, \frac{\pi}{2})$ and $n = 0, 1, 2, ...$ are [83, 155]

$$\mathrm{ce}_n(z,q) = C_n(q)\left(e^{2\sqrt{q}\sin z}h_n^+(z)\sum_{k=0}^{\infty}\frac{f_k^+(z)}{q^{k/2}} + e^{-2\sqrt{q}\sin z}h_n^-(z)\sum_{k=0}^{\infty}\frac{f_k^-(z)}{q^{k/2}}\right), \qquad (B.49)$$

$$\mathrm{se}_{n+1}(z,q) = S_{n+1}(q)\left(e^{2\sqrt{q}\sin z}h_n^+(z)\sum_{k=0}^{\infty}\frac{f_k^+(z)}{q^{k/2}} - e^{-2\sqrt{q}\sin z}h_n^-(z)\sum_{k=0}^{\infty}\frac{f_k^-(z)}{q^{k/2}}\right), \qquad (B.50)$$

where

$$h_n^+(z) = 2^{n+\frac{1}{2}}\frac{\left[\cos\left(\frac{1}{2}z + \frac{\pi}{4}\right)\right]^{2n+1}}{(\cos z)^{n+1}} = \sqrt{\frac{(1-\sin z)^n}{(1+\sin z)^{n+1}}}, \qquad (B.51)$$

$$h_n^-(z) = 2^{n+\frac{1}{2}}\frac{\left[\sin\left(\frac{1}{2}z + \frac{\pi}{4}\right)\right]^{2n+1}}{(\cos z)^{n+1}} = \sqrt{\frac{(1+\sin z)^n}{(1-\sin z)^{n+1}}}, \qquad (B.52)$$

and the coefficients $C_n(q)$ and $S_{n+1}(q)$ are given explicitly in [155]. The coefficients $f_k^\pm(z)$ can be computed through the recursive formulas given in [83], e.g.

$$f_0^\pm(z) = 1, \qquad f_1^\pm(z) = \frac{2n + 1 \mp (n^2 + n + 1)\sin z}{8\cos(z)^2}.$$

When q is large enough, one can truncate the asymptotic expansions (B.49, B.50) by keeping only two terms ($k = 0, 1$) and get accurate approximations for ce_n and se_{n+1}, as illustrated on Fig. B.3. It is convenient to define the functions

$$G_n^\pm(z,q) = h_n^+(z) \pm e^{-4\sqrt{q}\sin(z)}h_n^-(z) + h_n^+(z)\sum_{k=1}^{\infty}\frac{f_k^+(z)}{q^{k/2}} \pm e^{-4\sqrt{q}\sin(z)}h_n^-(z)\sum_{k=1}^{\infty}\frac{f_k^-(z)}{q^{k/2}},$$

in order to write

$$\mathrm{ce}_n(z,q) = C_n(q)e^{2\sqrt{q}\sin(z)}G_n^+(z,q), \qquad \mathrm{se}_{n+1}(z,q) = S_{n+1}(q)e^{2\sqrt{q}\sin(z)}G_n^-(z,q).$$

In what follows, we will estimate the functions $G_n^\pm(z,q)$ by their leading terms, given that the remaining
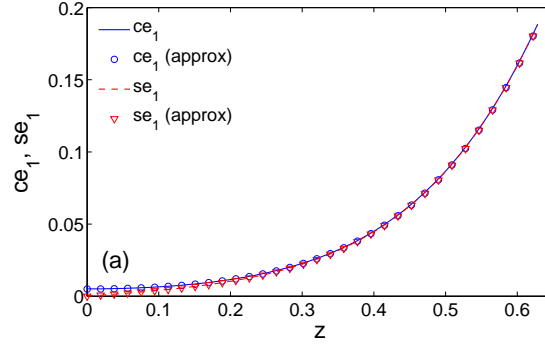
Figure B.3:   The functions $ce_1(z, q)$ and $se_1(z, q)$ (solid and dashed lines), computed by our algorithm with $K_{max} = 200$, and their approximations (circles and triangles) by the asymptotic expansions (B.49, B.50) truncated to two terms ($k = 0, 1$), with $q = 20$.

part is getting small for large q:

Lemma B4.1. *For $\gamma \in (0, \frac{\pi}{2})$, there exists $N_{\gamma,n} > 0$ such that for $q > N_{\gamma,n}$ and $z \in (0, \gamma)$*

$$\left| \sum_{k=1}^{\infty} \frac{f_k^{\pm}(z)}{q^{k/2}} \right| < \frac{1}{2}. \tag{B.53}$$

Now, we establish the upper and lower bounds for the functions $G_n^{\pm}$.

Lemma B4.2. *Let $\alpha \in (0, \frac{\pi}{2})$, $\gamma \in (\alpha, \frac{\pi}{2})$. Then, there exists $N_{\gamma,n} > 0$ such that for any $\beta \in (\alpha, \gamma)$ and $q > N_{\gamma,n}$:*

$$|G_n^{\pm}(z_1, q)| \quad < \quad \frac{3}{2} \left(1 + h_n^{-}(\alpha) e^{-4\sqrt{q}\sin(z_1)} \right) \qquad \forall\, z_1 \in (0, \alpha), \tag{B.54}$$

$$|G_n^{\pm}(z_2, q)| \quad > \quad \frac{1}{2} h_n^{+}(\gamma) \qquad \forall\, z_2 \in (\beta, \gamma), \tag{B.55}$$

Proof. From Lemma B4.1, there exists $N_{\gamma,n} > 0$ such that for $q > N_\gamma$ and $z_1 \in (0, \alpha)$, one has

$$\left| G_n^{\pm}(z_1, q) \right| < \frac{3}{2} \left(h_n^{+}(z_1) + h_n^{-}(z_1) e^{-4\sqrt{q}\sin(z_1)} \right) < \frac{3}{2} \left(1 + h_n^{-}(\alpha) e^{-4\sqrt{q}\sin(z_1)} \right).$$

For $q > N_{\gamma,n}$ and $z_2 \in (\beta, \gamma)$, one has

$$\left| G_n^{+}(z_2, q) \right| > \frac{1}{2} \left(h_n^{+}(z_2) + h_n^{-}(z_2) e^{-4\sqrt{q}\sin(z_2)} \right) > \frac{1}{2} h_n^{+}(\gamma) > 0$$

and

$$\left| G_n^{-}(z_2, q) - \left(h_n^{+}(z_2) - h_n^{-}(z_2) e^{-4\sqrt{q}\sin(z_2)} \right) \right| < \frac{1}{2} \left(h_n^{+}(z_2) + h_n^{-}(z_2) e^{-4\sqrt{q}\sin(z_2)} \right).$$

The last inequality implies

$$|G_n^-(z_2, q)| > \min\left\{\left(h_n^+(z_2) - h_n^-(z_2)e^{-4\sqrt{q}\sin(z_2)}\right), \frac{1}{2}\left(h_n^+(z_2) - 3h_n^-(z_2)e^{-4\sqrt{q}\sin(z_2)}\right)\right\}.$$

Since $h_n^-(z_2) > 0$ and $h_n^+(z_2)$ is a decreasing function, one gets

$$|G_n^-(z_2, q)| > \frac{1}{2}h_n^+(\gamma),$$

that completes the proof. □

B5   Proofs for elliptical domains

Now we can prove Theorem 3.3.1.

We first consider the case $i = 1$. Using the symmetric properties of Mathieu functions [234], one has

$$\frac{\|u_{nk1}\|_{L^p(\Omega\setminus\Omega_\alpha)}^p}{\|u_{nk1}\|_{L^p(\Omega_\alpha)}^p} = \frac{\int_0^\alpha |\mathrm{ce}_n(z_1, q_{nk1})|^p dz_1}{\int_\alpha^{\pi/2} |\mathrm{ce}_n(z_2, q_{nk1})|^p dz_2}.$$

Choosing $\beta = \frac{\pi}{4} + \frac{\alpha}{2}$ and $\gamma = \frac{3\pi}{8} + \frac{\alpha}{4}$, one gets

$$\frac{\int_0^\alpha |\mathrm{ce}_n(z_1, q_{nk1})|^p dz_1}{\int_\alpha^{\pi/2} |\mathrm{ce}_n(z_2, q_{nk1})|^p dz_2} < \frac{\int_0^\alpha |\mathrm{ce}_n(z_1, q_{nk1})|^p dz_1}{\int_\beta^\gamma |\mathrm{ce}_n(z_2, q_{nk1})|^p dz_2}.$$

From Lemma B4.2, there exists $N_{\gamma,n} > 0$ such that for $q > N_{\gamma,n}$,

$$\begin{aligned}
\int_0^\alpha |\mathrm{ce}_n(z_1, q)|^p dz_1 &= (C_n(q))^p \int_0^\alpha e^{2p\sqrt{q}\sin z_1} |G_n^+(z_1, q)|^p dz_1 \\
&< (C_n(q))^p \left(\frac{3}{2}\right)^p \int_0^\alpha \left(\sum_{k=0}^p \binom{p}{k}[e^{2\sqrt{q}\sin z_1}]^{p-2k}(h_n^-(\alpha))^k\right) dz_1 \\
&\le \alpha(C_n(q))^p \left(\frac{3}{2}\right)^p \left(\sum_{k=0}^{[p/2]} \binom{p}{k}[e^{2\sqrt{q}\sin\alpha}]^{p-2k}(h_n^-(\alpha))^k + \sum_{k=[p/2]+1}^p \binom{p}{k}(h_n^-(\alpha))^k\right),
\end{aligned}$$

where the terms $e^{m\sqrt{q}\sin z_1}$ were bounded by $e^{m\sqrt{q}\sin\alpha}$ for $m > 0$, and by 1 for $m \le 0$ (here $[x]$ denotes

the integer part of x). In addition,

$$\int_{\beta}^{\gamma} |\text{ce}_n(z_2, q)|^p dz_2 \quad > \quad (C_n(q))^p \left(\frac{1}{2}\right)^p (h_n^+(\gamma))^p \int_{\beta}^{\gamma} e^{2p\sqrt{q}\sin z_2} dz_2$$

$$> \quad (C_n(q))^p \left(\frac{1}{2}\right)^p (h_n^+(\gamma))^p (\gamma - \beta) e^{2p\sqrt{q}\sin\beta},$$

from which

$$\frac{\|u_{nk1}\|_{L^p(\Omega\backslash\Omega_\alpha)}^p}{\|u_{nk1}\|_{L^p(\Omega_\alpha)}^p} < \frac{3^p\alpha}{(\gamma-\beta)(h_n^+(\gamma))^p} e^{-2p\sqrt{q_{nk1}}(\sin\beta-\sin\alpha)}\left(1 + \right.$$

$$\left.\left[\sum_{k=1}^{[p/2]} \binom{p}{k}(e^{2\sqrt{q}\sin\alpha})^{-2k}(h_n^-(\alpha))^k + e^{-2p\sqrt{q}\sin\alpha}\sum_{k=[p/2]+1}^{p} \binom{p}{k}(h_n^-(\alpha))^k\right]\right).$$

Taking q large enough, one can make the terms in large brackets smaller than any prescribed threshold ϵ. For $\epsilon = 1$, one can simplify the estimate as

$$\frac{\|u_{nk1}\|_{L^p(\Omega\backslash\Omega_\alpha)}^p}{\|u_{nk1}\|_{L^p(\Omega_\alpha)}^p} < 2\frac{3^p\alpha}{(\gamma-\beta)(h_n^+(\gamma))^p} \exp\left[-2p\sqrt{q_{nk1}}(\sin\beta - \sin\alpha)\right].$$

Substituting $\beta = \pi/4 + \alpha/2$ and $\gamma = 3\pi/8 + \alpha/4$, one gets Eq. (3.27) after trigonometric simplifications. For $i = 2$, one has

$$\frac{\|u_{nk2}\|_{L^p(\Omega\backslash\Omega_\alpha)}^p}{\|u_{nk2}\|_{L^p(\Omega_\alpha)}^p} = \frac{\int_0^\alpha |\text{se}_{n+1}(z_1, q_{nk2})|^p dz_1}{\int_\alpha^{\pi/2} |\text{se}_{n+1}(z_2, q_{nk2})|^p dz_2}$$

and similar analysis is applicable.

B6 Proofs for equilateral triangles

We denote the vertices of an equilateral triangle Ω as $O(0,0)$, $A\left(\sqrt{3}/2, 1/2\right)$, $B(1,0)$. Let Ω_1 be an equilateral triangle inside Ω (Figure B.4) as following

$$\Omega_1 = \left\{y_0 \le y \le x\sqrt{3} + x_0, y \le \sqrt{3}(x_1 - x)\right\}, \tag{B.56}$$

whose three vertices are $O_1(x_{O_1}, y_{O_1})$, $A_1(x_{A_1}, y_{A_1})$ and $B_1(x_{B_1}, y_{B_1})$. It is not difficult to see that

$$x_{O_1} = \frac{y_0 - x_0}{\sqrt{3}}, \quad x_{B_1} = \frac{\sqrt{3}x_1 - y_0}{\sqrt{3}} \tag{B.57}$$

$$x_{A_1} = \frac{\sqrt{3}x_1 - x_0}{2\sqrt{3}}, \quad y_{O_1} = y_{B_1} = y_0, \quad y_{A_1} = \frac{\sqrt{3}x_1 + x_0}{2}. \tag{B.58}$$

If $H(x_H, y_H)$ is the middle of the side O_1B_1, $x_H = \frac{\sqrt{3}x_1 - x_0}{2\sqrt{3}}$ and $y_H = y_0$. For any positive integer p, we
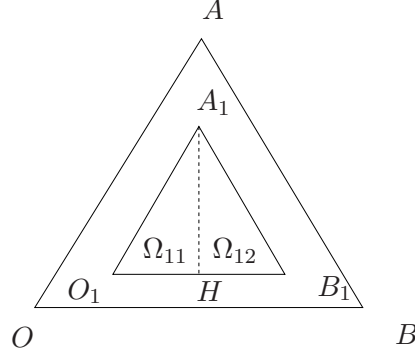
Figure B.4: An equilateral triangle Ω with three vertices: O, A and B.

consider

$$A_p = \int\limits_{\Omega_1} u_{0,p}^2(x,y)dxdy, \qquad B_p = \int\limits_{\Omega} u_{0,p}^2(x,y)dxdy. \tag{B.59}$$

We call Ω_{11} the triangle with vertices O_1, A_1, and H, and Ω_{12} the triangle with vertices O_1, B_1, and H. From Eq. (3.34), we have

$$\begin{aligned}
u_{0,p}^2(x,y) &= \frac{3}{2} - \frac{1}{2}\left[\cos\left(4\pi p\overline{d_1}\right) + \cos\left(4\pi p\overline{d_2}\right) + \cos\left(4\pi p\overline{d_3}\right)\right] + \cos\left(2\pi p\left(\overline{d_1} - \overline{d_2}\right)\right) \\
&\quad + \cos\left(2\pi p\left(\overline{d_1} - \overline{d_3}\right)\right) + \cos\left(2\pi p\left(\overline{d_2} - \overline{d_3}\right)\right) \\
&\quad - \left[\cos\left(2\pi p\overline{d_1}\right) + \cos\left(2\pi p\overline{d_2}\right) + \cos\left(2\pi p\overline{d_3}\right)\right]
\end{aligned}$$

where $\overline{d_1}$, $\overline{d_2}$ and $\overline{d_3}$ are defined in Eq. (3.34). We will compute the following integrals:

+ The first term:

$$
\begin{aligned}
I_{11}(p) &= \int_{\Omega_{11}} \cos\left(4\pi p \overline{d_1}\right) dy\, dx = \int_{x_{O_1}}^{x_H} \int_{y_0}^{x\sqrt{3}+x_0} \cos\left(4\pi p \frac{2y}{\sqrt{3}}\right) dy\, dx \\
&= \frac{\sqrt{3}}{(8\pi p)^2}\left[\cos\left[\frac{8\pi p}{\sqrt{3}}\left(x_{O_1}\sqrt{3}+x_0\right)\right] - \cos\left[\frac{8\pi p}{\sqrt{3}}\left(x_H\sqrt{3}+x_0\right)\right]\right] \\
&\quad - \frac{\sqrt{3}}{8\pi p}\left(x_H - x_{O_1}\right)\sin\left[\frac{8\pi p}{\sqrt{3}}y_0\right] \\
&= \frac{\sqrt{3}}{(8\pi p)^2}\left[\cos\left[\frac{8\pi p}{\sqrt{3}}y_0\right] - \cos\left[\frac{8\pi p}{\sqrt{3}}y_{A_1}\right]\right] \\
&\quad - \frac{\sqrt{3}}{8\pi p}\left(x_H - x_{O_1}\right)\sin\left[\frac{8\pi p}{\sqrt{3}}y_0\right] \\
I_{12}(p) &= \int_{\Omega_{12}} \cos\left(4\pi p \overline{d_1}\right) dy\, dx = \int_{x_H}^{x_{B_1}} \int_{y_0}^{\sqrt{3}(x_1-x)} \cos\left(4\pi p \frac{2y}{\sqrt{3}}\right) dy\, dx \\
&= -\frac{\sqrt{3}}{(8\pi p)^2}\left[\cos\left[8\pi p\left(x_1 - x_{B_1}\right)\right] - \cos\left[8\pi p\left(x_1 - x_H\right)\right]\right] \\
&\quad - \frac{\sqrt{3}}{8\pi p}\left(x_{B_1} - x_H\right)\sin\left[\frac{8\pi p}{\sqrt{3}}y_0\right] \\
&= -\frac{\sqrt{3}}{(8\pi p)^2}\left[\cos\left[\frac{8\pi p}{\sqrt{3}}y_0\right] - \cos\left[\frac{8\pi p}{\sqrt{3}}y_{A_1}\right]\right] \\
&\quad - \frac{\sqrt{3}}{8\pi p}\left(x_{B_1} - x_H\right)\sin\left[\frac{8\pi p}{\sqrt{3}}y_0\right]
\end{aligned}
$$

+ The second term:

$$
\begin{aligned}
I_{21}(p) &= \int_{\Omega_{11}} \cos\left(4\pi p \overline{d_2}\right) dy\, dx = \int_{x_{O_1}}^{x_H} \int_{y_0}^{x\sqrt{3}+x_0} \cos\left(4\pi p\left(x - \frac{y}{\sqrt{3}}\right)\right) dy\, dx \\
&= -\frac{\sqrt{3}}{(4\pi p)^2}\left[\cos\left[4\pi p\left(x_H - \frac{y_0}{\sqrt{3}}\right)\right] - \cos\left[4\pi p\left(x_{O_1} - \frac{y_0}{\sqrt{3}}\right)\right]\right] \\
&\quad + \frac{\sqrt{3}}{4\pi p}\left(x_H - x_{O_1}\right)\sin\left[\frac{4\pi p}{\sqrt{3}}x_0\right] \\
I_{22}(p) &= \int_{\Omega_{12}} \cos\left(4\pi p \overline{d_2}\right) dy\, dx = \int_{x_H}^{x_{B_1}} \int_{y_0}^{\sqrt{3}(x_1-x)} \cos\left(4\pi p\left(x - \frac{y}{\sqrt{3}}\right)\right) dy\, dx \\
&= -\frac{\sqrt{3}}{(4\pi p)^2}\left[\cos\left[4\pi p\left(x_{B_1} - \frac{y_0}{\sqrt{3}}\right)\right] - \cos\left[4\pi p\left(x_H - \frac{y_0}{\sqrt{3}}\right)\right]\right] \\
&\quad + \frac{\sqrt{3}}{2(4\pi p)^2}\left[\cos\left[4\pi p\left(2x_{B_1} - x_1\right)\right] - \cos\left[4\pi p\left(2x_H - x_1\right)\right]\right]
\end{aligned}
$$

+ The third term:

$$
\begin{aligned}
I_{31}(p) &= \int_{\Omega_{11}} \cos\left(4\pi p \overline{d_3}\right) dy dx = \int_{x_{O_1}}^{x_H} \int_{y_0}^{x\sqrt{3}+x_0} \cos\left(4\pi p \left(x + \frac{y}{\sqrt{3}}\right)\right) dy dx \\
&= \frac{\sqrt{3}}{(4\pi p)^2} \left[\cos\left[4\pi p \left(x_H + \frac{y_0}{\sqrt{3}}\right)\right] - \cos\left[4\pi p \left(x_{O_1} + \frac{y_0}{\sqrt{3}}\right)\right]\right] \\
&\quad - \frac{\sqrt{3}}{2(4\pi p)^2} \left[\cos\left[4\pi p \left(2x_H + \frac{x_0}{\sqrt{3}}\right)\right] - \cos\left[4\pi p \left(2x_{O_1} + \frac{x_0}{\sqrt{3}}\right)\right]\right]
\end{aligned}
$$

$$
\begin{aligned}
I_{32}(p) &= \int_{\Omega_{12}} \cos\left(4\pi p \overline{d_3}\right) dy dx = \int_{x_H}^{x_{B_1}} \int_{y_0}^{\sqrt{3}(x_1-x)} \cos\left(4\pi p \left(x + \frac{y}{\sqrt{3}}\right)\right) dy dx \\
&= \frac{\sqrt{3}}{(4\pi p)^2} \left[\cos\left[4\pi p \left(x_{B_1} + \frac{y_0}{\sqrt{3}}\right)\right] - \cos\left[4\pi p \left(x_H + \frac{y_0}{\sqrt{3}}\right)\right]\right] \\
&\quad + \frac{\sqrt{3}}{4\pi p} (x_{B_1} - x_H) \sin[4\pi p x_1]
\end{aligned}
$$

+ The fourth term:

$$
\begin{aligned}
I_{41}(p) &= \int_{\Omega_{11}} \cos\left(2\pi p \overline{d_1}\right) dy dx = \int_{x_{O_1}}^{x_H} \int_{y_0}^{x\sqrt{3}+x_0} \cos\left(2\pi p \frac{2y}{\sqrt{3}}\right) dy dx \\
&= \frac{\sqrt{3}}{(4\pi p)^2} \left[\cos\left[\frac{4\pi p}{\sqrt{3}} \left(x_{O_1}\sqrt{3} + x_0\right)\right] - \cos\left[\frac{4\pi p}{\sqrt{3}} \left(x_H\sqrt{3} + x_0\right)\right]\right] \\
&\quad - \frac{\sqrt{3}}{4\pi p} (x_H - x_{O_1}) \sin\left[\frac{4\pi p}{\sqrt{3}} y_0\right] \\
&= \frac{\sqrt{3}}{(4\pi p)^2} \left[\cos\left[\frac{4\pi p}{\sqrt{3}} y_0\right] - \cos\left[\frac{4\pi p}{\sqrt{3}} y_{A_1}\right]\right] \\
&\quad - \frac{\sqrt{3}}{4\pi p} (x_H - x_{O_1}) \sin\left[\frac{4\pi p}{\sqrt{3}} y_0\right]
\end{aligned}
$$

$$
\begin{aligned}
I_{42}(p) &= \int_{\Omega_{12}} \cos\left(2\pi p \overline{d_1}\right) dy dx = \int_{x_H}^{x_{B_1}} \int_{y_0}^{\sqrt{3}(x_1-x)} \cos\left(2\pi p \frac{2y}{\sqrt{3}}\right) dy dx \\
&= -\frac{\sqrt{3}}{(4\pi p)^2} \left[\cos\left[4\pi p (x_1 - x_{B_1})\right] - \cos\left[4\pi p (x_1 - x_H)\right]\right] \\
&\quad - \frac{\sqrt{3}}{4\pi p} (x_{B_1} - x_H) \sin\left[\frac{4\pi p}{\sqrt{3}} y_0\right] \\
&= -\frac{\sqrt{3}}{(4\pi p)^2} \left[\cos\left[\frac{4\pi p}{\sqrt{3}} y_0\right] - \cos\left[\frac{4\pi p}{\sqrt{3}} y_{A_1}\right]\right] \\
&\quad - \frac{\sqrt{3}}{4\pi p} (x_{B_1} - x_H) \sin\left[\frac{4\pi p}{\sqrt{3}} y_0\right]
\end{aligned}
$$

+ The fifth term:

$$
\begin{aligned}
I_{51}(p) &= \int_{\Omega_{11}} \cos\left(2\pi p\overline{d_2}\right) dy dx = \int_{x_{O_1}}^{x_H} \int_{y_0}^{x\sqrt{3}+x_0} \cos\left(2\pi p\left(x - \frac{y}{\sqrt{3}}\right)\right) dy dx \\
&= -\frac{\sqrt{3}}{(2\pi p)^2}\left[\cos\left[2\pi p\left(x_H - \frac{y_0}{\sqrt{3}}\right)\right] - \cos\left[2\pi p\left(x_{O_1} - \frac{y_0}{\sqrt{3}}\right)\right]\right] \\
&\quad + \frac{\sqrt{3}}{2\pi p}(x_H - x_{O_1})\sin\left[\frac{2\pi p}{\sqrt{3}}x_0\right]
\end{aligned}
$$

$$
\begin{aligned}
I_{52}(p) &= \int_{\Omega_{12}} \cos\left(2\pi p\overline{d_2}\right) dy dx = \int_{x_H}^{x_{B_1}} \int_{y_0}^{\sqrt{3}(x_1-x)} \cos\left(2\pi p\left(x - \frac{y}{\sqrt{3}}\right)\right) dy dx \\
&= -\frac{\sqrt{3}}{(2\pi p)^2}\left[\cos\left[2\pi p\left(x_{B_1} - \frac{y_0}{\sqrt{3}}\right)\right] - \cos\left[2\pi p\left(x_H - \frac{y_0}{\sqrt{3}}\right)\right]\right] \\
&\quad + \frac{\sqrt{3}}{2(2\pi p)^2}\left[\cos\left[2\pi p\left(2x_{B_1} - x_1\right)\right] - \cos\left[2\pi p\left(2x_H - x_1\right)\right]\right]
\end{aligned}
$$

+ The sixth term:

$$
\begin{aligned}
I_{61}(p) &= \int_{\Omega_{11}} \cos\left(2\pi p\overline{d_3}\right) dy dx = \int_{x_{O_1}}^{x_H} \int_{y_0}^{x\sqrt{3}+x_0} \cos\left(2\pi p\left(x + \frac{y}{\sqrt{3}}\right)\right) dy dx \\
&= \frac{\sqrt{3}}{(2\pi p)^2}\left[\cos\left[2\pi p\left(x_H + \frac{y_0}{\sqrt{3}}\right)\right] - \cos\left[2\pi p\left(x_{O_1} + \frac{y_0}{\sqrt{3}}\right)\right]\right] \\
&\quad - \frac{\sqrt{3}}{2(2\pi p)^2}\left[\cos\left[2\pi p\left(2x_H + \frac{x_0}{\sqrt{3}}\right)\right] - \cos\left[2\pi p\left(2x_{O_1} + \frac{x_0}{\sqrt{3}}\right)\right]\right]
\end{aligned}
$$

$$
\begin{aligned}
I_{62}(p) &= \int_{\Omega_{12}} \cos\left(2\pi p\overline{d_3}\right) dy dx = \int_{x_H}^{x_{B_1}} \int_{y_0}^{\sqrt{3}(x_1-x)} \cos\left(2\pi p\left(x + \frac{y}{\sqrt{3}}\right)\right) dy dx \\
&= \frac{\sqrt{3}}{(2\pi p)^2}\left[\cos\left[2\pi p\left(x_{B_1} + \frac{y_0}{\sqrt{3}}\right)\right] - \cos\left[2\pi p\left(x_H + \frac{y_0}{\sqrt{3}}\right)\right]\right] \\
&\quad + \frac{\sqrt{3}}{2\pi p}(x_{B_1} - x_H)\sin\left[2\pi p x_1\right]
\end{aligned}
$$

+ The seventh term:

$$
\begin{aligned}
I_{71}(p) &= \int_{\Omega_{11}} \cos\left(2\pi p\left(\overline{d_1} - \overline{d_2}\right)\right) dydx = \int_{x_{O_1}}^{x_H} \int_{y_0}^{x\sqrt{3}+x_0} \cos\left(2\pi p\left(x - \sqrt{3}y\right)\right) dydx \\
&= -\frac{\sqrt{3}}{6\left(2\pi p\right)^2}\left[\cos\left[2\pi p\left(2x_H + \sqrt{3}x_0\right)\right] - \cos\left[2\pi p\left(2x_{O_1} + \sqrt{3}x_0\right)\right]\right] \\
&\quad -\frac{\sqrt{3}}{3\left(2\pi p\right)^2}\left[\cos\left[2\pi p\left(x_H - \sqrt{3}y_0\right)\right] - \cos\left[2\pi p\left(x_{O_1} - \sqrt{3}y_0\right)\right]\right]
\end{aligned}
$$

$$
\begin{aligned}
I_{72}(p) &= \int_{\Omega_{12}} \cos\left(2\pi p\left(\overline{d_1} - \overline{d_2}\right)\right) dydx = \int_{x_H}^{x_{B_1}} \int_{y_0}^{\sqrt{3}(x_1-x)} \cos\left(2\pi p\left(x - \sqrt{3}y\right)\right) dydx \\
&= \frac{\sqrt{3}}{12\left(2\pi p\right)^2}\left[\cos\left[2\pi p\left(4x_{B_1} - 3x_1\right)\right] - \cos\left[2\pi p\left(4x_H - 3x_1\right)\right]\right] \\
&\quad -\frac{\sqrt{3}}{3\left(2\pi p\right)^2}\left[\cos\left[2\pi p\left(x_{B_1} - \sqrt{3}y_0\right)\right] - \cos\left[2\pi p\left(x_H - \sqrt{3}y_0\right)\right]\right]
\end{aligned}
$$

+ The eighth term:

$$
\begin{aligned}
I_{81}(p) &= \int_{\Omega_{11}} \cos\left(2\pi p\left(\overline{d_1} - \overline{d_3}\right)\right) dydx = \int_{x_{O_1}}^{x_H} \int_{y_0}^{x\sqrt{3}+x_0} \cos\left(2\pi p\left(x + \sqrt{3}y\right)\right) dydx \\
&= -\frac{\sqrt{3}}{12\left(2\pi p\right)^2}\left[\cos\left[2\pi p\left(4x_H + \sqrt{3}x_0\right)\right] - \cos\left[2\pi p\left(4x_{O_1} + \sqrt{3}x_0\right)\right]\right] \\
&\quad +\frac{\sqrt{3}}{3\left(2\pi p\right)^2}\left[\cos\left[2\pi p\left(x_H + \sqrt{3}y_0\right)\right] - \cos\left[2\pi p\left(x_{O_1} + \sqrt{3}y_0\right)\right]\right]
\end{aligned}
$$

$$
\begin{aligned}
I_{82}(p) &= \int_{\Omega_{12}} \cos\left(2\pi p\left(\overline{d_1} - \overline{d_3}\right)\right) dydx = \int_{x_H}^{x_{B_1}} \int_{y_0}^{\sqrt{3}(x_1-x)} \cos\left(2\pi p\left(x + \sqrt{3}y\right)\right) dydx \\
&= \frac{\sqrt{3}}{12\left(2\pi p\right)}\left[\cos\left[2\pi p\left(2x_{B_1} - 3x_1\right)\right] - \cos\left[2\pi p\left(2x_H - 3x_1\right)\right]\right] \\
&\quad +\frac{\sqrt{3}}{3\left(2\pi p\right)^2}\left[\cos\left[2\pi p\left(x_{B_1} + \sqrt{3}y_0\right)\right] - \cos\left[2\pi p\left(x_H + \sqrt{3}y_0\right)\right]\right]
\end{aligned}
$$

+ The last term:

$$
\begin{aligned}
I_{91}(p) &= \int_{\Omega_{11}} \cos\left(2\pi p\left(\overline{d_2} - \overline{d_3}\right)\right) dydx = \int_{x_{O_1}}^{x_H} \int_{y_0}^{x\sqrt{3}+x_0} \cos\left(4\pi px\right) dydx \\
&= \frac{\sqrt{3}}{(4\pi p)}\left[x_H \sin\left(4\pi px_H\right) - x_{O_1}\sin\left(4\pi px_{O_1}\right)\right] + \frac{\sqrt{3}}{(4\pi p)^2}\left[\cos\left(4\pi px_H\right)\right] \\
&\quad - \frac{\sqrt{3}}{(4\pi p)^2}\left[\cos\left(4\pi px_{O_1}\right)\right] + \frac{x_0 - y_0}{4\pi p}\left[\sin\left(4\pi px_H\right) - \sin\left(4\pi px_{O_1}\right)\right] \\
I_{92}(p) &= \int_{\Omega_{12}} \cos\left(2\pi p\left(\overline{d_2} - \overline{d_3}\right)\right) dydx = \int_{x_H}^{x_{B_1}} \int_{y_0}^{\sqrt{3}(x_1-x)} \cos\left(4\pi px\right) dydx \\
&= -\frac{1}{(4\pi p)}\left[x_{B_1} \sin\left(4\pi px_{B_1}\right) - x_H \sin\left(4\pi px_H\right)\right] - \frac{1}{(4\pi p)^2}\left[\cos\left(4\pi px_{B_1}\right)\right] \\
&\quad + \frac{1}{(4\pi p)^2}\left[\cos\left(4\pi px_H\right)\right] + \frac{\sqrt{3}x_1 - y_0}{4\pi p}\left[\sin\left(4\pi px_{B_1}\right) - \sin\left(4\pi px_H\right)\right]
\end{aligned}
$$

Finally, one can see that $A_p = \frac{3}{2}|\Omega_1| + \sum_{i=1}^{9}\sum_{j=1}^{2} I_{ij}(p) = \frac{3}{2}|\Omega_1| + O\left(\frac{1}{p}\right)$. Similarly, $B_p = \frac{3}{2}|\Omega_1| + O\left(\frac{1}{p}\right)$. From Theorem 2.1.12, $A_p > 0, B_p > 0, \forall p = 1, 2, \dots$. Moreover, $\lim_{p\to\infty} A_p = \frac{3}{2}|\Omega_1|$ and $\lim_{p\to\infty} B_p = \frac{3}{2}|\Omega_1|$. Then, there exists a universal constant $C_{\Omega_1} > 0$, independent of p, such that $B_p \le C_{\Omega_1} A_p$, for any positive integer p. It is equivalent to

$$
\int_{\Omega} u_{3p,0}^2(x,y) dxdy \le C_{\Omega_1} \int_{\Omega_1} u_{3p,0}^2 dxdy, \quad \forall p = 1, 2, \dots \tag{B.60}
$$

As a consequence, one obtains the conclusion for a general open subset $V \subset \Omega$.

Appendix C

Algorithms for computing Mathieu functions

C1 Calculation of Mathieu functions

Several algorithms have been proposed for a numerical computation of Mathieu functions [5, 103, 143, 197, 220]. The main difficulty is the computation of Mathieu characteristic numbers (MCNs). Alhargan introduced a complete method for calculating these MCNs of integer orders by using some new recurrence relations for MCNs [5]. His algorithm is a good compromise between complexity, acurracy, speed and ease of use. However, we use a simpler approach by Zhang *et al.* [234].

a. Angular Mathieu functions

The common formulas for angular Mathieu functions $\text{ce}_n(z, q)$ and $\text{se}_n(z, q)$ are

$$
\begin{aligned}
\text{ce}_{2r}(z, q) &= \sum_{k=0}^{\infty} A_{2k}^{2r} \cos 2kz, \\
\text{ce}_{2r+1}(z, q) &= \sum_{k=0}^{\infty} A_{2k+1}^{2r+1} \cos (2k+1)z, \\
\text{se}_{2r+1}(z, q) &= \sum_{k=0}^{\infty} B_{2k+1}^{2r+1} \sin (2k+1)z, \\
\text{se}_{2r+2}(z, q) &= \sum_{k=0}^{\infty} B_{2k+2}^{2r+2} \sin (2k+2)z,
\end{aligned}
\tag{C.1}
$$

in which $\text{ce}_{2r}(z, q)$ and $\text{ce}_{2r+1}(z, q)$ are even functions of z with periods π and 2π, respectively, while $\text{se}_{2r+1}(z, q)$ and $\text{se}_{2r+2}(z, q)$ are odd functions of z with periods π and 2π, respectively. Specifically, when $q = 0$, the angular Mathieu functions become $\text{ce}_n(z, 0) = \cos nz$ and $\text{se}_n(z, 0) = \sin nz$ (since $\sin nz$ becomes 0 for $n = 0$, $\text{se}_0(z, q)$ was excluded from the analysis). The above coefficients satisfy the following recurrent relations:

- for the series $\{A_{2k}^{2r}\}$:

$$cA_0^{2r} - qA_2^{2r} = 0$$
$$(c-4)A_2^{2r} - q\left(2A_0^{2r} + A_4^{2r}\right) = 0 \tag{C.2}$$
$$\left[c - (2k)^2\right]A_{2k}^{2r} - q\left(A_{2k-2}^{2r} + B_{2k+2}^{2r}\right) = 0 \quad (k \geq 2).$$

- for the series $\left\{A_{2k+1}^{2r+1}\right\}$:

$$(c-1-q)A_1^{2r+1} - qA_1^{2r+1} = 0$$
$$\left[c - (2k+1)^2\right]A_{2k+1}^{2r+1} - q\left(A_{2k-1}^{2r+1} + B_{2k+3}^{2r+1}\right) = 0 \quad (k \geq 1). \tag{C.3}$$

- for the series $\left\{B_{2k+1}^{2r+1}\right\}$:

$$(c-1+q)B_1^{2r+1} - qB_1^{2r+1} = 0$$
$$\left[c - (2k+1)^2\right]B_{2k+1}^{2r+1} - q\left(B_{2k-1}^{2r+1} + B_{2k+3}^{2r+1}\right) = 0 \quad (k \geq 1). \tag{C.4}$$

- for the series $\left\{B_{2k+2}^{2r+2}\right\}$:

$$(c-4)B_2^{2r+2} - qB_4^{2r+2} = 0$$
$$\left[c - (2k+2)^2\right]B_{2k+2}^{2r+2} - q\left(B_{2k}^{2r+2} + B_{2k+4}^{2r+2}\right) = 0 \quad (k \geq 1). \tag{C.5}$$

Due to the orthogonal relations of the Mathieu functions, the normalization relations can be obtained as

$$2\left(A_0^{2r}\right)^2 + \sum_{k=1}^{\infty}\left(A_{2k}^{2r}\right)^2 = \sum_{k=0}^{\infty}\left(A_{2k+1}^{2r+1}\right)^2 = 1,$$
$$\sum_{k=0}^{\infty}\left(B_{2k+1}^{2r+1}\right)^2 = \sum_{k=0}^{\infty}\left(B_{2k+2}^{2r+2}\right)^2 = 1. \tag{C.6}$$

Using these relations, one can reduce the problem of calculating expansion coefficients to an eigenproblem for infinite-dimensional tridiagonal matrices C_i, $i = 1, 2, 3, 4$, as shown in Appendix C2. In particular, the characteristic value c can be determined as an eigenvalue of each matrix C_i, while the expansion coefficient series is given by the corresponding eigenvector. In practice, one has to truncate the above expansions for angular Mathieu functions at some $k = K_{max}$ (see Appendix C3 and C4 for details).

b. Radial Mathieu functions

Index	$\frac{k\tilde{c}}{2}$	$\sqrt{4q}$
1	4.21899612	4.2189961192
2	5.30803620	5.3080361961
3	6.29769953	6.2976995316
4	7.24310924	7.2431092413
5	8.16335720	8.1633572021
6	9.06741194	9.0674119150
7	9.96018976	9.9601897419
8	10.84465048	10.844650431
9	11.72268331	11.722683203
10	12.59552397	12.595523897

Table C.1:   Comparison of the first 10 values of $\frac{k\tilde{c}}{2}$ with $R_0 = 2$, $a = 1$, and $\tilde{c} = 2$ between our algorithm and Chen *et al.* [41] (second column).

For radial Mathieu functions, ones uses the classical repsresentation

$$\mathrm{Mc}_{2r}^{(j)}(z,q) = \frac{1}{A_0^{2r}} \sum_{k=0}^{\infty} (-1)^{k+r} A_{2k}^{2r}(q) J_k(u_1) Z_k^{(j)}(u_2),$$

$$\mathrm{Mc}_{2r+1}^{(j)}(z,q) = \frac{1}{A_1^{2r+1}} \sum_{k=0}^{\infty} (-1)^{k+r} A_{2k+1}^{2r+1}(q) \left[J_k(u_1) Z_{k+1}^{(j)}(u_2) + J_{k+1}(u_1) Z_k^{(j)}(u_2) \right],$$

$$\mathrm{Ms}_{2r+1}^{(j)}(z,q) = \frac{1}{B_1^{2r+1}} \sum_{k=0}^{\infty} (-1)^{k+r} B_{2k+1}^{2r+1}(q) \left[J_k(u_1) Z_{k+1}^{(j)}(u_2) - J_{k+1}(u_1) Z_k^{(j)}(u_2) \right], \tag{C.7}$$

$$\mathrm{Mc}_{2r+2}^{(j)}(z,q) = \frac{1}{B_2^{2r+2}} \sum_{k=0}^{\infty} (-1)^{k+r} A_{2k+2}^{2r+2}(q) \left[J_k(u_1) Z_{k+2}^{(j)}(u_2) - J_{k+2}(u_1) Z_k^{(j)}(u_2) \right],$$

where $u_1 = \sqrt{q}e^{-z}$ and $u_2 = \sqrt{q}e^{z}$. The index $j \in \{1,2\}$ distinguishes two kinds of radial Mathieu functions for which $Z_k^{(1)}(x) = J_k(x)$ and $Z_k^{(2)}(x) = Y_k(x)$ are Bessel functions of the first and second kinds. Since the computation of radial Mathieu functions employs the expansion coefficients of angular Mathieu functions, one needs to compute the characteristic values and the expansion coefficients only once.

Since we have rebuilt the computation of Mathieu functions and modified Mathieu functions, we check the accuracy of the numerical algorithm by comparing their values to whose published in the literature [41, 129, 234]. We also checked that the truncation of tridiagonal matrices to the size $K_{max} = 200$ was enough for getting very accurate results.

Example C1.1. *In Table C1, we choose $a = 1$ and compare numerical values of the modified Mathieu function $\mathrm{Ce}_5(1,q)$ by our algorithm and several other algorithms. From this table, we conclude that our numerical results are very accurate.*

Example C1.2. *In this example, we check again all results in [41] by our algorithm. In [41], the authors compute the first 28 roots $\frac{k\tilde{c}}{2}$ of the equation $\mathrm{Ce}_{11}(R_0,q)$, with $R_0 = 2$ and $a = 1$. Note that, the notations $k^2 = \frac{16q}{\tilde{c}^2}$ and $\tilde{c} = 2$ were used in [41], so it is equivalent that $\frac{k\tilde{c}}{2} = \sqrt{4q}$, where q is the zero of the function*

q	Chen's	Our algorithm	Kirkpatrick's
1	54.60629927	54.606299266	54.6063
2	39.51952105	39.519521053	39.5195
3	28.02845421	28.028454209	29.0285
4	19.37904040	19.379040397	19.3790
5	12.95741669	12.957416687	12.9574
6	8.26755682	8.267556817	8.2676
7	4.91210250	4.912102499	4.9121
8	2.57540926	2.575409256	2.5754
9	1.00823869	1.008238689	1.0082
10	0.01416872	0.014168715	0.01418
12	-0.84047602	-0.840476022	-0.84049
14	-0.86017691	-0.860176915	-0.86016
16	-0.54740402	-0.547404017	-0.54741
18	-0.17203806	-0.172038062	-0.17196
20	0.12766301	0.127663014	-0.12777

Table C.2:   Comparison of the modified Mathieu function $\mathrm{Ce}_5(1, q)$, obtained by Chen's algorithm (second column, from [41]), by our algorithms (third column), and by Kirkpatrick (last column, from [129], Table 6).

$\mathrm{Ce}_{11}(R_0, q) = 0$ *in our algorithm. In Table C1, we solve this equation again and compare the first* 10 *values.*

C2   Computation of Characteristic Values

The characteristic values $c(q)$ can be determined by solving an eigenvalue problem for infinite-dimensional tridiagonal matrices C_1, C_2, C_3 and C_4 [234]:

$$
C_1 \;=\; \begin{pmatrix}
0 & q & 0 & 0 & \ldots & 0 & \ldots \\
2q & 4 & q & 0 & \ldots & 0 & \ldots \\
0 & q & 16 & q & \ldots & 0 & \ldots \\
\ldots & \ldots & \ldots & \ldots & \ldots & \ldots & \ldots \\
0 & \ldots & \ldots & q & (2k)^2 & q & \ldots \\
\ldots & \ldots & \ldots & \ldots & \ldots & \ldots & \ldots
\end{pmatrix}
\tag{C.8}
$$

$$
C_2 \;=\; \begin{pmatrix}
1+q & q & 0 & 0 & \ldots & 0 & \ldots \\
2q & 9 & q & 0 & \ldots & 0 & \ldots \\
0 & q & 25 & q & \ldots & 0 & \ldots \\
\ldots & \ldots & \ldots & \ldots & \ldots & \ldots & \ldots \\
0 & \ldots & \ldots & q & (2k+1)^2 & q & \ldots \\
\ldots & \ldots & \ldots & \ldots & \ldots & \ldots & \ldots
\end{pmatrix}
\tag{C.9}
$$

$$C_3 = \begin{pmatrix} 1-q & q & 0 & 0 & \ldots & 0 & \ldots \\ 2q & 9 & q & 0 & \ldots & 0 & \ldots \\ 0 & q & 25 & q & \ldots & 0 & \ldots \\ \ldots & \ldots & \ldots & \ldots & \ldots & \ldots & \ldots \\ 0 & \ldots & \ldots & q & (2k+1)^2 & q & \ldots \\ \ldots & \ldots & \ldots & \ldots & \ldots & \ldots & \ldots \end{pmatrix} \qquad \text{(C.10)}$$

$$C_4 = \begin{pmatrix} 4 & q & 0 & 0 & \ldots & 0 & \ldots \\ 2q & 16 & q & 0 & \ldots & 0 & \ldots \\ 0 & q & 36 & q & \ldots & 0 & \ldots \\ \ldots & \ldots & \ldots & \ldots & \ldots & \ldots & \ldots \\ 0 & \ldots & \ldots & q & (2k+2)^2 & q & \ldots \\ \ldots & \ldots & \ldots & \ldots & \ldots & \ldots & \ldots \end{pmatrix} \qquad \text{(C.11)}$$

For computing angular and radial Mathieu functions, one can truncate the expansions in (C.7) at some $k = K_{max}$. After that, one can calculate the corresponding expansion coefficient series $\{A_{2k}^{2r}\}_{k=0}^{K_{max}}$, $\{A_{2k+1}^{2r+1}\}_{k=0}^{K_{max}}$, $\{B_{2k+1}^{2r+1}\}_{k=0}^{K_{max}}$ and $\{B_{2k+2}^{2r+2}\}_{k=0}^{K_{max}}$ by solving the eigenvalue problems for the truncated tridiagonal matrices $\tilde{C}_i$ of size $K_{max} + 1$.

It is important to note that these above matrices are sparse, and moreover, the matrix C_1 is non-symmetric only at one entry $(2, 1)$, while the other matrices are symmetric. The eigendecomposition problems for symmetric and tridiagonal matrices $\tilde{C}_i$, $i = 1, 2, 3, 4$ can thus be solved by standard routines (e.g., the function *eigs* in Matlab).

C3 Computation of Expansion Coefficients

We summarize all necessary algorithms as following

Algorithm C3.1. *(Computing $\{A_{2k}^{2r}\}_{k=0}^{K_{max}}$)*

- **Input:** r, q, K_{max}.

- **Step 1:** *One solves the eigenvalue problem of the truncated matrix $\tilde{C}_1$. Suppose that all eigenvalues are $c_0(q) < c_1(q) < \cdots < c_{K_{max}}(q)$ and the corresponding eigenvectors $\{u_k\}_{k=0}^{K_{max}}$.*

- **Step 2:** *Choose*

$$u_r = \begin{pmatrix} A_0^{2r} \\ A_2^{2r} \\ \ldots \\ A_{2K_{max}}^{2r} \end{pmatrix},$$

and normalize $\{A_{2k}^{2r}\}_{k=0}^{K_{max}}$ by (C.6).

- **Output:** $\left\{A_{2k}^{2r}\right\}_{k=0}^{K_{max}}$.

Algorithm C3.2. *(Computing $\left\{A_{2k+1}^{2r+1}\right\}_{k=0}^{K_{max}}$)*

- **Input:** r, q, K_{max}.

- **Step 1:** *One solves the eigenvalue problem of the truncated matrix $\tilde{C}_2$. Suppose that all eigenvalues are $c_0(q) < c_1(q) < \cdots < c_{K_{max}}(q)$ and the corresponding eigenvectors $\{u_k\}_{k=0}^{K_{max}}$.*

- **Step 2:** *Choose*

$$u_r = \begin{pmatrix} A_1^{2r+1} \\ A_3^{2r+1} \\ \dots \\ A_{2K_{max}+1}^{2r+1} \end{pmatrix},$$

and normalize $\left\{A_{2k+1}^{2r+1}\right\}_{k=0}^{K_{max}}$ by (C.6).

- **Output:** $\left\{A_{2k+1}^{2r+1}\right\}_{k=0}^{K_{max}}$.

Algorithm C3.3. *(Computing $\left\{B_{2k+1}^{2r+1}\right\}_{k=0}^{K_{max}}$)*

- **Input:** r, q, K_{max}.

- **Step 1:** *One solves the eigenvalue problem of the truncated matrix $\tilde{C}_3$. Suppose that all eigenvalues are $c_0(q) < c_1(q) < \cdots < c_{K_{max}}(q)$ and the corresponding eigenvectors $\{u_k\}_{k=0}^{K_{max}}$.*

- **Step 2:** *Choose*

$$u_r = \begin{pmatrix} B_1^{2r+1} \\ B_3^{2r+1} \\ \dots \\ B_{2K_{max}+1}^{2r+1} \end{pmatrix},$$

and normalize $\left\{B_{2k+1}^{2r+1}\right\}_{k=0}^{K_{max}}$ by (C.6).

- **Output:** $\left\{B_{2k+1}^{2r+1}\right\}_{k=0}^{K_{max}}$.

Algorithm C3.4. *(Computing $\left\{B_{2k+2}^{2r+2}\right\}_{k=0}^{K_{max}}$)*

- **Input:** r, q, K_{max}.

- **Step 1:** *One solves the eigenvalue problem of the truncated matrix $\tilde{C}_4$. Suppose that all eigenvalues are $c_0(q) < c_1(q) < \cdots < c_{K_{max}}(q)$ and the corresponding eigenvectors $\{u_k\}_{k=0}^{K_{max}}$.*

- **Step** 2: *Choose*

$$u_r = \begin{pmatrix} B_2^{2r+2} \\ B_4^{2r+2} \\ \ldots \\ B_{2K_{max}+2}^{2r+2} \end{pmatrix},$$

  and normalize $\left\{ B_{2k+2}^{2r+2} \right\}_{k=0}^{K_{max}}$ *by (C.6).*

- **Output:** $\left\{ B_{2k+2}^{2r+2} \right\}_{k=0}^{K_{max}}$.

C4 Computation of Mathieu functions

After computing the expansion coefficients, Mathieu functions are then computed by the recurrence relations (C.2), (C.3) ,(C.4), and (C.5):

Algorithm C4.1. *(Computing* $\mathrm{ce}_m(z,q)$*)*

- **Input:** m, z, q, K_{max}.

- **Step** 1:

  − *If* $m = 2r$*: use Algorithm C3.1 to compute*

  $$u = \begin{pmatrix} A_0^{2r} \\ A_2^{2r} \\ \ldots \\ A_{2K_{max}}^{2r} \end{pmatrix}, v = \begin{pmatrix} v_0 \\ v_1 \\ \ldots \\ v_{K_{max}} \end{pmatrix},$$

  where $v_k = \cos 2kz$.

  − *If* $m = 2r + 1$*: use Algorithm C3.2 to compute*

  $$u = \begin{pmatrix} A_1^{2r+1} \\ A_3^{2r+1} \\ \ldots \\ A_{2K_{max}+1}^{2r+1} \end{pmatrix}, v = \begin{pmatrix} v_0 \\ v_1 \\ \ldots \\ v_{K_{max}} \end{pmatrix},$$

  where $v_k = \cos (2k + 1) z$.

- **Step** 2: *Compute*

$$\mathrm{ce}_m(z, q) = u'v.$$

- **Output: return** $\mathrm{ce}_m(z,q)$.

Algorithm C4.2. *(Computing* $\mathrm{se}_m(z,q)$*)*

- **Input:** m, z, q, K_{max}.

- **Step** 1:

  - *If* $m = 2r + 1$*: use Algorithm C3.3 to compute*

$$
u = \begin{pmatrix} B_1^{2r+1} \\ B_3^{2r+1} \\ \ldots \\ B_{2K_{max}+1}^{2r+1} \end{pmatrix}, v = \begin{pmatrix} v_0 \\ v_1 \\ \ldots \\ v_{K_{max}} \end{pmatrix},
$$

  where $v_k = \sin\left(2k + 1\right)z$.

  - *If* $m = 2r + 2$*: use Algorithm C3.4 to compute*

$$
u = \begin{pmatrix} B_2^{2r+2} \\ B_4^{2r+2} \\ \ldots \\ B_{2K_{max}+2}^{2r+2} \end{pmatrix}, v = \begin{pmatrix} v_0 \\ v_1 \\ \ldots \\ v_{K_{max}} \end{pmatrix},
$$

  where $v_k = \sin\left(2k + 2\right)z$.

- **Step** 2: *Compute*

$$
\mathrm{se}_m(z,q) = u'v.
$$

- **Output: return** $\mathrm{se}_m(z,q)$.

Algorithm C4.3. *(Computing* $\mathrm{Mc}_m^{(j)}(z,q)$*)*

- **Input:** m, z, q, K_{max}.

- **Step** 1:

  - *If* $m = 2r$*: use Algorithm C3.1 to compute*

$$
u = \begin{pmatrix} A_0^{2r} \\ A_2^{2r} \\ \ldots \\ A_{2K_{max}}^{2r} \end{pmatrix}, v = \frac{1}{u(1,1)} \begin{pmatrix} v_0 \\ v_1 \\ \ldots \\ v_{K_{max}} \end{pmatrix},
$$

  where $v_k = (-1)^{k+r} J_k(u_1) Z_k^{(j)}(u_2)$.

− *If $m = 2r + 1$: use Algorithm C3.2 to compute*

$$
u = \begin{pmatrix} A_1^{2r+1} \\ A_3^{2r+1} \\ \dots \\ A_{2K_{max}+1}^{2r+1} \end{pmatrix}, v = \frac{1}{u(1,1)} \begin{pmatrix} v_0 \\ v_1 \\ \dots \\ v_{K_{max}} \end{pmatrix},
$$

where $v_k = (-1)^{k+r} \left[J_k(u_1) Z_{k+1}^{(j)}(u_2) + J_{k+1}(u_1) Z_k^{(j)}(u_2) \right]$.

Here, $u_1 = \sqrt{q} e^{-z}$, $u_2 = \sqrt{q} e^z$, $Z_k^{(1)}(x) = J_k(x)$ and $Z_k^{(2)}(x) = Y_k(x)$.

- **Step 2:** *Compute*

$$
\mathrm{Mc}_m^{(j)}(z, q) = u'v.
$$

- **Output: return** $\mathrm{Mc}_m^{(j)}(z, q)$.

Algorithm C4.4. *(Computing $\mathrm{Ms}_m^{(j)}(z, q)$)*

- **Input:** m, z, q, K_{max}.

- **Step 1:**

  − *If $m = 2r + 1$: use Algorithm C3.3 to compute*

$$
u = \begin{pmatrix} B_1^{2r+1} \\ B_3^{2r+1} \\ \dots \\ B_{2K_{max}+1}^{2r+1} \end{pmatrix}, v = \frac{1}{u(1,1)} \begin{pmatrix} v_0 \\ v_1 \\ \dots \\ v_{K_{max}} \end{pmatrix},
$$

where $v_k = (-1)^{k+r} \left[J_k(u_1) Z_{k+1}^{(j)}(u_2) - J_{k+1}(u_1) Z_k^{(j)}(u_2) \right]$.

  − *If $m = 2r + 2$: use Algorithm C3.4 to compute*

$$
u = \begin{pmatrix} B_2^{2r+2} \\ B_4^{2r+2} \\ \dots \\ B_{2K_{max}+2}^{2r+2} \end{pmatrix}, v = \frac{1}{u(1,1)} \begin{pmatrix} v_0 \\ v_1 \\ \dots \\ v_{K_{max}} \end{pmatrix},
$$

where $v_k = (-1)^{k+r} \left[J_k(u_1) Z_{k+2}^{(j)}(u_2) - J_{k+2}(u_1) Z_k^{(j)}(u_2) \right]$.

Here, $u_1 = \sqrt{q} e^{-z}$, $u_2 = \sqrt{q} e^z$, $Z_k^{(1)}(x) = J_k(x)$ and $Z_k^{(2)}(x) = Y_k(x)$.

- **Step 2:** *Compute*

$$
\mathrm{Ms}_m^{(j)}(z, q) = u'v.
$$

- **Output: return** $\mathrm{Ms}_m^{(j)}(z, q)$.

q	$m = 0$	$m = 1$	$m = 2$	$m = 3$	$m = 4$
0	0	1	4	9	16
1	-0.455138604	1.859108073	4.371300983	9.078368847	16.033832340
2	-1.513956885	2.379199880	5.172665133	9.370322484	16.141203786
3	-2.834391890	2.519039088	6.045196852	9.915506290	16.338720746
4	-4.280518818	2.318008170	6.829074835	10.671027103	16.649818907
5	-5.800046021	1.858187542	7.449109740	11.548832036	17.096581684
6	-7.368830832	1.214278164	7.870064475	12.465600683	17.688782955
7	-8.973742506	0.438349090	8.086623145	13.358421316	18.416608662
8	-10.606729236	-0.435943601	8.115238830	14.181880362	19.252705059
9	12.262414218	-1.386701566	7.982843163	14.903679668	20.160926386

Table C.3: Characteristic values of $\mathrm{ce}_m(z, q)$ with $K_{max} = 200$.

C5 Computing Mathieu functions at many points

In principle, for given m, q, one can use Algorithms C4.1, C4.2, C4.3 and C4.4 to compute values of angular Mathieu functions $\mathrm{ce}_m(z_0, q)$, $\mathrm{se}_{m+1}(z_0, q)$ and radial Mathieu functions $\mathrm{Mc}_m^{(j)}(z_0, q)$, $\mathrm{Ms}_{m+1}^{(j)}(z_0, q)$ at a point z_0. However, when computing these functions at many points, for example, calculating an eigenfunction at all points in an elliptical mesh by PDETool, it is not efficient to repeat these algorithms at each point. Assume that one needs to compute the values of these Mathieu functions at n points $\{z_1, z_2, \ldots, z_n\}$. In that case, one has to compute the expansion coefficient series only once, and then use these coefficients and Eq. (C.1) to get the results at z_i $(i = 1, \ldots, n)$. For this reason, one can use the following algorithm

Algorithm C5.1. *(Computing $\mathrm{ce}_m(z, q)$, $\mathrm{se}_{m+1}(z, q)$, $\mathrm{Mc}_m^{(j)}(z, q)$ or $\mathrm{Ms}_{m+1}^{(j)}(z, q)$ at n points $\{z_1, z_2, \ldots, z_n\}$)*

- **Input:** m, q, K_{max} *and* $\{z_1, z_2, \ldots, z_n\}$.

- **Step** 1: *For the expected Mathieu function, compute the corresponding expansion coefficients $\{A_{2k}^{2r}\}_{k=0}^{K_{max}}$, $\{A_{2k+1}^{2r+1}\}_{k=0}^{K_{max}}$, $\{B_{2k+1}^{2r+1}\}_{k=0}^{K_{max}}$ or $\{B_{2k+2}^{2r+2}\}_{k=0}^{K_{max}}$ by Algorithm C3.1, C3.2, C3.3 or C3.4.*

- **Step** 2: *For each $z_i \in \{z_1, z_2, \ldots, z_n\}$, use the expansion coefficients computed in Step 1 and z_i for truncating into Eq. (C.1) or (C.7) like Algorithms C4.1, C4.2, C4.3 and C4.4 to get the value of the expected Mathieu function at this point.*

- **Output:** *return all computed results.*

C6 Computational tables

Using the above algorithms, we created the following tables, which may be helpful for readers to check their calculation of Mathieu functions.

q	$m = 1$	$m = 2$	$m = 3$	$m = 4$	$m = 5$
0	1	4	9	16	25
1	-0.110248817	3.917024773	9.047739260	16.032970081	25.020840823
2	-1.390676501	3.672232706	9.140627738	16.127687953	25.083349030
3	-2.785379700	3.276921970	9.223132848	16.272701196	25.187079803
4	-4.259182901	2.746881027	9.261446132	16.452035290	25.330544872
5	-5.790080599	2.099460445	9.236327714	16.648219937	25.510816046
6	-7.363911012	1.351381155	9.137905846	16.844601644	25.723410652
7	-8.971202351	0.517545407	8.962385459	17.026660783	25.962447176
8	-10.605368139	-0.389361770	8.709914358	17.182527771	26.220999473
9	-12.261661653	-1.358810117	8.383119158	17.303010962	26.491547241

Table C.4:   Characteristic values of $\mathrm{se}_m(z,q)$ with $K_{max} = 200$.

k	$m = 0$	$m = 1$	$m = 2$	$m = 3$	$m = 4$
0	0.007626518	0.053598748	0.245888349	0.704827934	1.127106792
1	0.008631881	0.058224751	0.257429643	0.716794783	1.122152122
2	0.011890635	0.072755792	0.292515785	0.751420208	1.104754244
3	0.018163645	0.099129840	0.352270238	0.804576169	1.067584319
4	0.028821870	0.140469081	0.437663770	0.868480904	0.999481596
5	0.045973997	0.200791397	0.548111731	0.930742353	0.887476524
6	0.072581757	0.284372427	0.679528225	0.973858031	0.720264157
7	0.112481611	0.394589841	0.822112479	0.976023743	0.493186097
8	0.170197928	0.532165534	0.958512543	0.914144106	0.214008154
9	0.250418807	0.692937976	1.063412814	0.769537055	-0.092315174
10	0.357040942	0.865645544	1.105781366	0.535802627	-0.382664667
11	0.491801944	1.030591606	1.054662779	0.226789996	-0.601399228
12	0.6527102141	1.160289964	0.888276725	-0.118865411	-0.693815322
13	0.832706667	1.222990778	0.604409424	-0.440533066	-0.625176856
14	1.019145539	1.189187885	0.228347198	-0.667919481	-0.398957918
15	1.194634216	1.039919774	-0.185995131	-0.741313933	-0.065523331
16	1.339445822	0.774395216	-0.564604034	-0.633505011	0.285829580
17	1.435165432	0.413936167	-0.830827857	-0.364310367	0.552131051
18	1.468660471	0.000000000	-0.926759264	-0.000000000	0.651324612

Table C.5:   Mathieu functions $\mathrm{ce}_m(z,q)$ with $K_{max} = 200$, $q = 10$ and $z = \frac{k\pi}{36}$.

k	$m = 1$	$m = 2$	$m = 3$	$m = 4$	$m = 5$
0	0	0	0	0	0
1	0.004008864	0.022333463	0.075602285	0.173365551	0.294755345
2	0.009061572	0.048447659	0.157907189	0.349591356	0.573379470
3	0.016407523	0.082417037	0.253106061	0.529184405	0.816764588
4	0.027711005	0.128791303	0.366088158	0.707957455	1.001001300
5	0.045255052	0.192529657	0.499154634	0.874932104	1.097923031
6	0.072104509	0.278524592	0.650181014	1.011102993	1.079151892
7	0.112156846	0.390555937	0.810464774	1.090088042	0.924174575
8	0.169972731	0.529602733	0.962917266	1.081850768	0.631534785
9	0.250262080	0.691656459	1.081702815	0.960234992	0.229995316
10	0.356934814	0.865526742	1.134640982	0.713721899	−0.215738525
11	0.491736521	1.031519867	1.089327172	0.356717576	−0.610888766
12	0.652680162	1.162097406	0.922742898	−0.063405298	−0.851725542
13	0.832708813	1.225421853	0.632252755	−0.468942933	−0.859260387
14	1.019177082	1.191892921	0.244040712	−0.767449961	−0.614578909
15	1.194691443	1.042483685	−0.185605609	−0.878382249	−0.179275304
16	1.339523355	0.776398714	−0.579189641	−0.762530757	0.313448765
17	1.435256082	0.415035173	−0.856332566	−0.441982586	0.699950206
18	1.468755664	0.000000000	−0.956262144	−0.000000000	0.846038434

Table C.6: Mathieu functions $\text{se}_m(z, q)$ with $K_{max} = 200$, $q = 10$ and $z = \frac{k\pi}{36}$.

z	$m = 0$	$m = 1$	$m = 2$	$m = 3$	$m = 4$
0.0	0.332122615	0.371203150	0.441872647	0.546737927	0.467102045
0.2	0.129816272	0.215369357	0.335595266	0.495488437	0.474932079
0.4	0.230408874	−0.127448229	0.052166842	0.322398207	0.467346828
0.6	−0.251122288	−0.320089063	−0.254281879	0.016914506	0.352245174
0.8	0.139122673	−0.075999430	−0.278230676	−0.276099346	0.045538281
1.0	0.199455250	0.262138333	0.099390624	−0.194128818	−0.268958658
1.2	−0.220574331	−0.036427802	0.201921817	0.215214749	−0.074585906
1.4	0.102124849	−0.132183115	−0.218473516	−0.013980652	0.221009347
1.6	−0.056100683	0.159796027	0.168024720	−0.069527138	−0.203183617
1.8	0.115703622	−0.099125208	−0.174506332	0.019722580	0.184918357
2.0	−0.157345656	−0.083590927	0.121379496	0.131761064	−0.084989638

Table C.7: Modified Mathieu functions $\text{Mc}_m^{(1)}(z, q)$ with $K_{max} = 200$, $q = 10$.

k	$m = 0$	$m = 1$	$m = 2$	$m = 3$	$m = 4$
0.0	0.404999050	0.491467279	0.605582252	0.451660995	0.150452642
0.2	0.282688376	0.412368634	0.573364459	0.464496562	0.171886282
0.4	−0.016244620	0.189447366	0.462450425	0.488134607	0.235917413
0.6	−0.296077529	−0.112233018	0.244792612	0.472643070	0.331783123
0.8	−0.305807925	−0.332680285	−0.064878520	0.334290961	0.407276972
1.0	0.024144065	−0.250375761	−0.310204967	0.024731667	0.339075692
1.2	0.284535369	0.128913811	−0.203810720	−0.276718680	0.023636964
1.4	−0.024212844	0.232012077	0.197958688	−0.136838161	−0.273733535
1.6	−0.196630636	−0.193387510	0.091011737	0.240678789	0.014205214
1.8	0.214902382	0.050257739	−0.198179490	−0.123060552	0.154823555
2.0	−0.192891034	−0.015072841	0.191631508	0.071838061	−0.171071700

Table C.8: Modified Mathieu functions $\mathrm{Mc}_m^{(1)}(z, q)$ with $K_{max} = 200$, $q = 5$.

z	$m = 1$	$m = 2$	$m = 3$	$m = 4$	$m = 5$
0.0	0	0	0	0	0
0.2	0.301260817	−0.292997874	0.262742684	−0.197435311	0.110612450
0.4	0.217308520	−0.319932923	0.381448654	−0.355614796	0.240376373
0.6	−0.164516936	−0.012428757	0.227223019	−0.375166960	0.360546042
0.8	−0.243685476	0.284490373	−0.141265707	−0.131669932	0.336939817
1.0	0.166240482	0.058673840	−0.258284059	0.232676804	0.019419331
1.2	0.090851527	−0.241581481	0.150100227	0.116887381	−0.262672811
1.4	−0.192710753	0.178116954	0.052254263	−0.226626571	0.113144618
1.6	0.190647344	−0.121995786	−0.112631351	0.196841139	−0.003617280
1.8	−0.138757611	0.152755184	0.054956289	−0.184266632	0.035017342
2.0	−0.046228277	−0.142054020	0.113384891	0.096012978	−0.153042158

Table C.9: Modified Mathieu functions $\mathrm{Ms}_m^{(1)}(z, q)$ with $K_{max} = 200$, $q = 10$.

k	$m = 1$	$m = 2$	$m = 3$	$m = 4$	$m = 5$
0.0	0	0	0	0	0
0.2	0.281792834	−0.242707948	0.168187100	−0.081713955	0.027477039
0.4	0.382965213	−0.399693616	0.323068522	−0.181387073	0.071353497
0.6	0.207395869	−0.378714269	0.419826272	−0.301065998	0.149282364
0.8	−0.141453939	−0.130169641	0.366927451	−0.395710334	0.266916569
1.0	−0.309846112	0.213605299	0.090320416	−0.342937946	0.370317077
1.2	−0.015423176	0.262818916	−0.248584668	−0.033495361	0.291591224
1.4	0.259025162	−0.133302869	−0.165062010	0.271723102	−0.077445556
1.6	−0.132080769	−0.140826863	0.233116044	−0.009080134	−0.228729511
1.8	−0.010336083	0.211095806	−0.106550875	−0.157369244	0.202110727
2.0	0.029937230	−0.195913873	0.058550109	0.172382445	−0.143821849

Table C.10: Modified Mathieu functions $\mathrm{Ms}_m^{(1)}(z, q)$ with $K_{max} = 200$, $q = 5$.

z	$m = 0$	$m = 1$	$m = 2$	$m = 3$	$m = 4$
0.0	-0.000018408	-0.000902636	-0.019033459	-0.181989273	-0.632949374
0.2	0.301253662	0.292501273	0.249787992	0.060294155	-0.369846012
0.4	0.217317361	0.320105997	0.378827511	0.282210844	-0.100650087
0.6	-0.164507924	0.012885216	0.232784972	0.370212810	0.178982127
0.8	-0.243689096	-0.284378718	-0.135717179	0.169833197	0.333677609
1.0	0.166235498	-0.058926268	-0.259632019	-0.210488912	0.116529242
1.2	0.090855832	0.241601846	0.147417860	-0.136480311	-0.247620918
1.4	-0.192712313	-0.178025496	0.054533539	0.227584501	0.064274558
1.6	0.190648023	0.121907430	-0.114049409	0.192590816	0.034005206
1.8	-0.138758855	-0.152709560	0.056175370	0.183270584	0.007437921
2.0	-0.046226837	0.142083260	0.112673816	-0.101327038	-0.143357469

Table C.11: Modified Mathieu functions $\mathrm{Mc}_m^{(2)}(z, q)$ with $K_{max} = 200$, $q = 10$.

k	$m = 0$	$m = 1$	$m = 2$	$m = 3$	$m = 4$
0.0	-0.000753837	-0.025129572	-0.255352516	-0.807148299	-1.710397645
0.2	0.281296916	0.223746073	-0.035409095	-0.545721522	-1.068582676
0.4	0.382936918	0.391291381	0.186971269	-0.300026787	-0.699988306
0.6	0.207711848	0.380826057	0.359767146	-0.036471909	-0.438946008
0.8	-0.141151997	0.137870930	0.377094983	0.225906741	0.166475784
1.0	-0.309847897	-0.208367862	0.136827027	0.349615971	0.145446204
1.2	-0.015608838	-0.264652069	-0.223222487	0.136877618	0.317654592
1.4	0.259031081	0.130139217	-0.184667692	-0.237882859	0.058225775
1.6	-0.131990823	0.142868441	0.225585244	-0.048015125	-0.248104220
1.8	-0.010414477	-0.211482224	-0.093347521	0.182779665	0.159299197
2.0	0.029994822	0.195985747	0.048132472	-0.184881723	-0.102455629

Table C.12: Modified Mathieu functions $\mathrm{Mc}_m^{(2)}(z, q)$ with $K_{max} = 200$, $q = 5$.

z	$m = 1$	$m = 2$	$m = 3$	$m = 4$	$m = 5$
0.0	-0.332123704	0.371282329	-0.445221788	0.631637579	-1.199905424
0.2	-0.129802231	0.214807024	-0.328166170	0.489712364	-0.768490768
0.4	0.230418371	-0.128017698	-0.041343255	0.264428165	-0.496096931
0.6	0.251117149	-0.320141830	0.260287006	-0.047470970	-0.229199818
0.8	-0.139129930	-0.075668868	0.275967235	-0.300583079	0.101525038
1.0	-0.199451497	0.262209754	-0.103568450	-0.170627033	0.300138821
1.2	0.220576323	-0.036622843	-0.200135461	0.227843128	0.003837373
1.4	-0.102128068	-0.132069201	0.219127600	-0.030907762	-0.203048801
1.6	0.056103278	0.159732881	-0.169046942	-0.057873643	0.207283441
1.8	-0.115705193	-0.099058722	0.174929914	0.010664770	-0.182500908
2.0	0.157345265	-0.083643115	-0.120743781	0.135862108	0.067105124

Table C.13: Modified Mathieu functions $\mathrm{Ms}_m^{(2)}(z, q)$ with $K_{max} = 200$, $q = 10$.

k	$m = 1$	$m = 2$	$m = 3$	$m = 4$	$m = 5$
0.0	-0.405070673	0.496582932	-0.751974676	1.625573565	-5.120133530
0.2	-0.282283730	0.405279031	-0.604198406	1.038926043	-2.438115060
0.4	0.016765518	0.176436235	-0.416942550	0.698253660	-1.265592714
0.6	0.296344606	-0.123688032	-0.163940853	0.451596697	-0.741825701
0.8	0.305697116	-0.336689816	0.135615280	0.184465033	-0.451045741
1.0	-0.024390508	-0.246620568	0.331757914	-0.131574894	-0.166651837
1.2	-0.284556864	0.133322597	0.176733494	-0.315917231	0.167804420
1.4	0.024353432	0.230434311	-0.216580391	-0.065047406	0.278565228
1.6	0.196575692	-0.195025139	-0.072691797	0.248087833	-0.109463548
1.8	-0.214908984	0.052156550	0.192039143	-0.156575476	-0.098885996
2.0	0.192901735	-0.016505872	-0.189056381	0.100062369	0.140506961

Table C.14: Modified Mathieu functions $\mathrm{Ms}_m^{(2)}(z,q)$ with $K_{max} = 200$, $q = 5$.

m	$k = 1$	$k = 2$	$k = 3$	$k = 4$	$k = 5$
0	0.268144489	0.734309332	1.089382454	1.362969790	1.582095757
1	0.327751006	0.834992742	1.185871249	1.448171414	1.656703799
2	0.430950699	0.954525930	1.288098947	1.534732337	1.731154786
3	0.609782985	1.090863509	1.394975749	1.622544005	1.805704508
4	0.823744379	1.230182722	1.501184299	1.709076510	1.878962931
5	1.001027162	1.352184052	1.596756000	1.788283700	1.946828844
6	1.136859062	1.453768228	1.679465911	1.858481664	2.007978689
7	1.250044621	1.542334725	1.753333663	1.922183927	2.064120315
8	1.349499545	1.622091004	1.820864625	1.981052920	2.116432510
9	1.438776256	1.694950751	1.883272196	2.035923639	2.165520902

Table C.15: First k zeros of Modified Mathieu functions $\mathrm{Mc}_m^{(1)}(z,q)$ with $K_{max} = 200$, $q = 10$.

m	$k = 1$	$k = 2$	$k = 3$	$k = 4$	$k = 5$
1	0.515828312	0.924144038	1.234401061	1.478084351	1.676832399
2	0.606240826	1.024677860	1.325300928	1.557742976	1.746789213
3	0.725648125	1.134523114	1.418481630	1.637366815	1.815945297
4	0.866780341	1.247500982	1.510908834	1.715385079	1.883411453
5	1.009120767	1.355712997	1.598821200	1.789659594	1.947817635
6	1.137636317	1.454126090	1.679681872	1.858628569	2.008085894
7	1.250092565	1.542357660	1.753347831	1.922193726	2.064127557
8	1.349501690	1.622092062	1.820865291	1.981053387	2.116432859
9	1.438776330	1.694950789	1.883272219	2.035923656	2.165520915

Table C.16: First k zeros of Modified Mathieu functions $\mathrm{Ms}_m^{(1)}(z,q)$ with $K_{max} = 200$, $q = 10$.

m	$k=1$	$k=2$	$k=3$	$k=4$	$k=5$
1	0.268136947	0.734305362	1.089380284	1.362968477	1.582094891
2	0.327392889	0.834841832	1.185793965	1.448125165	1.656673167
3	0.424656219	0.952416576	1.287043221	1.534095319	1.730727477
4	0.571107814	1.078822161	1.388792213	1.618719756	1.803088757
5	0.740013296	1.201581947	1.485733151	1.699213177	1.872066301
6	0.896006033	1.312621322	1.574410247	1.773620911	1.936376823
7	1.030234520	1.411111872	1.654610032	1.841830789	1.995928471
8	1.146707405	1.499272735	1.727645638	1.904691278	2.051303212
9	1.249828826	1.579222993	1.794799128	1.963058208	2.103107601

Table C.17:   First k zeros of Modified Mathieu functions $\mathrm{Ms}_m^{(2)}(z,q)$ with $K_{max} = 200$, $q = 10$.

m	$k=1$	$k=2$	$k=3$	$k=4$	$k=5$
0	0.000009604	0.515833826	0.924146936	1.234402728	1.478085407
1	0.000526312	0.606468865	1.024783310	1.325359797	1.557780232
2	0.013201542	0.729033826	1.135968721	1.419288093	1.637883188
3	0.150818078	0.886124652	1.255852511	1.515694149	1.718517268
4	0.470769547	1.053290112	1.376128240	1.610988746	1.797834705
5	0.722818089	1.196542381	1.483091831	1.697547266	1.870908650
6	0.894443779	1.312121596	1.574137787	1.773444729	1.936252202
7	1.030141404	1.411080362	1.654592344	1.841819127	1.995920102
8	1.146703339	1.499271301	1.727644814	1.904690726	2.051302811
9	1.249828689	1.579222943	1.794799099	1.963058188	2.103107586

Table C.18:   First k zeros of Modified Mathieu functions $\mathrm{Mc}_m^{(2)}(z,q)$ with $K_{max} = 200$, $q = 10$.

k	$m = 1$	$m = 2$	$m = 3$	$m = 4$	$m = 5$
1	0.500000000	0.404217111	0.323838555	0.241683761	0.165614189
2		0.595782889	0.500000000	0.421713163	0.351471846
3			0.676161445	0.578286837	0.500000000
4				0.758316239	0.648528154
5					0.834385811
k	$m = 6$	$m = 7$	$m = 8$	$m = 9$	$m = 10$
1	0.117087626	0.090560661	0.074464765	0.063584125	0.055670378
2	0.293229923	0.247584677	0.212378563	0.185222263	0.164002338
3	0.433952567	0.379148346	0.333908116	0.296660163	0.265964368
4	0.566047433	0.500000000	0.445655071	0.400266182	0.362055548
5	0.706770077	0.620851654	0.554344929	0.500000000	0.454432315
6	0.882912374	0.752415323	0.666091884	0.599733818	0.545567685
7		0.909439339	0.787621437	0.703339837	0.637944452
8			0.925535235	0.814777737	0.734035632
9				0.936415875	0.835997662
10					0.944329622

Table C.19: Values $a_k = \frac{z_k}{\pi}$, where z_k are zeros of Mathieu functions $\mathrm{ce}_m(z, q)$ with $K_{max} = 200$, $q = 10$ in $[0, \pi]$.

k	$m = 1$	$m = 2$	$m = 3$	$m = 4$	$m = 5$
0	0	0	0	0	0
1	0.999999999	0.500000000	0.404693801	0.329222085	0.264337426
2		1.000000000	0.500000000	0.500000000	0.426669186
3			1.000000000	0.670777915	0.573330814
4				1.000000000	0.735662574
5					1.000000000
k	$m = 6$	$m = 7$	$m = 8$	$m = 9$	$m = 10$
0	0	0	0	0	0
1	0.211905613	0.173255479	0.145682200	0.125630336	0.110531870
2	0.365726121	0.315496693	0.274830356	0.242150638	0.215813606
3	0.500000000	0.440183133	0.390556786	0.349197076	0.314624955
4	0.634273879	0.559816867	0.500000000	0.450371221	0.408554591
5	0.788094387	0.684503307	0.609443214	0.549628779	0.500000000
6	1.000000000	0.826744521	0.725169644	0.650802924	0.591445409
7		1.000000000	0.854317800	0.757849362	0.685375045
8			1.000000000	0.874369664	0.784186394
9				1.000000000	0.889468130
10					1.000000000

Table C.20: Values $a_k = \frac{z_k}{\pi}$, where z_k are zeros of Mathieu functions $\mathrm{se}_m(z, q)$ with $K_{max} = 200$, $q = 10$ in $[0, \pi]$.

Appendix D

Exponential decay of Laplacian eigenfunctions in domains with branches

D1   Estimate for rectangular branch

From the inequality $\sinh x \leq \cosh x$, Eq. (4.4) is bounded as

$$||\nabla u||^2_{L^2(Q(x_0))} \leq \frac{b}{2} \sum_{n=1}^{\infty} c_n^2 \left[(\frac{\pi}{b}n)^2 + \tilde{\gamma}_n^2 \right] \int_{x_0}^{a} \cosh^2(\tilde{\gamma}_n(a-x))dx.$$

The last integral is estimated as

$$\int_{x_0}^{a} \cosh^2(\tilde{\gamma}_n(a-x))dx \leq \int_{x_0}^{a} e^{2\tilde{\gamma}_n(a-x)}dx =$$

$$\frac{e^{2\tilde{\gamma}_n a}}{2\tilde{\gamma}_n}\left(e^{-2\tilde{\gamma}_n x_0} - e^{-2\tilde{\gamma}_n a} \right) \leq \frac{e^{2\tilde{\gamma}_n a}}{2\tilde{\gamma}_n} e^{-2\tilde{\gamma}_n x_0} \leq \frac{e^{2\tilde{\gamma}_n a}}{2\tilde{\gamma}_n} e^{-2\tilde{\gamma}_1 x_0},$$

where we used the inequality $\cosh x \leq e^x$ for $x \geq 0$ and the fact that $\tilde{\gamma}_n = \sqrt{\pi^2 n^2/b^2 - \lambda}$ increases with n. We have then

$$||\nabla u||^2_{L^2(Q(x_0))} \leq \frac{b}{2} e^{-2\tilde{\gamma}_1 x_0} \sum_{n=1}^{\infty} c_n^2 \left[\frac{\pi^2}{b^2} \frac{n^2}{2\tilde{\gamma}_n} + \frac{\tilde{\gamma}_n}{2} \right] e^{2\tilde{\gamma}_n a}.$$

Writing two inequalities:

$$\tilde{\gamma}_n = \sqrt{\pi^2 n^2/b^2 - \lambda} \leq \frac{\pi}{b}n,$$

$$\frac{n^2}{\tilde{\gamma}_n} = \frac{n}{(\pi/b)\sqrt{1 - \lambda b^2/(\pi^2 n^2)}} \leq C_1 n,$$

187

where C_1 is a constant, one gets an upper bound in the order of n for the expression in large brackets. Finally, we have an estimate for $e^{2\tilde{\gamma}_n a}$ as

$$\sinh^2(2\tilde{\gamma}_n a) = \frac{e^{2\tilde{\gamma}_n a}}{4}(1 - e^{-2\tilde{\gamma}_n a})^2 \geq \frac{e^{2\tilde{\gamma}_n a}}{4}(1 - e^{-2\tilde{\gamma}_1 a})^2,$$

from which

$$e^{2\tilde{\gamma}_n a} \leq C_2 \sinh^2(2\tilde{\gamma}_n a),$$

with a constant $C_2 = 4/(1 - e^{-2\tilde{\gamma}_1 a})^2$. Bringing together these inequalities, we get the estimate (4.5).

Trace theorem

The trace theorem implies [147] that the series

$$f(x) \equiv \sum_{n=1}^{\infty} n\big(u(x,y), \sin(\pi n y/b)\big)^2_{L^2(0,b)},$$

which is equivalent to the squared norm of $u(x,y)$ in the Sobolev space $H^{1/2}_{(0,b)}$, may be estimated from above by the norm $||\nabla u||^2_{L^2(D)}$. For completeness, we provide the proof for our special case.

For a fixed x, we denote

$$X_n(x) \equiv \big(u(x,y), \sin(\pi n y/b)\big)_{L^2(0,b)}$$

the Fourier coefficients of the function $u(x,y)$:

$$u(x,y) = \frac{2}{b}\sum_{n=1}^{\infty} X_n(x)\sin(\pi n y/b).$$

On one hand, starting from $X_n(a) = 0$, one gets

$$X_n^2(x) = \left|\int_x^a (X_n^2)' dx_1\right| = 2\left|\int_x^a X_n X_n' dx_1\right|,$$

while the Cauchy inequality implies

$$2\left|\int_x^a X_n X_n' dx_1\right| \leq 2||X_n||_{L^2(0,a)}||X_n'||_{L^2(0,a)}.$$

The inequality $2\alpha\beta \leq \alpha^2 + \beta^2$ yields

$$2(\pi n/b)||X_n||_{L^2(0,a)}||X_n'||_{L^2(0,a)} \leq ||X_n'||^2_{L^2(0,a)} + (\pi n/b)^2||X_n||^2_{L^2(0,a)},$$

from which

$$(\pi n/b)X_n^2(x) \leq ||X_n'||^2_{L^2(0,a)} + (\pi n/b)^2||X_n||^2_{L^2(0,a)}.$$

On the other hand, we write explicitly the energetic norm of u:

$$||\nabla u||^2_{L^2(Q)} = \frac{2}{b} \sum_{n=1}^{\infty} \left(||X'_n||^2_{L^2(0,a)} + (\pi n/b)^2 ||X_n||^2_{L^2(0,a)} \right),$$

from which

$$f(x) = \sum_{n=1}^{\infty} n X_n^2(x) \leq \frac{b^2}{2\pi} ||\nabla u||^2_{L^2(Q)} \leq \frac{b^2}{2\pi} ||\nabla u||^2_{L^2(D)}.$$

Since the coefficients $X_n(x)$ and c_n are related as

$$X_n(x) = \frac{b}{2} c_n \sinh(\tilde{\gamma}_n(a - x)),$$

the substitution of $x = 0$ into this equation yields

$$\sum_{n=1}^{\infty} n c_n^2 \sinh^2(\tilde{\gamma}_n a) = \frac{4}{b^2} \sum_{n=1}^{\infty} n X_n(0)^2 = \frac{4}{b^2} f(0) \leq \frac{2\lambda}{\pi} ||u||^2_{L^2(D)} = \frac{2\lambda}{\pi} ||u||^2_{L^2(D)}. \tag{D.1}$$

For completeness, in what follows, we recall the derivation of several classical results [90, 147] which are well known for spectral analysts but may be unfamiliar for other readers.

D2   Rayleigh's principle

Let us start with the first eigenvalue λ_1 of the problem (4.1) which can be found as

$$\lambda_1 = \inf_{v \in \overset{\circ}{H}^1} \frac{(\nabla v, \nabla v)_{L^2(D)}}{(v, v)_{L^2(D)}}, \tag{D.2}$$

where $\overset{\circ}{H}^1 = \{v \in L^2(D),\ \partial v/\partial x_i \in L^2(D),\ i = 1, ..., n+1,\ v|_{\partial D} = 0\}$. Denoting ϕ_1 the first eigenfunction in Eq. (4.28), one takes

$$v = \begin{cases} \phi_1, & (x, \mathbf{y}) \in V, \\ 0, & (x, \mathbf{y}) \notin V, \end{cases}$$

as a trial function in Eq. (D.2) to obtain

$$\lambda_1 < \frac{(\nabla \phi_1, \nabla \phi_1)_{L^2(V)}}{(\phi_1, \phi_1)_{L^2(V)}} = \kappa_1,$$

i.e., the first eigenvalue λ_1 in the whole domain D is always smaller than the first eigenvalue κ_1 in its subdomain V. More generally, if there are n eigenvalues $\kappa_1 \leq \cdots \leq \kappa_n \leq \mu$ then there exist n eigenvalues $\lambda_1 \leq \cdots \leq \lambda_n < \mu$.

Note that the Friedrichs-Poincaré inequality (4.20) follows from (D.2).

D3   Rellich's identity

Let u be an eigenfunction which satisfies the equation

$$\Delta u + \lambda u = 0 \quad (x, \mathbf{y}) \in D, \quad u|_{\partial D} = 0.$$

We multiply this equation by $\frac{\partial u}{\partial x}$ and integrate over the domain $Q(x_0)$ defined by Eq. (4.23):

$$\int\limits_{Q(x_0)} \frac{\partial u}{dx} \Delta u \; dxd\mathbf{y} + \lambda \int\limits_{Q(x_0)} u \frac{\partial u}{dx} \; dxd\mathbf{y} = 0. \tag{D.3}$$

The second integral can be transformed as

$$\lambda \int\limits_{Q(x_0)} u \frac{\partial u}{dx} \; dxd\mathbf{y} = \frac{\lambda}{2} \int\limits_{Q(x_0)} \left(\frac{\partial}{\partial x} u^2 \right) dxd\mathbf{y} = -\frac{\lambda}{2} \int\limits_{\partial Q(x_0)} u^2(x_0, \mathbf{y})(\mathbf{e}_x, \mathbf{n}) dS = -\frac{\lambda}{2} \int\limits_{\Omega(x_0)} u^2(x_0, \mathbf{y}) d\mathbf{y}, \tag{D.4}$$

where $\mathbf{n} = \mathbf{n}(S)$ is the unit normal vector at $S \in \partial Q(x_0)$ and the boundary condition $u_{\partial D} = 0$ was used on $\Gamma(x_0) = \partial Q(x_0) \backslash \Omega(x_0)$.

Using the Green's formula, the first integral in Eq. (D.3) can be transformed to

$$\int\limits_{Q(x_0)} \frac{\partial u}{\partial x} \Delta u dxd\mathbf{y} = \int\limits_{\partial Q(x_0)} \frac{\partial u}{\partial x} \frac{\partial u}{\partial n} dS - \int\limits_{Q(x_0)} \left(\nabla u, \nabla \frac{\partial u}{\partial x} \right) dxd\mathbf{y}. \tag{D.5}$$

The first integral over $\partial Q(x_0)$ can be split in two terms:

$$\int\limits_{\partial Q(x_0)} \frac{\partial u}{\partial x} \frac{\partial u}{\partial n} dS = \int\limits_{\Gamma(x_0)} \frac{\partial u}{\partial x} \frac{\partial u}{\partial n} dS - \int\limits_{\Omega(x_0)} \left(\frac{\partial u}{\partial x} \right)^2 d\mathbf{y},$$

where $\partial/\partial n = (\mathbf{n}, \nabla)$ is the normal derivative pointing outwards the domain, and the sign minus appears because $\partial u/\partial n = -\partial u/\partial x$ at $\Omega(x_0)$.

The second integral in Eq. (D.5) is

$$\int\limits_{Q(x_0)} \left(\nabla u, \nabla \frac{\partial u}{\partial x} \right) dxd\mathbf{y} = \frac{1}{2} \int\limits_{Q(x_0)} \frac{\partial}{\partial x} (\nabla u, \nabla u) dxd\mathbf{y} = \frac{1}{2} \int\limits_{\Gamma(x_0)} (\nabla u, \nabla u)(\mathbf{e}_x, \mathbf{n}) dS + \frac{1}{2} \int\limits_{\Omega(x_0)} (\nabla u, \nabla u) d\mathbf{y}.$$

Taking into account the Dirichlet boundary condition $u|_{\Gamma(x_0)} = 0$, one has

$$(\nabla u)|_{\Gamma(x_0)} = \mathbf{n} \frac{\partial u}{\partial n} |_{\Gamma(x_0)},$$

$$\frac{\partial u}{\partial x} |_{\Gamma(x_0)} = (\mathbf{e}_x, \nabla u) = (\mathbf{e}_x, \mathbf{n}) \frac{\partial u}{\partial n} |_{\Gamma(x_0)}.$$

Combining these relations, one gets

$$\int\limits_{Q(x_0)} \frac{\partial u}{\partial x} \Delta u \; dxd\mathbf{y} = \frac{1}{2} \int\limits_{\Gamma(x_0)} \left(\frac{\partial u}{\partial n}\right)^2 (\mathbf{e}_x, \mathbf{n}) dS - \frac{1}{2} \int\limits_{\Omega(x_0)} \left(\frac{\partial u}{\partial x}\right)^2 d\mathbf{y} + \frac{1}{2} \int\limits_{\Omega(x_0)} (\nabla_\perp u, \nabla_\perp u) d\mathbf{y},$$

from which and Eqs. (D.3, D.4) the Rellich's identity (4.22) follows.

Appendix E

Trapped modes in finite waveguides

E1   Computation for bent strip

The computation of the coefficients β and σ_i is straightforward, while that for κ_i requires supplementary estimates.

Coefficient β. One has

$$(v_\alpha, v_\alpha)_{L^2(\Omega)} = \frac{\pi}{2} \int_0^1 r^{1-2\alpha} \sin^2(\pi r) dr = \frac{\pi}{4}\left[\frac{1}{2(1-\alpha)} - w_{2\alpha-1}(2\pi)\right],$$

where

$$w_\nu(q) \equiv \int_0^1 r^{-\nu} \cos(qr) dr.$$

Similarly,

$$(\nabla v_\alpha, \nabla v_\alpha)_{L^2(\Omega)} = \frac{\pi}{2} \int_0^1 r(v'_\alpha)^2 dr = \frac{\pi}{2} \int_0^1 r\left(\frac{\pi \cos \pi r}{r^\alpha} - \frac{\alpha \sin \pi r}{r^{1+\alpha}}\right)^2 dr.$$

Expanding the quadratic polynomial and integrating by parts, one gets

$$(\nabla v_\alpha, \nabla v_\alpha)_{L^2(\Omega)} = \frac{\pi^3}{4}\left[\frac{1}{2(1-\alpha)} + \frac{w_{2\alpha-1}(2\pi)}{1-2\alpha}\right].$$

Combining this term with the previous result yields

$$\beta = \frac{\pi^3}{4}\frac{2\alpha}{2\alpha-1}w_{2\alpha-1}(2\pi). \tag{E.1}$$

In the limit $\alpha \to 1/2$, one has

$$\lim_{\alpha \to 1/2} \frac{w_{2\alpha-1}(2\pi)}{2\alpha-1} = \frac{\text{Si}(2\pi)}{2\pi} \approx 0.2257,$$

where $\mathrm{Si}(x)$ is the integral sine function.

Coefficients σ_i. For these coefficients, one gets

$$(v_\alpha, \sin(\pi r))_{L^2(\Gamma_i)} = \int_0^1 r^{-\alpha} \sin^2(\pi r) dr = \frac{1}{2}\left(\frac{1}{1-\alpha} - w_\alpha(2\pi)\right),$$

from which

$$\sigma_1 = \sigma_2 = \frac{1}{2}\left(\frac{1}{1-\alpha} - w_\alpha(2\pi)\right)^2. \tag{E.2}$$

Coefficients κ_i. One considers

$$(v_\alpha, \sin(\pi n r))_{L^2(\Gamma_i)} = \int_0^1 r^{-\alpha} \sin(\pi r) \sin(\pi n r) dr = \frac{1}{2}\Big[w_\alpha(\pi(n-1)) - w_\alpha(\pi(n+1))\Big].$$

The function $w_\alpha(q)$ can be decomposed into two parts [93],

$$w_\alpha(q) = \int_0^\infty r^{-\alpha} \cos(qr) dr - \int_1^\infty r^{-\alpha} \cos(qr) dr = q^{\alpha-1}\frac{\sqrt{\pi}\,\Gamma(\frac{1-\alpha}{2})}{2^\alpha\Gamma(\frac{\alpha}{2})} - \tilde{w}_\alpha(q),$$

where

$$\tilde{w}_\alpha(q) \equiv \int_1^\infty r^{-\alpha} \cos(qr) dr.$$

We have

$$\kappa_i = 2\pi \sum_{n=2}^\infty \sqrt{n^2 - 1}\,(v, \sin(\pi n r))_{L^2(\Gamma_i)}^2 = 2\pi \sum_{n=2}^\infty \sqrt{n^2 - 1}\,(d_n - e_n)^2,$$

where

$$d_n = \frac{\pi^{\alpha-\frac{1}{2}}\,\Gamma(\frac{1-\alpha}{2})}{2^{1+\alpha}\Gamma(\frac{\alpha}{2})}\Big[(n-1)^{\alpha-1} - (n+1)^{\alpha-1}\Big],$$

$$e_n = \frac{1}{2}\Big[\tilde{w}_\alpha(\pi(n-1)) - \tilde{w}_\alpha(\pi(n+1))\Big].$$

In order to estimate the coefficients e_n, the function $\tilde{w}_\alpha(q)$ is integrated by parts that yields for $q = \pi(n\pm1)$:

$$\tilde{w}_\alpha(q) = \alpha\frac{\cos q}{q^2} - \alpha(\alpha+1)\frac{\tilde{w}_{\alpha+2}(q)}{q^2} = \alpha\frac{\cos q}{q^2}$$

$$- \alpha(\alpha+1)(\alpha+2)\frac{\cos q}{q^4} + \alpha(\alpha+1)(\alpha+2)(\alpha+3)\frac{\tilde{w}_{\alpha+4}(q)}{q^4}.$$

The inequality

$$(\alpha+3)|\tilde{w}_{\alpha+4}(q)| \le (\alpha+3)\int_1^\infty r^{-\alpha-4} dr = 1$$

leads to

$$\alpha\frac{\cos q}{q^2} - \alpha(\alpha+1)(\alpha+2)\frac{\cos q + 1}{q^4} \leq \tilde{w}_\alpha(q) \leq \alpha\frac{\cos q}{q^2} - \alpha(\alpha+1)(\alpha+2)\frac{\cos q - 1}{q^4},$$

from which

$$e_n^- \leq e_n \leq e_n^+,$$

where lower and upper bounds are

$$
\begin{aligned}
e_n^\pm = \frac{1}{2}\Bigg[&\left(\frac{\alpha}{\pi^2}\frac{(-1)^{n-1}}{(n-1)^2} - \frac{\alpha(\alpha+1)(\alpha+2)}{\pi^4}\frac{(-1)^{n-1}\mp 1}{(n-1)^4}\right) \\
&-\left(\frac{\alpha}{\pi^2}\frac{(-1)^{n+1}}{(n+1)^2} - \frac{\alpha(\alpha+1)(\alpha+2)}{\pi^4}\frac{(-1)^{n+1}\pm 1}{(n+1)^4}\right)\Bigg].
\end{aligned}
$$

Using these estimates, one gets

$$
\begin{aligned}
\sum_{n=2}^{\infty}\sqrt{n^2-1}\,d_n^2 &\equiv A_1, \\
\sum_{n=2}^{\infty}\sqrt{n^2-1}\,d_n e_n &\geq \sum_{n=2}^{\infty}\sqrt{n^2-1}\,d_n e_n^- \equiv A_2^-, \\
\sum_{n=2}^{\infty}\sqrt{n^2-1}\,e_n^2 &\leq \sum_{n=2}^{\infty}\sqrt{n^2-1}\,(e_n^+)^2 \equiv A_3^+,
\end{aligned}
$$

from which

$$\kappa_i \leq \kappa, \qquad \kappa \equiv 2\pi(A_1 - 2A_2^- + A_3^+). \tag{E.3}$$

Although the expressions for A_1, A_2^- and A_3^+ are cumbersome, the convergence of these series can be easily checked, while their numerical evaluation is straightforward.

The numerical computation of these coefficients shows that the threshold value η is maximized at $\alpha \approx 1/3$: $\eta \approx 0.7154$. Note that if the coefficients κ_i were computed by direct numerical integration and summation, the value of η for $\alpha = 1/3$ could be slightly improved to be 0.7256. The difference results from the estimates we used, and its smallness indicates that the estimates are quite accurate.

Appendix F

Several computations for survival probabilities in porous media

F1 Equidistributed arcs and sectors

When a reactive region A lies on the boundary of the unit disk, finding the elements of the matrix $\mathcal{B}$ is reduced to computation of integrals over the angular coordinate φ that can be performed analytically. For instance, if the reactive region is composed of M identical arcs of angle β which are equidistributed over the circle (Sect. 7.4.1), the truncated matrix $\mathcal{B}$ of size $N \times N$ takes a simple form for $M > 2N + 1$

$$\mathcal{B}_{nkl,n'k'l'} = \left[2\delta_{n,n'}\delta_{l,l'}(1 - \delta_{l,1}\delta_{l',1}\delta_{n,0}\delta_{n',0})\beta_{nk}\beta_{n'k'} \right] \frac{M\beta}{2\pi} \tag{F.1}$$

(when $M \leq 2N + 1$, a more complicated explicit formula can also be derived). When M increases in such a way that the total length $L = M\beta$ of the arcs is kept constant, the truncated matrix $\mathcal{B}$ is

$$\mathcal{B} = \frac{L}{2\pi} \, \mathcal{B}^{(\partial\Omega)},$$

where $\mathcal{B}^{(\partial\Omega)}$ denotes the matrix in the large brackets of Eq. (F.1) and corresponds to the matrix $\mathcal{B}$ for the reactive region $A = \partial\Omega$ (the whole boundary of the unit disk). As a consequence, the survival probability for a large number M of arcs (partly reactive boundary) turns out to approach the survival probability for the whole circle (fully reactive boundary) when $h = \infty$.

Similarly, when A is the union of M identical angular sectors of angle β which are equidistributed in the unit disk (Fig. 7.4b), the truncated matrix $\mathcal{B}$ gets a simple form

$$\mathcal{B} = \frac{S_A}{\pi} I,$$

where the identity matrix I is the matrix $\mathcal{B}$ for the unit disk.

F2   Analytical results for reactive disks

We consider the survival probability for infinitely reactive region ($h = \infty$) in the shape of a disk of radius r_0 centered at the origin (Fig. 7.4a). This problem is equivalent to diffusion in a circular layer $\Omega_1 = \{\mathbf{r} \in \mathbb{R}^2 : r_0 < |r| < 1\}$ with the absorbing inner circle of radius r_0 and the reflecting outer circle of radius 1. The smallest eigenvalue α^2 of the Laplace operator in this layer is determined by the first positive root α of the following equation [38, 55, 100]

$$J_0(\alpha r_0)Y_0'(\alpha) - Y_0(\alpha r_0)J_0'(\alpha) = 0, \tag{F.2}$$

where $J_0(z)$ and $Y_0(z)$ are the Bessel functions of the first and second kind, respectively. Solving numerically this equation, one can find the theoretical value $\gamma_0^\infty = \alpha^2$ for any r_0 between 0 and 1. In the limit of r_0 going to 1, the following asymptotic behavior can be derived

$$\gamma_0^\infty \approx \frac{\pi^2}{4(1 - r_0)^2} \quad (r_0 \to 1). \tag{F.3}$$

In the opposite limit of r_0 going to 0, the asymptotic behavior of Bessel functions allows one to reduce Eq. (F.2) to

$$\gamma_0^\infty \approx \frac{2}{\ln(a/r_0)} + \frac{\ln(\ln(a/r_0)/2)}{(\ln(a/r_0))^2} \quad (r_0 \to 0), \tag{F.4}$$

where $a = 2e^{-\gamma}$ and $\gamma = 0.5772157...$ is the Euler-Mascheroni constant. Although γ_0^∞ approaches 0 as $r_0 \to 0$, the decay is logarithmically slow so that even very small reactive regions may yield significant reaction rates, as shown on Fig. 7.7. Note that the logarithmically slow decay is the specific feature of the two-dimensional case.

It is worth noting that the limits $r_0 \to 1$ and $h \to \infty$ cannot be exchanged. In fact, for numerical computations, one always uses a large but finite value of h (e.g., $h = 10^8$). In this case, the asymptotic behavior of γ_0^h as $r_0 \to 1$ is different from Eq. (F.3). Denoting $\varepsilon = 1 - r_0$, we have

$$\mathcal{B} = \mathcal{B}^{(\Omega)} - \mathcal{B}^{(\Omega_1)} \approx I - \varepsilon\mathcal{B}^{(\partial\Omega)},$$

where $\mathcal{B}^{(\partial\Omega)}$ corresponds to $B(\mathbf{r}) = \mathbb{I}_{\partial\Omega}(\mathbf{r})$. The matrix $\Lambda + h\mathcal{B}$ can then be approximated as

$$\Lambda + h\mathcal{B} \approx (\Lambda + hI) - h\varepsilon\mathcal{B}^{(\partial\Omega)}.$$

For a finite h, the last term appears as a correction to the first one so that

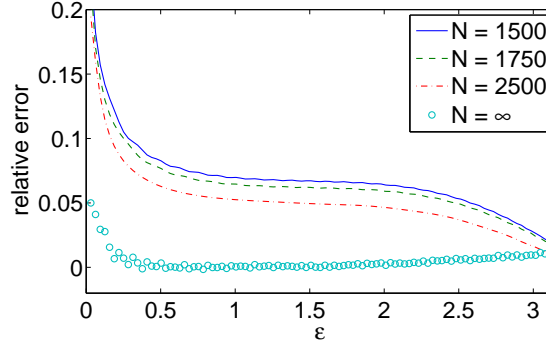$$\gamma_0^h \approx h(1 - O(\varepsilon)) \quad (\varepsilon \to 0).$$

Figure F.1: The relative error between the exact formula (F.5) and the truncated spectral representation (F.6) for the mean exit time from the unit disk whose boundary is reflecting but for an absorbing arc of length 2ε.

F3 Narrow escape problem

Singer and co-workers dealt with the exit problem from the unit disk with reflecting boundary, except for an absorbing arc of length 2ε [202, 203]. For Brownian motion $\mathbf{x}(t)$ started from the origin, the mean exit time is found to be

$$\mathbb{E}\left[\tau|\mathbf{x}(0)=(0,0)\right] = \frac{\sqrt{2}}{2\pi}\int\limits_{0}^{\pi-\varepsilon}\frac{u\sin\frac{u}{2}}{\sqrt{\cos u+\cos\varepsilon}}\,du+\frac{1}{4}. \tag{F.5}$$

When the absorbing part shrinks to zero, this formula yields the following asymptotic behavior

$$\mathbb{E}\left[\tau|\mathbf{x}(0)=\mathbf{0}\right] = \log\frac{1}{\varepsilon}+\log 2+\frac{1}{4}+O(\varepsilon).$$

These two analytical formulas can be used for checking spectral computations.
Starting from the origin is introduced into the spectral approach through the point-like initial density $\rho(\mathbf{r}_0)=\delta(\mathbf{r}_0)$, where $\delta(\mathbf{r}_0)$ is the Dirac distribution. The vector U becomes

$$U_{nkl} = \frac{\delta_{n,0}\delta_{l,0}}{J_n(\alpha_{nk})}, \quad n=0,1,\dots, \quad k=0,1,\dots, \quad l=0,1.$$

Since the weighting function $\tilde{\rho}(\mathbf{r})$ remains constant, the vector $\tilde{U}$ does not change:

$$\tilde{U}_{nkl} = \delta_{n,0}\delta_{k,0}\delta_{l,0}, \quad n=0,1,\dots, \quad k=0,1,\dots, \quad l=0,1.$$

Using Eq. (7.6), the mean exit time from the unit disk can be computed as

$$\mathbb{E}\left[\tau|\mathbf{x}(0)=(0,0)\right] = \sum_{m=0}^{\infty}\frac{A_m^{\infty}}{\gamma_m^{\infty}}. \tag{F.6}$$
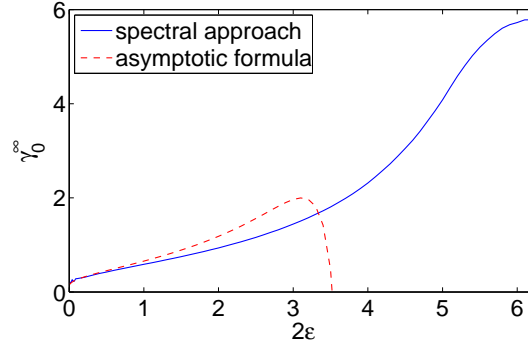
Figure F.2: The smallest eigenvalue γ_0^∞ for the unit disk when the reactive region is an arc of length 2ε (with $h = 10^8$). When 2ε goes to 2π (the whole circle), γ_0^∞ approaches the theoretical value 5.7829..., as expected. The asymptotic formula (F.7) is accurate for small ε but inapplicable for large ε.

Fig. F.1 helps to compare Eqs. (F.5, F.6) for the mean exit time as a function of ε. As we discussed in Sect. 7.3.3, the accuracy of the spectral approach decreases when ε is getting smaller. Since the spectral computation of the mean exit time includes both the truncation of the matrix $\Lambda + h\mathcal{B}$ and the truncation of the series in Eq. (F.6), the results are not as good as for the smallest eigenvalue γ_0^h. Nevertheless, an extrapolation helps to get reasonably accurate results even for small ε (up to 0.01).

A more direct comparison can be realized for the smallest eigenvalue γ_0^∞ whose asymptotic behavior was derived by Ward and co-workers [172]. For a single arc of length 2ε, their asymptotic formula reads as

$$\gamma_0^\infty \approx -\frac{1}{\ln(\varepsilon/2)} - \frac{1}{8[\ln(\varepsilon/2)]^2} + O([\ln(\varepsilon/2)]^{-3}). \tag{F.7}$$

Since the expansion parameter here is $\ln(\varepsilon/2)$ (and not ε itself), this formula is only applicable for small ε. On Fig. F.2, we compare the asymptotic result (F.7) to the γ_0^∞ computed by the spectral approach. As expected, two curves are close to each other for small ε. It is worth stressing again that, for smaller ε, the spectral computation requires larger matrices and takes longer time, while the asymptotic formula is getting more accurate. On the contrary, when 2ε exceeds 1, the asymptotic formula becomes less and less accurate, and it finally diverges at $\varepsilon = 2$.

In summary, when the reactive regions are very small, perturbative techniques are preferred [43, 44, 130, 172, 202, 203, 221]. In turn, the spectral approach is more appropriate for extended reactive regions, for which perturbative techniques become useless. These two approaches are complementary to each other.

F4 Optimal reactive region

Numerical evidences (Figs. 7.7, 7.9) suggest that a uniform filling of a confining domain provides the highest overall reaction rate γ_0^h under the condition that the total amount of reactive grains is fixed. We propose a theoretical argument in favor of this statement, although a rigorous proof is still missing. This argument relies on a perturbation theory applied to the matrix $\Lambda + h\mathcal{B}$. In the limit of small h, the

smallest eigenvalue γ_0^h can be written as a perturbation series in powers of h. Keeping the terms up to the second order in h, we get

$$\gamma_0^h \approx \lambda_0 + h\mathcal{B}_{0,0} - h^2 \sum_{m>0} \frac{\mathcal{B}_{0,m}\mathcal{B}_{m,0}}{\lambda_m - \lambda_0} = \frac{h}{S} \int_\Omega d\mathbf{r} \; B(\mathbf{r}) - h^2 \sum_{m>0} \frac{\mathcal{B}_{0,m}^2}{\lambda_m}$$

(since $\lambda_0 = 0$). The first term is the total amount of reactive grains (which may have spatially heterogeneous reactivities incorporated via $B(\mathbf{r})$). In our numerical examples, when $B(\mathbf{r}) = \mathbb{I}_A(\mathbf{r})$, the first term was simply hS_A/S. Since this term is supposed to be fixed, the influence of $B(\mathbf{r})$ on γ_0^h is represented through the second term. For a uniform filling with $A = \Omega$, $\mathcal{B}_{m,m'} = \delta_{m,m'}$ so that the second term is zero. Since $\lambda_m > 0$, the uniform filling is indeed optimal for getting the highest γ_0^h:

$$\gamma_0^h \leq \gamma_{0,\text{uni}}^h = h.$$

Further analysis is required for a rigorous proof of this result.

Appendix G

Localization in dumbbell domains

In previous chapters, we have discussed localized eigenmodes of the Laplace operator with Dirichlet boundary conditionc. In domains with branches, under certain conditions, the L^2-norm of Laplacian eigenfunctions decays exponentially along the branches that leads to the emergence of localized eigenfunctions. In this appendix, we continue discussing other kinds of low-frequency localization.

G1   Localization in dumbbell domains

One kind of localization happens in bounded domains which can be split into two or several sub-domains with narrow connections of width ε. A basic example is a dumbbell domain $\Omega_\varepsilon = \Omega_1 \cup Q_\varepsilon \cup \Omega_2$ (Fig. G.1). The asymptotic behavior of Laplacian eigenvalues and eigenfunctions was thoroughly investigated for both Dirichlet and Neumann boundary conditions. We start by considering Dirichlet boundary condition.

Dirichlet boundary condition

We assume that when ε tends to zero, the limiting domain Ω_0 can be split into N subdomains Ω_1, Ω_2, ..., Ω_N. In this case, the eigenproblem with Dirichlet boundary condition in the whole domain can be separately formulated for each subdomain. Let Λ_i be the set of all Dirichlet-Laplacian eigenvalues in the subdomain Ω_i. Each Dirichlet-Laplacian eigenvalue λ_ε of the domain Ω_ε approaches an eigenvalue λ_0 of one limiting subdomain Ω_i for certain i. Moreover, if

$$\Lambda_i \cap \Lambda_j = \emptyset \quad \forall \, i \neq j, \tag{G.1}$$

the space of eigenfunctions in the limiting (disconnected) domain Ω_0 is the direct product of spaces of eigenfunctions for each subdomain Ω_i (see [57] for discussion on the convergence and related issues). This is a basis for what we call "bottle-neck localization".

In fact, when ε tends to zero, each Dirichlet eigenfunction u_m^ε of the domain Ω_ε approaches an eigenfunction of the limiting domain Ω_0 which is fully localized in one subdomain Ω_i and zero in the others. Therefore, for a small ε, the eigenfunction u_m^ε is mainly localized in the corresponding i^{th} subdomain Ω_i, and is almost zero in the other subdomains. In other words, for any positive integer m, one can take the
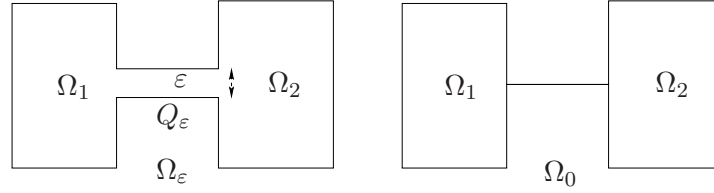
Figure G.1:   A dumbbell domain $\Omega_\varepsilon = \Omega_1 \cup Q_\varepsilon \cup \Omega_2$ with a narrow connection Q_ε of width ε. When $\varepsilon \to 0$, the limiting domain Ω_0 can be separated into two subdomains Ω_1 and Ω_2.

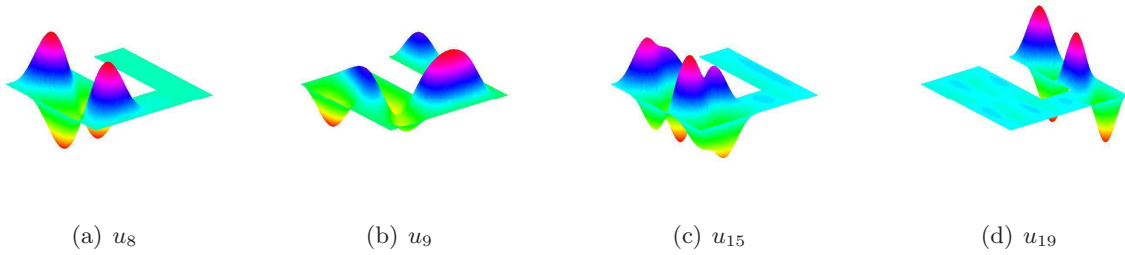(a) u_8 (b) u_9 (c) u_{15} (d) u_{19}

Figure G.2: Bottle-neck localization of Dirichlet eigenfunctions in a domain $\Omega_\varepsilon = \Omega_1 \cup Q_\varepsilon \cup \Omega_2$ (Fig. G.1), where $\varepsilon = 0.3$, Ω_1 is the unit square and Ω_2 is a rectangle of two sides $a = 1$ and $b = 0.5$. The 8th and 15th eigenfunctions are localized in Ω_1, while the 19th eigenfunction is localized in Ω_2. The 9th eigenfunction is not localized.

width ε small enough to ensure that the L^2-norm of the eigenfunction u_m^ε in one of Ω_i is close to that in the whole domain Ω_ε:

$$\forall m, \exists i \in \{1, ..., N\} \quad \forall\, \delta \in (0, 1) \quad \exists\, \varepsilon > 0 \; : \; \|u_m^\varepsilon\|_{L^2(\Omega_i)} > (1 - \delta)\|u_m^\varepsilon\|_{L^2(\Omega^\varepsilon)}. \tag{G.2}$$

Fig. G.2 illustrates this behavior for a domain Ω_ε which is decomposed into two rectangles Ω_1 and Ω_2 connected by a narrow connection Q_ε. One can find several eigenmodes (u_8, u_{15}, u_{19}, etc) localized in each subdomain Ω_i, while most of eigenfunctions are not localized, such as e.g the eigenfunction u_9. Most importantly, in this numerical example, the width $\varepsilon = 0.3$ is not too small. While the small ε asymptotic behavior of eigenfunctions was thoroughly investigated [8, 9, 18, 110, 119, 120], localization for moderate values of ε remains poorly understood.

It is important to emphasize that for fixed values of the width ε and the threshold δ, there may be infinitely many high-frequency *non-localized* eigenfunctions which do not satisfy the inequality (G.2). For a given domain Ω_ε, there may exist only a finite number of low-frequency localized eigenfuntions.

The condition (G.1) makes sure that the limiting eigenfunctions are fully localized in their respective subdomains. When this condition is not satisfied, there may exist degenerate eigenvalues in the limiting domain Ω, and a limiting eigenfunction would be a linear combination of eigenfunctions in different subdomains with the same eigenvalue. That would destroy the low-frequency localization.

Neumann boundary condition

For Neumann boundary condition, the situation is more complicated, as the eigenvalues and eigenfunctions may also approach the eigenvalues and eigenfunctions of the limiting connector (in the simplest case, the interval). Arrieta considered a planar dumbell domain Ω_ε consisting of two disjoint domains Ω_1 and Ω_2 joint by a channel Q_ε of variable profile $g(x)$: $Q_\varepsilon = \{\mathbf{r} \in \mathbb{R}^2 \ : \ 0 < x_1 < 1, \ 0 < x_2 < \varepsilon g(x_1)\}$, where $g \in C^1(0,1)$ and $g(x_1) \geq 0$ for all $x_1 \in [0,1]$. In the limit $\varepsilon \to 0$, each eigenvalue of the Laplace operator in Ω_ε with Neumann boundary condition was shown to converge either to an eigenvalue μ_k of the Neumann-Laplace operator in $\Omega_1 \cup \Omega_2$, or to an eigenvalue ν_k of the Sturm-Liouville operator $-\frac{1}{g}(g u_x)_x$ acting on a function u on $(0,1)$, with Dirichlet boundary condition [8, 9]. The first-order term in the small ε-asymptotic expansion was obtained. The special case of cylindrical channels (of constant profile) in higher dimensions was studied by Jimbo [119] (see also results by Hempel *et al.* [110]). Jimbo and Morita studied an N-dumbell domain, i.e. a family of N pairwise disjoint domains joint by thin channels [120]. They proved that $\lambda_m^\varepsilon = C_m \varepsilon^{d-1} + o(\varepsilon^{d-1})$ as $\varepsilon \to 0$ for $m = 1, 2, \ldots, N$, while $\lambda_{N+1}^\varepsilon$ is uniformly bounded away from zero, where d is the dimension of the embedding space, and C_m are shape-dependent constants. Jimbo also analyzed the asymptotic behavior of the eigenvalues λ_m^ε with $m > N$ under the condition that the sets $\{\mu_k\}$ and $\{\nu_k\}$ do not intersect [121]. In particular, for an eigenvalue λ_m^ε that converges to an element of $\{\mu_k\}$, the asymptotic behavior is $\lambda_m^\varepsilon = \mu_k + C_m \varepsilon^{d-1} + o(\varepsilon^{d-1})$.
Brown and co-workers studied upper bounds for $|\lambda_m^\varepsilon - \lambda_m^0|$ and showed [29]:
(i) If $\lambda_m^0 \in \{\mu_k\} \setminus \{\nu_k\}$,

$$
\begin{aligned}
|\lambda_m^\varepsilon - \lambda_m^0| &\leq C|\ln \varepsilon|^{-1/2} &&(d=2), \\
|\lambda_m^\varepsilon - \lambda_m^0| &\leq C\varepsilon^{(d-2)/d} &&(d \geq 3).
\end{aligned}
$$

(ii) If $\lambda_m^0 \in \{\nu_k\} \setminus \{\mu_k\}$,

$$
\begin{aligned}
|\lambda_m^\varepsilon - \lambda_m^0| &\leq C\varepsilon^{1/2}|\ln \varepsilon| &&(d=2), \\
|\lambda_m^\varepsilon - \lambda_m^0| &\leq C\varepsilon^{1/2} &&(d \geq 3).
\end{aligned}
$$

For a dumbbell domain in $\mathbb{R}^d$ with a thin cylindrical channel of a smooth profile, Gadyl'shin obtained the complete small ε asymptotics of the Neumann-Laplace eigenvalues and eigenfunctions and explicit formulas for the first term of these asymptotics, including multiplicities [84–86].
More recently, Arrieta and Krejcirik considered the problem of spectral convergence from another point of view [7]. They showed that if $\Omega_0 \subset \Omega_\varepsilon$ are bounded domains and if the eigenvalues and eigenfunctions of the Laplace operator with Neumann boundary condition in Ω_ε converge to the ones in Ω_0, then necessarily $\mu_d(\Omega_\varepsilon \backslash \Omega_0) \to 0$ as $\varepsilon \to 0$, while it is not necessarily true that $\text{dist}(\Omega_\varepsilon, \Omega_0) \to 0$. As a matter of fact, they constructed an example of a perturbation where the spectra behave continuously but $\text{dist}(\Omega_\varepsilon, \Omega_0) \to \infty$ as $\varepsilon \to 0$.
For example, we consider the eigenproblem with Neumann boundary condition in a dumbbell domain Ω_ε on Fig. G.3. In this domain, we found only two localized eigenmodes u_4 and u_{41} among first 45

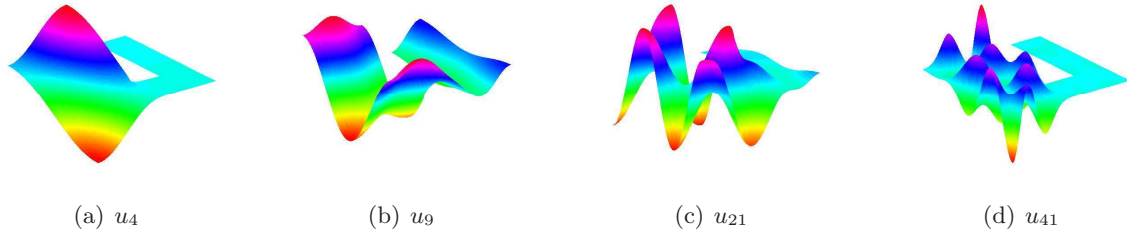(a) u_4 (b) u_9 (c) u_{21} (d) u_{41}

Figure G.3: Bottle-neck localization of Neumann eigenfunctions in a domain $\Omega_\varepsilon = \Omega_1 \cup Q_\varepsilon \cup \Omega_2$ (Fig. G.1), where $\varepsilon = 0.3$, Ω_1 is the unit square and Ω_2 is a rectangle of two sides $a = 1$ and $b = 0.5$. Among first 45 eigenfunctions, only the 4th and 41st eigenfunctions are localized (in Ω_1), while the others are not localized, such as e.g the eigenfunctions u_9 and u_{21}.

eigenfunctions. These eigenfunctions are localized in the subdomain Ω_1.

In [107], Heilman and co-workers gave several numerical examples of localized eigenfunctions of the Laplace operator with Neumann boundary condition in a "cow" domain (Fig. G.4a). They argued that one subdomain must possess an axis of symmetry for getting localized eigenfunctions. Since an anti-symmetric eigenfunction vanishes on the axis of symmetry, it is necessarily small near the bottle-neck that somehow "prevents" its extension to the other domain. Although the argument is plausible, it is worth emphasizing that such a symmetry is neither sufficient, nor necessary for localization. It is obviously not sufficient because even for symmetric domain, there exist plenty of non-localized eigenmodes (including the trivial example of the ground eigenmode which is a constant over the whole domain). In order to illustrate that the reflection symmetry is not necessary, Figs. G.4b and G.4c show several examples of localized eigenfunctions for modified domains for which the symmetry is broken [95]. Although rendering the upper subdomain less and less symmetric gradually reduces or even fully destroys localization (Fig. G.4d), its "mechanism" remains poorly understood.
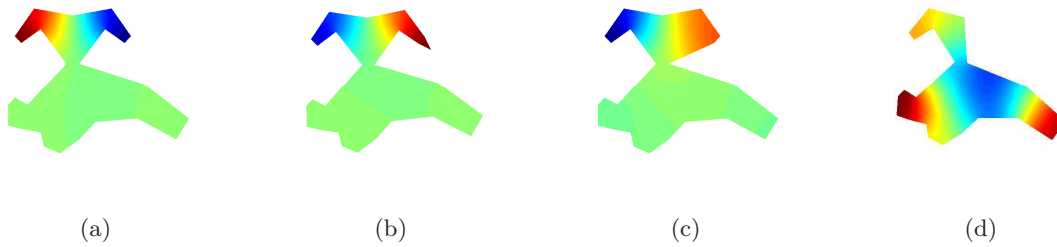

(a)   (b)   (c)   (d)

Figure G.4: Localized Neumann eigenfunction u_4 in the original "cow" domain from [107] (a) and in three modified domains (b,c,d), in which the reflection symmetry of the upper subdomain is broken. This eigenfunction is localized for the first three domains (a,b,c), while the last domain with the stronger modification shows no localization (d). Colors represent the amplitude of an eigenfunction, from the most negative value (dark blue), through zero (green), to the largest positive value (dark red).

G2 Conclusion

In this appendix, we have discussed the low-frequency localization in dumbbell domains. In this domains, the existence of low-frequency localization depends on the width ε of narrow connectors and occurs for both Dirichlet and Neumann boundary condition. For Dirichlet boundary condition, an eigenfunction may be localized in one subdomain of the limiting domain Ω_0. For Neumann boundary condition, there may exist several eigenmodes localized in the connectors. For a given dumbbell domain Ω_ε, there may be a finite number of localized Neumann (Dirichlet) eigenfunctions. Other discussions can be found in [95].

Bibliography

[1] M. Abramowitz and I. A. Stegun, *Handbook of Mathematical Functions* (Dover Publisher, New York, 1965).

[2] S. Agmon, *Lectures on Exponential Decay of Solution of Second-Order Elliptic Equation* (Princton Univercity Press, 1982).

[3] F. Albert, T. Braun, T. Heindel, C. Schneider, S. Reitzenstein, S. Höfling, L. Worschech, and A. Forchel, *Whispering gallery mode lasing in electrically driven quantum dot micropillars*, Appl. Phys. Lett. **97** (2010), 101108.

[4] G. Alessandrini, *Nodal lines of eigenfunctions of the fixed membrane problem in general convex domains*, Comment. Math. Helv. **69** (1994), 142-154.

[5] F. A. Alhargan, *A Complete Method for the Computations of Mathieu characteristic numbers of integer orders*, SIAM Rev. **38** (1996), pp. 239-255.

[6] P. W. Anderson, *Absence of Diffusion in Certain Random Lattice*, Phys. Rev. **109** (1958), 1492.

[7] J. M. Arrieta and D. Krejcirik, *Geometric versus spectral convergence for the Neumann Laplacian under exterior perturbations of the domain*, Integral methods in science and engineering. Vol. 1, 9-19, (Birkhäuser Boston, Inc., Boston, MA, 2010).

[8] J. M. Arrieta, *Rates of eigenvalues on a dumbell domain, simple eigenvalue case* Trans. Am. Math. Soc. **347** (1995), pp. 3503-3531.

[9] J. M. Arrieta, *Neumann eigenvalue problems on exterior pertubations of the domain*, J. Diff. Eq. **118** (1995), pp. 54-103.

[10] M. S. Ashbaugh and P. Exner, *Lower bounds to bound state energies in bent tubes*, Phys. Lett. A **150** (1990), 183-186.

[11] R. Aurich and F. Steiner, *Exact theory for the quantum eigenstates of a strongly chaotic system*, Physica D **48** (1991), pp. 445-470.

[12] Y. Avishai, D. Bessis, B. G. Giraud, and G. Mantica, *Quantum bound states in open geometries*, Phys. Rev. B **44** (1991), 8028-8034.

[13] V. M. Babich and V. F. Lazutkin, *Eigenfunction concentrated near a closed geodesic*, Topics in Math. Phys. Vol 2 (Ed. by M. S. Birman), Consultant's Bureau, New York, 1968, pp. 9-18.

[14] A. Bäcker, R. Schubert, and P. Stifter, *On the number of bouncing ball modes in billiards*, J. Phys. A **30** (1997), pp. 6783-6795.

[15] A. Bäcker and R. Schubert, *Rate of quantum ergodicity in Euclidean billiards*, Phys. Rev. A **57** (1998), 5.

[16] Balagurov B. Ya. and Vaks V. G.: Random walks of a particle on lattices with traps, J. Exper. Theor. Phys. **38**, 968 (1974)

[17] A. H. Barnett, *Asymptotic rate of quantum ergodicity in chaotic Euclidean billiards*, Comm. Pure Appl. Math. **59** (2006), pp. 1457-1488.

[18] J. T. Beale, "Scattering Frequencies of Resonators", Comm. Pure and Appl. Math. **26** (4), 549-564 (1973).

[19] D. Belitz and T. R. Kirkpatrick, *The Anderson-Mott transition*, Rev. Mod. Phys. **66** (1994), 261.

[20] O. Bénichou, D. S. Grebenkov, P. Levitz, C. Loverdo, R. Voituriez, *Optimal Reaction Time for Surface-Mediated Diffusion*, Phys. Rev. Lett. **105** (2010), 150606.

[21] O. Bénichou, D. S. Grebenkov, P. Levitz, C. Loverdo, R. Voituriez, *Mean first-passage time of surface-mediated diffusion in spherical domains*, J. Stat. Phys. **142** (2011), 657-685.

[22] O. Bénichou and R. Voituriez, *Narrow-Escape Time Problem: Time Needed for a Particle to Exit a Confining Domain through a Small Window*, Phys. Rev. Lett. **100** (2008), 168105.

[23] T. Berry, S. M. Heilman, and R. S. Strichartz, *Outer Approximation of the Spectrum of a Fractal Laplacian*, Exp. Math. **18** (2009), pp. 449-480.

[24] W. Bies, L. Kaplan, M. Haggerty, E. Heller, *Localization of eigenfunctions in the stadium billiards*, Phys. Rev. E **63** (2001).

[25] D. A. Bini, L. Gemignani and F. Tisseur, *The Ehrlich-Aberth Method for the Nonsymmetric Tridiagonal Eigenvalue Problem*, SIAM.J.Matrix Anal.& Appl. **27** (2005), pp. 153–175.

[26] M. S. Birman, *O spektre singulyarnix granichnix zadach*, Math. Sb. **55** (1961), pp. 125-174 [in Russian].

[27] A. S. Bonnet-Ben Dhia and P. Joly, *Mathematical analysis of guided water waves*, SIAM J. Appl. Math. **53** (1993), pp. 1507-1550.

[28] F. Bowman, *Introduction to Bessel functions*, 1st Ed. (Dover Publications Inc., 1958).

[29] R. Brown, P. D. Hislop and A. Martinez, *Eigenvalues and resonances for domains with tubes: Neumann boundary conditions*, J. Diff. Eq. **115** (1995), pp. 458-476.

[30] K. R. Brownstein, C. E. Tarr: Importance of classical diffusion in NMR studies of water in biological cells, Phys. Rev. A, **19** (1979), pp. 2446-2453.

[31] E. N. Bulgakov, P. Exner, K. N. Pichugin, and A. F. Sadreev, *Multiple bound states in scissor-shaped waveguides*, Phys. Rev. B **66** (2002), 155109.

[32] W. Bulla, F. Gesztesy, W. Renger and B. Simon, *Weakly coupled bound states in quantum waveguides*, Proc. Amer. Math. Soc. **125** (1997), pp. 1487-1495.

[33] J. R. Bunch, C. P. Nielsen, and D. C. Sorensen, *Rank-one modification of symmetric eigenproblem*, Numerische Mathematik (1978), pp. 31-48.

[34] N. Burq and M. Zworski, *Bouncing Ball Modes and Quantum Chaos*, SIAM Rev. **47** (2005), pp. 43-49.

[35] J. P. Carini, J. T. Londergan, K. Mullen and D. P. Murdock, "Bound states and resonances in waveguides and quantum wires", Phys. Rev. B **46**, 15538-15541 (1992).

[36] J. P. Carini, J. T. Londergan, K. Mullen and D. P. Murdock, *Multiple bound states in sharply bent waveguides*, Phys. Rev. B **48** (1993), pp. 4503-4515.

[37] J. P. Carini, J. T. Londergan, D. P. Murdock, D. Trinkle and C. S. Yung, *Bound states in waveguides and bent quantum wires. I. Applications to waveguide systems*, Phys. Rev. B **55** (1997), 9842.

[38] H. S. Carslaw and J. C. Jaeger, *Conduction of Heat in Solids*, 2nd ed. (Clarendon, Oxford, 1959).

[39] J. Carrier, L. Greengard, and V. Rokhlin, *A fast adaptive multipole algorithm for particle simulations*, SIAM Journal on Scientific and Statistical Computing **9** (1988), 4, pp. 669-686.

[40] L. G. Chambers, *An Upper Bound for the First Zero of Bessel Functions*, Math. Comput. **38** (1982), pp. 589-591.

[41] G. Chen, P. J. Morris, and J. Zhou, *Visualization of special eigenmodes shapes of a vibrating elliptical membrane*, SIAM Rev. **36** (1994), pp. 453-469.

[42] B. Chenaud, P. Duclos, P. Freitas, D. Krejcirík, *Geometrically induced discrete spectrum in curved tubes*, Diff. Geom. Appl. **23** (2005), pp. 95-105.

[43] A. F. Cheviakov , M. J. Ward , and r. Straube, *An Asymptotic Analysis of the Mean First Passage Time for Narrow Escape Problems: Part II. The Sphere*, SIAM Multiscale Model. Simul. **8** (2010), pp. 836-870.

[44] A. Cheviakov and M. J. Ward, *Optimizing the Principal Eigenvalue of the Laplacian in a Sphere with Interior Traps*, Math. Computer Modeling, **53** (2011), 7-8, pp. 1394-1409.

[45] Y. Colin de Verdière, *Ergodicité et fonctions propres du laplacien*, Comm. Math. Phys. **102** (1985), pp. 497-502.

[46] Condamin S., Bénichou O., and Moreau M., First-Passage Times for Random Walks in Bounded Domains, Phys. Rev. Lett. **95**, 260601 (2005)

[47] Condamin S., Bénichou O., and Moreau M.: First-exit times and residence times for discrete random walks on finite lattices, Phys. Rev. E **72**, 016127 (2005)

[48] Condamin S., Bénichou O., Tejedor V., Voituriez R., and Klafter J.: First-passage time in complex scale-invariant media, Nature **450**, 77 (2007)

[49] Condamin S., Bénichou O., and Moreau M.: Random walks and Brownian motion: A method of computation for first-passage times and related quantities in confined geometries, Phys. Rev. E **75**, 021111 (2007)

[50] Condamin S., Tejedor V., and Bénichou O.: Occupation times of random walks in confined geometries: From random trap model to diffusion-limited reactions, Phys. Rev. E **76**, 050102R (2007)

[51] M. Conti, S. Terracini, G. Veizini, *An optimal partition problem related to nonlinear eigenvalues*, J. Funct. Anal. **198** (2003), 1, pp. 160-196.

[52] M. Conti, S. Terracini, G. Veizini, *On a class of optimal partition problems related to Fucik spectrum and to the monotonicity formulae*, Calc. Var. Partial Differential Equations **22** (2005), 1, pp. 45-72.

[53] M.-O. Coppens, *The effect of fractal surface roughness on diffusion and reaction in porous catalysts: from fundamentals to practical application*, Catalysis Today **53** (1999), pp. 225-243.

[54] R. Courant and D. Hilbert, *Methods of Mathematical Physics* (Wiley, New York, 1989).

[55] J. Crank, *The Mathematics of Diffusion*, 2nd ed. (Claredon, Oxford, 1975).

[56] J. J. M. Cuppen *A divide and conquer method for the symmetric tridiagonal eigenproblem*, Numerische Mathematik **36**(1980), pp. 177-195.

[57] D. Daners, *Dirichlet problems on varying domains*, J. Diff. Eq. **188** (2003), pp. 591-624.

[58] B. Daudert and M. Lapidus, *Localization on Snowflake Domains*, Fractals **15** (2007), 255.

[59] E. B. Davies and L. Parnovski, *Trapped modes in acoustic waveguides*, Q. J. Mech. Appl. Math. **51** (1998), pp. 477-492.

[60] A. Delitsyn, B. T. Nguyen, D. S. Grebenkov, *Exponential decay of Laplacian eigenfunctions in domains with branches of variable cross-sectional profiles*, European Physical Journal B **35** (2012), 371.

[61] A. Delitsyn, B. T. Nguyen, D. S. Grebenkov, *Trapped modes in finite quatum waveguides*, European Physical Journal B **85** (2012), 6.

[62] A. L. Delitsyn, *The Discrete Spectrum of the Laplace Operator in a Cylinder with Locally Perturbed Boundary*, Diff. Eq. **40** (2004), pp. 207-217.

[63] I. S. Dhillon *A new $O(N^2)$ algorithm for the symmetric tridiagonal eigenvalue/eigenvector problem*, PhD thesis, Berkeley, CA, USA, 1998. UMI Order No. GAX98-03176.

[64] J. Dittrich and J. Kríz, *Curved planar quantum wires with Dirichlet and Neumann boundary conditions*, J. Phys. A: Math. Gen. **35** (2002), pp. 269-275.

[65] H. Donnelly, *Quantum unique ergodicity*, Proc. Amer. Math. Soc. **131** (2003), pp. 2945-2951.

[66] H. Donnelly, *Spectral gap for convex planar domains*, Math. Z. **269** (2011), pp. 1-3.

[67] P. Duclos and P. Exner, *Curvature-induced bound states in quantum waveguides in two and three dimensions*, Rev. Math. Phys. **7** (1995), pp. 73-102.

[68] A. Elbert, *Some recent results on the zeros of Bessel functions and orthogonal polynomials*, J. Comput. Appl. Math. **133** (2001), pp. 65-83.

[69] D. V. Evans, *Trapped acoustic modes*, IMA J. Appl. Math. **49** (1992), pp. 45-60.

[70] D. V. Evans, M. Levitin and D. Vassiliev, *Existence theorems for trapped modes*, J. Fluid Mech. **261** (1994), pp. 21-31.

[71] C. Even, S. Russ, V. Repain, P. Pieranski and B. Sapoval, *Localizations in Fractal Drums: An Experimental Study*, Phys. Rev. Lett. **83** (1999), 726.

[72] F. Evers and A. D. Mirlin, *Anderson transitions*, Rev. Mod. Phys. **80** (2008), 1355.

[73] P. Exner, P. Freitas and D. Krejčiřík, *A lower bound to the spectral threshold in curved tubes*, Proc. R. Soc. Lond. A **460** (2004), pp. 3457-3467.

[74] P. Exner and P. Seba, *Bound states in curved quantum waveguides*, J. Math. Phys. **30** (1989), pp. 2574-2580.

[75] P. Exner, P. Seba, M. Tater and D. Vanek, *Bound states and scattering in quantum waveguides coupled laterally through a boundary window*, J. Math. Phys. **37** (1996), 4867.

[76] S. Felix, M. Asch, M. Filoche and B. Sapoval, *Localization and increased damping in irregular acoustic cavities*, J. Sound. Vibr. **299** (2007), 965.

[77] M. Filoche and S. Mayboroda, *Strong Localization Induced by One Clamped Point in Thin Plate Vibrations*, Phys. Rev. Lett. **103** (2009), 254301.

[78] M. Filoche and S. Mayboroda, *The Hidden Landscape of Localization*, ArXiv:1107.0397v1 (2011).

[79] G. J. F. Francis *The QR transformation*, parts I and II, Computer J. pages 4:265-271, 332-345, 1961-62.

[80] P. Freitas and D. Krejcirik, *Unbounded planar domains whose second nodal line does not touch the boundary*, Math. Res. Lett. **14** (2007), 1, pp. 107-111.

[81] P. Freitas and D. Krejčiřík, *Waveguides with Combined Dirichlet and Robin Boundary Conditions*, Math. Phys. Anal. Geom. **9** (2006), pp. 335-352.

[82] P. Freitas and D. Krejčiřík, *A sharp upper bound for the first Dirichlet eigenvalue and the growth of the isoperimetric constant of convex domains*, Proc. Amer. Math. Soc. **136** (2008), pp. 2997-3006.

[83] D. Frenkel and R. Portugal, *Algebraic methods to compute Mathieu functions*, J. Phys. A: Math. Gen. **34** (2001), pp. 3541-3551.

[84] R. R. Gadyl'shin, *On the eigenvalues of a dumb-bell with a thin handle*, Izvestiya: Mathematics **69**:2 (2005), pp. 265-329.

[85] R. R. Gadyl'shin, *Characteristic frequencies of bodies with thin spikes. I. Convergence and estimates*, Mathematical Notes **54** (1993), 6, pp.1192-1199.

[86] R. R. Gadyl'shin, *Characteristic frequencies of bodies with thin spikes. II. Asymptotics*, Mathematical Notes **55** (1994), 1, pp. 14-23.

[87] M. Gu and S. C. Eisenstat *A stable and efficient algorithm for the rank-one modification of the symmetric eigenproblem*, SIAM J. Mat. Anal. Appl. **15** (1994), 4, pp. 1266-1276. Yale Tech report YALEU/DCS/RR-916, Sept 1992.

[88] M. Gu and S. C. Eisenstat *A divide-and-conquer algorithm for the symmetric tridiagonal eigenproblem*, SIAM J. Matrix Anal. Appl. **16** (1995), pp. 172-191.

[89] P. Gérard and E. Leichtnam, *Ergodic properties of eigenfunctions for the Dirichlet problem*, Duke Math. J. **71** (1993), pp. 559-607.

[90] I. M. Glazman, *Direct Methods of Qualitative Spectral Analysis of Singular Differential Operators* (Fizmathgiz, Moscow, 1963; Translated in English in 1965).

[91] J. Goldstone and R. L. Jaffe, *Bound states in twisting tubes*, Phys. Rev. B **45** (1992), pp. 14100-14107.

[92] L. Greengard and V.Rokhlin *A fast algorithm for particle simulations*, Journal of Computational Physics **73**(1987), 2, pp. 325-348.

[93] I. S. Gradshteyn and I. M. Ryzhik, *Table of Integrals, Series and Products* (New York: Academic Press, 1980).

[94] Grassberger P. and Procaccia I.: The long time properties of diffusion in a medium with static traps, J. Chem. Phys. **77**, 6281-6284 (1982)

[95] D. S. Grebenkov, B. T. Nguyen, *Geometrical structure of Laplacian eigenfunctions*, http://arxiv.org/abs/1206.1278, (submitted).

[96] D. S. Grebenkov, *Multiple correlation function approach: rigorous results for simples geometries*, Diff. Fundam. **5** (2007), 1.

[97] D. S. Grebenkov, *Residence times and other functionals of reflected Brownian motion*, Phys. Rev. E **76** (2007), 041139.

[98] D. S. Grebenkov, *NMR survey of reflected Brownian motion*, Rev. Mod. Phys. **79** (2007), pp. 1077-1137.

[99] D. S. Grebenkov, *Laplacian eigenfunctions in NMR I. A numerical tool*, Concepts Magn. Reson. A **32** (2008), pp. 277-301.

[100] D. S. Grebenkov, *Analytical solution for restricted diffusion in circular and spherical layers under inhomogeneous magnetic fields*, J. Chem. Phys. **128** (2008), 134702.

[101] D. S. Grebenkov, *Subdiffusion in a bounded domain with a partially absorbing/reflecting boundary*, Phys. Rev. E **81** (2010), 021128.

[102] P. Grisvard, *Elliptic Problem for nonsmooth domain* (Pitman Advanced Publishing Company, Boston, 1985).

[103] The Group Numerical Analysis at Delft University of Technology, *On the Computation of Mathieu functions*, J. Engnr. Math. **7** (1973), pp. 39-61.

[104] O. Haeberle, B. Sapoval, K. Menou and H. Vach, *Observation of vibrational modes of irregular drums*, Appl. Phys. Lett. **73** (1998), 3357.

[105] A. Hassell, *Ergodic billiards that are not quantum unique ergodic*, Ann. Math. **171** (2010), pp. 605-618.

[106] B. Hébert, B. Sapoval and S. Russ, *Experimental study of a fractal acoustical cavity*, J. Acoust. Soc. Am. **105** (1999) 1567.

[107] S. M. Heilman and R. S. Strichartz, *Localized Eigenfunctions: Here You See Them, There You Don't*, Notices Amer. Math. Soc. **57** (2010), pp. 624-629.

[108] B. Helffer, T. Hoffmann-Ostenhof, *Converse spectral problems for nodal domains*, Mos. Math. Journal **7**, 1 (2007), pp. 67-84.

[109] B. Helffer, T. Hoffmann-Ostenhof, S. Terracini, *Nodal domains and spectral minimal partitions*, Ann. I. H. Poin. **26** (2009), pp. 101-138.

[110] R. Hempel, L. Seco and B. Simon, *The essential spectrum of Neumann Laplacians on some bounded singular domain*, J. Funct. Anal. **102** (1991), pp. 448-483.

[111] M. Hoffmann-Ostenhof, T. Hoffmann-Ostenhof, and N. Nadirashvili, *The nodal line of the second eigenfunction of the Laplacian in $\mathbb{R}^2$2 can be closed*, Duke Math. J. **90**, 3 (1997), pp. 631-640.

[112] D. Holcman, A. Marchewka, and Z. Schuss, *Survival probability of diffusion with trapping in cellular neurobiology*, Phys. Rev. E **72** (2005), 031910.

[113] A. S. Householder, *Unitary triangularization of a nonsymmetric matrix*, J. ACM **5** (1958), pp. 339-342.

[114] B. D.Hughes, *Random Walks and Random Environments* (Clarendon Press, Oxford, 1995).

[115] J. D. Jackson, *Classical Electrodynamics*, 3rd Ed. (Wiley & Sons, New York, 1999). , p. 360.

[116] D. Jakobson, N. Nadirashvili and J. Toth, *Geometric properties of eigenfunctions*, Russ. Math. Surv. **56** (2001), pp. 1085-1105.

[117] D. Jakobson, N. Nadirashvili, *Eigenfunctions with a few critical points*, J. Diff. Geom. **53** (1999), pp. 177-182.

[118] D. Jerison, *The first nodal line of a convex planar domain*, Duke Math. J. **62** (1991), Internat. Math. Res. Notices **1** (1991), pp. 1-5.

[119] S. Jimbo, *The singularly pertubed domain and the characterization for the eigenfunctions with Neumann boundary conditions*, J. Diff. Eq. **77** (1989), pp. 322-350.

[120] S. Jimbo and Y. Morita, *Remarks on the behavior of certain eigenvalues on a singularly pertubed domain with several thin channels*, Comm. Part. Diff. Eq. **17** (1992), pp. 523-552.

[121] S. Jimbo, *Pertubation formula of eigenvalues in a singularly pertubed domain*, J. Math. Soc. Japan **45** (1993), pp. 339-356.

[122] D. S. Jones, *The eigenvalues of $\nabla^2 u + \lambda u = 0$ when the boundary conditions are on semi-infinite domains*, Math. Proc. Camb. Phil. Soc. **49** (1953), pp. 668-684.

[123] P. W. Jones, M. Maggioni, and R. Schul, *Manifold parametrizations by eigenfunctions of the Laplacian and heat kernels,*

[124] Kansal A. R. and Torquato S.: Prediction of trapping rates in mixtures of partially absorbing spheres, J. Chem. Phys. **116**, 10589 (2002).

[125] L. Kaplan and E. Heller, *Weak quantum ergodicity*, Phys. D **121** (1998), pp. 1-18. Proc. Nat. Ac. Sci. **105** (2008), pp. 1803-1808.

[126] Kayser R.F. and Hubbard J. B.: Diffusion in a Medium with a Random Distribution of Static Traps, Phys. Rev. Lett. **51**, 79 (1983)

[127] Kayser R. F. and Hubbard J. B.: Reaction diffusion in a medium containing a random distribution of nonoverlapping traps, J. Chem. Phys. **80**, 1127 (1984)

[128] J. B. Keller and S. I. Rubinow, *Asymtotic solution of eigenvalue problems*, Ann. Phys. **9** (1960), pp. 24-75.

[129] E. T. Kippatrick, *Tables of values of the modified Mathieu function*, Math. Comp. **14** (1960), pp. 118-129.

[130] T. Kolokolnikov, M. S. Titcombe, and M. J. Ward, *Optimizing the Fundamental Neumann Eigenvalue for the Laplacian in a Domain with Small Traps*, Eur. J. Appl. Math. **16** (2005), 161.

[131] P. Kröger, *On the Ground State Eigenfunction of a Convex Domain in Euclide Space*, Pot. Anal. **5** (1996), pp. 103-108.

[132] V. N. Kublanovskaya *On some algorithms for the solution of the complete eigenvalue problem*, Zh. Vychisl. Mat. Mat. Fiz., pages 555-570, 1961.

[133] J. R. Kuttler and V. G. Sigillito, *Eigenvalues of the Laplacian in two Dimensions*, SIAM Review **26** (1984), pp. 163-193.

[134] M. Lapidus, *Fractal Drum, Inverse Spectral Problems for Elliptic Operators and a Partial Resolution of the Weyl-Berry Conjecture*, Trans. Am. Math. Soc. **325** (1991), 465.

[135] M. L. Lapidus and M. M. H. Pang, *Eigenfunctions of the Koch snowflake domain*, Commun. Math. Phys. **172** (1995), pp. 359-376.

[136] M. L. Lapidus, J. W. Neuberger, R. J. Renka and C. A. Griffith, *Snowflake Harmonics and Computer Graphics: Numerical Computation of Spectra on Fractal Drums*, Int. J. Bifur. Chaos **6** (1996), pp. 1185-1210.

[137] V. F. Lazutkin, *Construction of an asymptotic series of eigenfunctions of the bouncing ball type*, Proc. Steklov Inst. Math. **95** (1968), pp. 106-118.

[138] V. F. Lazutkin, *The existence of caustics for a billiard problem in a convex domain*, Math. USSR Izv. **7** (1973), pp. 185-214.

[139] V. F. Lazutkin, *Vypuklyj billiard i sobstvennye funkcii operatora Laplasa* (Leningr. univ., 1981) [in Russian].

[140] V. F. Lazutkin, *KAM theory and semiclassical approximations to eigenfunctions* (Ergebnisse der Mathematik und ihrer Grenzgebiete (3), Vol. 24, 1993).

[141] S. Y. Lee, S. Rim, J. W. Ryu, T. Y. Kwon, M. Choi, and C. M. Kim, *Quasiscarred Resonances in a Spiral-Shaped Microcavity*, Phys. Rev. Lett. **93** (2004), 164102.

[142] Lee S. B., Kim I. C. , Miller C. A., and Torquato S.: Random-walk simulation of diffusion-controlled processes among static traps, Phys. Rev. B **39**, 11833 (1989)

[143] W. R. Leeb, *Algorithm 537: Characteristic values of Mathieu's differential equation*, ACM. Trans. Math. Software **5** (1979), pp. 112-117.

[144] Levitz, P. E., Grebenkov D. S., Zinsmeister M., Kolwankar K., and Sapoval B.: Brownian flights over a fractal nest and first passage statistics on irregular surfaces, Phys. Rev. Lett. **96**, 180601 (2006)

[145] C. S. Lin, *On the second eigenfunctions of the Laplacian in* $\mathbb{R}^2$, Comm. Math. Phys. **111** (1987), 161-166.

[146] C. M. Linton and P. McIver, *Embedded trapped modes in water waves and acoustics*, Wave Motion **45** (2007), pp. 16-29.

[147] J. L. Lions and E. Magenes, *Non-homogeneous boundary value problems and applications* (Berlin, New York: Springer-Verlag, 1972).

[148] C. C. Liu, T. H. Lu, Y. F. Chen, and K. F. Huang, *Wave functions with localizations on classical periodic orbits in weakly perturbed quantum billiards*, Phys. Rev. E **74** (2006), 046214.

[149] J. T. Londergan, J. P. Carini, and D. P. Murdock, *Binding and Scattering in Two-Dimensional Systems: Applications to Quantum Wires, Waveguides and Photonic Crystals* (Springer, Berlin, 1999).

[150] S. N. Majumdar, *Brownian functionals in Physics and Computer Science*, Curr. Sci. **89** (2005), 2076.

[151] J. Marlof and Z. Rudnick, *Almost all eigenfunctions of a rational polygon are uniformly distributed* Journal of. Spectral Theory **2** (2012), pp. 107–113.

[152] V. P. Maslov, *Perturbation theory and asymptotic methods* (Moscow State Univ., Moscow, 1965) [in Russian].

[153] V. P. Maslov, *The behavior at infinity of eigenfunctions of the Schrödinger equation*, Sov. Math. Surv. **19** (1964), 1 (115), pp. 199-201 [in Russian].

[154] P. N. McGraw and M. Menzinger, *Laplacian spectra as a diagnostic tool for network structure and dynamics*, Phys. Rev. E **77** (2008), 031102.

[155] N. W. McLachlan, *Theory and Application of Mathieu functions* (Oxford University Press, 1947).

[156] A. D. Melas, *On the nodal line of the second eigenfunction of the Laplacian in* $\mathbb{R}^2$, J. Differential Geom. **35** (1992), pp. 255-263.

[157] Miller C. A. and Torquato S.: Diffusion-controlled reactions among spherical traps: Effect of polydispersity in trap size, Phys. Rev. B **40**, 7101 (1989)

[158] Miller C. A., Kim I. C. and Torquato S.: Trapping and flow among random arrays of oriented spheroidal inclusions, J. Chem. Phys. **94**, 5592 (1991)

[159] Armando G. M. Neves, *Eigenmodes and eigenfrequencies of vibrating elliptic membranes: a Klein oscillation theorem and numerical calculations*, Communications on Pure and Applied Analysis, **9**, 3 (2010), pp. 611-624.

[160] B. T. Nguyen, D. S. Grebenkov, *Localization of Laplace eigenfunctions in circular, spherical and elliptical domains*, http://arxiv.org/abs/1203.5022, (submitted).

[161] B. T. Nguyen, L. T. A. Duc, N. D. Thuc, B. V. Thach, *A divide-and-conquer algorithm for a symmetric tri-block-diagonal matrix*, Proceedings of IEEE SoutheastCon 2012 (2012).

[162] B. T. Nguyen, D. S. Grebenkov, *A Spectral Approach to Survival Probability in Porous Media*, J. Stat. Phys. **141** (2010), pp. 532-554.

[163] O. Olendski and L. Mikhailovska, *Theory of a curved planar waveguide with Robin boundary conditions*, Phys. Rev. E **81**, 036606 (2010).

[164] F. W. J. Olver, *A further method for the evaluation of zeros of Bessel functions, and some new asymptotic expansions for zeros of functions of large order*, Proc. Cambridge Philos. Soc. **47** (1951), pp. 699-712.

[165] F. W. J. Olver, *Some new asymptotic expansions for Bessel functions of large orders*, Proc. Cambridge Philos. Soc. **48** (1952), pp. 414-427.

[166] Y. B. Orocko, "On the Application of the Spectral Theory to Obtain Estimates of Solutions of Schrödinger Equation", Math. USSR Sb. **22** (2) 167-186 (1974).

[167] M. Pang, *Approximation of ground state eigenfunction on the snowflake region* , Bull. London. Math. Soc. **28** (1996), pp. 488-494

[168] M. Pang, *Approximation of ground state eigenvalues and eigenfunctions of Dirichlet Laplacians*, Bull. London. Math. Soc. **29** (1997), pp. 720-730.

[169] R. Parker, *Resonance effects in wake shedding from parallel plates: some experimental observations*, J. Sound Vib. **4** (1966), pp. 62-72.

[170] R. Parker, *Resonance effects in wake shedding from parallel plates: calculation of resonance frequencies*, J. Sound Vib. **5** (1967), pp. 330-343.

[171] L. Payne, *On two conjectures on the fixed membrane eigenvalue problem*, Z. Angew. Math. Phys. **24** (1973), pp. 720-729.

[172] S. Pillay, M. J. Ward, A. Peirce, and T. Kolokolnikov, *An Asymptotic Analysis of the Mean First Passage Time for Narrow Escape Problems: Part I. Two-Dimensional Domains*, SIAM Multiscale Model. Simul. **8** (2010), pp. 803-835.

[173] M. A. Pinsky, *The Eigenvalues of an Equilateral Triangle*, SIAM J. Math. Anal. **11** (1980), pp. 819-827.

[174] M. A. Pinsky, *Completeness of the Eigenfunctions of the Equilateral Triangle*, SIAM J. Math. Anal. **16** (1985), pp. 848-851.

[175] T. Prosen and M. Robnik, *Survey of the eigenfunctions of a billiard system between integrability and chaos*, J. Phys. A **26** (1993), pp. 5365.

[176] R. Putter, *On the nodal line of second eigenfunctions of the fixed membrane problem*, Comment. Math. Helv **65** (1990), 96-103.

[177] C. V. Raman and G. A. Sutherland, *Whispering gallery phenomana at St. Paul's Cathedral*, Nature **108** (1921), 42.

[178] C. V. Raman and G. A. Sutherland: *On the whispering-gallery phenomenon*, Proc. Royal Soc. A **100** (1922), pp. 424-428.

[179] L. O. M. Rayleigh, *The problem of the whispering gallery*, Phil. Mag. **20** (1910), pp. 1001-1004.

[180] S. Redner, A Guide to First-Passage Processes (Cambrigde University Press, Cambridge, England, 2001).

[181] F. Rellich, *Das Eigenwertproblem von in Halbrohren*, (New York, Studies and Essays Presented to R. Courant, 1948), pp. 329-344.

[182] Richards P. M.: Diffusion to Finite-Size Traps, Phys. Rev. Lett. **56**, 1838 (1986)

[183] Richards P. M.: Diffusion to nonoverlapping or spatially correlated traps, Phys. Rev. B **35**, 248 (1987)

[184] Richards P. M. and Torquato S.: Upper and lower bounds for the rate of diffusion-controlled reactions, J. Chem. Phys. **87**, 4612 (1987)

[185] Rubinstein J. and Torquato S.: Diffusion-controlled reactions: Mathematical formulation, variational principles, and rigorous bounds, J. Chem. Phys. **88**, 6372 (1988)

[186] Z. Rudnick and P. Sarnak, *The behaviour of eigenstates of arithmetic hyperbolic manifolds*, Comm. Math. Phys. **161** (1994), pp. 195-213.

[187] S. Russ and B. Sapoval, *Increased damping of irregular resonators*, Phys. Rev. E **65** (2002), 036614.

[188] S. Russ, B. Sapoval and O. Haeberle, *Irregular and fractal resonators with Neumann boundary conditions: Density of states and localization*, Phys. Rev. E **55** (1997), 1413.

[189] N. Saito, *Data analysis and representation on a general domain using eigenfunctions of Laplacian*, Applied and Computational Harmonic Analysis **25** (2008), 1, pp.68-97.

[190] B. Sapoval, *Experimental observation of local modes of fractal drums*, Physica D **38** (1989), pp. 296-298.

[191] B. Sapoval, T. Gobron and A. Margolina, *Vibrations of fractal drums*, Phys. Rev. Lett. **67** (1991), 2974.

[192] B. Sapoval and T. Gobron, *Vibrations of strongly irregular or fractal resonators*, Phys. Rev. E **47** (1993), 3013.

[193] B. Sapoval, O. Haeberle and S. Russ, *Acoustical properties of irregular and fractal cavities*, J. Acoust. Soc. Am. **102** (1997), 2014.

[194] E. E. Schnol', "On Behaviour of the eigenfunctions of Schrödinger's Equation", Mat. Sb. **42** (84) 273-286 (1957).

[195] R. L. Schult, D. G. Ravenhall and H. W. Wyld, *Quantum bound states in a classically unbound system of crossed wires*, Phys. Rev. B **39** (1989), pp. 5476-5479.

[196] J. Schwinger, *On the bound states of a given potential*, Proc. Nat. Acad. Sci. **47** (1961), pp. 122-129.

[197] R. B. Shirts, *The Computation of Eigenvalues and solutions of Mathieu's differential equation for noninteger order*, ACM Trans. Math. Software **19** (1993), pp. 377-390.

[198] A. Shnirelman, *Ergodic properties of eigenfunctions*, Uspechi Math. Nauk **29** (1974), pp. 181-182.

[199] K. M. Siegel, *An inequality involving Bessel functions of argument nearly equal to their orders*, Proc. Amer. Math. Soc. **4** (1953), pp. 858-859.

[200] Ya. G. Sinai, *Introduction to Ergodic Theory* (Princeton University, Princeton, NJ, 1976).

[201] Ya. G. Sinai, *Dynamical systems with elastic reflections: ergodic properties of dispersing billiards*, Russ. Math. Surv. **25** (1970), pp. 137-189.

[202] A. Singer, Z. Schuss, D. Holcman, and R. S. Eisenberg, *Narrow Escape. Part I*, J. Stat. Phys. **122** (2006), 437.

[203] A. Singer, Z. Schuss, and D. Holcman , *Narrow Escape. Part II: The Circular Disk*, J. Stat. Phys. **122** (2006), 465.

[204] J. Slemons, *Toward the Solution of the Eigenproblem: Nonsymmetric Tridiagonal Matrices* PhD thesis, University of Washington (2007).

[205] Smoluchowski M. V.: Phys. Z. **17**, 557 (1916).

[206] S. Sridhar, *Experimental observation of scarred eigenfunctions of chaotic microwave cavities*, Phys. Rev. Lett. **67** (1991), pp. 785-788.

[207] S. Sridhar, D. O. Hogenboom and B. A. Willemsen, *Microwave experiments on chaotic billiards*, J. Stat. Phys. **68** (1992), pp. 239-258.

[208] G. Timp, H. U. Baranger, P. deVegvar, J. E. Cunningham, R. E. Howard, R. Behringer and P. M. Mankiewich, "Propagation around a Bend in a Multichannel Electron Waveguide", Phys. Rev. Lett. **60**, 2081-2084 (1988).

[209] Torquato S. and Kim I. C.: Efficient simulation technique to compute effective properties of heterogeneous media, Appl. Phys. Lett. **55**, 1847 (1989)

[210] Torquato S. and Avellaneda M.: Diffusion and reaction in heterogeneous media: pore-size distribution, relaxation times, and mean survival time, J. Chem. Phys. **95**, 6477 (1991)

[211] Torquato S.: Diffusion and reaction among traps: some theoretical and simulation results, J. Stat. Phys. **65**, 1173 (1991)

[212] Torquato S. and Yeong C. L. Y.: Universal scaling for diffusion-controlled reactions among traps, J. Chem. Phys. **106**, 8814 (1997)

[213] J. Toth, S. Zelditch, *Counting nodal lines which touch the boundary of an analytic domain*, J. Differential Geom., **81**, 3 (2009), pp. 649-686.

[214] L. N. Trefethen and David Bau *Numerical Linear Algebra*, SIAM, June 1997.

[215] A. Truman and D. Williams, *Diffusion Processes and Related Problems in Analysis*, Vol.1, Ed. Pinsky (Birkhauser: Boston, 1990).

[216] F. Ursell, *Trapping modes in the theory of surface waves*, Math. Proc. Camb. Phil. Soc. **47** (1951), pp. 347-358.

[217] F. Ursell, *Mathematical aspects of trapping modes in the theory of surface waves*, J. Fluid Mech. **183** (1987), pp. 421-437.

[218] F. Ursell, *Trapped Modes in a Circular Cylindrical Acoustic Waveguide*, Proc. R. Soc. Lond. A **435** (1991), pp. 575-589.

[219] G. Veble, M. Robnik, and J. Liu, *Study of regular and irregular states in generic systems*, J. Phys. A **32** (1999), pp. 6423-6444.

[220] V. K. Vlasov, M. N. Glukhova, L. N. Korolev, S. N. Razumovskii and O. L. Olasik, *On the computation of Mathieu functions*, Moscow Uni. Comput. Math. Cybenetics **1** (1992), pp. 59-63.

[221] M. J. Ward, *Asymptotic Methods for Reaction-Diffusion Systems: Past and Present*, Bull. Math. Biol. **68**, 1151 (2006).

[222] G. N. Watson, *A treatise on the theory of Bessel functions* (Cambridge Mathematical Library 1995).

[223] G. H. Weiss , *Aspects and Applications of the Random Walk*, (North-Holland, Amsterdam, 1994).

[224] G. H. Weiss, *Overview of theoretical models for reaction rates*, J. Stat. Phys. **42** (1986), 3.

[225] H. Weyl, *Über die asymptotische Verteilung der Eigenwerte*, Gott. Nach. (1911), pp. 110-117.

[226] H. Weyl, *Das asymptotische Verteilungsgesetz der Eigenwerte linearer partieller Differentialgleichungen*, Math. Ann. **71** (1912), pp. 441-479.

[227] J. Wiersig, *Structure of whispering-gallery modes in optical microdisks pertubed by nanoparticles*, Phys. Rev. A **84** (2011), 063828.

[228] S. T. Yau, *Problem Section*, Seminar on Differential Geometry, Anna. of Math. Stud **102** (1982), pp. 669-706.

[229] S. T. Yau, *Open problems in geometry*, Differential geometry: partial differential equations on manifolds, Proc. Symp. Pure Math. **54**(1993), pp. 1-28.

[230] S. T. Yau, *A note on the distribution of critical points of eigenfunctions*, Tsing Hua Lectures in Geometry and Analysis (1997), pp. 315-317, Internat. Press.

[231] Yuste S. B., Oshanin G., Lindenberg K., Bénichou O., and Klafter J.: Survival probability of a particle in a sea of mobile traps: A tale of tails, Phys. Rev. E **78**, 021105 (2008)

[232] S. Zelditch and M. Zworski, *Ergodicity of eigenfunctions for ergodic billiards*, Commun. Math. Phys. **175** (1996), pp. 673-682.

[233] S. Zelditch, *Quantum mixing*, J. Funct. Anal. **140** (1996), pp. 68-86.

[234] S.-J. Zhang and J.-M. Jin, *Computation of Special Functions*, (John Wiley and Sons Inc., New York, 1996).

[235] R. Zwanzig and A. Szabo, *Time dependent rate of diffusion-influenced ligand binding to receptors on cell surfaces*, Biophys. J. **60** (1991), pp. 671-678.